frontiers | Research Topics

Multi-physics and multi-scale modeling and simulation methods for nuclear reactor application

Edited by
Xingjie Peng, Qingming He, Jingang Liang, Shichang Liu and Jiankai Yu

Published in
Frontiers in Energy Research

ISSN 1664-8714
ISBN 978-2-8325-4537-9
DOI 10.3389/978-2-8325-4537-9

About Frontiers

Frontiers is more than just an open access publisher of scholarly articles: it is a pioneering approach to the world of academia, radically improving the way scholarly research is managed. The grand vision of Frontiers is a world where all people have an equal opportunity to seek, share and generate knowledge. Frontiers provides immediate and permanent online open access to all its publications, but this alone is not enough to realize our grand goals.

Frontiers journal series

The Frontiers journal series is a multi-tier and interdisciplinary set of open-access, online journals, promising a paradigm shift from the current review, selection and dissemination processes in academic publishing. All Frontiers journals are driven by researchers for researchers; therefore, they constitute a service to the scholarly community. At the same time, the *Frontiers journal series* operates on a revolutionary invention, the tiered publishing system, initially addressing specific communities of scholars, and gradually climbing up to broader public understanding, thus serving the interests of the lay society, too.

Dedication to quality

Each Frontiers article is a landmark of the highest quality, thanks to genuinely collaborative interactions between authors and review editors, who include some of the world's best academicians. Research must be certified by peers before entering a stream of knowledge that may eventually reach the public - and shape society; therefore, Frontiers only applies the most rigorous and unbiased reviews. Frontiers revolutionizes research publishing by freely delivering the most outstanding research, evaluated with no bias from both the academic and social point of view. By applying the most advanced information technologies, Frontiers is catapulting scholarly publishing into a new generation.

What are Frontiers Research Topics?

Frontiers Research Topics are very popular trademarks of the *Frontiers journals series*: they are collections of at least ten articles, all centered on a particular subject. With their unique mix of varied contributions from Original Research to Review Articles, Frontiers Research Topics unify the most influential researchers, the latest key findings and historical advances in a hot research area.

Find out more on how to host your own Frontiers Research Topic or contribute to one as an author by contacting the Frontiers editorial office: frontiersin.org/about/contact

Multi-physics and multi-scale modeling and simulation methods for nuclear reactor application

Topic editors

Xingjie Peng — Nuclear Power Institute of China (NPIC), China
Qingming He — Xi'an Jiaotong University, China
Jingang Liang — Tsinghua University, China
Shichang Liu — North China Electric Power University, China
Jiankai Yu — Massachusetts Institute of Technology, United States

Citation

Peng, X., He, Q., Liang, J., Liu, S., Yu, J., eds. (2024). *Multi-physics and multi-scale modeling and simulation methods for nuclear reactor application*.
Lausanne: Frontiers Media SA. doi: 10.3389/978-2-8325-4537-9

Table of contents

frontiers | Frontiers in Energy Research

TYPE Editorial
PUBLISHED 20 February 2024
DOI 10.3389/fenrg.2024.1361541

OPEN ACCESS

EDITED AND REVIEWED BY
Shripad T. Revankar,
Purdue University, United States

*CORRESPONDENCE
Shichang Liu,
liu-sc@ncepu.edu.cn

RECEIVED 26 December 2023
ACCEPTED 30 January 2024
PUBLISHED 20 February 2024

CITATION
Peng X, Liu S, He Q, Liang J and Yu J (2024), Editorial: Multi-physics and multi-scale modeling and simulation methods for nuclear reactor application.
Front. Energy Res. 12:1361541.
doi: 10.3389/fenrg.2024.1361541

Editorial: Multi-physics and multi-scale modeling and simulation methods for nuclear reactor application

Xingjie Peng[1], Shichang Liu[2]*, Qingming He[3], Jingang Liang[4] and Jiankai Yu[5]

[1]Science and Technology on Reactor System Design Technology Laboratory, Nuclear Power Institute of China, Chengdu, China, [2]North China Electric Power University, Beijing, China, [3]Xi'an Jiaotong University, Xi'an, China, [4]Tsinghua University, Beijing, China, [5]Massachusetts Institute of Technology Cambridge, Cambridge, MA, United States

KEYWORDS

multi-physics, multi-scale, modeling and simulation, nuclear reactor, radiation damage

Editorial on the Research Topic
Multi-physics and multi-scale modeling and simulation methods for nuclear reactor application

A nuclear reactor works within an intricate circumstance characterized by complicated multi-physics and multi-scale interactions. Its operation necessitates a comprehensive analysis of the interplay among neutronics, fuel property, thermal and hydraulic engineering, chemical kinetics, and the interconnection among the reactor core and the primary loop. By utilizing high fidelity numerical simulations, taking into account the coupling between diverse physics, and providing formidable numerical simulation tools, achieving security, reliable, and cost-effective operation is attainable. Historically, reduced models were employed to represent certain physics phenomena. However, recent advancements in numerical calculation theory, software development, and the capabilities of HPC have propelled the evolution of reactor computational tools towards a paradigm that embraces multi-physics and high-fidelity simulations.

Many research has been conducted by coupling multi-physics and multi-scale codes, such as deterministic/Monte Carlo neutronics codes (Liu et al., 2017; Fang et al.), fuel thermodynamics codes (Yu et al., 2020a; Liu et al.), system codes (Barbe et al., 1999), subchannel codes (Wang et al., 2017; Yu et al., 2020b), Computational Fluid Dynamics (CFD) codes (Bakanov et al., 2004; Dai et al., 2020), etc. The modeling and simulation of multi-physics and multi-scale phenomena will benefit the nuclear industry by capturing more realistic physical behaviors inside the reactor core.

We have collected three papers on nuclear reactor multi-physics and multi-scale coupling approach advance by Hu et al., Fang et al., and Liu et al. Hu et al. pioneered the application of the FEM to imitate the fluid-structure interplay between fuel assembly and cooling material within the Xi'an Pulsed Reactor core. Their work revealed that, under the specified earthquake conditions, the fluid-structure interplay effect in this reactor core is notably weak. Consequently, it has been established that this interaction does not pose a threat to the security of the reactor core and is safely

disregarded. In a separate study, Fang et al. conducted a comprehensive analysis of the full-core neutronics/thermal-hydraulics (NE/TH) coupling in the Small Lead-based Fast Reactor (SLFR). The interconnection evaluation results for SLFR demonstrated that crucial thermal-hydraulic factors, such as the cladding, fuel's highest temperature, and coolant, as well as the peak flow rate of coolant, all conform to the specified design criteria. Furthermore, the thermal-hydraulic response imparted negative reactivity feedback (approximately −200 pcm), exerting only a minimal impact upon power dispersion (less than 0.5%). In another noteworthy contribution, Liu et al. developed a sophisticated several physics interconnected model for fuel rod behavior using the COMSOL in conjunction with the 3D Monte Carlo neutron transport code RMC.

We have gathered three articles on phase field study of nuclear reactor materials by Ma et al., Wu et al., and Ma et al. In their study, Ma et al. utilized a phase-field model to explore the nucleation and growth phenomena of grains in U_3Si_2, and a statistical Rayleigh distribution was formulated to depict the grain size distribution. This statistical analysis shows that grain size evolution behavior in U_3Si_2 obeys Rayleigh distribution. Wu et al.'s work studied the statistical and dynamic characteristics of material structure and flaw evolution in materials with varying alloying element compositions and temperatures. Ma et al.'s work studied the time-space kinetics of Xe bubble development in U_3Si_2 by using the mesoscopic phase field method. It is found that a effective phase field method for studying the evolution of Xe bubbles in U_3Si_2. This methodology exhibits potential for further exploration into swelling behaviors in various fuels, laying a robust foundation for the advancement of Accident Tolerant Fuel (ATF) assembly development.

We have collected two papers on advanced coupling algorithm developments by Zhang and Zhou and Wang et al. Zhang and Zhou's work proposed a parallel Jacobian-Free Newton Krylov discrete ordinates method (comePSn_JFNK) in their work to address the solution of multi-dimensional multi-group pin-by-pin neutron transport models. This approach maximizes the effectiveness and parallel processing capabilities offered by the JFNK structure, while conc urrently leveraging the high-precision associated with the Sn method for extensive simulations. In their research, Wang et al. successfully developed a full neutron spectrum code known as FSAR, specifically tailored to meet the demands of advanced reactors characterized by a broad neutron energy range. This innovative code serves as a valuable tool for simulations targeting advanced reactor scenarios.

We have collected one paper on reactor behavior analyses using advanced coupling tools by Hu et al. Hu et al.'s work developed a novel nuclear data processing code named AXSP, outlining its methodology and evaluating its operational efficiency.

Through the incorporation of modeling and simulation that spans various physics and scales, a "digital reactor" can be constructed, which can improve efficiency, reduce costs, and enhance safety by providing assistances on the design and construction of new reactors, operation and maintenance of in-service reactors, retirement and lifespan extension of old reactors. In the future, the efficiency, versatility and flexibility of coupling should be improved by unified solving framework, which is a key direction for the advance of digital reactor technique.

Author contributions

XP: Writing–original draft, Writing–review and editing. SL: Conceptualization, Funding acquisition, Writing–original draft, Writing–review and editing. QH: Writing–original draft, Writing–review and editing. JL: Writing–original draft, Writing–review and editing. JY: Writing–original draft, Writing–review and editing.

Funding

The author(s) declare financial support was received for the research, authorship, and/or publication of this article. This work was partially supported by Project 12175067/U2330117 of the National Natural Science Foundation of China, the Natural Science Foundation of Hebei Province (no. A2022502008).

Conflict of interest

The authors declare that the research was conducted in the absence of any commercial or financial relationships that could be construed as a potential conflict of interest.

Publisher's note

References

Bakanov, V. V., Zhitnik, A. K., Motlokhov, V. N., Ognev, S. P., Romanov, V. I., Ryabov, A. A., et al. (2004). TDMCC Monte-Carlo package coupled with STAR-CD thermal-hydraulics code. in *Transactions of the American nuclear society*, 250–251.

Barber, D. A., Wang, W., Miller, R. M., Downar, T. J., Joo, H. G., Mousseau, V. A., et al. (1999). *Application of a generalized interface module to the coupling of PARCS with both RELAP5 and TRAC-M (No. LA-UR-99-856; CONF-990605-)*. Los Alamos, NM (United States): Los Alamos National Lab LANL.

Dai, T., Cao, L., He, Q., Wu, H., and Shen, W. (2020). A two-way neutronics/thermal-hydraulics coupling analysis method for fusion blankets and its application to CFETR. *Energies* 13 (16), 4070. doi:10.3390/en13164070

Liu, S., Liang, J., Wu, Q., Guo, J., Huang, S., Tang, X., and Wang, K. (2017). BEAVRS full core burnup calculation in hot full power condition by RMC code. *Ann. Nucl. Energy* 101, 434–446.

Wang, K., Liu, S., Li, Z., Wang, G., Liang, J., Yang, F., et al. (2017). Analysis of BEAVRS two-cycle benchmark using RMC based on full core detailed model. *Prog. Nucl. Energy* 98, 301–312. doi:10.1016/j.pnucene.2017.04.00

Wang, L., Zhang, B., Lu, D., Zhao, C., and Liu, J. (2023). FSAR: full neutron spectrum code for advanced reactor simulation. *Front. Energy Res.* 11, 1123714.

Weng, M., Liu, S., Liu, Z., Qi, F., Zhou, Y., and Chen, Y. (2021). Development and application of Monte Carlo and COMSOL coupling code for neutronics/thermohydraulics coupled analysis. *Ann. Nucl. Energy* 161, 108459. doi:10.1016/j.anucene.2021.108459

Yu, J., Lee, H., Kim, H., Zhang, P., and Lee, D. (2020a). Coupling of FRAPCON for fuel performance analysis in the Monte Carlo code MCS. *Comput. Phys. Commun.* 251, 106748. doi:10.1016/j.cpc.2019.03.001

Yu, J., Lee, H., Kim, H., Zhang, P., and Lee, D. (2020b). Coupled neutronics–thermal-hydraulic simulation of BEAVRS cycle 1 depletion by the MCS/CTF code system. *Nucl. Technol.* 206 (5), 728–742. doi:10.1080/00295450.2019.1677107

frontiers | Frontiers in Energy Research

TYPE Original Research
PUBLISHED 13 September 2022
DOI 10.3389/fenrg.2022.1009515

OPEN ACCESS

EDITED BY
Jiankai Yu,
The University of Tennessee,
United States

REVIEWED BY
Zhaoyuan Liu,
Qilu University of Technology
(Shandong Academy of Sciences), China
Mohammad Alrwashdeh,
Khalifa University, United Arab Emirates

*CORRESPONDENCE
Xubo Ma,
maxb@ncepu.edu.cn

SPECIALTY SECTION
This article was submitted to Nuclear Energy,
a section of the journal
Frontiers in Energy Research

RECEIVED 02 August 2022
ACCEPTED 17 August 2022
PUBLISHED 13 September 2022

CITATION
Hu K, Ma X, Ma X, Huang Y, Zhang C and Chen Y (2022), Development and verification of a new nuclear data processing code AXSP.
Front. Energy Res. 10:1009515.
doi: 10.3389/fenrg.2022.1009515

Development and verification of a new nuclear data processing code AXSP

Kui Hu, Xubo Ma*, Xuan Ma, Yuqin Huang, Chen Zhang and Yixue Chen

North China Electric Power University, School of Nuclear Science and Engineering, Beijing, China

The advanced reactor design needs an accurate cross-section generation code. In this study, a new nuclear data processing code AXSP is developed, and the method and performance of which are described. Compared with the NJOY program, the precision of the unresolved resonance processing module UnresXS has been significantly improved due to the adoption of a more accurate solution method and the consideration of in-sequence overlap integrals. The time consumption of PUnresXS has been decreased significantly due to an optimized sorting algorithm. At the same time, other modules of AXSP are relatively comprehensive. The function of resolved resonance cross-section reconstruction and linearization is the ReconXS module. The Doppler broadening module is BroadXS by using Gauss–Hermite quadrature and Gauss–Legendre quadrature from 0 K temperature pointwise cross section to any temperature which is defined by the user. The shielding factor in the unresolved resonance energy region is calculated by the UnresXS or the PUnresXS module, which are developed based on the Bondarenko method and the probability table method, respectively. The ACE formatted cross sections for the Monte Carlo code is processed by the ACEXS module, and the multigroup cross sections are generated by the GroupXS module. The cross sections processed by different modules were verified by the NJOY2016 code, and the multigroup cross sections were also verified by using the critical benchmarks. The multiplication factor difference between AXSP and NJOY2016 is less than 20 pcm. In addition to this, the ZPR6/7 fast reactor is used for ACE format library verification. The results show that the criticality calculated by AXSP has a good agreement with that of NJOY2016.

KEYWORDS

nuclear data processing code, NJOY data processing, AXSP, ENDF format, advanced reactor design

Introduction

A total of six advanced reactor concepts have been selected for Generation IV reactor and are being investigated to meet the challenging goals of effective resource utilization and waste minimization. The cross section is one of the most fundamental quantities for the reactor design. The evaluated nuclear data files have been updated over the years with

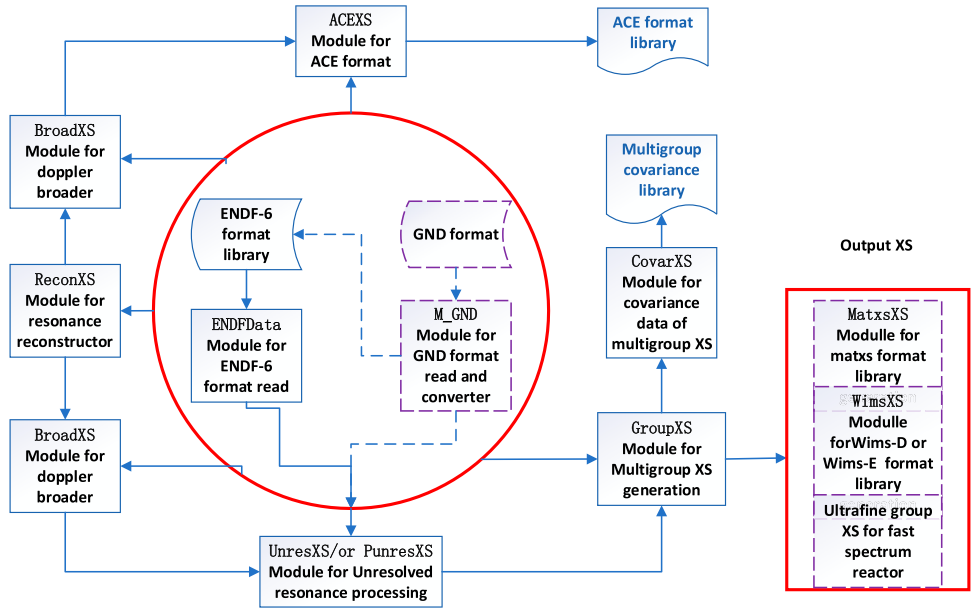

FIGURE 1
Schematic diagram of the AXSP structure.

reflecting progress on nuclear modeling, new nuclear experiment measurement, and a lot of feedback from the benchmark analysis. The cross-sections' data library of neutronics calculation codes is generated by processing the evaluated nuclear data files when it is updated. Therefore, the nuclear data processing code is very important for connecting the evaluated nuclear data file and the reactor analysis and design codes. The motivation for the development of the advanced cross-section process (AXSP) code is to establish a platform to research some new methods of nuclear processing to satisfy the demands on accurate cross sections for the advanced reactor design. For example, in the design of a mixed-spectrum reactor, it is necessary to consider not only the anisotropic scattering in the high-energy region but also the influence of the broad resonances and the upper scattering problems in the low-energy region. The problem of generating a high-precision multigroup cross section cannot be well resolved. Because if we want to better solve the problem of the hybrid spectrum reactor, we need to consider not only the anisotropic scattering in the high-energy region but also the solution of the moderation equation in the all-energy region. There are still many works to be carried out.

Currently, NJOY (Abou Jaoude, 2017), PREPRO (Cullen, 2017), and AMPX (Wiarda et al., 2016) are well-known nuclear data processing codes in the world. There are also some newly developed nuclear data processing codes. For example, RXSP (Jian-kai et al., 2013) (Li and WangKan, 2017) (Liu et al., 2020) (Li, 2012) (Yu, 2015) of Tsinghua University and FRENDY (Tada et al., 2017) of the Japan Atomic Energy Agency (JAEA) have developed to produce an ACE format library for the Monte Carlo code. Ruller (Liu et al., 2016) of the China Institute of Atomic Energy and NECP-Atlas (Zu et al., 2019) of Xi'an Jiao Tong University have been developed to provide a multigroup library. At the same time, EXUS-F of South Korea was developed for a faster reactor multigroup cross-section generation by direct processing of the evaluated nuclear data file.

For the nuclear data processing, the open source nuclear data processing system NJOY is still not perfectly processing the evaluated nuclear data for the advanced nuclear reactor analysis when it is used to calculate the KERMA factors and DPA cross sections (Konno et al., 2016) (Wen et al., 2020) because of some bugs.

Recently, the nuclear data format has been considered to change from the traditional ENDF-6 format to the generalized nuclear data (GND) format (Mattoon et al., 2012) by utilizing the Extensible Markup Language. Since the GND format is completely different from the current ENDF-6 format, which was defined several decades ago, the NJOY code cannot treat such a new format without extensive modification. To solve this problem, several nuclear data processing systems, such as NJOY21 (Conlin, 2015), FUDGE (Beck and Mattoon, 2014), and AMPX-2000, are under development in a few countries.

In this study, the outline of the development, method, and capability of AXSP are described in the *Theory and processing method* section. In *Numerical calculation results* section, the verification of each module of AXSP is investigated, and the results of AXSP are compared with those of NJOY 2016. The

TABLE 1 Time consumption for the unresolved resonance processing with different codes.

Isotope	PURR/s	PUnresXS/s	PURR/PUnresXS
^{241}Am	2,484	2,420	1.03
^{251}Cf	2,809	2,703	1.04
^{239}Pu	3,995	3,881	1.03
^{235}U	2,036	1,880	1.08

critical benchmarks from the ICSBEP handbook are applied to demonstrate the accuracy of the multigroup cross section with the Bondarenko method, and ZPR6/7 was used to verify the ACE format library generated by the ACEXS module. The last section is conclusion.

Theory and processing method

AXSP is developed to solve the problems of the current nuclear data processing systems and satisfy the demands on accurate cross sections (XS) for the advanced reactor. Therefore, modern programming techniques are utilized to make the code more maintainable, modularized, portable, and flexible; it was written in Fortran 2003 by using the object-oriented programming techniques and allocatable memory techniques. Each module has its own class, and the modification of the class does not affect the other classes. The ENDF data class can be easily reused in other modules. The schematic diagram of the AXSP structure is shown in Figure 1. The solid lined modules have already been implemented, while the dotted lined modules are still in development. The GND format is not finalized. Now, the GroupXS module is still based on the Bondarenko method, and on the other hand, the ultrafine group method and hyperfine group method for the fast reactor design will be developed in the future.

The ReconXS module is used to reconstruct resonance cross sections from resonance parameters and to reconstruct cross sections from ENDF nonlinear interpolation schemes by using a traditional inverted-stack method. The BroadXS module generates Doppler-broadened cross sections in the PENDF format from piecewise linear cross sections in the PENDF format from 0 K temperature. To improve the calculation efficiency and maintain the calculation accuracy at the same time, the Gauss–Hermite quadrature has been used in some energy regions, and two points of Gauss–Legendre quadrature are used in other energy ranges (Li, 2012).

The UnresXS module is used to produce effective self-shielded cross sections for resonance reactions in the unresolved energy range. In the unresolved energy range, it is not possible to define precise values for the cross sections of the resonance reactions $\sigma_x(E)$, where x stands for the reaction type, such as total, elastic, fission, or capture. It is only possible to define average values. The average cross sections in the vicinity of E* can be written as

$$\bar{\sigma}_{0x}(E^*) = b_x(E^*) + \frac{\bar{\sigma} I_{0x}}{1 - I_{0t}} \tag{1}$$

and

$$\bar{\sigma}_{1x}(E^*) = b_t(E^*) + \frac{\bar{\sigma} I_{1x}}{1 - I_{0t} - I_{1t}}, \tag{2}$$

where $b_x(E^*)$ is the background cross section for the reaction type x, $b_t(E^*)$ is the background cross section for the total cross section, and I_{0x} and I_{1t} are the two types of "fluctuation integrals: ". $\bar{\sigma}(E^*)$ is written as

$$\bar{\sigma}(E^*) = b_t(E^*) + \sigma_0. \tag{3}$$

The background cross section σ_0 is defined in the input file of AXSP by the user. If we assume that the resonances are widely separated and only the "self" term will be important, the fluctuation integrals become

$$I_{0x} = \sum_s A_{xs}, \tag{4}$$

$$A_{xs} = (B_{xs} - V_{0xs})\left[1 - \sum_{s' \neq s} A_{ts'}\right], \tag{5}$$

and

$$I_{1t} = \sum_s (D_{ts} - V_{1ts})\left[1 - \sum_{s' \neq s} A_{ts'}\right]^2, \tag{6}$$

where B_{xs} and D_{ts} are the first kinds including the isolated resonance integrals and V_{0xs} and V_{1ts} are the in-sequence overlap

TABLE 2 Comparison time consumption between the shell sort algorithm and bubble sort algorithm.

Isotope	Shell sort algorithm/s	Bubble sort algorithm/s	(Shell sort)/(bubble sort)
^{58}Co	56.522	1,037.479	0.05
^{74}As	584.553	4,326.493	0.14
^{102}Ru	38.004	788.142	0.05
^{135}Cs	104.814	1,977.199	0.05
^{238}U	938.732	5,262.513	0.18
^{241}Pu	779.576	2,631.492	0.30
^{232}Th	758.535	4,271.325	0.18

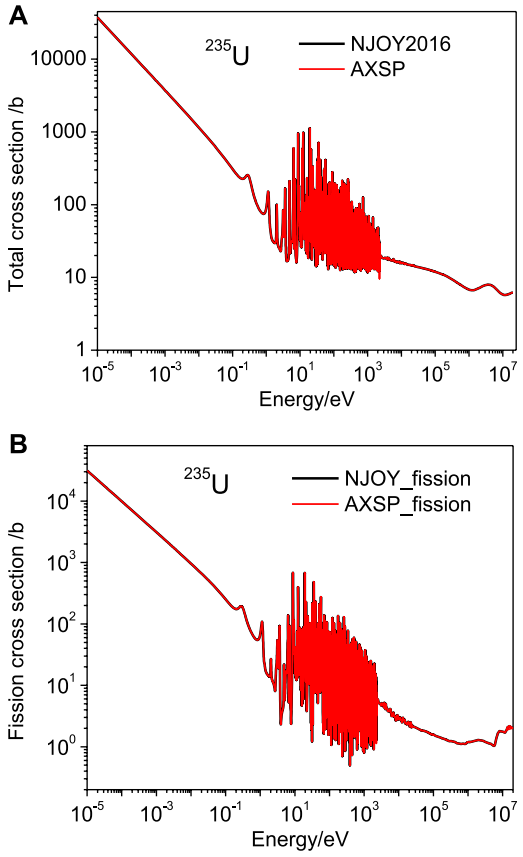

FIGURE 2
Comparison of total **(A)** and fission **(B)** cross sections of ^{235}U produced by NJOY2016 and AXSP, respectively.

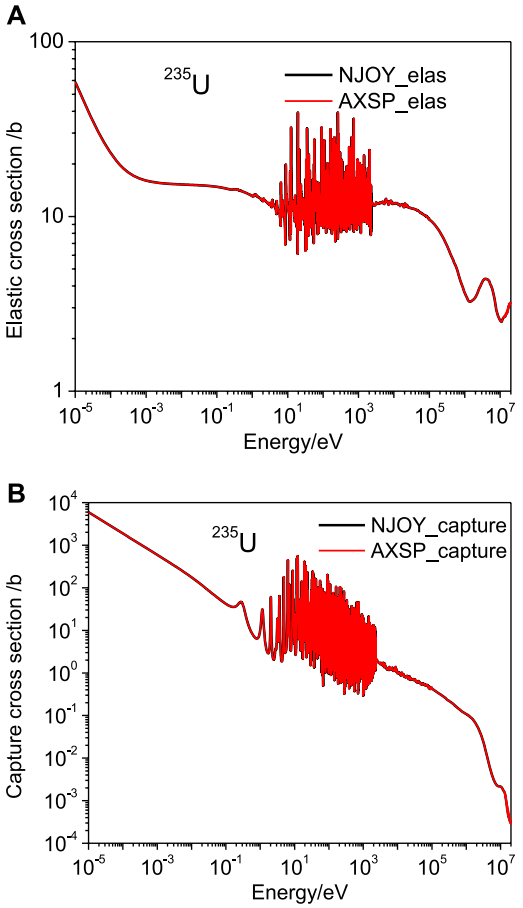

FIGURE 3
Comparison of elastic **(A)** and capture **(B)** cross sections of ^{235}U produced by NJOY2016 and AXSP.

integrals. In the UNRESR module of the NJOY code, the in-sequence overlap corrections V_{0xs} and V_{1ts} are neglected. This approximation is based on the assumption that resonance repulsion will reduce the overlap between resonances in different sequences as the dominant overlap effect. In the UnresXS module of AXSP, the in-sequence overlap correction V_{0xs} was calculated by using the method for computing J, which has been developed by Hang for MC^2-2 (Henryson et al., 1976). The improvement of UnresXS comparison with that of UNRESR will be discussed in the *Numerical calculation results* section.

The unresolved self-shielding data generated by UnresXS are suitable for multigroup methods after processing by GroupXS based on the Bondarenko method. However, the Bondarenko method is not suitable for continuous-energy Monte Carlo codes like MCNP and RMC. Therefore, the PUnresXS module is developed by the ladder-sampling method to generate the probability table for the Monte Carlo code. On the other hand, the PUnresXS module can generate the effective self-shielded cross section which can be used for the multigroup cross-section generation. The disadvantage of PUnresXS is time consumption. To solve this problem, we have optimized the sorting method in the program, which greatly saves the calculation time while ensuring the accuracy. Previous research (Yu, 2015) has shown that the time consumption of the PURR module is mainly related to the sorting algorithm used, and the bubble sort algorithm has been applied in the PURR module. If the bubble sort algorithm was also used in the PUnresXS module of AXSP, the time consumption for the unresolved resonance processing with different codes is shown in Table 1. As shown in Table 1, the time consumption of the PUnresXS module is almost the same as the PURR module of NJOY if the same bubble sort algorithm is used. We also compared the impact of selection sort, quicksort, heap sort, and shell sort on time; the shell sort algorithm was selected and applied in the PUnresXS module because of the better calculation speed. The time consumption with the shell sort algorithm and bubble sort algorithm in PUnresXS for different isotopes is shown in Table 2. As shown in Table 2, for most isotopes, the computation time using the shell sort algorithm is

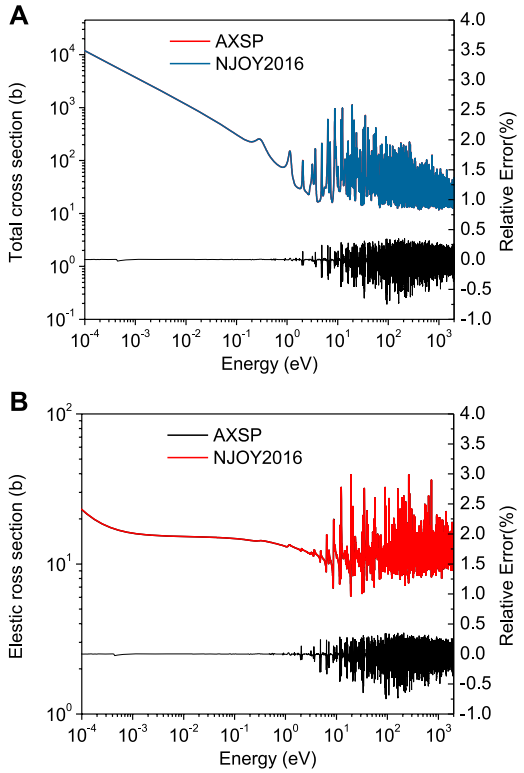

FIGURE 4
Comparison of broaden total **(A)** and elastic **(B)** cross sections of ^{235}U produced by NJOY2016 and AXSP.

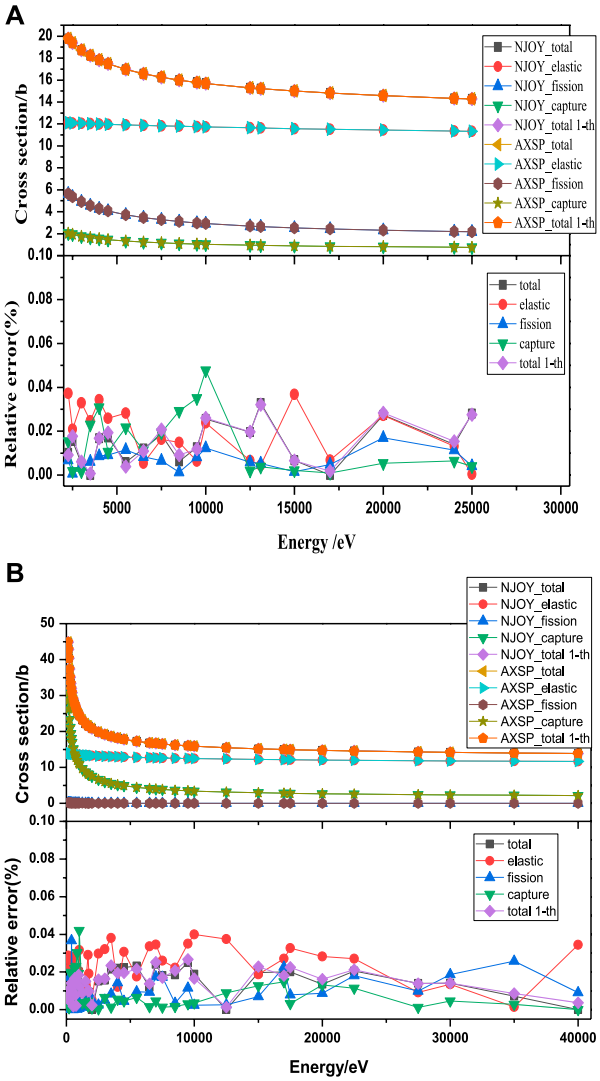

FIGURE 5
Self-shielding cross section of ^{235}U **(A)** and ^{241}Am **(B)** at unresolved energy range at 293.6 K and the self-shielding cross section relative error between NJOY2016 and AXSP.

18% of the computation time of the bubble sort, or less. After using the shell sort algorithm, the calculation time is significantly reduced, and the calculation speed is significantly improved.

Multigroup constants are normally used by computer codes that calculate the distribution of neutrons and/ or photons in space and energy, and these compute various responses to these distributions. The GroupXS module in AXSP was developed to calculate the multigroup constants. The GroupXS module computes not only group average cross sections but also the group-to-group scattering matrix. The average cross sections and group-to-group scattering matrix can be represented as

$$\bar{\sigma}_{i,x,g} = \frac{\int_{\Delta E_g} \sigma_{x,i}(E)\phi_0(E)dE}{\int_{\Delta E_g} \phi_0(E)dE}, \quad (7)$$

where i, x, and g are the indices for isotopes, reaction type, and multigroup number, respectively. $\phi_0(E)$ is the neutron spectrum. In the group where the boundary between resolved and unresolved resonance ranges is located, both the resolved and unresolved resonances are self-shielded simultaneously. By dividing the integration interval into the resolved and unresolved resonance intervals, the self-shielding cross section is determined as

$$\bar{\sigma}_{i,x,g} = \frac{\int_{\Delta E_{resolved}} \sigma_{x,i}(E)\phi_0(E)dE + \int_{\Delta E_{unresolved}} \sigma_{x,i}(E)\phi_0(E)dE}{\int_{\Delta E_{resolved}} \phi_0(E)dE + \int_{\Delta E_{unresolved}} \phi_0(E)dE}, \quad (8)$$

where the integrals over the resolved resonance interval are evaluated in Eq. 7. When the integrals over the unresolved interval are evaluated, the self-shielding factor generated by the UnresXS or PUnresXS module should be used to be taken into account the self-shielding effects. The GroupXS module calculates the scattering matrix for neutron-induced scattering reactions such as elastic scattering, discrete inelastic scattering, and continuum inelastic scattering. The scattering matrix is also calculated for (n, 2n) and (n, 3n) reactions, including anisotropy

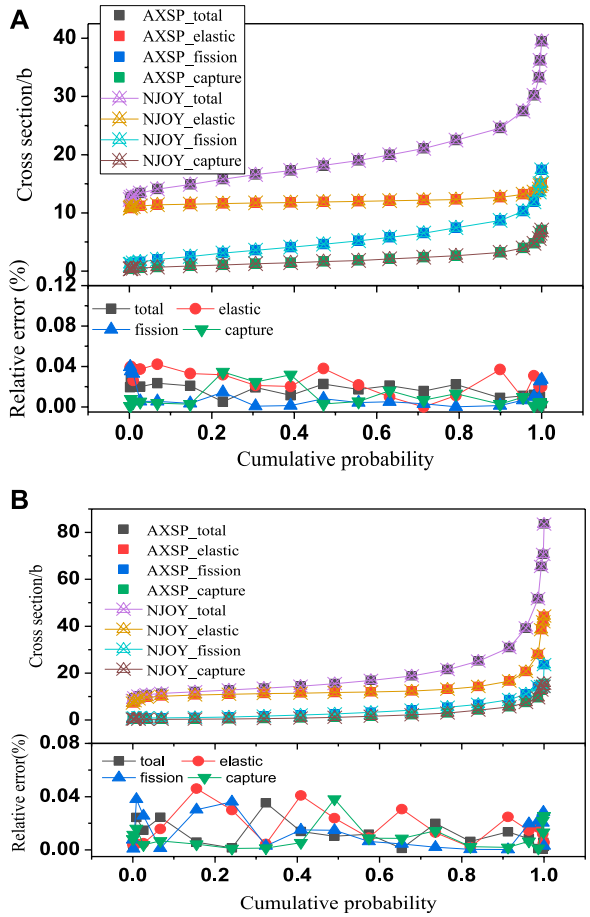

FIGURE 6
Probability table of ^{235}U **(A)** and ^{239}Pu **(B)** at energy 2.5 keV at 293.6 K and the relative error between NJOY2016 and AXSP.

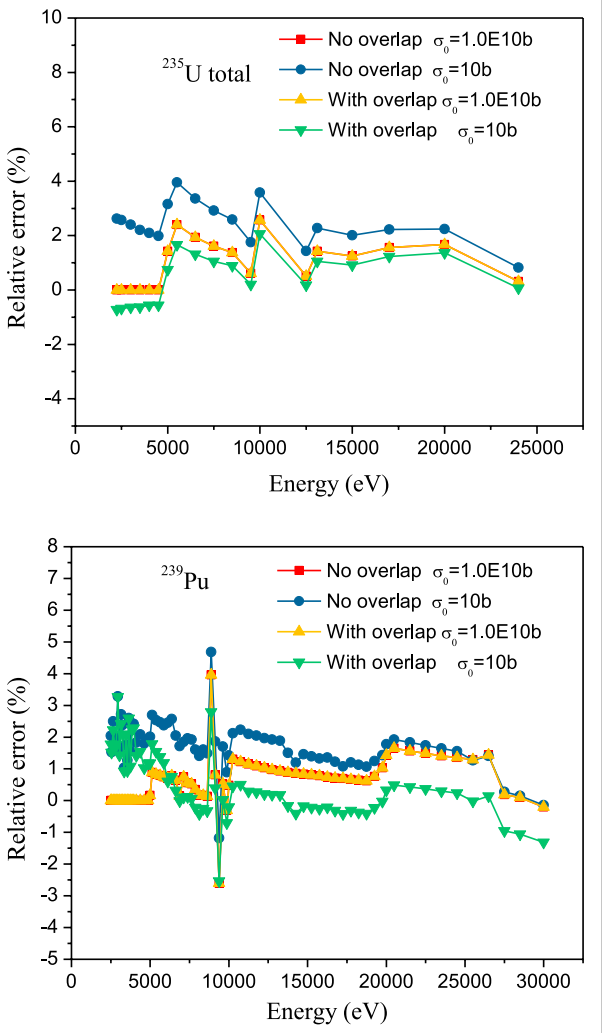

FIGURE 7
In-sequence overlap integral effects to the self-shielding total cross sections of ^{235}U and ^{239}Pu with different background cross sections (the temperature is set as 293.6 K).

by using the ENDF-formatted nuclear data library. The scattering matrix for the l – th anisotropic scattering can be resented as

$$\bar{\sigma}^{l}_{i,x,g'\to g} = \frac{\int_{\Delta E_g} dE \int_{\Delta E_{g'}} \sigma_{i,x}\phi_l(E')f(E'\to E,\mu_s)P_l(\mu_s)d\mu_s dE'}{\int_{\Delta E_{g'}} \phi^l(E)dE}, \tag{9}$$

where $f(E'\to E,\mu_s)$ is the scattering transfer probability from the incident energy E' to the outgoing energy E and the cosine of the scattering angle μ_s in the laboratory system. $\phi_l(E)$ is the l – th moment of the neutron flux, and $P_l(\mu_s)$ is the l – th order Legendre polynomial. With a given transfer probability, the element of the scattering transfer matrix can be determined by evaluating the integrals numerically. There are three ways to give the transfer probability, according to the data types given in nuclear data files: the angular distribution in file 4, the angular distribution in file 4 and the energy distribution in file 5, and the energy-angle distribution in file 6.

For the multigroup constant generation, it is important to select the continuum energy neutron flux and flux moment $\phi_l(E)$. In many cases of practical interest, the neutron flux and flux moment $\phi_l(E)$ will contain dips corresponding to the absorption resonances of various materials, and these dips will reduce the effect of the corresponding resonance, which is also called self-shielding. If the Bondarenko narrow-resonance weight scheme (MacFarlane, 2012) is used, the flux can be written as

$$\phi^i_l(E) = \frac{C(E)}{\left[\sigma^i_t(E)+\sigma^i_0\right]^{l+1}}, \tag{10}$$

where $\sigma^i_t(E)$ is the microscopic total cross section for the isotope i, C(E) is the smooth function of energy, and σ^i_0 is a constant background cross section, which represents all the other isotope

TABLE 3 Number of materials in ENDF/B-VII.1 for specific File 5 formats for total fission, first-chance neutron-induced fission, and (n, 2n) reactions.

Reaction type MT	18	19	16
Total number of isotopes	82	3	176
LF = 1	68 (^{235}U)	1 (^{234}U)	158 (^{241}Pu)
LF = 7	11 (^{241}Pu)	2 (^{236}U, ^{240}U)	—
LF = 9	—	—	18 (^{23}Na)
LF = 11	1 (^{233}U)	—	—
LF = 12	2 (^{241}Am, ^{243}Am)	—	—

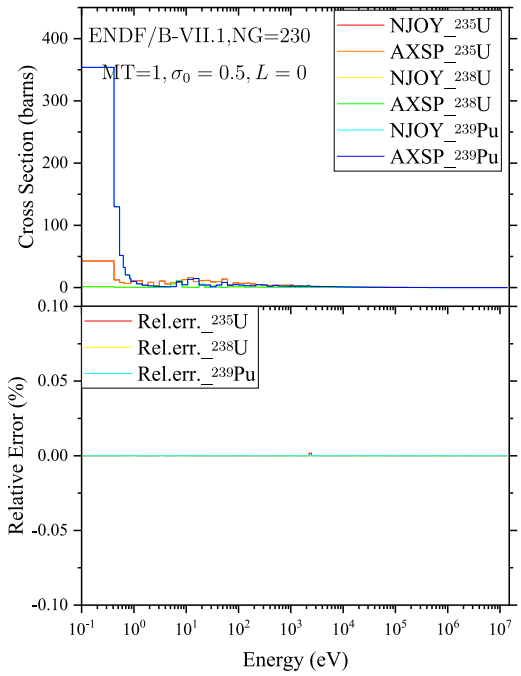

FIGURE 8
Comparison of the average total cross sections of ^{235}U, ^{238}U, and ^{239}Pu calculated by NJOY2016 and AXSP.

effects to the flux. However, we know that the Bondarenko method is more suitable for fast spectral reactors, and for thermal reactors, this method will introduce relatively large errors due to the need to consider the broad resonance in the low-energy region. Therefore, in the future, we will use the method of solving the continuous energy neutron transport equation to obtain the energy spectrum so that the generated multigroup cross sections will be more accurate, such as the CENTRM module (Williams and Hollenbach, 2011) in SCALE6.1 and RMET21 (Leszczynski, 2001). The disadvantage of the current version of GroupXS is that it can only handle neutron evaluated data, not yet unable to handle photon evaluated data. Therefore, there still exist some important

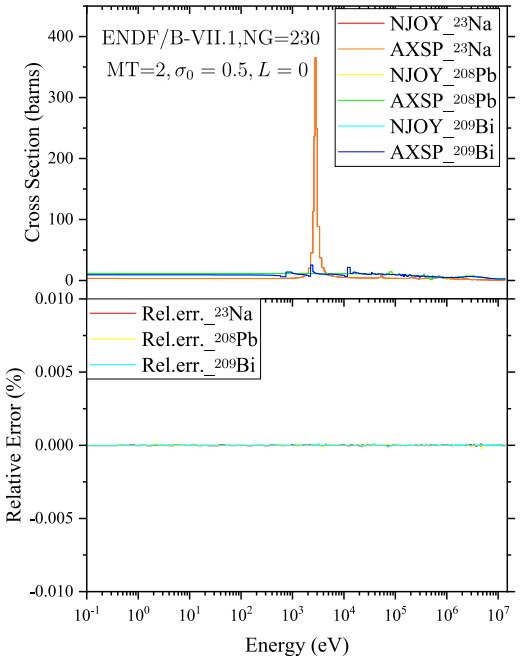

FIGURE 9
Comparison of the average elastic cross sections of ^{23}Na, ^{208}Pb, and ^{209}Bi calculated by NJOY2016 and AXSP.

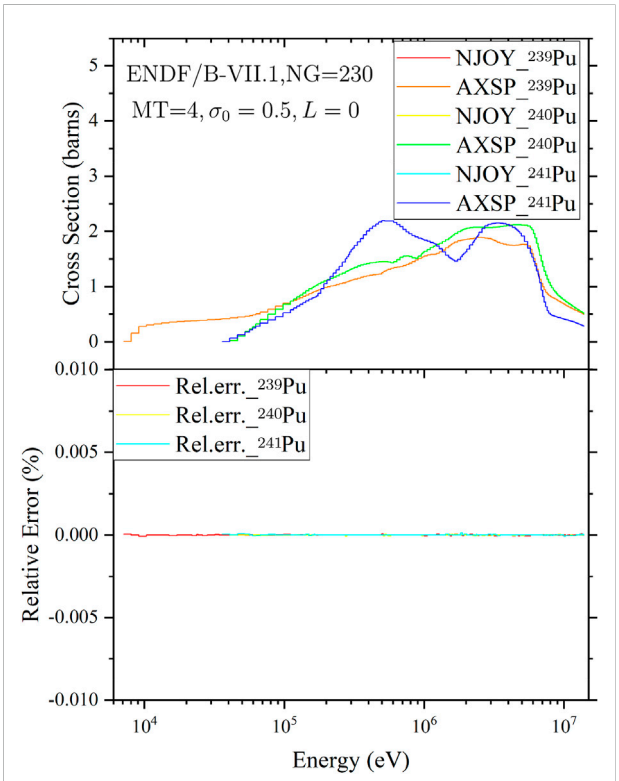

FIGURE 10
Comparison of the average inelastic cross sections of ^{239}Pu, ^{240}Pu, and ^{241}Pu calculated by NJOY2016 and AXSP.

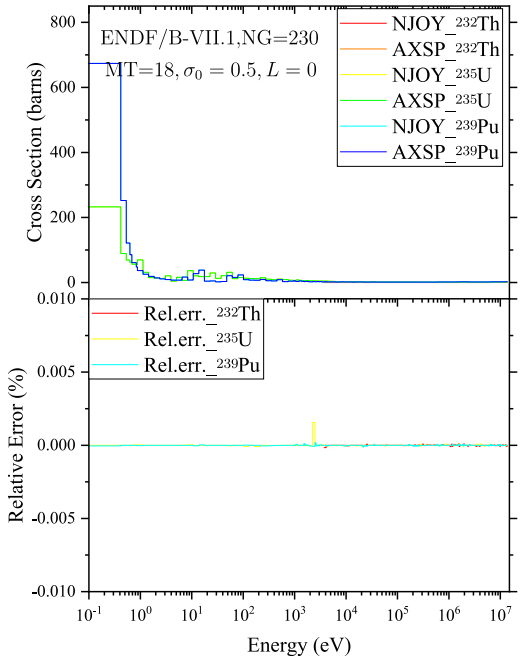

FIGURE 11
Comparison of the average fission cross sections of ^{232}Th, ^{235}U, and ^{239}Pu calculated by NJOY2016 and AXSP.

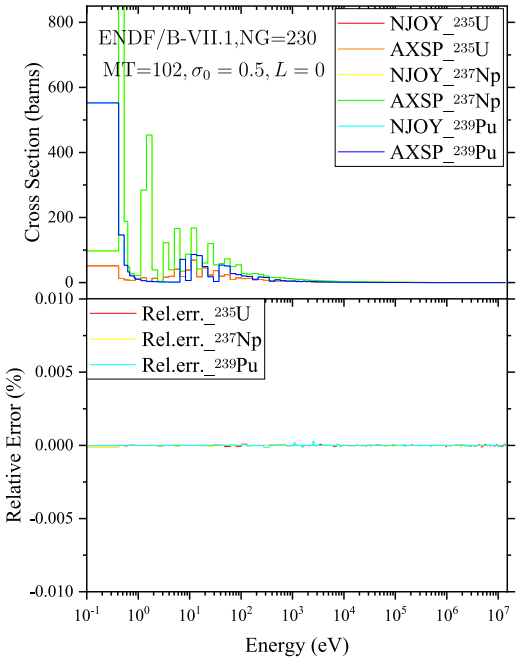

FIGURE 12
Comparison of the average capture cross sections of ^{235}U, ^{237}Np, and ^{239}Pu calculated by NJOY2016 and AXSP.

functions which need to develop in the future, such as treating the thermal neutron cross sections and produce the MATXS format library, and Wims-D and Wims-E format libraries. In the following verification, the MATXS format library was produced by using MATXSR of NJOY.

Numerical calculation results

Cross-section comparison

The ReconXS module was verified by comparing the cross sections which were generated with AXSP with that of NJOY 2016. Almost all the isotopes in ENDF/B-VII.1 (Chadwicka et al., 2011), ENDF/B-VIII.0 (Brown et al., 2018), and CENDL-3.2 (Ge et al., 2020) are used for testing. The results show that the cross sections generated by AXSP are in good agreement with those of NJOY2016. The cross sections of ^{235}U for total, fission, elastic, and capture are shown in Figure 2 and Figure 3. As shown in the figures, the relative error between AXSP and NJOY2016 is all less than 0.5%, which is the maximum relative error setting for the cross-section reconstruction.

The BroadXS module was tested by using BROADR of NJOY. The Doppler-broadened cross sections of ^{235}U for the total and elastic cross sections at 300 K are shown in Figure 4, and the relative errors of the cross sections between AXSP and NJOY2016 are all less than 0.25% in all energy ranges. Therefore, the Doppler-broadened cross section calculated by AXSP is in good agreement with the calculation results of NJOY2016.

The UnresXS module has been developed to calculate the shielding factor for the multigroup cross-section generation. To verify the UnresXS module, first, the UnresXS has been developed by the same calculation method as the UNRESR of NJOY 2016; the UNRESR module of NJOY2016 has been used to perform the comparison. The self-shielding cross section of ^{235}U and ^{241}Am at its unresolved energy range at 293.6 K is shown in Figure 5. As shown in Figure 5, the absolute relative error between AXSP and NJOY2016 for all the energy points is less than 0.04%. The probability table for the Monte Carlo calculation has been calculated by the PUnresXS module of AXSP, and the probability table of ^{235}U and ^{239}Pu at energy 2.5 KeV and temperature at 293.6 K is shown in Figure 6. The probability table calculated by AXSP is also in good agreement with PURR of NJOY2016, and the absolute relative errors are less than 0.4%. Second, we improved the UnresXS module to make it to take into account the in-sequence overlap integrals, as shown in Equation 5. The in-sequence overlap integral effects have been shown in Figure 7. In the study, the PURR module calculation results have been set as the reference results, and the relative errors with in-sequence overlap integrals and without in-sequence overlap integrals for ^{235}U and ^{239}Pu have been obtained. As shown in

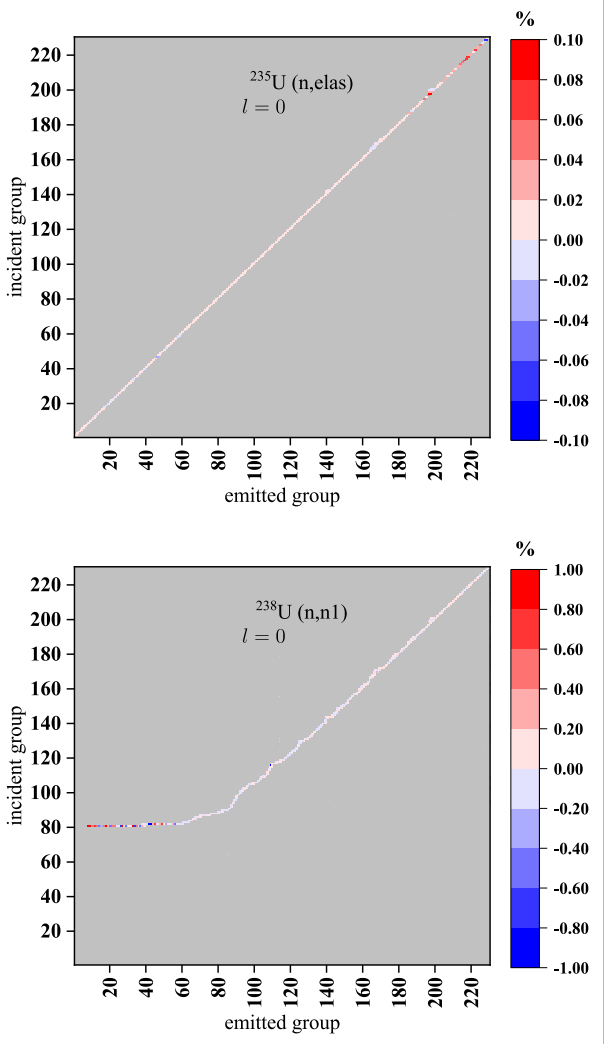

FIGURE 13
Relative error distribution of the elastic scattering matrix of ^{235}U and (n, n1) scattering matrix of ^{238}U between NJOY2016 and AXSP.

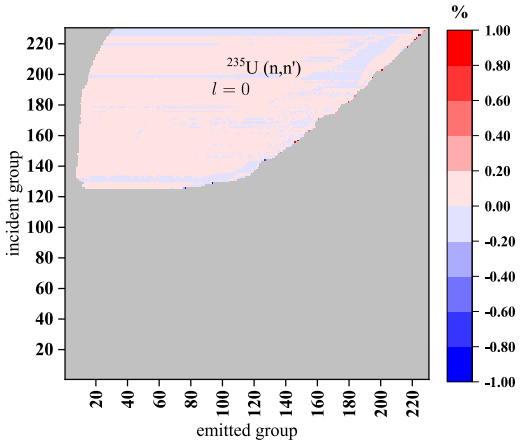

FIGURE 14
Relative error of the (n, n`) scattering matrix of ^{235}U between NJOY2016 and AXSP.

Figure 7, when the background cross section is very large, there is almost no improvement by consideration of the overlap integrals. However, the improvement is more pronounced when the background cross section is relatively small and the self-shielding effects are strong.

The calculation accuracy of the reactor physics is directly related to the calculation accuracy of the multigroup cross section. To verify the accuracy of the multigroup cross section generated by the GroupXS module and to facilitate the comparison with the calculation results of the NJOY2016 results, the ANL-230 energy group structures and the Bondarenko method were used to calculate the multigroup cross section and group-to-group matrix. The self-shielding cross section with different background cross sections was calculated. Currently, the GroupXS module can process the average cross sections and scattering matrices of all reaction channels in the Evaluated Nuclear Data File with the ENDF-6 format. These Evaluated Nuclear Data Files mainly include ENDF/B-VII.1, ENDF/B-VIII.0, and CENDL-3.2. Taking ENDF/B-VII.1 as an example, the number of materials in ENDF/B-VII.1 for specific file 5 formats for total fission, first-chance neutron-induced fission, and (n, 2n) reactions are shown in Table 3. A total of 261 materials were given in the format of file 5, in which the number of materials given by the (n, 2n) reaction in the file 5 format is 176, and among these 176 materials, 158 of which are given in the data format of LF = 1, and the rest are given in the data format of LF = 9. Different LF numbers represent different energy distribution laws. The LF = 1 law is the arbitrary tabulated function, and the LF = 9 law is the evaporation spectrum.

The average cross sections calculated by GroupXS (Hu et al., 2022) and GROUPR for different isotopes and different reaction types are shown in Figure 8 ~ Figure 12. The average total cross sections of ^{235}U, ^{238}U, and ^{239}Pu with the background cross section $\sigma_0 = 0.5barn$ and 0-th order Legendre polynomial are shown in Figure 8. The average elastic cross sections of ^{23}Na, ^{208}Pb, and ^{209}Bi, the average inelastic cross sections of ^{239}Pu, ^{240}Pu, and ^{241}Pu, the average fission cross sections of ^{232}Th, ^{235}U, and ^{239}Pu, and the average capture cross sections of ^{235}U, ^{237}Np, and ^{239}Pu with the background cross section $\sigma_0 = 0.5barn$ are shown in Figures 9–12, respectively. In general, the value of the background cross section represents the strength of the resonance self-shielding effect. The smaller the background cross-section value, the stronger the resonance self-shielding effect is. The larger the background cross-section value, the weaker the resonance self-shielding effect is. For example, for the background section, if it is infinite, it means that there is no

TABLE 4 k_{eff} results for different critical benchmarks.

Benchmark	NJOY2016	AXSP	Difference/pcm
hmf1	1.00010	1.00024	14
HMF2	1.00214	1.00225	11
HMF41	1.00448	1.00459	11
IMF3	1.00312	1.00319	7
IMF4	1.00739	1.00745	6
IMF6	1.00151	1.00157	6
pmf2	0.99431	0.99430	−1
pmf5	0.99937	0.99937	0
pmf6	0.99685	0.99685	0
pmf9	1.00526	1.00539	13
pmf10	0.99623	0.99623	0
pmf23	0.99635	0.99635	0
pmf25	0.99925	0.99928	3
umf1	0.99996	1.00010	14
umf2	0.99924	0.99935	11
umf4	0.99981	0.99993	11

resonance self-shielding effect. The case where the background cross section is relatively small is selected for cross-section comparison because the cross section in this case is more difficult to calculate accurately. As shown from Figures 8–12, the results of GroupXS are in good agreement with those of GROUPR, and the maximum error is less than 0.005%. The relative error of elasticity of ^{235}U, the (n, n1) scattering matrix of ^{238}U, and the (n, n`) scattering matrix of ^{235}U are given in Figures 13, 14. As seen from the previous figures, for almost all the group-to-group scattering matrix, the relative error is less than 0.1%. Therefore, the scattering matrix calculated by GroupXS is correct, and it can be used for future reactor calculation.

Critical benchmark verification

To verify the accuracy of the multigroup cross sections generated by AXSP, the criticality benchmarks from the International Criticality Safety Benchmark Evaluation Project (ICSBEP) are used. The reason why these critical benchmarks are selected to verify the accuracy of multigroup cross sections is that the energy spectrum of these critical devices is mostly hard, and the neutrons are mostly concentrated in the middle- and high-energy regions. In these energy regions, the cross sections generated by the Bondarenko method, which is used in AXSP and NJOY, have higher accuracy.

The effective multiplication factor k_{eff} for different critical benchmarks is shown in Table 4. As shown in Table 4, the k_{eff} results calculated by the AXSP program agree very well with the results calculated by NJOY 2016. The difference is defined as the results of AXSP minus the results of NJOY2016. The maximum difference is 14 pcm. Compared with the experimental results, almost all the errors are less than 500 pcm, except IMF4 and pmf2 benchmarks, and the reason for the bias needs further study.

TABLE 5 k_{eff} results for ZPR6/7.

	ACER	ACEXS	Difference/pcm
k_{eff}	0.98714	0.98708	6

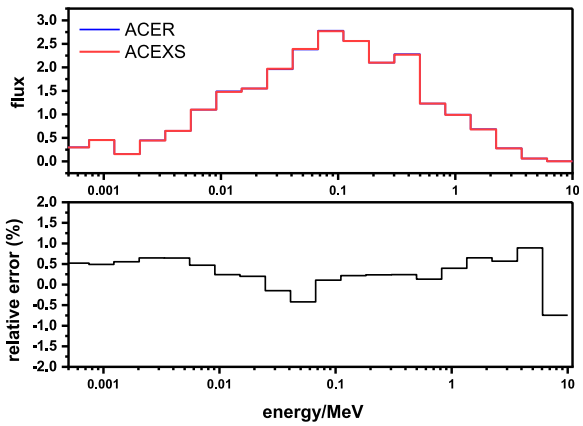

FIGURE 15
Neutron flux of the inner core for the ZPR6/7 benchmark with a different nuclear library.

ACE format library generation

To verify the ability of the ACEXS module to generate the ACE format section library, ZPR6/7 was selected because of its fast neutron spectrum. The loading of ZPR-6 Assembly 7 (Smith et al., 2003) began in July 1970, and experiments on this assembly continued through October 1971. The particular configuration judged most suitable for a criticality safety benchmark was Loading 12 with a fissile loading of 15.4 kg ^{235}U and 1118.1 kg ^{239}Pu + ^{241}Pu. The specifications of this experiment are provided in the "International Handbook of Evaluated Reactor Physics Benchmark Experiments" under the name "ZPR-LMFR-EXP-001" in the liquid metal fast reactor chapter. The homogeneous R-Z model and associated dimension are shown in Smith et al. (2003).

The ACE format nuclear library was generated based on the ENDF/B-VII.1 evaluated nuclear data file by using NJOY2016 and AXSP. In this calculation, the ACEXS module of AXSP was used to generate the library. However, the resonance reconstruction and the other module of NJOY2016 were applied. The reactor Monte Carlo RMC,

which was developed by Tsinghua University, was used to calculate the ZPR6/7 benchmark.

The k_{eff} results (Ma et al., 2022) for ZPR6/7 with different modules are shown in Table 5. As shown in Table 5, the k_{eff} results calculated by the ACEXS module are in good agreement with those of the ACER module, and the difference is only 6 pcm. The neutron flux of the inner core (Ma et al., 2022) is shown in Figure 15. As shown in Figure 15, the relative error is less than 0.5%. Therefore, the nuclear library processed by the ACEXS module is in good agreement with that of ACER of NJOY.

Conclusion

In this study, a new nuclear process code AXSP was developed, and the basic function of the process-evaluated nuclear data file has been verified by using NJOY2016. The critical benchmarks from the ICSBEP handbook were used to verify the multigroup cross section, and the effective multiplication factor maximum difference between AXSP and NJOY2016 is 14 pcm. The ZPR6/7 benchmark was used to verify the ACE format library generation for the Monte Carlo code, and the k_{eff} results calculated by the ACEXS module are in good agreement with that of the ACER module, and the difference is only 6 pcm. Therefore, the results of AXSP are in good agreement with that of NJOY2016. Compared with the NJOY program, the precision of the unresolved resonance processing module UnresXS has been significantly improved due to the adoption of a more accurate solution method and the consideration of in-sequence overlap integrals. The improvement is more pronounced when the background cross section is relatively small and the self-shielding effects are strong. The time consumption of PUnresXS has been decreased significantly due to an optimized sorting algorithm. The computation time using the shell sort algorithm is 18% of the computation time of the bubble sort algorithm, or less. After using the shell sort algorithm, the calculation time is significantly reduced, and the calculation speed is significantly improved. In the future, we will use the method of solving the continuous energy neutron transport equation to obtain the energy spectrum in order to obtain more accurate multigroup cross sections, and the module of processing the MATXS format library, and Wims-D and Wims-E format libraries will also be developed (Lim et al., 2018).

Data availability statement

The original contributions presented in the study are included in the article/Supplementary Material. Further inquiries can be directed to the corresponding author.

Author contributions

KH: GroupXS module development and data analysis. XbM: supervision, conceptualization, methodology, and software. XaM: ACEXS module development and data analysis. YH: data analysis and check. CZ: UnresXS module development and data analysis. YC: supervision and conceptualization.

Funding

This study was supported by the National Natural Science Foundation of China (No. 11875128).

Conflict of interest

The authors declare that the research was conducted in the absence of any commercial or financial relationships that could be construed as a potential conflict of interest.

Publisher's note

All claims expressed in this article are solely those of the authors and do not necessarily represent those of their affiliated organizations, or those of the publisher, the editors, and the reviewers. Any product that may be evaluated in this article, or claim that may be made by its manufacturer, is not guaranteed or endorsed by the publisher.

References

Abou Jaoude, A. (2017). "Design of a mixed-spectrum long-lived reactor with improved proliferation resistance," PHD thesis (Georgia Institute of Technology).

Beck, R. B., and Mattoon, M. C. (2014). *FUDGE: a toolkit for nuclear data management and processing*. Livermore, USA: Lawrence Livermore National Laboratory. LLNL-PROC-648476).

Brown, D. A., Chadwick, M. B., Capote, R., Kahler, A., Trkov, A., Herman, M., et al. (2018). ENDF/B-VIII.0: The 8 th major release of the nuclear reaction data library with CIELO-project cross sections, new standards and thermal scattering data. *Nucl. Data Sheets* 148, 1–142. doi:10.1016/j.nds.2018.02.001

Chadwicka, M. B., Hermanb, M., and Obložinský, P. (2011). ENDF/B-VII.1 nuclear data for science and Technology: Cross sections, covariances, fission product yields and decay data. *Nucl. Data Sheets* 112 (12), 2887–2996. doi:10.1016/j.nds.2011.11.002

Conlin, L. J. (2015). *Modernization of NJOY: creating NJOY21*. Los Alamos, USA: Los Alamos National Laboratory. LA-UR-15-24644.

Cullen, D. E. (2017). *PREPRO 2017 2017 ENDF/B Pre-processing codes*. Vienna, Austria: International Atomic Energy Agency. IAEA-NDS-39.

Ge, Z., Ge, Z., and Xu, R. (2020). CENDL-3.2: The new version of Chinese general purpose evaluated nuclear data library. *EPJ Web Conf.* 239, 09001. doi:10.1051/epjconf/202023909001

Henryson, H., II, Toppel, B. J., and Stenberg, C. G. (1976). MC2-2: A code to calculate fast neutron spectra and multigroup cross sections. *Argonne Natl. Lab. Rep*. ANL-8144 (ENDF-239). doi:10.2172/7143331

Hu, K., Ma, X., and Ma, X. (2022). "Development and verification of multigroup cross section generation module," in GroupXS in AXSP, 29th International Conference on Nuclear Engineering, ICONE29, Shenzhen, China, August 8-12.

Jian-kai, Y., Song-yang, L., and Wang, K. (2013). Development and validation of nuclear cross section processing code for reactor analysis – RXSP. *Nucl. Power Eng.* 34. doi:10.1115/ICONE21-15442

Konno, C., Sato, S., Ohta, M., Kwon, S., and Ochiai, K. (2016). New remarks on KERMA factors and DPA cross section data in ACE files. *Fusion Eng. Des.* 109–111, 1649–1652. doi:10.1016/j.fusengdes.2015.10.038

Leszczynski, F., NRSC: Neutron resonance spectrum calculation system version 2001.0, user's manual, 2001.

Li, W., and WangKan, Y. G. (2017). Thermal scattering data processing and development of Thermc module. *High Power laser Part. Beams* 29 (3). doi:10.11884/HPLPB201729.160326

Li, S. (2012). "Research on the methods of online Doppler broadening and nuclear cross section processing," PHD thesis (Tsinghua University).

Lim, C., Han, G., Won, S., and Yang, W. S. (2018). Development of a fast reactor multigroup cross section generation code EXUS-F capable of direct processing of evaluated nuclear data files. *Nucl. Eng. Technol.* 50, 340–355. doi:10.1016/j.net.2018.01.013

Liu, P., Wu, X., and Ge, Z. (2016). "Progress on China nuclear data processing code system," in Proceedings of the ND2016, Bruges, Bergium, 2016 Sep 11–16.

Liu, S., Wang, K., and Chen, Y. (2020). Research on on-the-fly Doppler broading based on modified gauss-hermite method. *Atomic Energy Sci. Technol.* 54. doi:10.7538/yzk.2019.youxian.0466

Ma, X., Ma, X., and Huang, Y. (2022). Development and verification of continuous point section processing module ACEXS based on evaluated nuclear database. *Nucl. Sci. Technol.* 10 (3), 152–164. doi:10.12677/nst.2022.103016

MacFarlane, R. E. (2012). *The NJOY nuclear data processing system, version 2012. LA-UR-12-27079*.

Mattoon, M. C., Beck, R. B., Patel, R. N., Summers, N., Hedstrom, G., and Brown, D. (2012). Generalized nuclear data: a new structure (with supporting infrastructure) for handling nuclear data. *Nucl. Data Sheets* 113, 3145–3171. doi:10.1016/j.nds.2012.11.008

Smith, M. A., Lell, R. M., and Pedro, M. (2003). ZPR-6 assembly 7: A cylindrical assembly with mixed (Pu,U)-Oxide fuel and sodium with A thick depleted-uranium reflector. Nea/nsc/ doc(95)03/vi, mix-comp-fast-001.

Tada, K., Nagaya, Y., Kuieda, S., Suyama, K., and Fukahori, T. (2017). Development and verification of a new nuclear data processing system FRENDY. *J. Nucl. Sci. Technol.* 54, 806–817. doi:10.1080/00223131.2017.1309306

Wen, Y., Zu, T., Cao, L., and Wu, H. (2020). Development and verification of heat production and radiation damage energy production cross section module in the nuclear data processing code NECP-Atlas. *Ann. Nucl. Energy* 144, 107544. doi:10.1016/j.anucene.2020.107544

Wiarda, D., Dunn, M. E., Greene, N. M., Williams, M. L., Celik, C., and Petrie, L. M. (2016). *AMPX-6: A modular code system for processing ENDF/B*. USA: Oak Ridge National Laboratory. ORNL/TM-2016/43.

Williams, M. L., and Hollenbach, D. F., (2011). CENTRM: A one-dimensional neutron transport code for computing pointwise energy spectra, ORNL/TM-2005/39.

Yu, J. (2015). "Research on the key method s of evaluation, processing and application of important nuclear data for reactor and code development," PHD thesis (Tsinghua University).

Zu, T., Xu, J., Tang, Y., Bi, H., Zhao, F., Cao, L., et al. (2019). NECP-atlas: A new nuclear data processing code. *Ann. Nucl. Energy* 123, 153–161. doi:10.1016/j.anucene.2018.09.016

frontiers | Frontiers in Energy Research

TYPE Original Research
PUBLISHED 13 January 2023
DOI 10.3389/fenrg.2023.1088718

OPEN ACCESS

EDITED BY
Turgay Korkut,
Sinop University, Türkiye

REVIEWED BY
Pavel Tsvetkov,
Texas A&M University, United States
Haochun Zhang,
Harbin Institute of Technology, China

*CORRESPONDENCE
Xingjie Peng,
pengxingjiets@126.com
Lianjie Wang,
wanglianjie@tsinghua.org.cn

SPECIALTY SECTION
This article was submitted to Nuclear Energy,
a section of the journal
Frontiers in Energy Research

RECEIVED 03 November 2022
ACCEPTED 02 January 2023
PUBLISHED 13 January 2023

CITATION
Fang C, Peng X, Zhao C, Lou L, Zhang B, Wang L, Chen Z and Li Q (2023), Neutronics and thermal-hydraulics coupling analysis for a small lead-based fast reactor based on the discrete ordinate nodal and parallel channel method. *Front. Energy Res.* 11:1088718. doi: 10.3389/fenrg.2023.1088718

Neutronics and thermal-hydraulics coupling analysis for a small lead-based fast reactor based on the discrete ordinate nodal and parallel channel method

Chao Fang, Xingjie Peng*, Chen Zhao, Lei Lou, Bin Zhang, Lianjie Wang*, Zhang Chen and Qing Li

Science and Technology on Reactor System Design Technology Laboratory, Nuclear Power Institute of China, Chengdu, China

The full-core neutronics/thermal-hydraulics (NE/TH) coupling analysis for a small lead-based fast reactor (SLFR) was presented. The NE-to-TH coupling occurs *via* power distribution, whereas the TH-to-NE coupling occurs *via* the material cross section, which is related to the temperature distribution. In the NE module, a discrete ordinate (SN) nodal solver is implemented based on the hexagonal prism mesh. In the TH module, a parallel channel model is implemented with each hexagonal fuel assembly as a channel. The mass flow of each channel is searched according to the same pressure drop, the temperature and density of the coolant within each channel is calculated with a one-dimensional axial heat convection model, and the temperature distribution along the fuel pin is calculated with a one-dimensional radial heat conduction model. In order to update the cross section, a temperature-dependent homogenized microscopic cross-section library is prepared in advance, and based on the temperature distribution obtained from the TH calculation, the cross-section data required by the NE calculation are obtained by interpolation. The results of the NE/TH coupling analysis for SLFR indicate that the TH parameters (the maximum temperature of the fuel, cladding, and coolant and the maximum velocity of the coolant) are all within the design limits, and the TH feedback provides negative reactivity feedback (about −200 pcm) and has a fairly small effect on the power distribution (<1.0%).

KEYWORDS

small lead-based fast reactor, neutronics/thermal-hydraulics coupling, discrete ordinate method, hexagonal prism nodal method, parallel channel method

1 Introduction

Climate change caused by excessive greenhouse gas emission has become a major challenge for mankind; carbon neutrality and low-carbon energy transformation are becoming the long-term development visions of all countries around the word, which provides opportunities for the development of clean and low-carbon energy, including nuclear energy.

The innovation of nuclear energy technology is getting more and more attention among the world's nuclear powers, the development of advanced Generation IV (Pioro, 2016) reactors is accelerating, and fast reactors are the dominant route because of significant advantages in terms of fuel utilization and nuclear non-proliferation (Cochran et al., 2010). In order to supply power for remote isolated areas and other special fields, miniaturization and modularization (Wang

et al., 2015; Wu et al., 2016) have become important directions of reactor development. Lead-based alloys, including lead and lead-bismuth eutectic (LBE) (Concetta, 2015), are good choices as coolants for small fast reactors, owing to their good neutronic characteristics, high thermal conductivity, and strong natural circulation capability. These advantages can simplify the system design and make the reactor more compact and reliable.

Numerical simulation is the basis of reactor design, safety analysis, and optimization (YANG WS, 2012). A nuclear reactor is a complex multi-physical coupling system (Christophe, 2020), which includes neutronics, thermal-hydraulics, mechanicals, materials, and chemistry. Among them, the coupling between neutronics and thermal-hydraulics is relatively strong, and coupled numerical simulation of NE/TH is of great importance in the design stage of a nuclear reactor core.

The purpose of neutronics calculation is to obtain the effective multiplication factor (keff) and power distribution, which provide the heat source to the thermal-hydraulics calculation. The most high-fidelity option is to use the Monte Carlo (MC) method, but it has low efficiency, and the mesh mapping between neutronics and thermal-hydraulics is complicated. The most efficient option is to use the traditional few-group diffusion method, but for SLFR, due to the strong leakage and anisotropy of fast neutrons and complex energy spectrum, this method will lead to large calculation error of flux and keff. The discrete ordinates (SN) nodal method can balance the calculation accuracy and efficiency well. Due to the fact that the average free path of fast neutrons tends to reach one assembly width, it is not necessary to subdivide the assembly into smaller meshes; the nodal can use the hexagonal prism mesh directly.

The purpose of thermal-hydraulics calculation is to obtain the temperature distribution of the fuel, cladding, and coolant and the velocity and density distribution of coolant, which provide parameters to feedback on and design the reactor. The most high-fidelity option is to use the computational fluid dynamics (CFD) method, but it also has low computational efficiency. In this work, a parallel channel model is implemented. Due to the fact that typical assemblies of SLFR are canned, this model assumes each hexagonal fuel assembly as a channel and there is no mass, momentum, and energy exchange between the channels, which implies a uniform distribution of different (NE and TH) relevant parameters at the assembly level. A 1D axial heat convection model is developed to calculate coolant temperatures within each flow channel. The heat source of the assembly is distributed to each fuel rod equally, and a 1D radial heat conduction model is developed to obtain the temperature distribution of the fuel and cladding. The mass flow and velocity of coolants are calculated by iterative research studies to ensure the same pressure drop in each channel.

The NE/TH coupling solution strategies (Wang, Wang and Ding, 2020a) can be divided into tight coupling and loose coupling. Tight coupling refers to solving the NE and TH simultaneously, while loose coupling means to solve them separately, and coupling is realized by exchanging data between them. Loose coupling can be further divided into internal and external couplings. Internal coupling refers to exchange data through memory, while external coupling means transfer data through input and output files. In this work, a loose internal coupling strategy is adopted to achieve the NE/TH coupling. The Picard iteration method is used to transfer the coupling parameters, and the data exchange is repeated until both the NE and TH fields have converged.

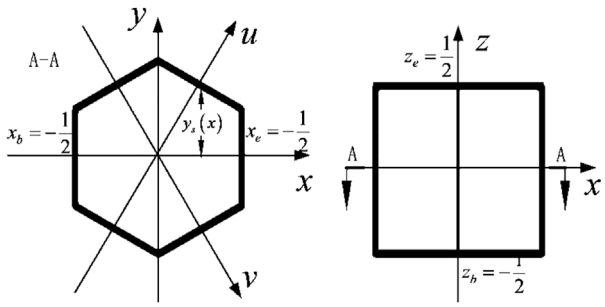

FIGURE 1
Hexagonal prism in the calculated coordinate system.

This paper is organized as follows: Section 2 introduces the neutronics model, derives the SN nodal method in detail, and obtains the nodal response relation with the hexagonal prism nodal by transverse integral technology and nodal equivalence finite difference (NEFD) method (Wang et al., 2020). Section 3 introduces the thermal-hydraulics model and derives the parallel channel method, which include the 1D axial heat convection model, flow rate distribution model, and 1D radial heat conduction model. Section 4 describes the cross-section update model and coupling calculation process. Section 5 presents the NE/TH coupling analysis for a native designed small lead-based fast reactor (SLBR) (Zhao et al., 2022, *p*. 50). Finally, the study is summarized and some conclusions are drawn in Section 6.

2 Neutronics model

Considering the balance of calculation accuracy and efficiency, the SN nodal method with the hexagonal prism mesh is adopted in the neutronics model. This method decouples the 3-dimensional problem into four 1-dimensional problems, using the weighted orthogonal polynomials to expand the unknowns as test functions to do the Galerkin projection. The nodal response relation is obtained by the nodal equivalence finite difference (NEFD) method, and then, the equation can be solved by sweeping to improve the computational efficiency. The detail theory model is as follows.

2.1 Neutron transport equations

The steady-state neutron transport equation can be written as follows:

$$\begin{aligned}&\boldsymbol{\Omega}\cdot\nabla\psi(\boldsymbol{r},\boldsymbol{\Omega},E)+\Sigma_t(\boldsymbol{r},E)\psi(\boldsymbol{r},\boldsymbol{\Omega},E)=\\&\int_0^{\infty}\int_{4\pi}\Sigma_s(\boldsymbol{r},\boldsymbol{\Omega}'\rightarrow\boldsymbol{\Omega},E'\rightarrow E)\psi(\boldsymbol{r},\boldsymbol{\Omega}',E')d\boldsymbol{\Omega}'dE'+\\&\frac{\chi(\boldsymbol{r},E)}{4\pi k_{eff}}\int_0^{\infty}\nu\Sigma_f(\boldsymbol{r},E')\int_{4\pi}\psi(\boldsymbol{r},\boldsymbol{\Omega}',E')d\boldsymbol{\Omega}'dE',\end{aligned}\tag{1}$$

where $\boldsymbol{r},\boldsymbol{\Omega},E$ are the space, angle, and energy; ψ is the angular neutron flux ($cm^{-2}s^{-1}$); Σ_t is the total macroscopic cross section (cm^{-1}); Σ_s is the scattering macroscopic cross section (cm^{-1}); χ is the fission spectrum;

$\nu\Sigma_f$ is the production macroscopic cross section (cm^{-1}); k_{eff} is the effective multiplication factor.

Multi-group approximation is adopted for energy, and the discrete ordinate method is adopted for angular discretization. After that, a single group neutron transport equation in each direction can be obtained.

$$\boldsymbol{\Omega}^m \cdot \nabla \psi_g^m(\boldsymbol{r}) + \Sigma_{t,g}(\boldsymbol{r})\psi_g^m(\boldsymbol{r}) = Q_{s,g}^m(\boldsymbol{r}) + Q_{f,g}(\boldsymbol{r}), \tag{2}$$

where m represents the direction index, g represents the energy group index, and Q_s, Q_f represent scattering source and fission source, respectively. This equation can be solved by energy group in each direction, and the different energy groups and directions can be coupled through the right hand side source term.

Ignoring m and g indexes, the transport equation for the hexagonal prism in the calculated coordinate system (Figure 1) can be written as

$$\sum_{s=x,y,z} \frac{\mu_s}{h_s} \frac{\partial}{\partial s} \psi(x,y,z) + \Sigma_t \psi(x,y,z) = Q(x,y,z), \tag{3}$$

where $x, z \in (-1/2, 1/2)$ and $y \in (-y_s(x), y_s(x))$, $y_s(x) = (1-|x|)/\sqrt{3}$. $h_x = h_y = h_r$ is the actual opposite side distance of the hexagon, and h_z is actual height of the hexagonal prism.

2.2 Transverse integral

Three-dimensional transport equations can be decoupled into three radial and one axial equation by transverse integral technique. Integral Eq. 3 within $y \in (-y_s(x), y_s(x))$ and $z \in (-1/2, 1/2)$, and the transverse integral equation along x direction can be obtained:

$$\frac{d}{dx}\left[y_s(x)\psi_x(x)\right] + \frac{\Sigma_t h_r}{\mu_x} y_s(x)\psi_x(x) = q_x(x). \tag{4}$$

Let $\varepsilon_x \equiv e^{-\Sigma_t h_r/\mu_x}$ solve the ordinary differential Eq. 4, and the nodal radial integral equation can be obtained.

$$y_s(x)\psi_x(x) = \frac{\sqrt{3}}{6}\psi_x^- \varepsilon_x^{(x+1/2)} + \int_{-1/2}^{x} q(x')\varepsilon_x^{(x-x')}dx'. \tag{5}$$

Then, the outgoing integral flux can be obtained as

$$\psi_x^+ = \psi_x^- \varepsilon_x + 2\sqrt{3}\int_{-1/2}^{1/2} q(x')\varepsilon_x^{(1/2-x')}dx'. \tag{6}$$

Similar equations can be obtained for the direction of u, v, and z.

2.3 Polynomial expansion

The transverse integral flux, source, and axial leakage term can be expanded by orthogonal polynomials with weights as

$$\psi_x(x) = \sum_{i=0}^{3} \psi_{xi} h_i(x), \tag{7}$$

$$Q_x(x) = \sum_{i=0}^{3} Q_{xi} h_i(x). \tag{8}$$

The first three order polynomials are defined as follows:

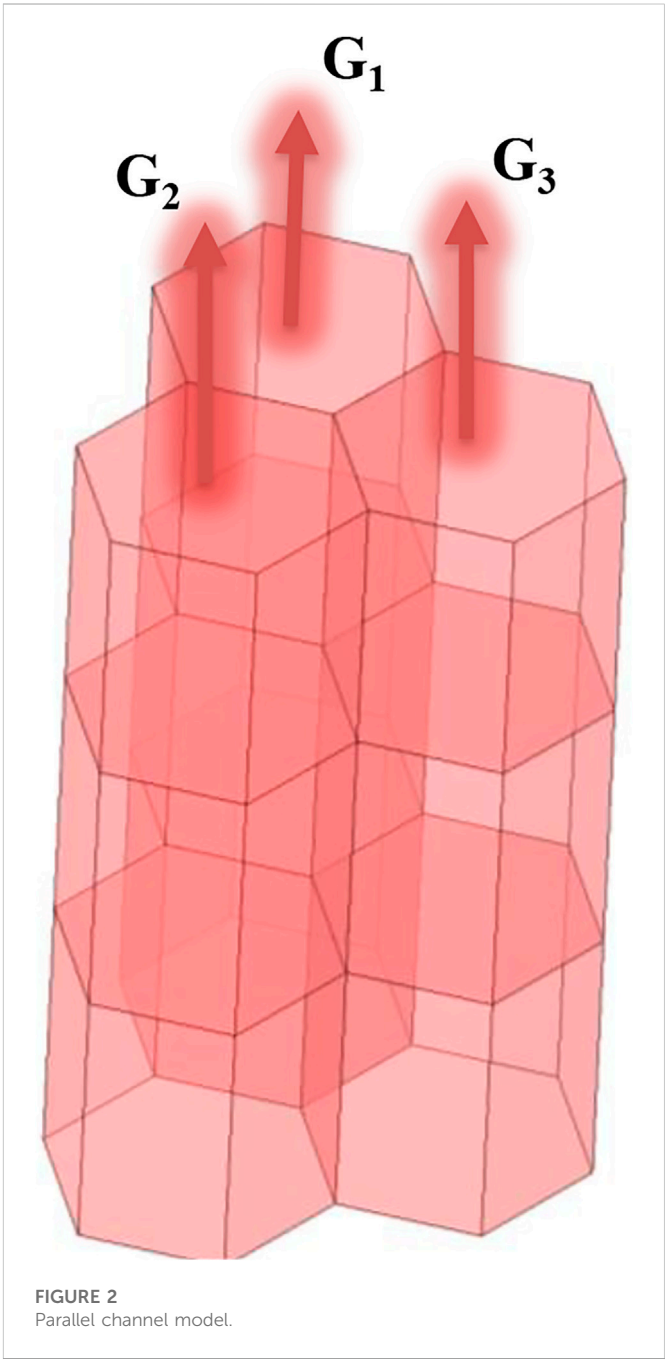

FIGURE 2
Parallel channel model.

$$\{h_i(x)\} = \{1,\ \mathrm{sgn}(\mu_x)x,\ x^2 - 5/72,\ \mathrm{sgn}(\mu_x)(x^3 - 7/50x)\}. \tag{9}$$

We insert Eq. 7 and Eqs 8–5, then multiply both sides of the equation by the basis function, and integrate over the nodal, so the nodal response relationship can be obtained. We insert Eq. 7 and Eqs 8–6, and the relationship of the outgoing surface flux with the incoming surface flux can be obtained.

2.4 Nodal response relation

In hexagonal prism geometry, for any given direction of the quadrature with 60° symmetry, there are three radial planes, one axial plane as the incoming plane, and the remaining planes as the

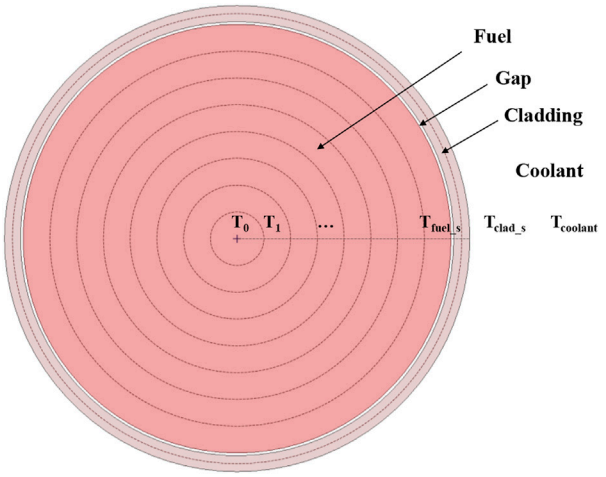

FIGURE 3
Fuel pin temperature calculation model.

outgoing planes. The response relationship of the outgoing surface flux with the nodal average flux and incoming surface flux can be expressed as

$$\psi_s^+ = A_s\bar{\psi} + (1 - B_s)\psi_s^- + C_s, \tag{10}$$

where the coefficients and derivation process can be referred to Wang et al. (2020. Integrating Eq. 3 within a nodal, the neutron balance equation can be obtained.

$$\sum_{s=v,x,u,z} \alpha_s\mu_s\left(\psi_s^+ - \psi_s^-\right) + \Sigma_t\bar{\psi} = \overline{Q}, \tag{11}$$

where $\alpha_v = \alpha_x = \alpha_u = 2/(3h_r), \alpha_z = 1/h_z$. Combining Eqs 10, 11, the nodal average flux can be calculated from the incoming surface flux:

$$\bar{\psi} = \frac{\sum_{s=v,x,u,z} \alpha_s\mu_s\left(B_s\psi_s^- - C_s\right) + \bar{Q}}{\Sigma_t + \sum_{s=v,x,u,z} \alpha_s\mu_s A_s}. \tag{12}$$

According to the sweeping order determined in advance, the average flux of the nodal is calculated by Eq. 12 with incoming boundary condition, and then, the outgoing surface flux is calculated by Eq. 10 and taken as the incoming boundary condition of the next nodal. The flux distribution and keff are obtained by iterative of the nodal, direction, and energy group, and then, the power distribution can be obtained as

$$q(\boldsymbol{r}) = \sum_{g=1}^{G} \Sigma_{f-kapa,g}(\boldsymbol{r})\phi_g(\boldsymbol{r}), \tag{13}$$

where q is the power distribution, Σ_{f-kapa} is the energy release cross section, and ϕ is the scalar flux distribution. Once q is obtained, the TH calculation can be performed.

3 Thermal-hydraulics model

Due to the typical assemblies of SLFR being canned, a parallel channel model (Teng-Yue et al., 2015) is implemented for the TH calculation, and this model assumes each hexagonal fuel assembly as a channel with no mass, momentum, or energy exchange between channels. The first step of this model is to search the flow rate of each coolant channel according to the same pressure drop of each inlet and outlet, in which the pressure drop is obtained by solving axial 1D momentum conservation equations, and then, the axial coolant temperature distribution of each channel is calculated by the 1D axial heat convection model. Finally, the temperature distribution of the fuel and cladding is calculated by the 1D radial heat conduction model.

3.1 Axial heat convection model

3.1.1 Conservation equations

The conservation equations of the 1D single-channel model can be expressed as follows.

Mass conservation equation:

$$\frac{\partial G}{\partial z} = 0. \tag{14}$$

Momentum conservation equation:

$$-\frac{\partial P}{\partial z} = \rho g\cos\theta + \frac{f|G|G}{2D_e\rho} + \frac{\partial}{\partial z}\left(\frac{G^2}{\rho}\right). \tag{15}$$

Energy conservation equation:

$$\frac{\partial}{\partial z}(Gh) = \frac{q'P_h}{A} + \frac{G}{\rho}\left(\frac{\partial P}{\partial z} + \frac{f|G|G}{2D_e\rho}\right), \tag{16}$$

where G is the mass flow rate (kg·m^{-2}s^{-1}); P is the pressure (Pa); ρ is the coolant density (/kg·m^{-3}); f is the friction factor; D_e is the equivalent channel diameter (m); h is the coolant specific enthalpy (J·kg^{-1}); q' is the heat flux (W·m^{-2}); P_h is the heat perimeter of the channel (m); A is the flow area of the channel (m^2).

It can be assumed that all enthalpy rises are converted into coolant temperature rises, thus the average temperature rises of the coolant within a nodal can be calculated as

$$\Delta T = \frac{q'}{C_pG}, \tag{17}$$

where C_p is the specific heat capacity of the coolant(J·kg^{-1}·K^{-1}), and the coolant temperature of the nodal i can be calculated as

$$T_{coolant,i} = T_{coolant,i-1} + \Delta T_i. \tag{18}$$

The heat transfer between the cladding surface and the coolant is mainly single-phase convection, thus the cladding surface temperature can be calculated as

$$T_{clad\_s} = T_{coolant} + \frac{q'}{h_c}, \tag{19}$$

where h_c is the convective heat transfer coefficient(W·m^{-2}·K^{-1}).

3.1.2 Flow rate distribution model

For the parallel channel model, the pressure drop of each channel is a function of the mass flow rate and is equal, which can be expressed as

$$\Delta P_1(G_1) = \Delta P_2(G_2) = \cdots = \Delta P_I(G_I) = \Delta P = P_{out} - P_{in}, \tag{20}$$

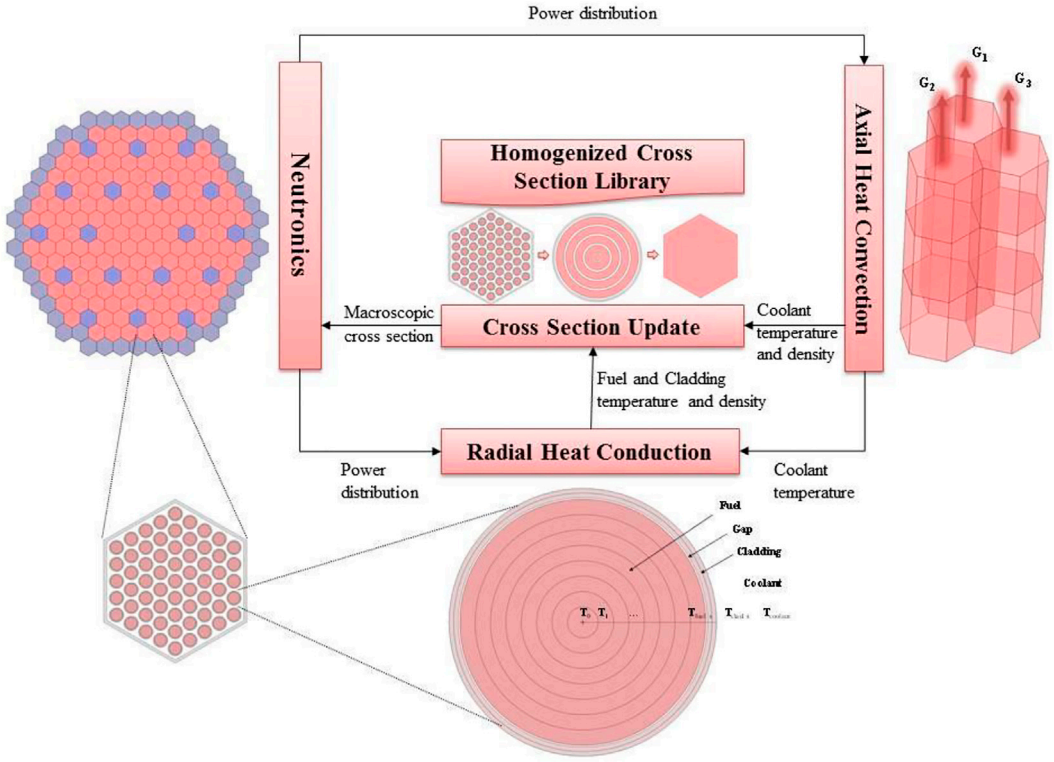

FIGURE 4
NE/TH coupling calculation process.

$$\sum_{i=1}^{I} A_i G_i = W_T. \tag{21}$$

The first-order Taylor expansion can be performed on the pressure drop function as

$$\Delta P_i^{(n+1)} = \Delta P_i^{(n)} + a_i^n \left(G_i^{(n+1)} - G_i^{(n)} \right), i = 1, 2, \cdots I, \tag{22}$$

where

$$a_i^n = \left. \frac{\mathrm{d}(\Delta P_i)}{\mathrm{d}(G_i)} \right|_{G_i = G_i^n} \simeq \frac{\Delta P_i^{(n)} - \Delta P_i^{(n-1)}}{G_i^{(n)} - G_i^{(n-1)}}. \tag{23}$$

Thus, the mass flow rate can be updated with the following formula:

$$G_i^{(n+1)} = G_i^{(n)} + \frac{1}{a_i^n} \left[\Delta P - \Delta P_i^{(n)} \right], i = 1, 2, \cdots I. \tag{24}$$

The diagrammatic drawing of the parallel channel model is shown in Figure 2.

The calculation process of the flow distribution and coolant temperature distribution can be summarized as follows:

(1) Initial flow rate distribution is determined based on the flow area of each channel.
(2) The temperature distribution and pressure drop of each channel are obtained by solving the conservation equations.
(3) If the pressure drops of all channels are the same, end the calculation. Otherwise, redistribute the flow rate and go to step (2).

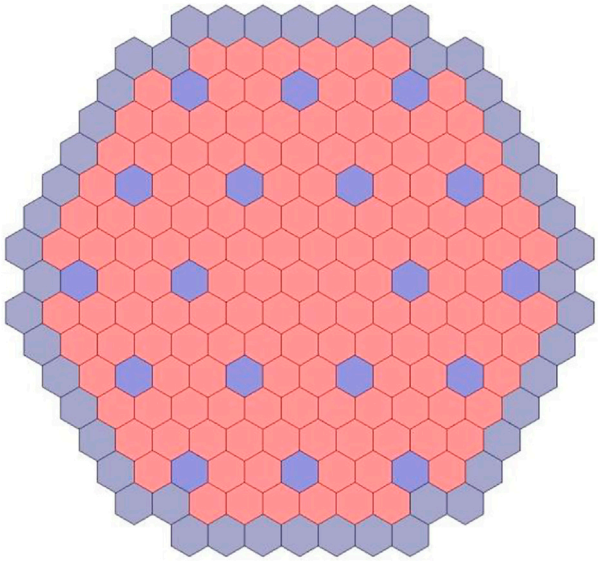

FIGURE 5
SLBR-50 configuration.

3.2 Radial heat conduction model

In the steady state and ignoring the axial heat transfer, the heat transfer equation and boundary condition in the cylindrical coordinate system are as follows:

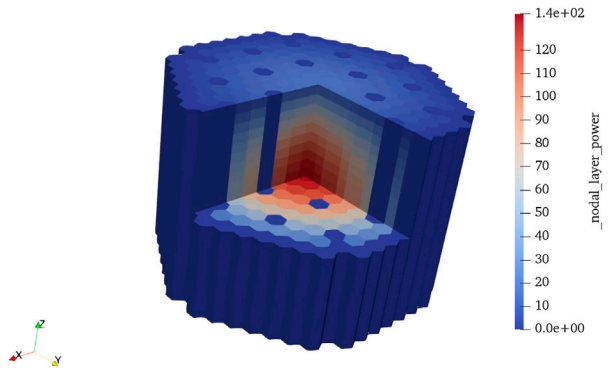

FIGURE 6
Power distribution.

$$\frac{1}{\rho C_p}\frac{1}{r}\frac{\mathrm{d}}{\mathrm{d}r}\left(rk\frac{\mathrm{d}T}{\mathrm{d}r}\right)+\frac{1}{\rho C_p}Q=0, \tag{25}$$

$$\frac{\mathrm{d}T}{\mathrm{d}r}=0, r=0; T=T_{clad\_s}, r=R_{pin}, \tag{26}$$

where ρ is the material density (kg·m^{-3}); C_p is the specific heat capacity (J·kg^{-1}K.$^{-1}$); k is the heat conductivity (W·m^{-2}K.$^{-1}$); Q is the heat source (W·m^{-3}).

Integrating the equation over the space, the following equation can be obtained:

$$rk\frac{\mathrm{d}T}{\mathrm{d}r}+Q\frac{r^2}{2}=0. \tag{27}$$

The finite difference method (FDM) is used to solve Eq. (27).The fuel is divided into more than five segments, the gap is one segment, and the cladding is at least two segments (as shown in Figure 3). The radial temperature distribution of the fuel pin can be obtained by solving the linear equations generated by FDM.

4 Neutronics/thermal-hydraulics coupling model

A loose internal coupling strategy is adopted to do the NE/TH coupling calculation. The NE-to-TH coupling *via* power distribution can be transferred directly through the memory, whereas the TH-to-NE coupling *via* the temperature-dependent material cross sections can be calculated by interpolating within temperature-dependent cross-section tables.

4.1 Cross-section update

The temperature-dependent cross-section library is generated by the external program, which uses 1D cylindrical geometry to equivalent the hexagonal assembly, superfine group method to do the resonance calculation, and super homogenization (SPH) method to do cross-section homogenization. Once the cross-section library of the fuel, cladding, and coolant at tabulated temperature is generated, the cross section at any temperature can be obtained by interpolation. The linear interpolation formula is as follows:

$$\sigma=(1-w)\sigma_1+w\sigma_2, \tag{28}$$

where σ is the cross section at the temperature point T, σ_1 and σ_2 are the cross sections at two adjacent temperature points T_1 and T_2 ($T_1<T_2$), and w is a weighting coefficient. For fuel materials, the temperature dependence of cross sections is dominated by the Doppler effect, which is proportional to the square-root of temperature; therefore, the cross sections are interpolated using the square root of temperature interpolation. Thus,

$$w=\frac{\sqrt{T}-\sqrt{T_1}}{\sqrt{T_2}-\sqrt{T_1}}. \tag{29}$$

For cladding and coolant materials, the cross sections are linearly interpolated by temperature. Thus,

$$w=\frac{T-T_1}{T_2-T_1}. \tag{30}$$

Based on the temperature distribution obtained from the TH calculation, the cross section data required by the NE calculation can be obtained.

The macroscopic cross section is related to the microscopic cross section and density of nuclides, both of which vary with temperature. The microscopic cross section can be obtained by interpolation described previously, while the variation in the nuclide density with temperature is mainly due to the variation in material density. Assuming that the material density at temperature T_0 is ρ_0 and the nuclide density is N_0, the nuclide density at temperature T is

$$N(T)=N_0\frac{\rho(T)}{\rho_0}, \tag{31}$$

where $\rho(T)$ is the material density at temperature T. The macroscopic cross section at temperature T can be calculated as

$$\Sigma(T)=N(T)\sigma(T). \tag{32}$$

4.2 Coupling calculation process

The NE/TH coupling calculation process can be divided into four parts. First, the homogeneous microscopic cross-section library of the hexagonal assembly at different state points is obtained by the assembly calculation. Then, the cross section is interpolated according to the temperature distribution (taking the design temperature for the first calculation) to obtain the cross section at the actual state point. Next, neutronics calculation is carried out to obtain the power distribution. Finally, the power distribution is set as the heat source for TH calculation and the temperature distribution of the fuel, cladding, and coolant in the reactor core is obtained. The calculation and data transfer process are shown in Figure 4. The Picard iteration method is adopted to do the NE/TH coupling calculation, which keeps iterating until the NE fields and TH fields have converged.

5 Coupling analysis for a small lead-based fast reactor

In this section, the NE/TH coupling analysis for a native designed small lead-based fast reactor (SLBR) is presented.

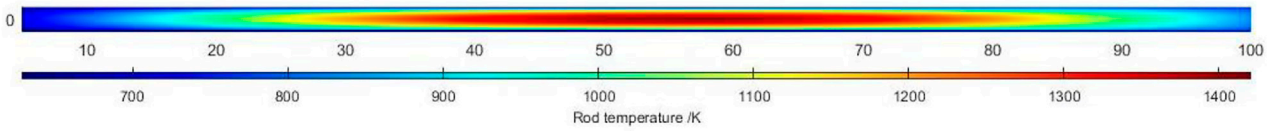

FIGURE 7
Temperature distribution of the fuel rod in the central assembly.

TABLE 1 Maximum temperature of different material regions.

Maximum temperature of the coolant (K)	751.82
Maximum temperature of the cladding outer surface (K)	758.19
Maximum temperature of the cladding inner surface (K)	767.05
Maximum temperature of the fuel (K)	1426.22

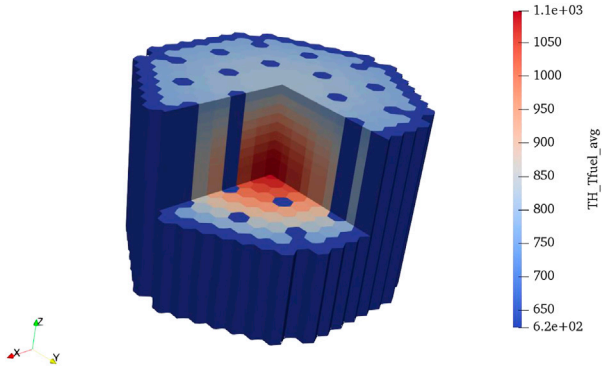

FIGURE 8
Average temperature distribution of the fuel.

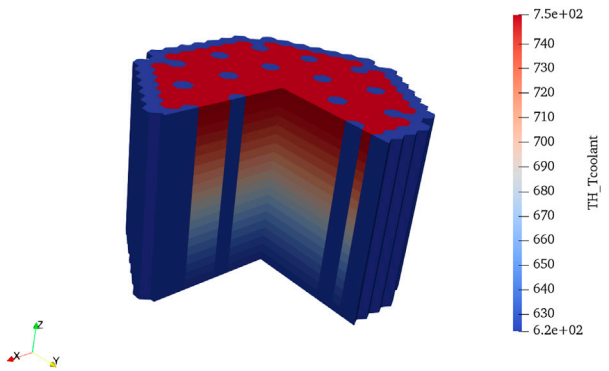

FIGURE 9
Temperature distribution of the coolant.

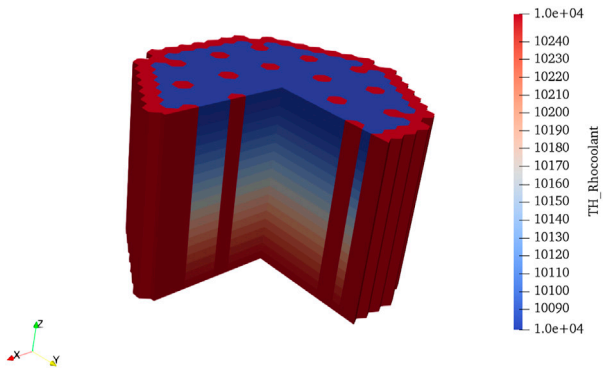

FIGURE 10
Density distribution of the coolant.

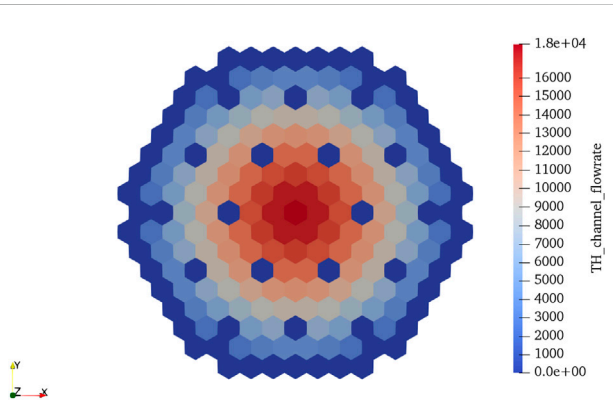

FIGURE 11
Flow rate distribution of the coolant.

5.1 Model description

The thermal power of the reactor is 50 MW, the material of the fuel is 19.95% enrichment UO_2, the control-rod absorber material is B_4C, the reflector material is BeO, and the coolant material is the lead-bismuth eutectic (LBE) (44.5% Pb and 55.5% Bi). The reactor core consists of 144 fuel assemblies, 18 control-rod assemblies, and 48 reflector assemblies, each assembly consists of 61 rods, which are arranged in a triangular grid, and the configuration is shown in Figure 5. The detailed core parameters can be found in the work of Zhao et al. (2022, *p*. 50).

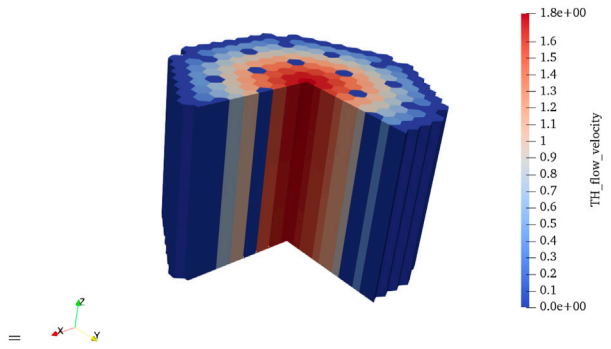

FIGURE 12
Velocity distribution of the coolant.

TABLE 2 Comparison of neutronics parameters with and without TH feedback.

Parameter	Keff	Radial power peak factor	Axial power peak factor
With TH feedback	1.12566	1.995	1.4937
Without TH feedback	1.12359	2.015	1.4930
Difference (%)	.18	.99	.05

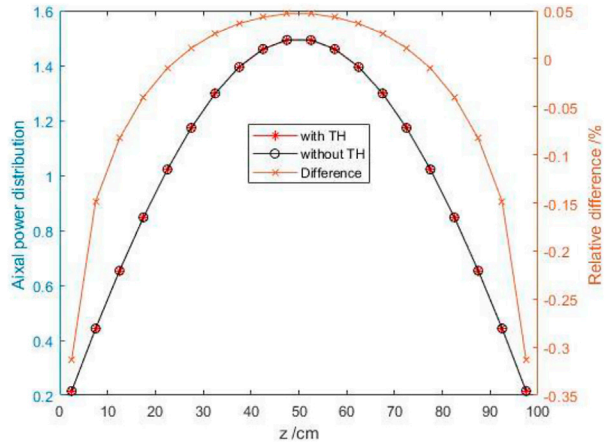

FIGURE 13
Compare axial power distribution between with TH and without TH calculation.

5.2 Physical parameters

The physical properties of the materials in SLBR refer to Sobolev, (2007) and Roelofs, (2019), and the thermal conductivity of fuel material varies with temperature as

$$k = 1.0/\left(0.042 + 2.71 \times 10^{-4}T\right) + 6.9 \times 10^{-11}T^3. \quad (33)$$

The thermal conductivity of cladding materials varies with temperature as

$$k = 462.0 + 0.134T. \quad (34)$$

The melting point of the LBE coolant is 397 K and the boiling point is 1943 K. When using liquid metals as coolants and the fuel rods are arranged in triangular grids with $1.1 \le P/D \le 1.5$ (where P is the pitch of fuel rods and D is the diameter of fuel rods) and $80 \le Pe \le 4000$, the correlation (Mikityuk, 2009) for the Nusselt number is obtained as

$$\mathrm{Nu} = 0.72\mathrm{Re}^{0.45}\mathrm{Pr}^{0.45}, \quad (35)$$

where Pe is the Peclet number, Re is the Reynolds number, and Pr is the Prandtl number. The heat transfer coefficient of LBE can be obtained by the Nusselt number. To avoid corrosion of the cladding by the liquid metal coolant, the velocity of LBE should not exceed 2 m/s.

5.3 Result analysis

When making the cross section library, the selected temperature points should cover all working states, thus, the microscopic cross sections at 600, 700, 800, 1000, and 1200 K are made for fuel, cladding, and coolant materials. For the NE calculation, the order of discrete ordinates is set at S6, the radial mesh is used to create hexagonal assembly, and the axial mesh is 5 cm per layer. For the TH calculation, only fuel assemblies are considered, the axial mesh is computed using the NE calculation, the radial mesh is divided into five segments for fuel, one segment for gap, and two segments for cladding. The power distribution result is shown in Figure 6.

The maximum power location is at the central fuel assembly, and the fuel–rod temperature distribution at the central assembly is shown in Figure 7. The maximum temperature of the fuel, cladding, and coolant is all presented in this assembly, which is shown in Table 1.

Figures 8, 9, 10, 11, 12 show the average fuel temperature, coolant temperature, coolant density, coolant flow rate, and coolant velocity distribution, which are outputted with the hexagonal nodal mesh, respectively. It can be seen that the average temperature distribution of the fuel is similar to the power distribution, and the maximum average temperature of the fuel is less than 1200 K. Since the single-channel model is applied to each parallel channels, the coolant temperature presents a one-dimensional distribution, the density of the coolant changes very little, and its distribution is the opposite of the temperature distribution. The flow rate and velocity distribution are similar to the two-dimensional power distribution, the maximum velocity is equal to 1.8 m/s, which is less than the limit 2 m/s.

The NE/TH coupling calculation converges after two iterations, and the results of neutronics parameters with and without the TH feedback are shown in Table 2. As we can see, whether TH feedback is considered has little influence on the results of the NE calculation. After considering TH feedback, the effective multiplication factor is reduced by 207 pcm, and the axial and radial power peak factors have small changes. Figure 13 compares the axial power distribution between with TH feedback and without TH feedback and the power distribution almost stays the same. It can be considered that, in steady-state calculation of the fast reactor, the TH calculation has little influence on the NE calculation, and TH feedback calculation is generally not required.

6 Conclusion

A neutronics and thermal-hydraulics loose internal coupling code system was developed in this paper, where the neutronics calculation was based on the SN nodal method with the hexagonal prism mesh, and the thermal-hydraulics calculation was based on the parallel channel model. The neutron flux, the temperature distribution of the fuel, cladding, and coolant, and the velocity, density, and pressure distribution of the coolant in each hexagonal nodal can be obtained through this code system.

Application of the code system could be used for steady-state neutronics thermal-hydraulics coupling analysis for a conceptually designedsmall lead-based fast reactor (SLFR-50). The power distribution and thermal-hydraulics parameters are analyzed, which show that the maximum temperature of the fuel, cladding, coolant, and the maximum velocity of the coolant are all within the design limits. The coupling calculation converges rapidly and the thermal-hydraulics feedback provides negative reactivity feedback (about −200 pcm) and has a fairly small effect on the power distribution (<1.0%).

The results of the NE/TH coupling analysis for SLFR-50 show that the thermal-hydraulics feedback has a fairly small effect on the effective multiplication factor and power distribution; it can be reasonably believed that the power distribution obtained by neutronics calculation can be directly used in the thermal-hydraulics calculation for metal-cooled fast spectrum reactors and the iterative calculation is not required. Theoretically, one reason for this phenomenon is that the number of neutrons in the resonance energy group for fast spectrum reactors is much less than that of thermal spectrum reactors. The Doppler effect has little effect on the neutronics calculation results, and another reason is that the small gradients of temperature distribution and little changes of material density make the macroscopic cross section change a little. The dimensional changes with temperature will have a great impact on the neutronics results for the fast reactor, which needs to be considered for more accurate simulation.

In the future, the neutronics thermal-hydraulics and thermal-mechanic coupling analyses for the fast spectrum reactor will be studied, and the effects of thermal-hydraulics feedback on the neutronics calculation with different energy spectrums will be compared. Experimental studies will be used to validate this code system.

Data availability statement

The original contributions presented in the study are included in the article/Supplementary Material; further inquiries can be directed to the corresponding authors.

Author contributions

CF: main research and manuscript writing. CZ, LL, and BZ: research. XP, LW, ZC, and QL: advice and directing.

Funding

This work was financially supported by the China Association for Science and Technology (Young Elite Scientists Sponsorship Program 2019QNRC001).

Conflict of interest

The authors declare that the research was conducted in the absence of any commercial or financial relationships that could be construed as a potential conflict of interest.

Publisher's note

All claims expressed in this article are solely those of the authors and do not necessarily represent those of their affiliated organizations, or those of the publisher, the editors, and the reviewers. Any product that may be evaluated in this article, or claim that may be made by its manufacturer, is not guaranteed or endorsed by the publisher.

References

Christophe, D. (2020). *Modelling of nuclear reactor multi-physics: From local balance equations to macroscopic models in neutronics and thermal-hydraulics*. Cambridge, United States: Academic Press.

Cochran, T. B., Feiveson, H. A., Patterson, W., Pshakin, G., Ramana, M. V., Schneider, M., et al. (2010). 'Fast breeder reactor programs: History and status'. *International Panel on Fissile Materials*. Paris, France: OECD, 128.

Concetta, F. (2015). Handbook on lead-bismuth eutectic alloy and lead properties, materials compatibility, thermal-hydraulics and technologies. Accessed Available at: http://publications.jrc.ec.europa.eu/repository/handle/JRC100764 November 1, 2022).

Mikityuk, K. (2009). Heat transfer to liquid metal: Review of data and correlations for tube bundles. *Nuclear Engineering and Design*. 239 (4), 680–687. doi:10.1016/j.nucengdes.2008.12.014

Pioro, I. L. (2016). "Handbook of generation IV nuclear reactors," in *Handbook of generation IV nuclear reactors*. Editor Igor L. Pioro (Sawston, United Kingdom: Woodhead Publishing (Woodhead Publishing Series in Energy), 37–54.

Roelofs, F. (2019). *Thermal hydraulics aspects of liquid metal cooled nuclear reactors*. Sawston, United Kingdom: Woodhead Publishing.

Sobolev, V. (2007). Thermophysical properties of lead and lead–bismuth eutectic. *Journal of Nuclear Materials*. 362 (2), 235–247. doi:10.1016/j.jnucmat.2007.01.144

Teng-Yue, M. A., (2015). 'Neutronics and thermal-hydraulics coupled calculation for ADS based on single-channel model'. *Atomic Energy Science Technology* 49, 604–608. [Preprint] Available at: http://en.cnki.com.cn/Article_en/CJFDTOTAL-YZJS201504005.htm (Accessed November 1, 2022).

Wang, J., Wang, Q., and Ding, M. (2020a). Review on neutronic/thermal-hydraulic coupling simulation methods for nuclear reactor analysis. *Annals of Nuclear Energy* 137, 107165. doi:10.1016/j.anucene.2019.107165

Wang, M., Lian, C., Li, Y., Wang, D., Jiang, J., and Wu, Y. (2015). Preliminary conceptual design of a lead–bismuth cooled small reactor (CLEAR-SR). *International Journal of Hydrogen Energy* 40 (44), 15132–15136. doi:10.1016/j.ijhydene.2015.03.097

Wang, Y., Xu, Z., Zheng, Y., and Wu, H. (2020b). A new hexagonal-Z nodal SN method in SARAX code system. *Annals of Nuclear Energy* 144, 107546. doi:10.1016/j.anucene.2020.107546

Wu, Y., Bai, Y., Song, Y., Huang, Q., Zhao, Z., and Hu, L. (2016). Development strategy and conceptual design of China lead-based research reactor. *Annals of Nuclear Energy* 87, 511–516. doi:10.1016/j.anucene.2015.08.015

Yang, W. S. (2012). 'Fast reactor physics and computational methods', Nuclear engineering and technology. *International Jornal of Korean Nuclear Society* 44 (2), 177–198. doi:10.5516/net.01.2012.504

Zhao, C., Lou, L., Zhang, B., Zhou, B., Wang, L., and Peng, X. (2022). Neutronics performance improvement based on the small lead-based fast reactor SLBR-50. *Frontiers in Energy Research*. 10, 982101. doi:10.3389/fenrg.2022.982101

frontiers | Frontiers in Energy Research

TYPE Original Research
PUBLISHED 18 January 2023
DOI 10.3389/fenrg.2022.1101050

OPEN ACCESS

EDITED BY
Jingang Liang,
Tsinghua University, China

REVIEWED BY
Jingyu Zhang,
North China Electric Power University, China
Yinan Cai,
Massachusetts Institute of Technology, United States

*CORRESPONDENCE
Xiafeng Zhou,
zhouxiafeng@hust.edu.cn

SPECIALTY SECTION
This article was submitted to Nuclear Energy, a section of the journal Frontiers in Energy Research

RECEIVED 17 November 2022
ACCEPTED 30 November 2022
PUBLISHED 18 January 2023

CITATION
Zhang Y and Zhou X (2023), Parallel Jacobian-free Newton Krylov discrete ordinates method for pin-by-pin neutron transport models.
Front. Energy Res. 10:1101050.
doi: 10.3389/fenrg.2022.1101050

Parallel Jacobian-free Newton Krylov discrete ordinates method for pin-by-pin neutron transport models

Yangyi Zhang[1] and Xiafeng Zhou[1,2]*

[1]Department of Nuclear Engineering and Technology, School of Energy and Power Engineering, Huazhong University of Science and Technology, Wuhan, China, [2]Institute of Interdisciplinary Research for Mathematics and Applied Science, Huazhong University of Science and Technology, Wuhan, China

A parallel Jacobian-Free Newton Krylov discrete ordinates method (comePSn_JFNK) is proposed to solve the multi-dimensional multi-group pin-by-pin neutron transport models, which makes full use of the good efficiency and parallel performance of the JFNK framework and the high accuracy of the Sn method for the large-scale models. In this paper, the k-eigenvalue and the scalar fluxes (rather than the angular fluxes) are chosen as the global solution variables of the parallel JFNK method, and the corresponding residual functions are evaluated by the Koch–Baker–Alcouffe (KBA) algorithm with the spatial domain decomposition in the parallel Sn framework. Unlike the original Sn iterative strategy, only a "flattened" power iterative process which includes a single outer iteration without nested inner iterations is required for the JFNK strategy. Finally, the comePSn_JFNK code is developed in C++ language and, the numerical solutions of the 2-D/3-D KAIST-3A benchmark problems and the 2-D/3-D full-core MOX/UOX pin-by-pin models with different control rod distribution show that comePSn_JFNK method can obtain significant efficiency advantage compared with the original power iteration method (comePSn) for the parallel simulation of the large-scale complicated pin-by-pin models.

KEYWORDS

parallel Jacobian-free Newton-Krylov method, parallel discrete ordinates method, pin-by-pin neutron transport model, three-dimensional multi-group k-eigenvalue problem, acceleration algorithm

1 Introduction

The efficient parallel algorithms and the acceleration methods of discrete ordinates methods (Sn) (Carlson, 1953) for multi-dimensional large-scale neutron transport models are research hotspots in the reactor simulation field. In the past few decades, many parallel Sn neutron transport codes are developed by using overloading spatial domain decomposition (Bailey and Falgout, 2009) or Koch–Baker–Alcouffe (KBA) algorithms (Baker and Koch, 1998), including DENOVO (Evans et al., 2010), PARTISN (Alcouffe et al., 2005), NECP-hydra (Xu et al., 2018), ARES (Zhang et al., 2017) and so on. To

accelerate the calculation of the original Sn iterative strategies based on the power iteration methods (PI), a batch of numerical methods can be employed, such as Wielandt shifts methods, Chebyshev acceleration methods, coarse mesh finite difference methods, diffusion synthetic acceleration method. In this paper, the parallel Jacobian-free Newton-Krylov (JFNK) (Knoll and Keyes, 2004) methods are adopted.

The JFNK methods have good computational efficiency due to the fast and robust convergence, which are widely used to solve the atmospheric convection problem (Hossain and Alam, 2012), the sea ice simulation (Yaremchu and Panteleev, 2022), two-phase flow calculation (Hajizadeh et al., 2018), the neutron diffusion/transport models (Gill, 2009; Knoll et al., 2011), thermal hydraulics simulation (Esmaili et al., 2020) and multi-physics coupled problems (Walker et al., 2019). Meanwhile, some popular multi-physics coupled environments (or platforms), such as MOOSE (Gaston et al., 2009), LIME (Pawlowski et al., 2011) and VERA (Turner et al., 2016), employ the JFNK framework to solve the complicated reactor coupled systems. Recently, we have also developed an efficient JFNK framework based on coarse mesh finite difference and nodal expansion method in the COupling Multiphysics Environment (COME) to solve the steady/transient neutronics and neutronics-thermal hydraulic coupled problems (Zhou, 2022a; Zhou, 2022b; Zhou et al., 2022; Zhou, 2023). To take advantages of the good efficiency and parallel performance of the JFNK framework in COME, in this paper, the parallel JFNK method is combined with the parallel Sn method to solve the multi-dimensional large-scale neutron transport models.

Therefore, a parallel Jacobian-free Newton Krylov discrete ordinates method (comePSn_JFNK) is proposed to solve the multi-dimensional multi-group pin-by-pin neutron transport k-eigenvalue problems, which makes full use of the fast and robust convergence of the parallel JFNK framework and the high accuracy of the Sn method based on the KBA algorithm. The key to implement the JFNK framework into the Sn algorithm is to choose the k-eigenvalue and the scalar fluxes (rather than the angular fluxes) as the global solution variables for parallel JFNK, which are the minimal subset of the non-linear system. The corresponding residual functions are directly constructed from the neutron transport equations and evaluated based on the parallel Sn transport sweeping process by using a "flattened" power iterative process including a single outer iterative step without nested inner iterations.

This paper is organized as follows. The detailed theories of the comePSn_JFNK method are presented in Section 2, including the parallel JFNK method, the parallel Sn method, the residual function evaluation and the solution strategies. In Section 3, the numerical results for the 2-D/3-D full-core pin-by-pin models are analyzed to test the accuracy and efficiency of the comePSn_JFNK method. The conclusions are given in Section 4.

2 Methodologies of the comePSn_JFNK method

2.1 Parallel JFNK

JFNK method is one of the inexact Newton-Krylov methods, which are the combinations of Newton's methods for solving non-linear equations, Krylov subspace methods for solving the linear Newton correction equations, and "Jacobian-free" technology for approximately solving Jacobian-vector product (Knoll and Keyes, 2004). The non-linear equations can be generally written by $\mathbf{F}(\mathbf{x}) = 0$. The Newton iteration step (where n is the index) is to solve the discrete equations as

$$\begin{aligned} \mathbf{Ja}\left(\mathbf{x}^{(n)}\right)\delta\mathbf{x}^{(n)} &= -\mathbf{F}\left(\mathbf{x}^{(n)}\right), \\ \mathbf{x}^{(n+1)} &= \mathbf{x}^{(n)} + \delta\mathbf{x}^{(n)}, \end{aligned} \tag{1}$$

where $\mathbf{x}$ is the vector of global solution variables, $\mathbf{F}$ represents the non-linear discrete system, and $\mathbf{Ja}$ represents the Jacobian matrix. For Krylov methods, the Jacobian matrix needs not to be formed explicitly because the product of Jacobian matrix and a vector ($\mathbf{v}$) rather than the Jacobian matrix is required. Using the first-order finite difference approximation, the Jacobian-vector product can be solved by

$$\mathbf{Ja}\left(\mathbf{x}^{(n)}\right)\mathbf{v} = \frac{\mathbf{F}\left(\mathbf{x}^{(n)} + \varepsilon\mathbf{v}\right) - \mathbf{F}\left(\mathbf{x}^{(n)}\right)}{\varepsilon} \tag{2}$$

where ε is a perturbation parameter which can be specified by $\mathbf{x}^{(n)}$ and $\mathbf{v}$.

For the parallel JFNK method, only the residual functions, the dot products and the norms of vectors are considered to be evaluated synchronously in multiple processors, which are easily developed in the parallel framework. In addition, residual functions are evaluated from the parallel Sn method based on KBA sweeping algorithm as shown in the following sections.

2.2 Evaluation of residual functions from parallel Sn

The multi-group neutron Boltzmann transport equations for the k-eigenvalue problem can be written as

$$\hat{\Omega}_n \cdot \nabla\psi_{g,n}(\vec{r}) + \Sigma_{t,g}(\vec{r})\psi_{g,n}(\vec{r}) = \sum_{g'=1}^{G}\Sigma_{s,g'\to g}(\vec{r})\phi_{g'}(\vec{r}) + \frac{\chi_g}{k_{eff}}\sum_{g'=0}^{G}\nu\Sigma_{f,g'}(\vec{r})\phi_{g'}(\vec{r}), \tag{3}$$

$$\phi_g(\vec{r}) = \sum_{n=1}^{N}\omega_n\psi_{g,n}(\vec{r}), \tag{4}$$

where $\psi_{g,n}(\vec{r})$ = Angular neutron flux, $\phi_g(\vec{r})$ = Scalar neutron flux, k_{eff} = Effective multiplication factor (k-eigenvalue), $\Sigma_{t,g}$ = Macroscopic total cross section, $\Sigma_{s,g'\to g}$ = Macroscopic scattering cross section, χ_g = Fission spectrum, $\nu\Sigma_{f,g}$ = Macroscopic production cross section, g = Energy group index and G = Total number of

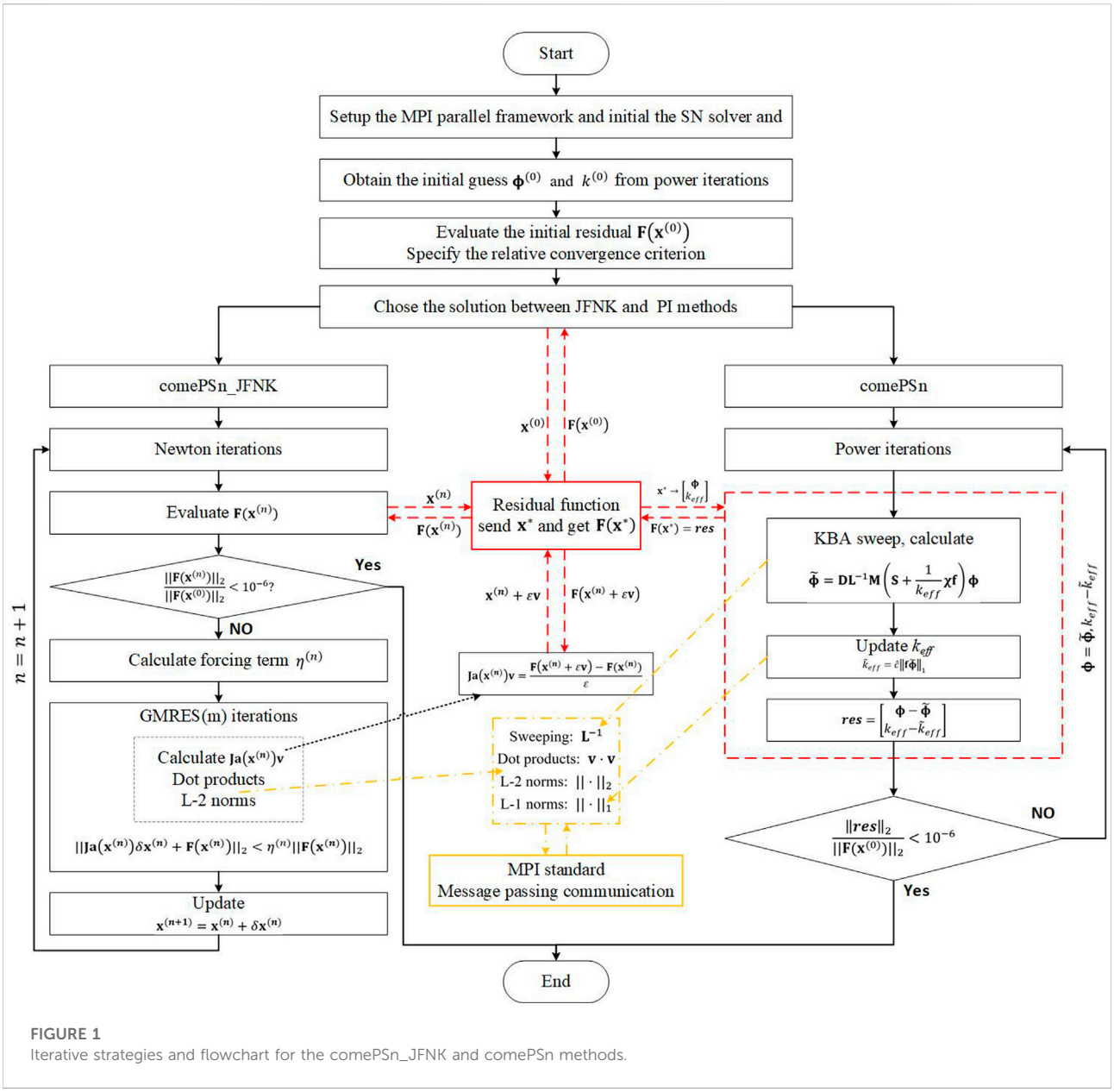

FIGURE 1
Iterative strategies and flowchart for the comePSn_JFNK and comePSn methods.

energy group, n = Discrete angle index and N = Total number of discrete angles, $\vec{r}$ = Spatial position vector and $\hat{\Omega}_n$ = Unit direction vector for discrete angle n, ω_n = Quadrature weight for discrete angle n.

Eq. 3 can be written in operator notation form as

$$\mathbf{L}\psi = \mathbf{MS}\phi + \frac{1}{k_{eff}}\mathbf{M}\chi\mathbf{f}\phi, \tag{5}$$

where ψ and ϕ are vectors which contain the angular fluxes and scalar fluxes, respectively. $\mathbf{L}$ denotes the sum of the streaming operator and removal operator. $\mathbf{M}$ is the scalar-to-discrete operator and $\mathbf{D}$ is the discrete-to-scalar operator; in the case of isotropic scattering, $\mathbf{D}$ represents the action which integrates the angular fluxes to the scalar fluxes as shown is Eq. 4, i.e., $\phi = \mathbf{D}\psi$. $\mathbf{S}$ is the matrix of group-to-group scattering cross sections, $\mathbf{f}$ is the matrix of production cross sections and χ is the fission spectrum matrix. The parallel transport sweeping based on the KBA algorithm with the spatial domain decomposition (Baker, 2017) is employed to directly inverse $\mathbf{L}$ into $\mathbf{L}^{-1}$, which marches across the spatial domain cells in the direction of neutron travel.

Multiplied by $\mathbf{DL}^{-1}$, Eq. 5 becomes

$$\begin{aligned}\phi &= \mathbf{DL}^{-1}\mathbf{MS}\phi + \frac{1}{k_{eff}}\mathbf{DL}^{-1}\mathbf{M}\chi\mathbf{f}\phi \\ \Rightarrow (\mathbf{I} - \mathbf{DL}^{-1}\mathbf{MS})\phi &= \frac{1}{k_{eff}}\mathbf{DL}^{-1}\mathbf{M}\chi\mathbf{f}\phi.\end{aligned} \tag{6}$$

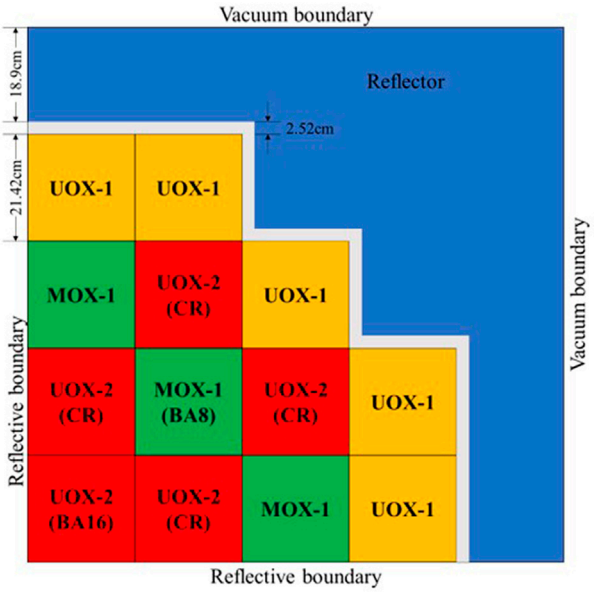

FIGURE 2
Radial geometry of the KAIST-3A benchmark problem.

It is an eigenvalue problem, whose solution is to get an eigenpair vector $(\phi^{\mathrm{T}}, k_{\mathrm{eff}})^{\mathrm{T}}$. Traditionally, it can be solved by power iteration method (PI) which includes two-level nested iterations. The outer iteration can be written as

$$\boldsymbol{\phi}^{(l+1)} = \left(\mathbf{I} - \mathbf{DL}^{-1}\mathbf{MS}\right)^{-1} \frac{1}{k_{eff}^{(l)}} \mathbf{DL}^{-1}\mathbf{M}\boldsymbol{\chi}\mathbf{f}\boldsymbol{\phi}^{(l)}, \tag{7}$$

$$k_{eff}^{(l+1)} = \hat{c}||\mathbf{f}\boldsymbol{\phi}^{(l+1)}||_1, \tag{8}$$

where l is the outer iterative index, $\|\cdot\|_1$ denotes the L-1 norm. $\hat{c}$ is a fixed value during iteration and it can be assigned form the iterative initial value as

$$\hat{c} \equiv \frac{k_{eff}^{(0)}}{||\mathbf{f}\boldsymbol{\phi}^{(0)}||_1}. \tag{9}$$

For each outer iteration, Eq. 7 is equivalent to a fixed source problem, which can generally be calculated using fixed point iteration method (which is the inner iteration) as

$$\boldsymbol{\phi}^{(m+1,l)} = \mathbf{DL}^{-1}\mathbf{M}\left(\mathbf{S}\boldsymbol{\phi}^{(m,l)} + \frac{1}{k_{eff}^{(l)}}\boldsymbol{\chi}\mathbf{f}\boldsymbol{\phi}^{(l)}\right), \tag{10}$$

where m is the inner iterative index. In this paper, this power iterative strategy is called comePSn method. To efficiently get the simultaneous solution of the non-linear system using the parallel JFNK method, the k-eigenvalue and the scalar fluxes (rather than the angular fluxes) are finally chosen as the global solution variables, and $\mathbf{x} = [\boldsymbol{\phi}^{\mathrm{T}}, k_{\mathrm{eff}}]^{\mathrm{T}}$.

Meanwhile, $\mathbf{x}$ is also the minimal subset of all the variables for the discrete non-linear system based on the parallel Sn method, which indicates that the JFNK solution has the least number of global solution variables and can obtain good numerical efficiency.

Then, according to the PI strategy for the parallel Sn method as shown in Eq. 7 and Eq. 8, the corresponding residual functions for the parallel JFNK method can be easily expressed as

$$\mathbf{F}(\mathbf{x}) \equiv \begin{bmatrix} \mathbf{F}_{\phi}(\mathbf{x}) \\ \mathbf{F}_{k}(\mathbf{x}) \end{bmatrix} = \begin{bmatrix} \boldsymbol{\phi} - \left(\mathbf{I} - \mathbf{DL}^{-1}\mathbf{MS}\right)^{-1} \frac{1}{k_{eff}} \mathbf{DL}^{-1}\mathbf{M}\boldsymbol{\chi}\mathbf{f}\boldsymbol{\phi} \\ k_{eff} - \hat{c}||\mathbf{f}\left(\mathbf{I} - \mathbf{DL}^{-1}\mathbf{MS}\right)^{-1} \frac{1}{k_{eff}} \mathbf{DL}^{-1}\mathbf{M}\boldsymbol{\chi}\mathbf{f}\boldsymbol{\phi}||_1 \end{bmatrix}, \tag{11}$$

where $\mathbf{F}_{\phi}(\mathbf{x})$ and $\mathbf{F}_{\mathrm{k}}(\mathbf{x})$ denotes the residual functions for ϕ and k_{eff}, respectively. However, as mentioned above, the solution of the $(\mathbf{I} - \mathbf{DL}^{-1}\mathbf{MS})^{-1}$ operation needs nested inner iterations with a certain amount of transport sweeping steps (multiple calculation of $\mathbf{L}^{-1}$), which can lead to significantly expensive cost when evaluating residual functions. In fact, only one transport sweeping step is enough for the evaluation of the residual functions for JFNK. As a result, in this paper, the residual functions are constructed according to Eq. 6 and 8 as

$$\begin{aligned} \mathbf{F}_{\phi}(\mathbf{x}) &= \boldsymbol{\phi} - \mathbf{DL}^{-1}\mathbf{MS}\boldsymbol{\phi} - \frac{1}{k_{eff}}\mathbf{DL}^{-1}\mathbf{M}\boldsymbol{\chi}\mathbf{f}\boldsymbol{\phi} \\ &= \boldsymbol{\phi} - \mathbf{DL}^{-1}\mathbf{M}\left(\mathbf{S} + \frac{1}{k_{eff}}\boldsymbol{\chi}\mathbf{f}\right)\boldsymbol{\phi}, \end{aligned} \tag{12}$$

$$\mathbf{F}_{\mathrm{k}}(\mathbf{x}) = k_{eff} - \hat{c}||\mathbf{f}\mathbf{DL}^{-1}\mathbf{M}\left(\mathbf{S} + \frac{1}{k_{eff}}\boldsymbol{\chi}\mathbf{f}\right)\boldsymbol{\phi}||_1, \tag{13}$$

where the evaluation is equivalent to a "flattened" power iterative process (Gill, 2009) including a single outer iteration without nested inner iterations as shown in Eq. 10. In this paper, the combined strategy of the parallel JFNK method and the parallel Sn method is called comePSn_JFNK method.

2.3 Parallel code design for evaluation of residual functions

In this paper, the comePSn and comePSn_JFNK codes are parallelly designed on spatial domain decomposition with the Message Passing Interface (MPI) standard. For the comePSn_JFNK code, the message communication between MPI ranks is mainly required for the evaluation of the residual functions, the dot products and the norms. The parallel dot products and norms of vectors can be easily calculated by using the MPI_Allreduce function. And the evaluation of residual functions employs the KBA algorithm, which can directly calculate the inversion of $\mathbf{L}$ in the parallel Sn framework.

KBA is constructed on the (N-1)-dimensional spatial domain decomposition for N-dimensional models. For 3-D rectangular coordinate system, the spatial grid is divided into domains on the XY layout of CPU cores (or MPI ranks). Each domain is further decomposed into computational chunks, which are solved in the

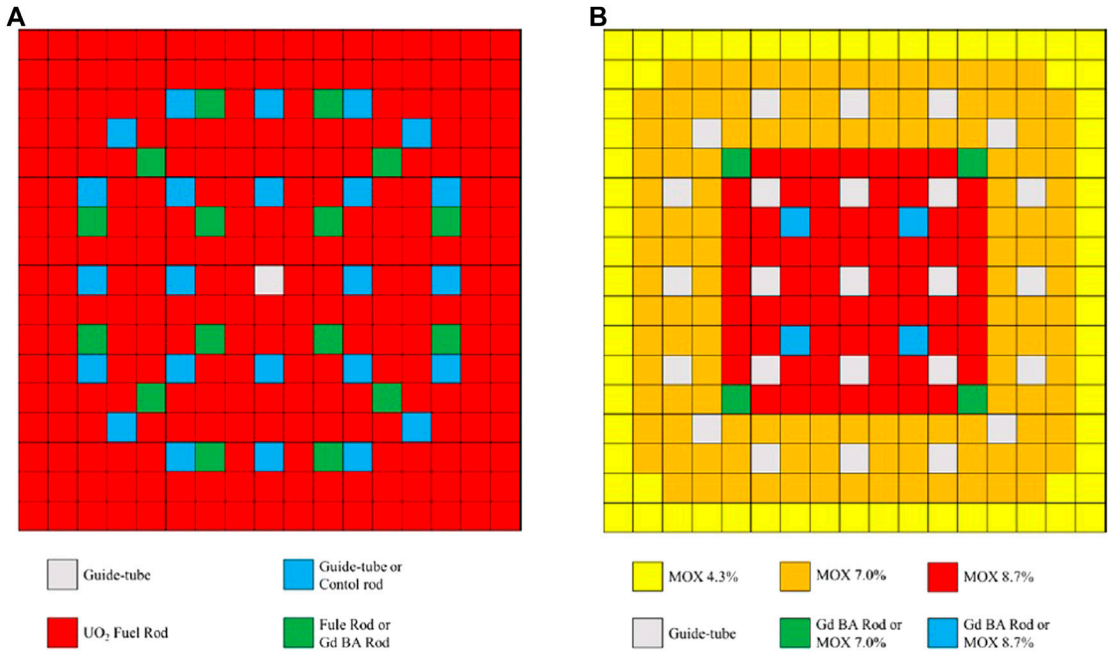

FIGURE 3
Fuel assembly configuration of the KAIST-3A benchmark problem: **(A)** UOX fuel assembly and **(B)** MOX fuel assembly.

TABLE 1 Results of k-eigenvalues on different mesh sizes per pin for 2-D KAIST-3A benchmark problems.

Case	Method	1 × 1	2 × 2	4 × 4	32 × 32
ARO	comePSn	1.12886	1.13086	1.13083	1.13088
	comePSn_JFNK	1.12886	1.13086	1.13083	1.13088
ARI	comePSn	0.96706	0.97401	0.97421	0.97452
	comePSn_JFNK	0.96706	0.97401	0.97421	0.97452

"wavefront" ordering. Each computational chunk, in a single octant with N/8 discrete angles for a single energy group, is solved after receiving the incoming angular fluxes from the upstream chunks (or from the boundary conditions), and then the outer angular fluxes are sent to the downstream chunks if required. The "simultaneous in angle, successive in quadrants" pipelining method described in the reference (Baker and Koch, 1998) are chosen in this paper. In addition, to reduce the idle time, the sweeps start at all the four corners of the spatial grid at the same time (Bailey and Falgout, 2009).

As mentioned above, the KBA transport sweeping process can be easily applied to evaluate the residual functions for the parallel JFNK framework. In this work, the evaluation of the residual functions is a three-step process. 1) Map $\mathbf{x}$ to ϕ and k_{eff} in each MPI rank. 2) Calculate the new scalar fluxes $\tilde{\phi}$ by using the KBA algorithm where $\tilde{\phi} = \mathbf{DL}^{-1}\mathbf{M}(\mathbf{S} + 1/k_{\text{eff}}\boldsymbol{\chi}\mathbf{f})\phi$, and then get the new k-eigenvalue as $\tilde{k}_{\text{eff}} = \hat{c}||\mathbf{f}\tilde{\phi}||_1$. 3) Calculate the residual functions $\mathbf{F}(\mathbf{x})$ according to Eqs 12, 13, where $\mathbf{F}(\mathbf{x}) = \begin{bmatrix} \phi - \tilde{\phi} \\ k_{eff} - k_{\text{eff}} \end{bmatrix}$.

2.4 Solution strategy

Based on the above methodologies, the parallel comePSn_JFNK and comePSn codes are respectively developed in the unified COME using C++ language to study the numerical accuracy, the efficiency and the parallel performance for the 3-D/2-D pin-by-pin neutron transport models. The iterative strategies and the flowchart are shown in Figure 1. The good initial guess $\mathbf{x}^{(0)}$ of the comePSn_JFNK code comes from the solution after 5 power iterative steps. The CPU time and iterative properties of the comePSn code after 5 iterative steps are also compared with those of the comePSn_JFNK code. In addition, the number of inner steps is fixed as one per outer step for the comePSn code, which ensures that a single power iterative step for the comePSn code is equivalent to one calling calculation of residual functions for the comePSn_JFNK code. Then, the relative convergence criterion for both comePSn_JFNK and comePSn codes is

$$\frac{\left\|\mathbf{F}\left(\mathbf{x}^{(n)}\right)\right\|_2}{\left\|\mathbf{F}\left(\mathbf{x}^{(0)}\right)\right\|_2} < 10^{-6}, \tag{14}$$

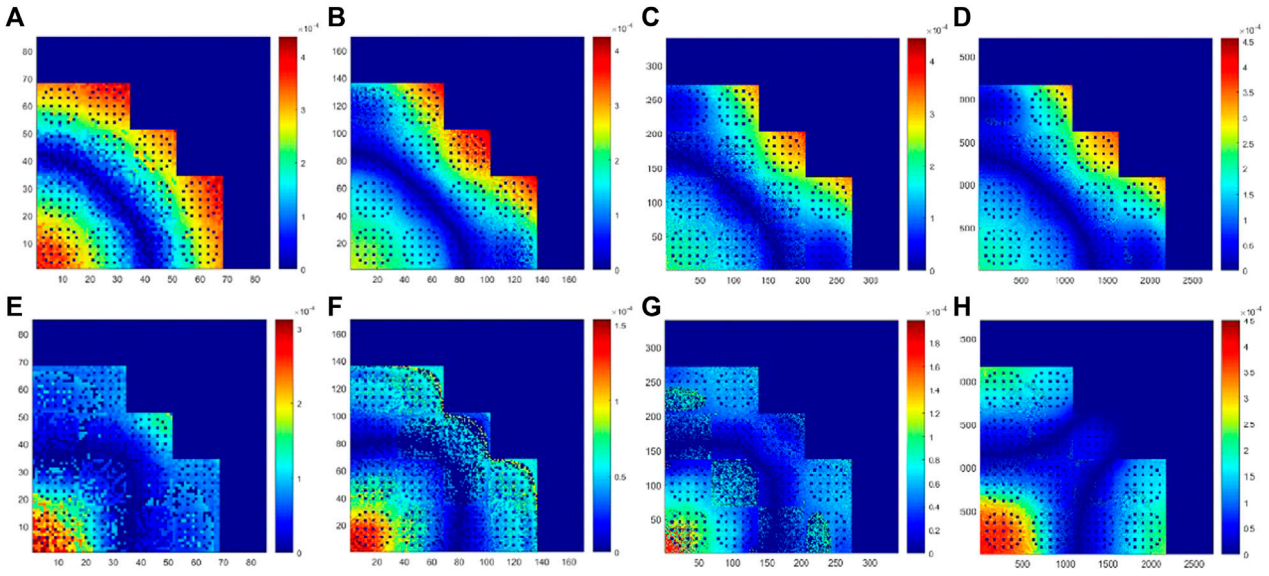

FIGURE 4
Relative error (%) of power density between comePSn_JFNK and comePSn codes on different mesh sizes per pin for 2-D KAIST-3A benchmark problems: **(A)** 1 × 1 for ARO, **(B)** 2 × 2 for ARO, **(C)** 4 × 4 for ARO, **(D)** 32 × 32 for ARO, **(E)** 1 × 1 for ARI, **(F)** 2 × 2 for ARI, **(G)** 4 × 4 for ARI and **(H)** 32 × 32 for ARI.

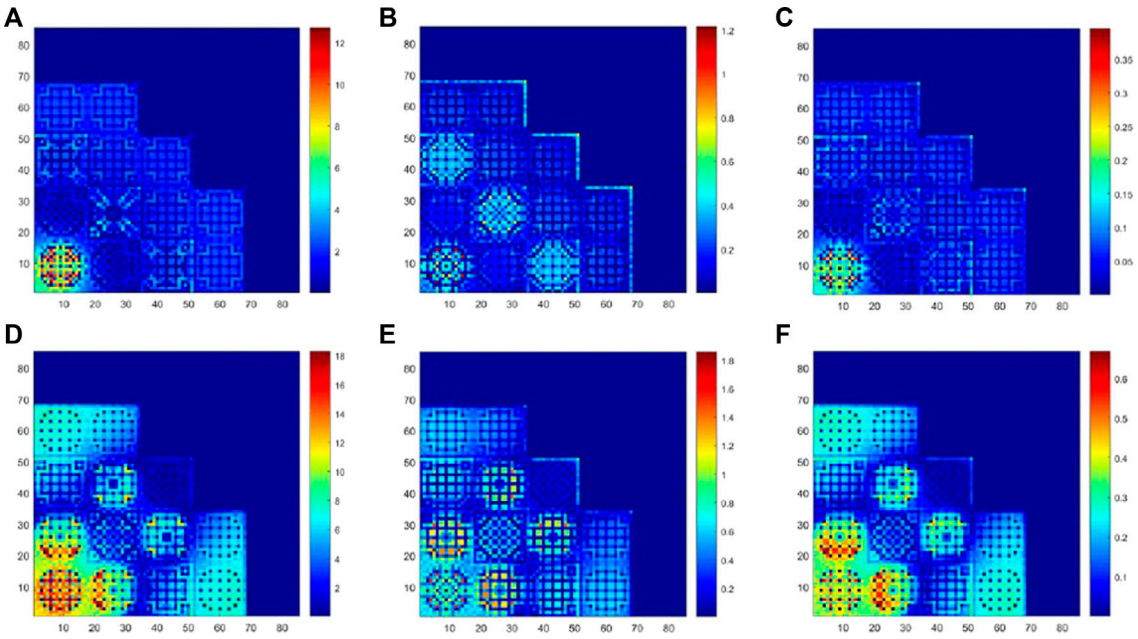

FIGURE 5
Relative error (%) of pin-wise power density on different mesh sizes per pin compared with those on 32 × 32 meshes per pin for 2-D KAIST-3A benchmark problems using the comePSn_JFNK code: **(A)** 1 × 1 for ARO, **(B)** 2 × 2 for ARO, **(C)** 4 × 4 for ARO, **(D)** 1 × 1 for ARI, **(E)** 2 × 2 for ARI and **(F)** 4 × 4 for ARI.

TABLE 2 Comparison of the computational cost for 2-D KAIST-3A benchmark problems.

Case	Meshes per pin	Code	Newton/Power steps	Krylov iterative number	Number of calling residuals	CPU time (s)	Speed up
ARO	1 × 1	comePSn	1,382	—	—	35.26	—
		comePSn_JFNK	6	155	162	4.28	8.24
	2 × 2	comePSn	1,410	—	—	140.67	—
		comePSn_JFNK	6	176	183	19.28	7.30
	4 × 4	comePSn	1,411	—	—	568.94	—
		comePSn_JFNK	6	177	184	78.13	7.28
	32 × 32*	comePSn	1,412	—	—	1,296.44	—
		comePSn_JFNK	6	177	184	211.04	6.14
ARI	1 × 1	comePSn	1,580	—	—	39.96	—
		comePSn_JFNK	6	156	163	4.41	9.06
	2 × 2	comePSn	1,571	—	—	156.93	—
		comePSn_JFNK	5	143	149	15.59	10.07
	4 × 4	comePSn	1,570	—	—	628.50	—
		comePSn_JFNK	5	143	149	63.71	9.86
	32 × 32*	comePSn	1,566	—	—	1,404.90	—
		comePSn_JFNK	5	146	151	175.32	8.01

*the simulation on 32 × 32 meshes per pin is solved using 32 CPU, cores and the others are on one CPU, core.

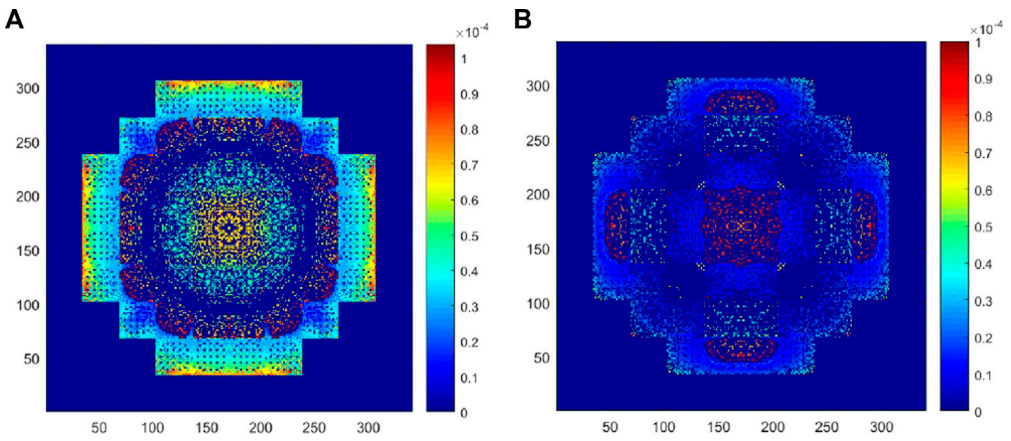

FIGURE 6
Relative error (%) of radial average power density between comePSn_JFNK and comePSn codes for 3-D KAIST-3A benchmark problems: **(A)** ARO and **(B)** ARI.

where $\|\cdot\|_2$ denotes the L-2 norm and $\mathbf{F}(\mathbf{x}^{(0)})$ denotes the residuals of the iterative initial value. In each Newton step (n), the adaptive convergence criterion with the Eisenstat-Walker forcing term $\eta^{(n)}$ (Eisenstat and Walker, 1996) is

$$\left\|\mathbf{J}\mathbf{a}\left(\mathbf{x}^{(n)}\right)\delta\mathbf{x}^{(n)} + \mathbf{F}\left(\mathbf{x}^{(n)}\right)\right\|_2 < \eta^{(n)}\left\|\mathbf{F}\left(\mathbf{x}^{(n)}\right)\right\|_2, \tag{15}$$

$$\eta^{(n)} = 0.1\left(\frac{\mathbf{F}\left(\mathbf{x}^{(n)}\right)}{\mathbf{F}\left(\mathbf{x}^{(n-1)}\right)}\right)^{2.0}. \tag{16}$$

The restarted GMRES (Generalized Minimal REsidual) method (Saad and Schultz, 1986) is adopted to solve Eq. 15 and the maximum Krylov subspace dimension is set to 20. At last, the global convergent

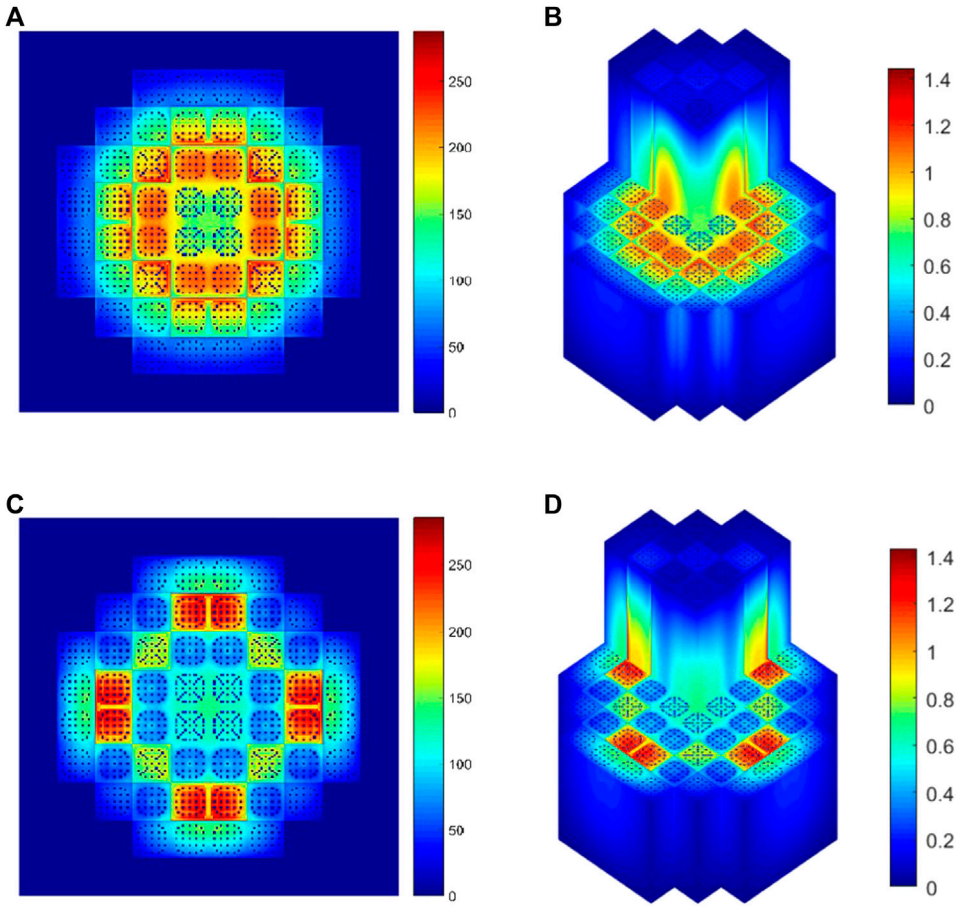

FIGURE 7
Radial average power density and 3-D power density distribution for 3-D KAIST-3A benchmark problems using the comePSn_JFNK code: **(A)** radial power density for ARO, **(B)** 3-D power density for ARO, **(C)** radial power density for ARI and **(D)** 3-D power density for ARI.

TABLE 3 Comparison of the computational cost for 3-D KAIST-3A benchmark problems (100 CPU cores).

Case	Code	Newton/Power steps	Krylov iterative number	Number of calling residuals	CPU time (s)	Speed up
ARO	comePSn	7120	—	—	24337	—
	comePSn_JFNK	7	494	502	1961	12.41
ARI	comePSn	6,914	—	—	24056	—
	comePSn_JFNK	6	408	414	1,643	14.64

backtracking algorithm (Eisenstat and Walker, 1994) is employed to ensure the global convergence of come_PSn_JFNK.

3 Numerical results and analysis

In this section, we apply the comePSn_JFNK and comePSn codes to two series of complicated multi-dimensional pin-by-pin neutron transport models. First, the popular 2-D/3-D KAIST-3A benchmark problems with Gd burnable absorbers are simulated to analyze the numerical accuracy, the parallel performance and the computational efficiency of the comePSn_JFNK and comePSn codes. Then, the more complicated 2-D/3-D full-core MOX/UOX pin-by-pin models with different insertion forms of the control rods are further employed to test the high numerical efficiency of the comePSn_JFNK code compared with the

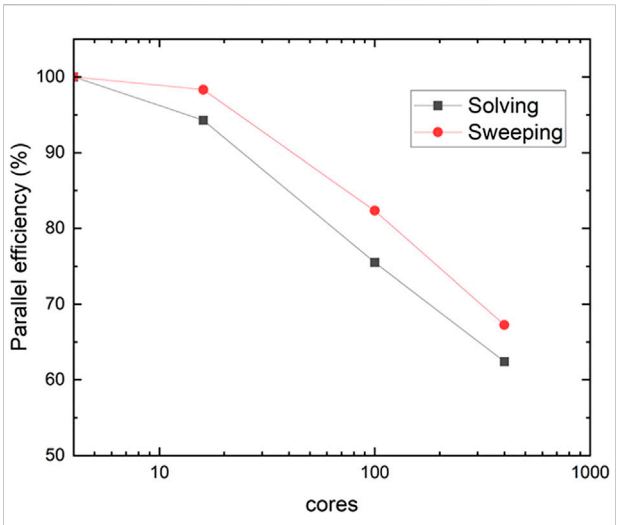

FIGURE 8
Parallel efficiency for 3-D KAIST-3A ARO case of the comePSn_JFNK code.

comePSn code in an order of 1000 CPU cores on the computer clusters with Hygon C86 7185 32-core processors. In all of our numerical simulations, the S_8 Carlson quadrature set (Longoni, 2004) is adopted to discretize the angular direction space.

3.1 KAIST-3A benchmark problem

KAIST-3A benchmark problems are published by KAIST Nuclear Reactor Analysis and Particle Transport laboratory (Cho, 2000), whose model is a simplified PWR core. The quarter symmetric radial geometry is illustrated in Figure 2. The core consists of two types of fuel assemblies, Uranium (UOX, including UOX-1 with 2.0% enrichment and UOX-2 with 3.3% enrichment) and Plutonium (MOX), which are surrounded by the baffle and reflector. Each fuel assembly follows a 17 × 17 lattice design of 21.42 cm width with a 1.26 cm pin pitch, which includes 264 fuel rods (or burnable absorber rods), 24 guide tubes (or control rods inserted) and one instrument guide tube as shown in Figure 3. There are two cases: all rods out (ARO) and all rods in (ARI), based on the configurations with or without the control rods (CR) inserted into the four UOX-2 fuel assemblies. Seven-group macroscopic cross sections are provided in the benchmark report, including UO_2 fuel, MOX fuel, guide tube, BA (Burnable absorber) rod, control rod, baffle and reflector.

At first, the 2-D quarter symmetric models are simulated by comePSn_JFNK and comePSn codes. The pin cell is divided into 1 × 1, 2 × 2, 4 × 4 and 32 × 32 rectangular meshes, respectively.

Table 1 and Figure 4 respectively show the comparison of the k-eigenvalue and the relative errors (%) of power density for ARO and ARI with different mesh sizes per pin using comePSn_JFNK and comePSn codes. It can be seen that there is no obvious difference between the results from the two codes. To further analyze the accuracy of the two codes with different mesh sizes per pin, the relative errors (%) of pin-wise power density on 1 × 1, 2 × 2 and 4 × 4 meshes per pin are presented in Figure 5 compared with the results on 32 × 32 meshes per pin. For 1 × 1 mesh per pin, the maximum value of the relative errors reaches 12% for ARO and 18% for ARI, and the errors of the k-eigenvalues are about 200 pcm (for ARO) and 750 pcm (for

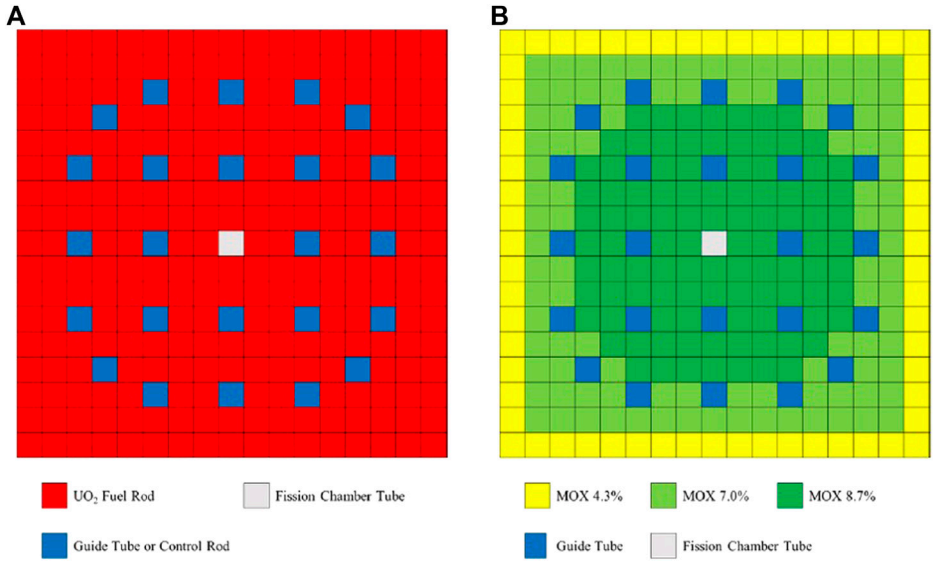

FIGURE 9
Fuel assembly configuration of the full-core MOX/UOX pin-by-pin models: **(A)** UOX fuel assembly and **(B)** MOX fuel assembly.

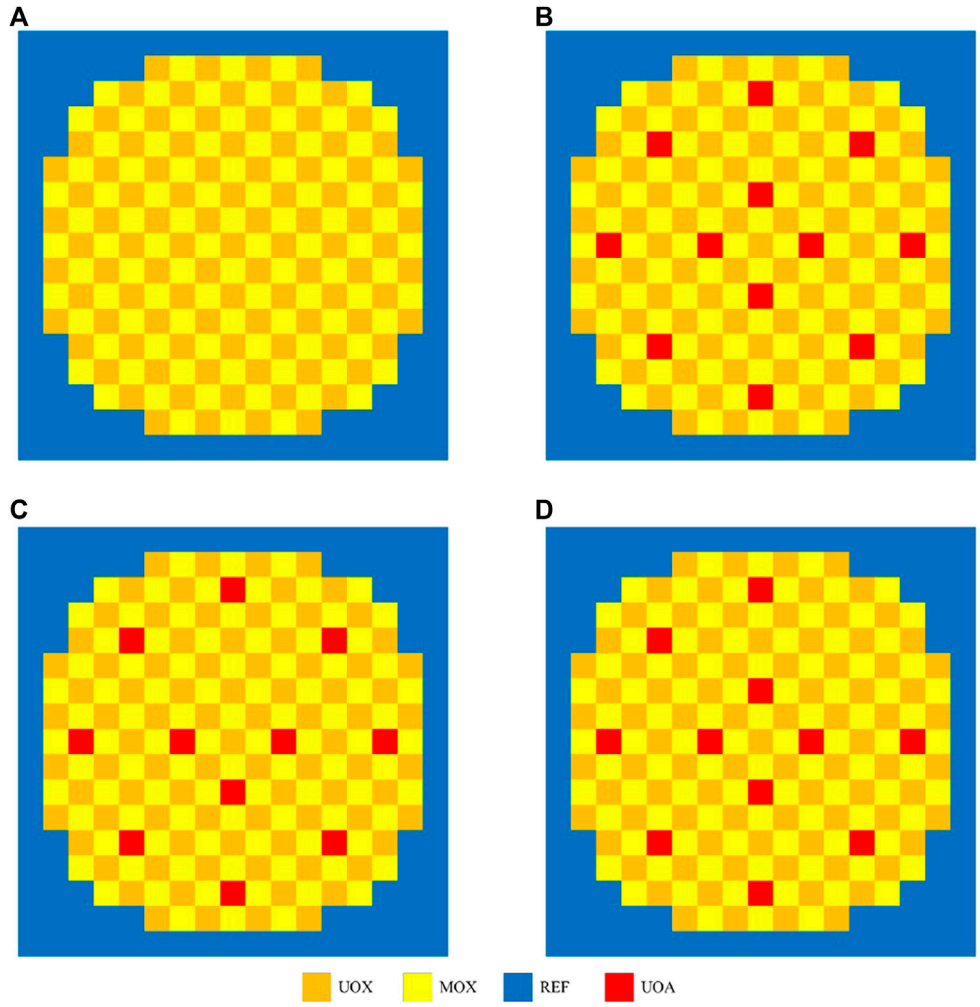

FIGURE 10
Radial core configuration of the full-core MOX/UOX pin-by-pin models: **(A)** model A, **(B)** model B, **(C)** model C and **(D)** model D.

TABLE 4 Results of k-eigenvalues for 2-D full-core MOX/UOX pin-by-pin models A–D.

Model	Code	Eigenvalue k_{eff}	Reference
A	comePSn	1.24449	1.24322
	comePSn_JFNK	1.24449	
B	comePSn	1.22596	1.22457
	comePSn_JFNK	1.22596	
C	comePSn	1.23055	1.22921
	comePSn_JFNK	1.23055	
D	comePSn	1.22812	1.22674
	comePSn_JFNK	1.22812	

ARI). While for 2 × 2 and 4 × 4 meshes per pin, the errors of the power density and the k-eigenvalues are respectively less than 2% and 50 pcm, and it indicates that the solution on 2 × 2 meshes per pin can obtain acceptable numerical accuracy.

To further analyze the numerical efficiency of comePSn_JFNK and comePSn codes, the CPU times and iteration numbers are presented in Table 2. It should be noted that the CPU times do not include the cost of the initialization, reading the input files and writing the output files. The results indicate that the different mesh sizes per pin make no obvious difference on the convergence rate for both comePSn_JFNK and comePSn codes. The computational efficiency of the comePSn_JFNK code is about 6–8 times as much as the comePSn code for ARO and about 8–10 for ARI.

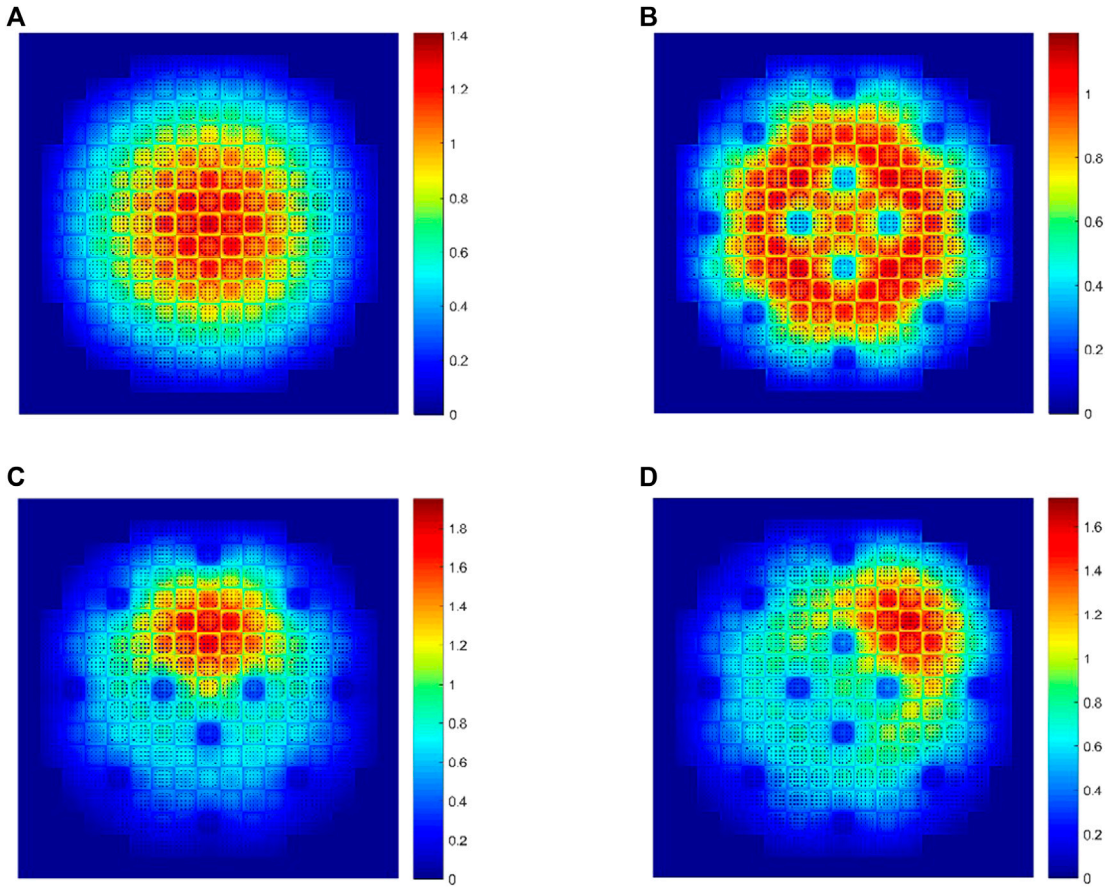

FIGURE 11
Power density distribution using the comePSn_JFNK code for 2-D full-core MOX/UOX pin-by-pin models: **(A)** model A, **(B)** model B, **(C)** model C and **(D)** model D.

Then the KAIST-3A 2-D quarter symmetric models are extend to 3-D full-core models with the same radial configuration, and axial reflectors are set at the top/bottom of the core. The active fuel length is 365.76 cm and the width of axial reactors is 21.42 cm. The control rods can be inserted from the top of the upper reflector to the bottom of the active fuel region in the UOX-2 (CR) assemblies. ARO and ARI cases are still simulated by comePSn_JFNK and comePSn codes.

The 3-D full-core model is divided into 340 × 340 × 340 meshes. Specifically, one pin cell is divided into 2 × 2 meshes in the radial direction; in the axial direction, the active region is divided into 300 meshes and the top/bottom reflectors are respectively divided into 20 meshes. Both comePSn_JFNK and comePSn codes solve the problems using 100 CPU cores. Figure 6 presents the relative errors (%) of radial average power density between the two codes and Figure 7 shows the radial average power density and 3-D power density distribution in the active regions calculated the comePSn_JFNK code. The numerical results of radial power density and the k-eigenvalues from the two codes also agree well with each other. The k-eigenvalues are respectively 1.12612 for ARO and 0.97063 for ARI.

To further analyze the efficiency of comePSn_JFNK and comePSn codes for 3-D models, the iterative properties and CPU times (on 100 CPU cores) are listed in Table 3. Compared with the comePSn code, the speedups of the comePSn_JFNK code are 12.41 for ARO and 14.64 for ARI. It is worth noting that the acceleration rates of the comePSn_JFNK code for 3-D models are higher than those for 2-D models, which shows the advantage of numerical efficiency of the comePSn_JFNK code for the complicated 3-D neutron transport problems.

In addition, the parallel efficiencies of the comePSn_JFNK code for the 3-D KAIST-3A ARO case using 4, 16, 100 and 400 CPU cores are shown in Figure 8. The “Solving” curve means the parallel efficiency of the total CPU time and the “Sweeping” curve indicates the parallel

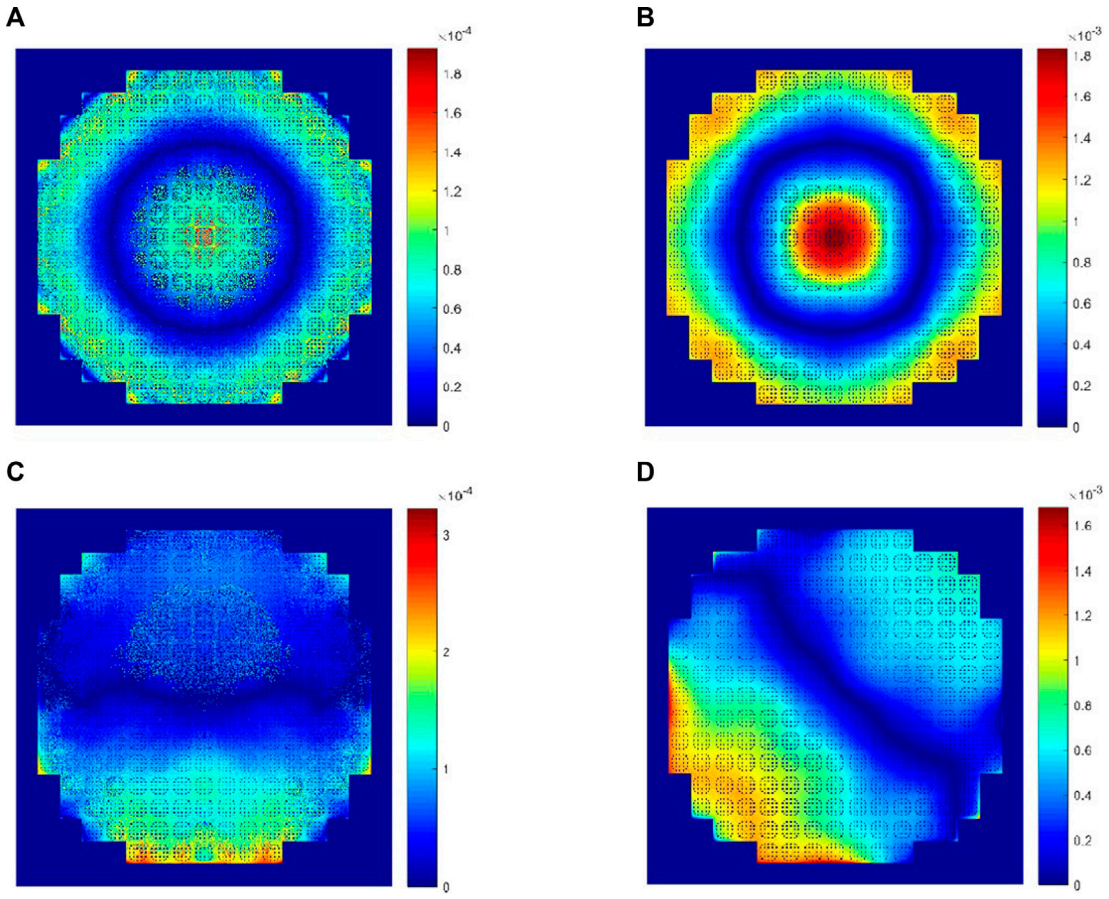

FIGURE 12
Relative errors (%) of radial average power density between comePSn_JFNK and comePSn codes for 2-D full-core MOX/UOX pin-by-pin models: **(A)** model A, **(B)** model B, **(C)** model C and **(D)** model D.

TABLE 5 Comparison of the computational cost for 2-D Full-core MOX/UOX pin-by-pin models A–D.

Model	Code	Newton/Power steps	Krylov iterative number	Number of calling residuals	CPU time (s)	Speed up
A	comePSn	7093	—	—	1956	—
	comePSn_JFNK	7	427	434	127	15.40
B	comePSn	5,551	—	—	1,543	—
	comePSn_JFNK	5	308	313	91.6	16.84
C	comePSn	19582	—	—	5,084	—
	comePSn_JFNK	7	571	578	170	29.90
D	comePSn	27041	—	—	7743	—
	comePSn_JFNK	10	885	895	261	29.67

efficiency of KBA sweeping. The efficiencies of "Solving" and "Sweeping" using 400 CPU cores are respectively about 63% and 68%, which can be further improved by optimizing the parallel performance of the Krylov subspace methods and the strategies of the KBA algorithm.

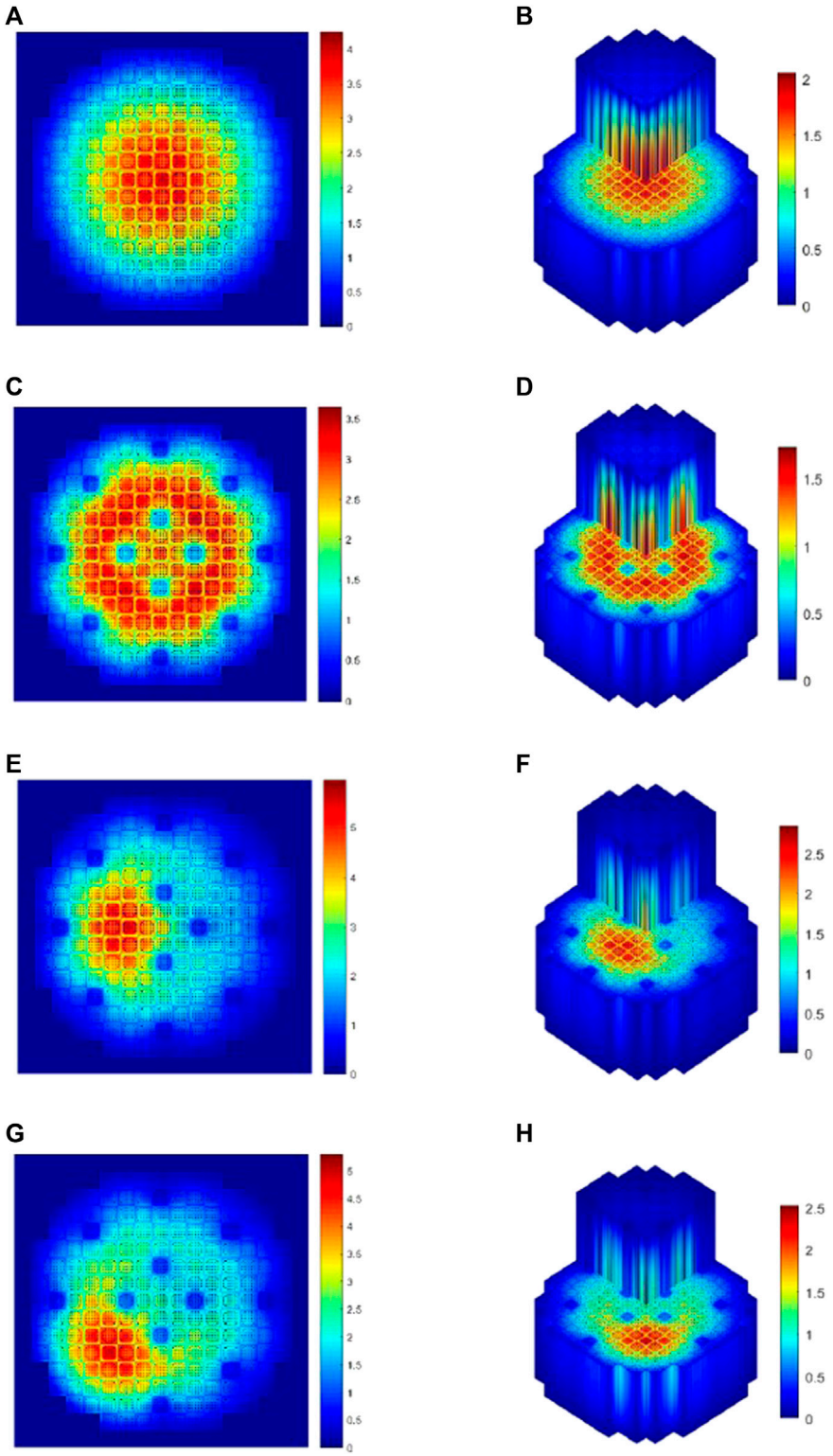

FIGURE 13
Radial average power and 3-D power density distribution for 3-D Full-core MOX/UOX pin-by-pin models: **(A)** radial power density for model A, **(B)** 3-D power density for model A, **(C)** radial power density for model B, **(D)** 3-D power density for model B, **(E)** radial power density for model C, **(F)** 3-D power density for model C, **(G)** radial power density for model D and **(H)** 3-D power density for model D.

TABLE 6 Comparison of the k-eigenvalues and the computational cost for 3-D full-core MOX/UOX pin-by-pin models (1024 CPU cores).

Model	Code	k-eigenvalue	Newton/Power steps	Krylov iterative number	Number of calling residuals	CPU time (s)	Speed up
A	comePSn	1.24080	9,947	—	—	27937	—
	comePSn_JFNK	1.24080	6	426	432	1,364	20.48
B	comePSn	1.22293	9,942	—	—	28616	—
	comePSn_JFNK	1.22293	5	392	397	1,268	22.57
C	comePSn	1.22731	19637	—	—	54921	—
	comePSn_JFNK	1.22731	7	562	569	2,203	24.93
D	comePSn	1.22493	26804	—	—	58552	—
	comePSn_JFNK	1.22493	8	690	698	2,214	26.45

3.2 Full-core MOX/UOX pin-by-pin models

A series of 3-D/2-D PWR full-core MOX/UOX pin-by-pin models with different insertion positions of control rods are simulated to further study the numerical properties of comePSn_JFNK and comePSn codes. The reactor core also consists of UOX and MOX fuel assemblies surrounded by reflector. As shown in Figure 9, each fuel assembly is 21.42 cm wide and is made up of 17 × 17 lattice with a 1.26 cm pin pitch, which includes 264 fuel pins, 24 guide tubes (or control rods inserted) and one instrument tube for fission chamber. The UOX and MOX assemblies are distributed in a checker-board configuration and four core models (A, B, C and D) are designed with different configurations of the UOX assemblies with control rods inserted (UOA) as illustrated in Figure 10. The active fuel length is 365.76 cm and there are 21.42 cm high axial reflectors at the top/bottom of the core just as the 3-D KAIST-3A models. It should be noted that the control rods are inserted form the top of the upper reflector to the bottom of the active fuel regions in the models B, C and D; and the control rods are still in the upper reflector if withdrawn in the models A, C and D. In this paper both 2-D and 3-D models are simulated by comePSn_JFNK and comePSn codes. The seven-group cross sections for pin cells are chosen form the C5G7 benchmark report (Smith et al., 2005). The pin cells are divided into 2 × 2 rectangular meshes in the radial direction; in the axial direction, the active fuel region is divided into 580 meshes and the top/bottom reflectors are respectively divided into 30 meshes.

Table 4 shows the results of the k-eigenvalues from comePSn_JFNK and comePSn codes and the reference solution is from the paper (Zhou, 2022a). It can be observed that the errors of k-eigenvalues from the two codes are about 150 pcm compared with the reference. Figure 11 shows the power density distribution from the comePSn_JFNK code and Figure 12 shows the corresponding relative errors (%) compared with the comePSn code. It can be observed that the power density distribution from the two codes agree well with each other, and even in the model B where the control rods are all inserted in, the maximum of the errors is less than 0.002%.

To analyze the numerical efficiency, Table 5 presents the comparation of the computational cost for the 2-D models from comePSn_JFNK and comePSn codes (using 1 core). Compared with the comePSn code, the speedups of the comePSn_JFNK code are respectively 15.40, 16.84, 29.90, and 29.67 for models A–D, which indicates that the acceleration rate of the comePSn_JFNK code for the asymmetric models C and D is higher than that for the symmetric models A and B. In addition, there is obvious difference of the iterative steps between the four models from the comePSn code, which range from 7093 to 27041. While the comePSn_JFNK code takes similar non-linear iterative steps (range from 5 to 10) due to the robust convergence of the JFNK methods.

To further test the computational properties of the comePSn_JFNK code for 3-D models, the radial average power density and the 3-D power density distribution calculated by the comePSn_JFNK code using 1024 CPU cores are presented in Figure 13, and the k-eigenvalues and the computational cost compared with the comePSn code is shown in Table 6. It can be seen that the acceleration rate of the comePSn_JFNK code are respectively 20.48, 22.57, 24.93 and 26.45 for models A– D, which indicates that the comePSn_JFNK code still has significant efficiency advantage for the complicated 3-D full-core pin-by-pin models with different control rod distributions.

4 Conclusion

In this paper, a parallel Jacobian-free Newton Krylov discrete ordinates method (comePSn_JFNK) is developed to solve the multi-dimensional multi-group pin-by-pin neutron transport problems, which combines the parallel JFNK framework and the parallel Sn method based on KBA algorithm. The comePSn_JFNK code exhibits the good efficiency compared with the traditional parallel Sn code with power iterative strategy (comePSn). Furthermore, by making full use of transport sweeping iterative framework, the corresponding residual functions of the parallel JFNK framework can be easily evaluated by only a "flattened" power iterative process which includes a single outer iteration without nested inner iterations. The comePSn_JFNK and the comePSn codes are developed in the unified COupled Multiphysics Environment (COME).

By simulating the 2-D/3-D KAIST-3A pin-by-pin benchmark problems and the 2-D/3-D full-core pin-by-pin MOX/UOX models, the speedups of the comePSn_JFNK code are 6–15 for the KAIST-3A benchmark problems and 15–30 for the full-core MOX/UOX pin-by-pin models, which indicates the comePSn_JFNK code has significant efficiency advantage for complicated 3-D full-core pin-by-pin models. Further study is to improve the parallel efficiency on the massively parallel computers, to apply the parallel coarse mesh finite difference methods and the parallel diffusion synthetic acceleration method as preconditioners, and to extend the comePSn_JFNK method to solve the pin-by-pin multi-physics coupled problems.

Data availability statement

The original contributions presented in the study are included in the article/Supplementary Material, further inquiries can be directed to the corresponding author.

Author contributions

YZ: Software, modeling, validation, data analysis and original draft preparation. XZ: Conception, methodology, software, review, editing and supervision.

Funding

This research was funded by National Natural Science Foundation of China: 12005073; National Key Research and Development Program of China: 2018YFE0180900; National Key Research and Development Program of China: 2020YFB1901600; Project of Nuclear Power Technology Innovation Center of Science Technology and Industry for National Defense: HDLCXZX-2021-HD-033.

Conflict of interest

The authors declare that the research was conducted in the absence of any commercial or financial relationships that could be construed as a potential conflict of interest.

Publisher's note

All claims expressed in this article are solely those of the authors and do not necessarily represent those of their affiliated organizations, or those of the publisher, the editors and the reviewers. Any product that may be evaluated in this article, or claim that may be made by its manufacturer, is not guaranteed or endorsed by the publisher.

References

Alcouffe, R. E., Baker, R. S., Dahl, J. A., Davis, E. J., Saller, T. G., and Turner, S. A. (2005). Partisn: A time-dependent parallel neutral Particle transport code system. LAUR-05-3925 (Los Alamos, NM, USA: Los Alamos National Laboratory).

Bailey, T. S., and Falgout, R. D. "Analysis of massively parallel discrete-ordinates transport sweep algorithms with collisions," in Proceedings of the International Conference on Mathematics, Computational Methods & Reactor Physics, Saratoga Springs, NY, USA, May 2009.

Baker, R. S. (2017). An SN algorithm for modern architectures. *Nucl. Sci. Eng.* 185, 107–116. doi:10.13182/nse15-124

Baker, R. S., and Koch, K. R. (1998). An Sn algorithm for the massively parallel CM-200 computer. *Nucl. Sci. Eng.* 128, 312–320. doi:10.13182/nse98-1

Carlson, B. G. (1953). Solution of the transport equation by Sn approximations. LA-1599 (Los Alamos, NM, USA: Los Alamos Scientific Laboratory Report).

Cho, N. Z. (2000). Daejeon, South Korea: Korea Advanced Institute of Science and Technology benchmark report. Available at: https://github.com/nzcho/Nurapt-Archives/tree/master/KAIST-Benchmark-Problems. *Benchmark problem 3A: MOX fuel-loaded small PWR coreMOX Fuel Zoning, 7 Group Homog. Cells.*

Eisenstat, S. C., and Walker, H. F. (1996). Choosing the forcing terms in an inexact Newton method. *SIAM J. Sci. Comput.* 17, 16–32. doi:10.1137/0917003

Eisenstat, S. C., and Walker, H. F. (1994). Globally convergent inexact Newton methods. *SIAM J. Optim.* 4, 393–422. doi:10.1137/0804022

Esmaili, H., Kazeminejad, H., Khalafi, H., and Mirvakili, S. (2020). Subchannel analysis of annular fuel assembly using the preconditioned Jacobian-free Newton Krylov methods. *Ann. Nucl. Energy* 146, 107616. doi:10.1016/j.anucene.2020.107616

Evans, T. M., Stafford, A. S., Slaybaugh, R. N., and Clarno, K. T. (2010). Denovo: A new three-dimensional parallel discrete ordinates code in scale. *Nucl. Technol.* 171, 171–200. doi:10.13182/nt171-171

Gaston, D., Newman, C., Hansen, G., and Lebrun-Grandie, D. (2009). Moose: A parallel computational framework for coupled systems of nonlinear equations. *Nucl. Eng. Des.* 239, 1768–1778. doi:10.1016/j.nucengdes.2009.05.021

Gill, D. F. (2009). "Newton-Krylov methods for the solution of the k-eigenvalue problem in multigroup neutronics calculations,". PhD thesis (Pennsylvania, PA, USA: Pennsylvania State University).

Hajizadeh, A., Kazeminejad, H., and Talebi, S. (2018). Formulation of a fully implicit numerical scheme for simulation of two-phase flow in a vertical channel using the Drift-Flux Model. *Prog. Nucl. Energy* 103, 91–105. doi:10.1016/j.pnucene.2017.11.009

Hossain, M. A., and Alam, J. M. (2012). Assessment of a symmetry-preserving JFNK method for atmospheric convection. *Comput. Phys. Commun.* 269, 108113. doi:10.1016/j.cpc.2021.108113

Knoll, D. A., and Keyes, D. E. (2004). Jacobian-free Newton–Krylov methods: A survey of approaches and applications. *J. Comput. Phys.* 193, 357–397. doi:10.1016/j.jcp.2003.08.010

Knoll, D. A., Park, H., and Newman, C. (2011). Acceleration of k-eigenvalue/criticality calculations using the jacobian-free Newton-Krylov method. *Nucl. Sci. Eng.* 167 (2), 133–140. doi:10.13182/nse09-89

Longoni, G. (2004). Advanced quadrature sets and acceleration and preconditioning techniques for the discrete ordinates method in parallel computing environments. PhD Thesis (Gainesville, FL, USA: University of Florida).

Pawlowski, R., Bartlett, R., Belcourt, N., Cannon, S. R., and Warren, H. R. (2011). A theory manual for multi-physics code coupling in LIME, version 1.0. SAND2011-2195 (Albuquerque, NM, USA: SAND Report).

Saad, Y., and Schultz, M. H. (1986). Gmres: A generalized minimal residual algorithm for solving nonsymmetric linear systems. *SIAM J. Sci. Stat. Comput.* 7, 856–869. doi:10.1137/0907058

Smith, M. A., Lewis, E. E., and Na, B. C. (2005). *Benchmark on deterministic transport calculations without spatial homogenization: MOX fuel assembly 3-D extension case*. Paris, France: Nuclear Energy Agency Organisation for Economic Co-Operation and Development, NEA/NSC/DOC.

Turner, J. A., Clarno, K., Sieger, M., Bartlett, R., Collins, B., Pawlowski, R., et al. (2016). The virtual environment for reactor applications (VERA): Design and architecture. *J. Comput. Phys.* 326, 544–568. doi:10.1016/j.jcp.2016.09.003

Walker, E. D., Collins, B., and Gehin, J. C. (2019). Low-order multiphysics coupling techniques for nuclear reactor applications. *Ann. Nucl. Energy* 132, 327–338. doi:10.1016/j.anucene.2019.04.022

Xu, L. F., Cao, L. Z., Zheng, Y. Q., and Wu, H. (2018). Hybrid MPI-communication for the multi-angular SN parallel sweep on 3-D regular grids. *Ann. Nucl. Energy* 116, 407–416. doi:10.1016/j.anucene.2018.03.003

Yaremchu, M., and Panteleev, G. (2022). On the Jacobian approximation in sea ice models with viscous-plastic rheology. *Ocean. Model. (Oxf).* 177, 102078. doi:10.1016/j.ocemod.2022.102078

Zhang, L., Zhang, B., Liu, C., Zheng, J., Zheng, Y., and Chen, Y. (2017). Calculation of the C5G7 3-D extension benchmark by ARES transport code. *Nucl. Eng. Des.* 318, 231–238. doi:10.1016/j.nucengdes.2017.04.011

Zhou, X. F. (2023). Jacobian-free Newton Krylov coarse mesh finite difference algorithm based on high-order nodal expansion method for three-dimensional nuclear reactor pin-by-pin multiphysics coupled models. *Comput. Phys. Commun.* 282, 108509. doi:10.1016/j.cpc.2022.108509

Zhou, X. F. (2022). Jacobian-free Newton Krylov two-node coarse mesh finite difference based on nodal expansion method. *Nucl. Eng. Technol.* 54, 3059–3072. doi:10.1016/j.net.2022.02.005

Zhou, X. F. (2022). Operator split, Picard iteration and JFNK methods based on nonlinear CMFD for transient full core models in the coupling multiphysics environment. *Ann. Nucl. Energy*. revised.

Zhou, X. F., Zhong, C. M., and Zhang, Y. Y. (2022). Jacobian-free Newton Krylov two-node coarse mesh finite difference based on nodal expansion method for multiphysics coupled models. *Ann. Nucl. Energy* 168, 108915. doi:10.1016/j.anucene.2021.108915

frontiers | Frontiers in Energy Research

TYPE Original Research
PUBLISHED 26 January 2023
DOI 10.3389/fenrg.2022.1080819

OPEN ACCESS

EDITED BY
Shichang Liu,
North China Electric Power University, China

REVIEWED BY
Mustafa Azeem,
Xi'an Jiaotong University, China
Di Yun,
Xi'an Jiaotong University, China

*CORRESPONDENCE
Lu Wu,
wulu1002@qq.com
Jing Zhang,
Jingzhang@nwpu.edu.cn

†These authors have contributed equally to this work

SPECIALTY SECTION
This article was submitted to Nuclear Energy, a section of the journal Frontiers in Energy Research

RECEIVED 26 October 2022
ACCEPTED 28 November 2022
PUBLISHED 26 January 2023

CITATION
Ma C, Zhao M, Xin T, Wu L, Pan R, Qin J and Zhang J (2023), Phase-field simulation of grain nucleation, growth, and Rayleigh distribution of U_3Si_2 nuclear fuel.
Front. Energy Res. 10:1080819.
doi: 10.3389/fenrg.2022.1080819

Phase-field simulation of grain nucleation, growth, and Rayleigh distribution of U_3Si_2 nuclear fuel

Cong Ma[1†], Min Zhao[1†], Tianyuan Xin[1], Lu Wu[1*], Rongjian Pan[1], Jiantao Qin[1] and Jing Zhang[2*]

[1]The First Sub-Institute, Nuclear Power Institute of China, Chengdu, China, [2]School of Material Science and Engineering, Northwestern Polytechnical University, Xi'an, China

U_3Si_2 is a potential accident-tolerant fuel (ATF) due to its high thermal conductivity and uranium density relative to UO_2. The grain size and distribution play an essential role in the service performance of U_3Si_2. However, the grain evolution is quite complicated and remains unclear, which limits further application of U_3Si_2 in the ATF assembly. In the present work, a phase-field model is employed to investigate the nucleation and growth of grains in U_3Si_2. Our results show that the number of grains rises rapidly at the nucleation stage until they occupy the whole system. After that, the grain radius and area continue to grow, and the grain number decays. The grain area increases in time according to the linear law, while the mean grain radius increases with time in a power law form with the scaling growth exponent z = 0.42, which is quite close to the theoretically predicted value. Finally, we performed statistical analysis and found that the grain size evolution of U_3Si_2 obeys Rayleigh distribution. Our simulation not only elucidates the nucleation and evolution of grains in U_3Si_2 during the thermal treatment process unambiguously but also provides a fundamental study on the investigation of grain growth, subdivision, and even amorphization in the irradiated condition, which is very important for U_3Si_2 used as ATF in the light water reactor.

KEYWORDS

U_3Si_2 fuel, phase-field simulation, grain nucleation and growth, exponential decaying, Rayleigh distribution

1 Introduction

Many novel nuclear fuels have been put forward to take the place of UO_2 since the Fukushima Daiichi accident. U_3Si_2 is extensively investigated among these fuels and is considered a promising next-generation ATF (Westinghouse Electric Company, 2015; Bischoff et al., 2016). Compared with the traditional UO_2 fuel, U_3Si_2 shows a series of unique advantages, such as higher thermal conductivity (λ equals ~ 7-8 W/(m·K) in UO_2 (Harding and Martin, 1989) and 15W/(m·K) in U_3Si_2 (White et al., 2015) at 573K, respectively), higher uranium density (11.31 g/cm^3 U in U_3Si_2 and 9.65 g/cm^3 U in UO_2) (White et al., 2015), and reinforced thermal conductivity at elevated temperature (White et al., 2015). All of these features can benefit superior safety in both regular operation and

the loss-of-coolant Accident (LOCA) (Terrani et al., 2014; Miao et al., 2017; Miao et al., 2018; Zhou and Zhou, 2018) and improve the power efficiency of the reactor.

The superior thermal conductivity and high uranium density promise U_3Si_2 an excellent accident-tolerant ability. In addition to this, the thermal properties and the mechanical performance are also determined by the fuels' microstructures. Manipulating grain and boundary areas through grain size control is essential for good performance. Generally, the fuels fail when they form a high burnup structure characterized by fine subgrain formation along grain boundaries. The grain boundaries are defect sinks that attract the gaseous fission products and vacancies, which cause bubbles nucleation and, consequently, severe stress concentration and swelling after. The gaseous atoms or small clusters dissolve the interior, cause limited lattice distortion, and are minor for swelling. The grain boundaries accommodate parts of fission gases that balance the interior and exterior of grains to maintain the performance stability. Grain coarsening or splitting into smaller subdivisions at the periphery at high temperatures and pressures will lead to out-of-balance, causing fuel failure.

U_3Si_2 consists of various grains with different crystallographic orientations. Many physical and chemical properties, such as corrosion resistance, thermal and electrical conductivity, mechanical properties (Davidge and Evans, 1969; Oguma, 1982; Kapoor et al., 2007), and fission gas release (Forsberg and Massih, 2001), depend on the mean grain size and distribution. However, due to the anisotropic crystallographic structure, grain evolution in U_3Si_2 is quite complicated. Up to now, even though there exist extensive investigations on U_3Si_2, the majority of these research studies focus on grain morphology. In contrast, grain growth, especially quantitative analysis of size distribution, is seldom investigated, which impedes the further understanding of grain subdivision and swelling behavior in U_3Si_2 under irradiation and restricts its extensive application in the field of ATF. Therefore, it is of great scientific and technological importance to investigate grain growth kinetics and perform a statistical analysis of grain evolution.

In recent years, with the rapid development of computer science and technology, numerical simulations have been gradually used to elucidate the mechanisms of grain growth spanning from the atomic to macroscopic scale (Atkinson HV, 1988). Computational studies are extremely useful since they permit isolation and analysis of the dominating factors of grain growth, contributing to microstructural evolution. Up to now, there have emerged various computational approaches to study microstructural evolution, such as the molecular dynamics (Azeem et al., 2019), Monte Carlo Potts model (Blikstein and Tschiptschin, 1999), surface evolver (Wakai et al., 2000), front tracking (Frost and Thopson, 1996), vertex dynamics (Weygand et al., 1998), cellular automata (Liu et al., 1997), and phase-field (Wen et al., 2006; Ansari et al., 2021) method. Among these methods, the phase-field approach has been extensively applied for grain growth modeling (Chen and Yang, 1994; Srezende et al., 1996; Fan and Chen, 1997; Kobayashi et al., 2000; Lobkovsky and Warren, 2001; III Krill and Chen, 2002) because it can deal with a large system involving thousands of grains, track individual grain boundaries, and apply specific constitutive relations to their motion. Currently, there are two main phase-field models for grain growth simulation. The earliest and most widely used model was developed by Chen and Yang, in which the grains of different crystallographic orientations are represented by a set of nonconserved order parameter fields (Chen and Yang, 1994). This model can be used in 2D (Fan and Chen, 1997) and 3D (III Krill and Chen, 2002) phase-field modeling simulations of grain growth. Srezende et al. proposed another class of multiphase-field model (Srezende et al., 1996) with a constraint on the order parameters, such that the sum of all order parameters at a given point yields unity, and the order parameters can represent the volume fraction of grains of different orientations. According to experimental data and molecular dynamics (M.D.) simulation results (Beeler et al., 2019), Cheniour et al. (2020) set up a phase-field model and investigated how grain size changes with time under ideal circumstances by giving a quantitative relationship. Nevertheless, how the microstructure evolves and whether an underlying mechanism dominates this process remain unknown.

In this work, we systematically investigated grain nucleation and growth in U_3Si_2 during thermal treatment through phase-field simulation. Microstructure evolution and grain size distribution within different thermal treatment stages are well examined. Our results show that the average grain size varies with time in a power law form, and grain size evolution in U_3Si_2 obeys Rayleigh distribution. Our work is organized as follows. Section 2 presents the phase-field formalism for grain growth and microstructure evolution modeling. Section 3.1 shows our simulated microstructure evolution of U_3Si_2 with thermal treatment time, while Section 3.2 and Section 3.3 exhibit the statistical method and result for corresponding grain size and distribution, respectively. Finally, in Section 4, we provide the main conclusions.

2 Phase-field model of grain nucleation and growth

Phase field is a mesoscale method that adopts the Ginzburg–Landau free energy constructed with one or multiple order parameters to depict the symmetry breaking of the system. The equation of motion for the phase-field methodology generally adopts the Cahn–Hilliard equation for conserved fields and the Allen–Cahn equation for nonconserved fields. It accommodates the macro contribution from ingredients and the environment, as well as the micro information on the surface and local stress heterogeneity. The phase-field method for grain growth of various metallics and ceramics has provided

valuable knowledge (Chen and Yang, 1994; Chen, 2002; Rest and Hofman, 2004; Millett et al., 2008; Ahmed et al., 2014; Tonks et al., 2014; Liang et al., 2016; Mei et al., 2016; Li et al., 2017; Cheniour et al., 2020), inspiring the understanding of U_3Si_2.

This work concerns the grain nucleation and growth of U_3Si_2, and nonconserved order parameters and the Allen–Cahn-type dynamic equation are adopted. The grain boundary energy and mobility of grains with different orientations are well formulated. The free energy is a function of the distribution of the order parameters. The grains were characterized by a set of order parameters $\{\eta_i\}_{i=1}^{n}$ for a microstructure consisting of n grains. A grain i is characterized by $\eta_i = 1$ and $\eta_{i \neq j} = 0$. The grain boundary is characterized by a smooth order parameter ranging from 0 to 1. The effective total free energy F describing the grain microstructure has the following form:

$$F = \int dr \left\{ F_0 \left[\sum_{i=1}^{M} \left(\frac{\eta_i^4}{4} - \frac{\eta_i^2}{2} \right) + \sum_{i=1}^{M} \sum_{i \neq j}^{M} \gamma_{ij} \eta_i^2 \eta_j^2 \right] + \frac{\mathrm{K}}{2} \sum_{i=1}^{M} |\nabla \eta_i|^2 \right\}, \tag{1}$$

where F_0 is the free-energy barrier coefficient,∇ is the Nabla operator, κ is the gradient energy coefficient, and γ_{ij} is the interface energy coefficient.

Using the free-energy functional, we can compute the specific grain boundary energy of the system of two grains η_i and η_j (with a flat interface $x = 0$ in a one-dimensional case) (Aagesen et al., 2020), which is given by the integral

$$\gamma = \int_{-\infty}^{+\infty} \left[F_0 f\left(\eta_i, \eta_j\right) + \frac{\kappa}{2} \left(\left(\nabla_x \eta_i\right)^2 + \left(\nabla_x \eta_j\right)^2 \right) \right] dx, \tag{2}$$

where x is the coordinate perpendicular to the grain boundary. A topographical view of the free-energy density (the term in square brackets in Eq. 1) is shown in Moelans et al. (2008a).

According to the principles of variational calculus, the functions $\eta_i(x)$ and $\eta_j(x)$ that extremize functional Eq. 1 satisfy the following equations:

$$\begin{aligned} F_0 \frac{\partial f}{\partial \eta_i} - \kappa \nabla_{xx}^2 \eta_i = 0, \\ F_0 \frac{\partial f}{\partial \eta_j} - \kappa \nabla_{xx}^2 \eta_j = 0. \end{aligned} \tag{3}$$

Or, equivalently, the integrated equation

$$F_0 f\left(\eta_i, \eta_j\right) - \frac{\kappa}{2} \left(\left(\nabla_x \eta_i\right)^2 + \left(\nabla_x \eta_j\right)^2 \right) = 0, \tag{4}$$

where boundary conditions are taken into account, the rearrangement of this equation gives

$$\nabla_x \eta_i = \sqrt{\frac{2F_0 f\left(\eta_i, \eta_j\right)}{\kappa \left(1 + \left[\partial \eta_i / \partial \eta_j\right]^2\right)}}, \nabla_x \eta_j = \sqrt{\frac{2F_0 f\left(\eta_i, \eta_j\right)}{\kappa \left(1 + \left[\partial \eta_j / \partial \eta_i\right]^2\right)}}. \tag{5}$$

A combination of these two equations in Eq. 4 gives

$$\begin{aligned} \gamma &= 2F_0 \int_{-\infty}^{+\infty} f\left(\eta_i, \eta_j\right) dx \\ &= \sqrt{2F_0 \kappa} \int_0^1 \sqrt{f\left(\eta_i, \eta_j\left(\eta_i\right)\right)} \sqrt{1 + \left[\frac{\partial \eta_j}{\partial \eta_i}\right]^2} d\eta_i. \end{aligned} \tag{6}$$

The model energetic parameter F_0 and interfacial energies γ_{ij} between grains and the gradient energy coefficient that penalizes non-zero gradients of the variables across the grain boundary can be expressed through the mean grain boundary energy $\bar{\gamma}$ and grain boundary interaction length l_{int} and grain boundary mobility $\bar{M}$ as follows (Moelans et al., 2008a; Moelans et al., 2008b):

$$\gamma = g\left(\gamma_{ij}\right) \sqrt{\kappa F_0}, \kappa = \frac{3}{4} \gamma l_{\mathrm{int}}, F_0 = \frac{6\gamma}{l_{\mathrm{int}}}, l_{\mathrm{int}} = \sqrt{8\kappa / F_0}. \tag{7}$$

As usual, for the special case $\gamma_{ij} = \frac{3}{2}$, it results to $g(\gamma_{ij} = 3/2) = \sqrt{2}/3$ (Aagesen et al., 2020).

The interface profile can be obtained by considering a symmetrical case, where $\eta_j = 1 - \eta_i$. In such a case, one gets

$$\nabla_x \eta_j = -\nabla_x \eta_i, \quad \nabla_{xx}^2 \eta_j = -\nabla_{xx}^2 \eta_i, \quad \frac{\partial \eta_j}{\partial \eta_i} = -1, \quad \frac{\partial \nabla_x \eta_j}{\partial \nabla_x \eta_i} = -1. \tag{8}$$

When applying $\gamma_{ij} = \frac{3}{2}$, one can get profiles from equations:

$$\begin{aligned} \nabla_{xx}^2 \eta_j &= \frac{F_0}{\kappa} \left(2\eta_i \left(2\eta_i^2 - 3\eta_i + 2\right)\right), \\ \nabla_{xx}^2 \eta_i &= \frac{F_0}{\kappa} \left(2\eta_j \left(2\eta_j^2 - 3\eta_j + 2\right)\right), \end{aligned} \tag{9}$$

$$\nabla_x \eta_i = -\sqrt{\frac{2F_0}{\kappa}} \eta_i \left(1 - \eta_i\right), \quad \nabla_x \eta_j = -\sqrt{\frac{2F_0}{\kappa}} \eta_j \left(1 - \eta_j\right). \tag{10}$$

The Allen–Cahn dynamical equation has the following form:

$$\partial_t \eta_i = -L_{\eta_i} \frac{\delta F}{\delta \eta_i} + \xi_v, \tag{11}$$

where $L_{\eta_i} = \frac{\bar{M}\gamma}{\kappa}$ and $L_{\eta i}$ is mobility. In order to embody the thermal fluctuations, we added noise terms ξ_v determined by the fluctuation–dissipation theorem to the governing Eq. 11. Substituting the free energy of Eq. 1 into Eq. 11, the numerical solution for Eq. 11 will give the temporal and spatial evolution of grains.

To compute appropriate values of both F_0 and κ, one can put $l_{\mathrm{int}} = \omega \delta_G$, where δ_G is the width of the grain boundary and ω is the constant defining diffusion grain boundary. In the computation procedure, the mesh size Δl is chosen in as $\Delta l = 3.33\delta_G$, by taking values for F_0 and κ from Rest and Hofman (2004). For all problem quantities of the order unity, the governing equations were non-dimensionalized using length, time, and energy scales $E^* = 63 \times 10^9 J/m^3$. Therefore, we can describe the parameterization of the order parameter mobility L_{η_i}. Using that approach, we set $\bar{L} = 1$, which leads to a dimensional value $L_{\eta_i} = \frac{\bar{L}}{E^* t^*} = 1.59 \times 10^{-10} m^3/(Js)$ (Aagesen et al., 2020). The physical parameters used for phase-field simulations are summarized in Table 1.

TABLE 1 Parameters used for phase-field simulations.

Parameter	Value
F_0	$6.84 \times 10^8 J/m^3$
κ	$1.92 \times 10^{-8} J/m$
ω	10
Δl	$10.7nm$
l_{int}	$20.7nm$
γ_{ij}	3/2
L_{η_i}	$1.59 \times 10^{-10} m^3/(Js)$
T	$600K$
N	256, 512

3 Simulation results and mathematical statistical analysis

3.1 Microstructure evolution

The simulations were performed at a typical operating temperature of 600 K with the characteristic length $L = N\Delta l$ on a mesh grid of 256 and 512 with $\Delta l = 10.7nm$. The implicit Fourier transformation method is employed to solve the Allen–Cahn equation. The iteration step t represents the time advances, and the unit of time is minute. A typical scenario of the grain nucleation and growth within a 256-mesh grid is shown in Figure 1. Several nuclei form at the beginning and grow up subsequently. It is well seen that grain nucleation and growth proceed simultaneously; the previously formed grains grow in size and interconnect with other growing grains. This process occurs until all grains are connected through grain boundaries. The value of the order parameter inside each grain is $\eta_i = 1$; at grain boundaries, it takes values less than 0.5, and it corresponds well to the prediction by the model. Moreover, we find that grains with several sides $n \neq 6$ are unstable, and they can grow or decrease the size depending on the neighbor grains' configuration.

3.2 Statistical analysis of the average grain size

It can be found that the grain boundary (G.B.) energy and mobility are the two main parameters required to be determined for grain growth in U_3Si_2, based on the analysis and research of Cheniour et al. (2020). During normal grain growth, the applied pressure on a grain boundary is given by

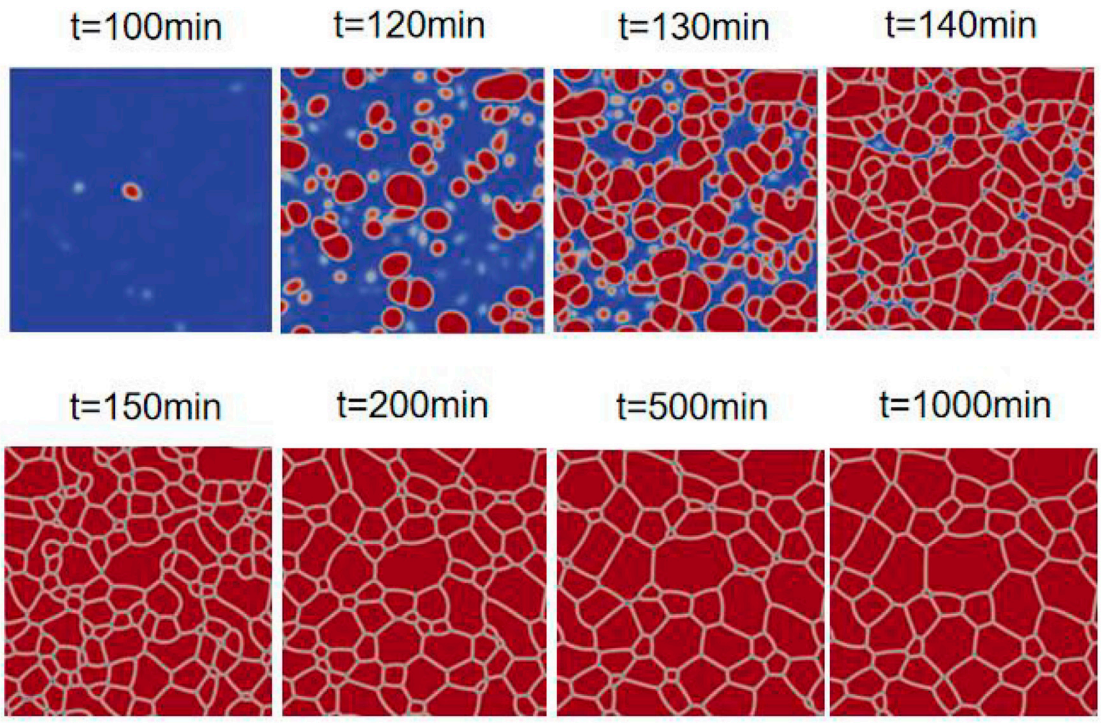

FIGURE 1
Typical scenario of the system evolution with N = 256, L = 2.739 μm, and T = 600 K, at various timesteps t.

$$P_a = \frac{\gamma}{R}, \tag{12}$$

where γ is the grain boundary energy and R is the radius of grain curvature. The grain boundary velocity is

$$v \equiv \frac{dR}{dt} = M(P_a - P_r) \geq 0, \tag{13}$$

where the constant M relates to the grain mobility andP_r is the resistive pressure. Sources of this resistive pressure include voids, pores, and precipitates that cannot diffuse with the boundary. As a result of grain growth, when the driving pressure P_a falls to the value P_r, there is no net pressure, and grain growth ceases at a limiting value. The term P_r is similar to the Zener pinning (Li et al., 2021) term, which accounts for a limiting grain size in two-phase materials.

The average grain size is defined as

$$D \equiv \alpha^{1/2}\overline{R}, \tag{14}$$

where grain topology is included into the geometric constant α. Therefore, dynamics of the grain size obey the following equation:

$$\partial_t D = \alpha\bar{M}\left(\frac{\bar{\gamma}}{D} - \alpha^{-1/2}P_r\right). \tag{15}$$

Here, $\bar{M}$ and $\bar{\gamma}$ are the averaged grain boundary mobility and energy, respectively. When taking into account the simplest case of no resistive pressure, one finds the solution in the form

$$D^2 - D_0^2 = Kt, \quad K \equiv 2\alpha\bar{M}\bar{\gamma}. \tag{16}$$

Temperature dependence of the grain boundary energy for U_3Si_2 by MD simulations (Beeler et al., 2019) was found:

$$\bar{\gamma}(T) = H(T) - TS(T), \tag{17}$$

$$H(T) = 1.21 \times 10^{-7}T^2 - 3.46 \times 10^{-5}T + 0.85 J/m^2, \tag{18}$$

$$S(T) = 4.58 \times 10^{-7}T - 1.72 \times 10^{-4} J/m^2K. \tag{19}$$

The rate constant and grain mobility dependencies on temperature were measured by experimental data (Cheniour et al., 2020):

$$K = 8.77 \times 10^{-18} \exp(-0.33eV/k_BT)m^2/s, \tag{20}$$

$$\bar{M} = 6.30 \times 10^{-18} \exp(-0.33eV/k_BT)m^4/Js. \tag{21}$$

By comparing Eqs 16, 17, 20, 21, we can obtain: $\alpha = 0.96$

Data analysis allows one to obtain the grain area, mean grain size, and amount of grains computed directly from the simulation procedure. The corresponding results are shown in Figure 2 for systems of the linear size L = 2.739 μm and L = 5.478 μm. From Figure 2A, it is seen that the grain area increases in time, according to the linear time law. Our simulated grain size is ~180 nm, which is two orders of magnitude smaller than the experimental values (between 16 and 18 μm from an initial irradiation experiment). It is to be noted that many factors, such as irradiation and heat treatment time, can influence the grain size; our simulation still can act as a reference for grain morphology investigation after heat treatment in the experiment. From Figure 2B one finds that the mean grain radius increases in time in a power law form with a scaling growth exponent of 0.42, which is

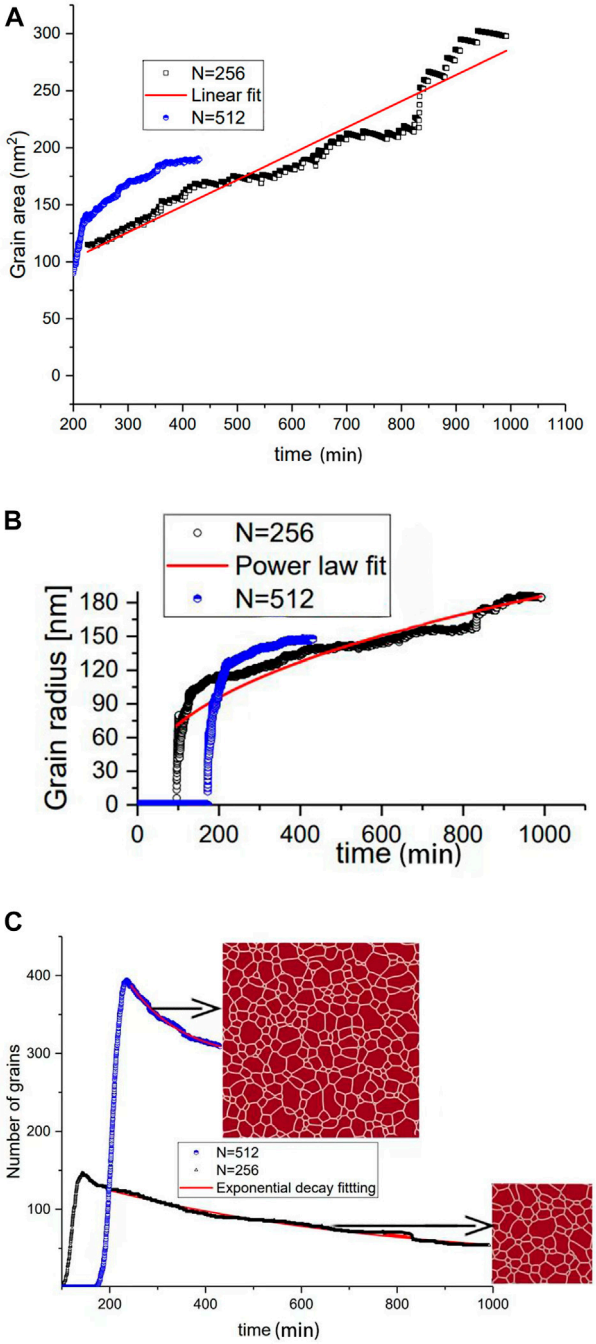

FIGURE 2
(A) Grain area dynamics,**(B)** grain radius dynamics, and **(C)** number of grains at N = 256 and L = 2.739 μm, and N = 512 and L = 5.478 μm.

quite close to the theoretically predicted value, 1/2 (Cheniour et al., 2020). It is important that this grain size variation is observed at a late stage when grain grows following the Ostwald ripening scenario in which large grains grow by consuming the small ones. In Figure 2C, we plot the time dependencies of the grain amount. It follows that the grain number increases rapidly at grain nucleation stages until grains occupy the whole system volume. One can clearly observe the scaling dynamics of the grain radius and area at the later stage when the number of grains decays. Usage of the fitting procedure allows one to find that this kind of decrease can be described well by the exponential decaying function; the exponential decaying function in red in Figure 2C coincides with the simulation results. One must point out that obtained results concerning the scaling behavior of described values are independent of the system size. The size of the system affects only the grain size and their amount due to the influence of periodic boundary conditions and a lack of grains with different morphology, as observed in systems with large sizes.

3.3 Statistical analysis of grain distribution

In general, Eq. 13 is written for the mean radius of grains. In further consideration, we put resistive pressure equals to zero and assume that some grains can decrease in size due to a change in the number of edges. During the system's evolution, the grains with edges of fewer than six disappear. This process is reoccurrence through a relaxation process with time τ_R. In such a case, we introduce a grain size distribution function $\Psi(R)$ that gives the grain density with radius R; then, $\Psi(R)dR$ is the total grains in a grain radius ranging between R and $R + dR$, and dR is a small increment of the grain radius. The growth and relaxation of grains are described as

$$\begin{aligned}\left[\frac{d\Psi}{dt}\right]_g dR &= -\frac{d}{dR}\left[\Psi(R)\frac{dR}{dt}\right]dR \\ \left[\frac{d\Psi}{dt}\right]_r &= -\Psi(R)/\tau_R.\end{aligned} \tag{22}$$

The total net change of the concentration of grains is

$$\left[\frac{d\Psi}{dt}\right]_{tot} = \left[\frac{d\Psi}{dt}\right]_g + \left[\frac{d\Psi}{dt}\right]_r. \tag{23}$$

An equilibrium grain population is defined in a stationary case resulting in the following equation:

$$\frac{d\Psi(R)}{dR_0}v(R) + \Psi(R)\frac{dv(R)}{dR} + \Psi(R)/\tau_R = 0. \tag{24}$$

A solution of Eq. 22 for the distribution function can be found in quadratures:

$$\begin{aligned}\Psi(R) &= \frac{C_0}{v(R)}\exp\left(-\frac{1}{\tau_R}\int_{R_0}^{R}\frac{dR'}{v(R')}\right), \\ C_0^{-1} &= \int_{R_0}^{\infty}\Psi(R)dR,\end{aligned} \tag{25}$$

where $v(R)$ is defined in Eq. 13, and C_0 is the integration constant giving the total number of grains.

Based on the substituting growth speed Eq. 16 into Eq. 25 and assuming $P_r \to 0$, one gets the Rayleigh distribution function:

$$\Psi(R) = \frac{C_0 R}{R_0\bar{M}\bar{\gamma}}\exp\left(-\frac{(R^2 - R_0^2)}{2\tau_R\bar{M}\bar{\gamma}}\right). \tag{26}$$

This distribution can be used in a fitting procedure to describe numerically obtained results and experimental observations.

In addition, in a nonstationary case, we exploit the Fourier method:

$$\begin{aligned}\Psi(R,t) &= \psi(t)\bar{\omega}\left(\frac{R(t)}{a(t)}\right), \\ y &= \frac{R(t)}{a(t)},\end{aligned} \tag{27}$$

where y is the grain radius scaled in a(t); $\psi(t)$ andϖ(y) are unknown functions. The time derivative of the grain radius is scaled as

$$dR/dt = \theta(t)\sigma(y), \tag{28}$$

where the corresponding time dependence defined by $\theta(t)$ should coincide with $\dot{a}(t)$, following the definition of the grain size derivative:$\theta(t) \equiv \dot{a}(t)$.

Through substituting time derivatives and spatial derivatives as $d\Psi/dt = \varpi(y)\dot{\psi}$, $dR/dt = \sigma(y)\dot{a}$, and $d/dR = d/ady$, one can separate parts describing time dependencies and size dependencies in the following form:

$$\frac{a(t)}{\dot{a}(t)}\left(\frac{\dot{\psi}(t)}{\psi(t)} + \tau_R^{-1}\right) = \frac{1}{\varpi(y)}\frac{d}{dy}\sigma(y)\varpi(y). \tag{29}$$

Next, we set both sides of Eq. 29 to the same constant $-C$ with $C > 0$; one gets two separate equations for time dependence and grain size dependence:

$$\frac{\dot{\psi}(t)}{\psi(t)} = -C\frac{\dot{a}(t)}{a(t)} - \tau_R^{-1}, \tag{30}$$

$$-C\varpi(y) = \frac{d}{dy}\sigma(y)\varpi(y). \tag{31}$$

Furthermore, we can get the following two equations of the form:

$$\psi(t) = \psi_0[a(t)]^{-C}\exp(-t/\tau_R), \tag{32}$$

$$\varpi(y) = \frac{\varpi_0}{\sigma(y)}\exp\left(-C\int_0^y\frac{dy'}{\sigma(y')}\right), \tag{33}$$

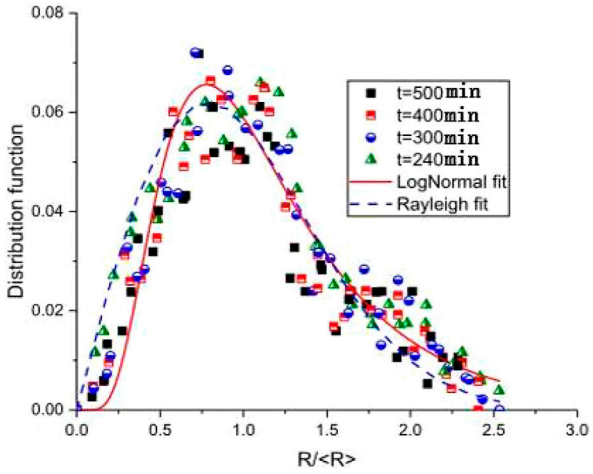

FIGURE 3
Grain size distribution function at N = 512 and L = 5.478 μm.

where ψ_0 and ϖ_0 are integration constants. Based on the aforementioned conclusions, we can further obtain the following formulas:

$$N(t) = N_0[a(t)]^{1-C}\exp(-t/\tau_R), \quad N_0 = \psi_0\int_0^\infty \varpi(y)dy, \tag{34}$$

$$R(t) = R_0 a(t), \quad R_0 = \frac{\int_0^\infty y\varpi(y)dy}{\int_0^\infty \varpi(y)dy}, \; a(t) \propto t^z. \tag{35}$$

Figure 3 shows our simulated grain size distribution along with grain area evolution at different times. It follows that all data are lying in statistically the same trend. Our result manifests a universal grain size distribution function as was predicted by theoretical studies (Vaz and Fortes, 1988). More importantly, the fitting procedure allows one to choose a more accurate distribution function for describing objects like voids, bubbles, and grains. In our case, the lognormal type and Rayleigh distribution function are used for data fitting. After comparing the χ-square error and the determination coefficient of fitting, we find that the Rayleigh distribution function (shown by the dashed curve in Figure 3) is more suitable for the grain growth behavior description of U_3Si_2 during the thermal treatment.

4 Conclusion

In our work, a phase-field simulation was provided at a temperature of 600 K at grids with characteristic length $L = N\Delta l$ with $N = 256$ and 512 by using the implicit Fourier transformation method. Grains' morphology evolution shows grain nucleation and growth simultaneously, and the larger ones coarsen by consuming smaller ones, leading to a decrease in the grain number at the latter stage. The grain area increases in time, according to the linear time law, while the mean grain radius increases in time in a power law form $a(t) \propto t^z$ with the scaling growth exponent z = 0.42, which is quite close to the theoretically predicted value 1/2. Finally, the grain size distribution of U_3Si_2 obeys the Rayleigh function by comparing the χ-square error and determination coefficient with a lognormal type fitting. Our results investigate grain growth dynamics and provide a quantitative description of grain size distribution in U_3Si_2 under the ideal circumstance, which not only lays a solid foundation for grain morphology investigation with voids and other second-phase precipitates but also is helpful for the study of grain subdivision, amorphization, and swelling in U_3Si_2.

Data availability statement

The original contributions presented in the study are included in the article/supplementary material; further inquiries can be directed to the corresponding authors.

Author contributions

CM: model development, data analysis, and writing the original draft. MZ: data analysis, checking, and writing the original draft. TX: conceptualization and methodology. LW: conceptualization, supervision, and funding acquisition. RP: methodology and data analysis. JQ: software, methodology, and data analysis. JZ: methodology, software, and supervision.

Funding

This work is supported by the Sichuan Science and Technology Program (Grant no. 2022JDGD0040).

Conflict of interest

The authors declare that the research was conducted in the absence of any commercial or financial relationships that could be construed as a potential conflict of interest.

Publisher's note

References

Aagesen, L. K., Andersson, D., Beller, B. W., Cooper, M. W., Gamble, K. A., Miao, Y., et al. (2020). Phase-field simulations of intergranular fission gas bubble behavior in U_3Si_2 nuclear fuel. *J. Nucl. Mater.* 541, 152415. doi:10.1016/j.jnucmat.2020.152415

Ahmed, K., Pakarinen, J., Allen, T., and El-Azab, A. (2014). Phase field simulation of grain growth in porous uranium dioxide. *J. Nucl. Mater.* 446, 90–99. doi:10.1016/j.jnucmat.2013.11.036

Ansari, T. Q., Huang, H., and Shi, S. Q. (2021). Phase field modeling for the morphological and microstructural evolution of metallic materials under environmental attack. *npj Comput. Mat.* 7 (1), 143–221. doi:10.1038/s41524-021-00612-7

Atkinson Hv, H. V. (1988). Overview no 65: Theories of normal grain growth in pure singlephase systems. *Acta Metall.* 36, 469.

Azeem, M. M., Wang, Q., Zhang, Y., Liu, S., and Zubair, M. (2019). Effect of grain boundary on diffusion of P in alpha-Fe: A molecular dynamics study. *Front. Phys.* 7, 97. doi:10.3389/fphy.2019.00097

Beeler, B., Baskes, M., Andersson, D., Cooper, M. W., and Zhang, Y. (2019). Molecular dynamics investigation of grain boundaries and surfaces in U_3Si_2. *J. Nucl. Mater.* 514, 290–298. doi:10.1016/j.jnucmat.2018.12.008

Bischoff, J., Blanpain, P., Brachet, J. C., Lorrette, C., Ambard, A., Strumpell, J., et al. (2016). *Development of fuels with enhanced accident tolerance, accident tolerant fuel concepts for light water reactors*. United States of America: IAEA Tecdoc. 1797:22-29.

Blikstein, P., and Tschiptschin, A. P. (1999). Monte Carlo simulation of grain growth. *Mat. Res.* 2, 133–137. doi:10.1590/s1516-14391999000300004

Chen, L. Q. (2002). Phase-field models for microstructure evolution. *Annu. Rev. Mat. Res.* 32, 113–140. doi:10.1146/annurev.matsci.32.112001.132041

Chen, L. Q., and Yang, W. (1994). Computer simulation of the domain dynamics of a quenched system with a large number of nonconserved order parameters: The grain-growth kinetics. *Phys. Rev. B* 50, 15752–15756. doi:10.1103/physrevb.50.15752

Cheniour, A., Tonks, M., Gong, B., Yao, T., He, L., Harp, J. M., et al. (2020). Development of a grain growth model for U_3Si_2 using experimental data, phase field simulation and molecular dynamics. *J. Nucl. Mater.* 532, 152069. doi:10.1016/j.jnucmat.2020.152069

Davidge, R. W., and Evans, A. G. (1969). The strength and fracture of stoichiometricpolycrystalline UO_2. *J. Nucl. Mater.* 33, 249–260. doi:10.1016/0022-3115(69)90019-1

Fan, D., and Chen, L. Q. (1997). Computer simulation of grain growth using a continuum field model. *Acta Mat.* 45, 611–622. doi:10.1016/s1359-6454(96)00200-5

Forsberg, K., and Massih, A. R. (2001). "Theory of fission gas release during grain growth," in the 16th International Conference on Structural Mechanics in Reactor Technology, Washington DC, August 2001.

Frost, H. J., and Thopson, C. V. (1996). Computer simulation of grain growth. *Curr. Opin. Solid State Mat. Sci.* 1, 361–368. doi:10.1016/s1359-0286(96)80026-x

Harding, J. H., and Martin, D. G. (1989). A recommendation for the thermal conductivity of UO_2. *J. Nucl. Mater.* 166 (3), 223–226. doi:10.1016/0022-3115(89)90218-3

III Krill, C. E., and Chen, L. Q. (2002). Computer simulation of 3D grain growth using a phase-field model. *Acta Mat.* 50, 3059–3075. doi:10.1016/s1359-6454(02)00084-8

Kapoor, K., Ahmad, A., Laksminarayana, A., and Hemanth Rao, G. V. (2007). Fracture properties of sintered UO_2 ceramic pellets with duplex microstructure. *J. Nucl. Mater.* 366, 87–98. doi:10.1016/j.jnucmat.2006.12.044

Kobayashi, R., Warren, J. A., and Carter, W. C. (2000). A continuum model of grain boundaries. *Phys. D. Nonlinear Phenom.* 140, 141–150. doi:10.1016/s0167-2789(00)00023-3

Li, Y., Hu, S., Sun, X., and Stan, M. (2017). A review: Applications of the phase field method in predicting microstructure and property evolution of irradiated nuclear materials. *npj Comput. Mat.* 3, 16. doi:10.1038/s41524-017-0018-y

Li, Y., Zhou, J., Li, R., and Zhang, Q. (2021). Molecular dynamics simulation of zener pinning by differently shaped and oriented particles. *Front. Mat.* 8, 152. doi:10.3389/fmats.2021.682422

Liang, L., Mei, Z. G., Kim, Y. S., Ye, B., Hofman, G., Anitescu, M., et al. (2016). Mesoscale model for fission-induced recrystallization in U-7Mo alloy. *Comput. Mat. Sci.* 124, 228–237. doi:10.1016/j.commatsci.2016.07.033

Liu, Y., Baudin, T., and Penelle, R. (1997). Simulation of normal grain growth by cellular automata. *Scr. Mat.* 34, 1679–1683. doi:10.1016/1359-6462(96)00055-3

Lobkovsky, A. E., and Warren, J. A. (2001). Sharp interface limit of a phase-field model of crystal grains. *Phys. Rev. E* 63, 051605. doi:10.1103/physreve.63.051605

Mei, Z. G., Liang, L., Kim, Y. S., Wiencek, T., O'Hare, E., Yacout, A. M., et al. (2016). Grain growth in U-7Mo alloy: A combined first-principles and phase field study. *J. Nucl. Mater.* 473, 300–308. doi:10.1016/j.jnucmat.2016.01.027

Miao, Y. B., Gamble, K. A., Andersson, D., Mei, Z. G., and Yacout, A. M. (2018). Rate theory scenarios study on fission gas behavior of U_3Si_2 under LOCA conditions in LWRs. *Nucl. Eng. Des.* 326, 371–382. doi:10.1016/j.nucengdes.2017.11.034

Miao, Y. B., Gamble, K. A., Andersson, D., Ye, B., Mei, Z. G., Hofman, G., et al. (2017). Gaseous swelling of U_3Si_2 during steady-state LWR operation: A rate theory investigation. *Nucl. Eng. Des.* 322, 336–344. doi:10.1016/j.nucengdes.2017.07.008

Millett, P. C., Wolf, D., Desai, T., Rokkam, S., and El-Azab, A. (2008). Phase-field simulation of thermal conductivity in porous polycrystalline microstructures. *J. Appl. Phys.* 104, 033512. doi:10.1063/1.2964116

Moelans, N., Blanpain, B., and Wollants, P. (2008). An introduction to phase field modeling of microstructure evolution. *Calphad* 32, 268–294. doi:10.1016/j.calphad.2007.11.003

Moelans, N., Blanpain, B., and Wollants, P. (2008). Quantitative analysis of grain boundary properties in a generalized phase field model for grain growth in anisotropic systems. *Phys. Rev. B* 78, 024113. doi:10.1103/physrevb.78.024113

Oguma, M. (1982). Microstructure effects on fracture strength of UO_2 fuel pellets. *J. Nucl. Sci. Technol.* 19, 1005–1014. doi:10.1080/18811248.1982.9734249

Rest, J., and Hofman, G. L. (2004). A model for fission-gas-bubble behavior in amorphous uranium silicide compounds. *J. Nucl. Mater.* 325, 107–117. doi:10.1016/j.jnucmat.2003.11.008

Srezende, J. L. L., Pezzolla, F., Nestler, B., SeeBelberg, M., Prieler, R., Schmitz, G., et al. (1996). A phasefield concept for multiphase systems. *Phys. D. Nonlinear Phenom.* 94, 135–147. doi:10.1016/0167-2789(95)00298-7

Terrani, K. A., Wang, D., Ott, L. J., and Montgomery, R. O. (2014). The effect of fuel thermal conductivity on the behavior of LWR cores during loss-of-coolant accidents. *J. Nucl. Mater.* 448 (1-3), 512–519. doi:10.1016/j.jnucmat.2013.09.051

Tonks, M. R., Zhang, Y., Bai, X., and Millett, P. C. (2014). Demonstrating the temperature gradient impact on grain growth in UO_2 using the phase field method. *Mat. Res. Lett.* 2, 23–28. doi:10.1080/21663831.2013.849300

Vaz, M. F., and Fortes, M. A. (1988). Grain size distribution: The lognormal and the gamma distribution functions. *Scr. Metall.* 22 (1), 35–40. doi:10.1016/s0036-9748(88)80302-8

Wakai, F., Enomoto, N., and Ogawa, H. (2000). Three dimensional microstructural evolution in ideal grain growth general statistics. *Acta Mat.* 48, 1297–1311. doi:10.1016/s1359-6454(99)00405-x

Wen, Y. H., Wang, B., Simmons, J. P., and Wang, Y. (2006). A phase-field model for heat treatment applications in Ni-based alloys. *Acta mater.* 54 (8), 2087–2099. doi:10.1016/j.actamat.2006.01.001

Westinghouse Electric Company (2015). *Development of LWR fuels with enhanced accident tolerance*. United States: Final Technical Report.

Weygand, D., Brechet, Y., and Lepinoux, A. (1998). A vertex dynamics simulation of grain growth in two dimensions. *Philos. Mag. B* 78, 329–352. doi:10.1080/014186398258014

White, J. T., Nelson, A. T., Dunwoody, J. T., Byler, D., Safarik, D., and McClellan, K. (2015). Thermophysical properties of U_3Si_2 to 1773 K. *J. Nucl. Mater.* 464, 275–280. doi:10.1016/j.jnucmat.2015.04.031

Zhou, W., and Zhou, W. (2018). Enhanced thermal conductivity accident tolerant fuels for improved reactor safety–A comprehensive review. *Ann. Nucl. Energy* 119, 66–86. doi:10.1016/j.anucene.2018.04.040

frontiers | Frontiers in Energy Research

TYPE Original Research
PUBLISHED 27 January 2023
DOI 10.3389/fenrg.2023.1088742

OPEN ACCESS

EDITED BY
Shichang Liu,
North China Electric Power University, China

REVIEWED BY
David Simeone,
Commissariat à l'Energie Atomique et aux Energies Alternatives (CEA), France
Yuexia Wang,
Fudan University, China

*CORRESPONDENCE
Vasyl O. Kharchenko,
vasiliy@ipfcentr.sumy.ua

SPECIALTY SECTION
This article was submitted to Nuclear Energy, a section of the journal Frontiers in Energy Research

RECEIVED 03 November 2022
ACCEPTED 18 January 2023
PUBLISHED 27 January 2023

CITATION
Wu L, Qin J, Kharchenko VO, Kharchenko DO and Lysenko OB (2023), Phase field modeling microstructural evolution of Fe-Cr-Al systems at thermal treatment. *Front. Energy Res.* 11:1088742. doi: 10.3389/fenrg.2023.1088742

Phase field modeling microstructural evolution of Fe-Cr-Al systems at thermal treatment

Lu Wu[1], Jiantao Qin[1], Vasyl O. Kharchenko[2,3]*, Dmitrii O. Kharchenko[1,2] and Oleg B. Lysenko[2]

[1]The First Sub-Institute, Nuclear Power Institute of China, Chengdu, China, [2]Institute of Applied Physics, National Academy of Sciences of Ukraine, Sumy, Ukraine, [3]Department of Applied Mathematics and Complex Systems Modeling, Sumy State University, Sumy, Ukraine

A phase field model to study dynamics of microstructure transformations and the evolution of defect structure during heat treatment of Fe-Cr-Al systems is developed. Statistical and kinetic properties of evolving microstructure and defect structure in alloys with different content of alloying elements and at different temperatures were studied. Point defects rearrangement during precipitation is discussed in details. Universality of statistical distributions over precipitate size is revealed for considered class of alloys.

KEYWORDS

phase-field modeling, phase decomposition, microstructure, precipitates, defects

1 Introduction

It is known that Fe-Cr-Al alloys are successfully used in many industrial applications where high temperature oxidation resistance is needed, for example, in fuel energy plants (Gulbransen and Andrew, 1959; Wukusick and Collins, 1964). Nuclear grade iron-based Fe-Cr-Al alloys have been developed as candidate materials for accident tolerant fuel cladding since the 1960s due to their corrosion resistance, radiation response, fuel-cladding chemical interaction, good mechanical properties for extended periods which do not significantly penalize the overall nuclear reactor operation [see discussion in Ref. (Yamamoto et al., 2015)].

By studying an influence of alloying elements on properties in these alloys it was found that the higher Cr content in these alloys would be beneficial for corrosion resistance in the high temperature water reactors and also high-temperature steam oxidation resistance (Stott et al., 1995). At the same time higher Cr content would result in potential embrittlement of these alloys at operating temperatures in the interval 288°C–320°C due to the formation of Cr-rich α'-phase (Mathon et al., 2003; Kobayashi and Takasugi, 2010; Ejenstam et al., 2015). The higher Al content is beneficial for high-temperature steam oxidation resistance, but it may raise the ductile-brittle transition temperature (Qu et al., 2013). It was shown that more than six at% of Al addition would be effective in reducing the stability of α' precipitates, a further Al addition results in increasing the solution limit of Cr in the matrix (Kobayashi and Takasugi, 2010; Li et al., 2013; Ejenstam et al., 2015).

Extensive studies of ternary Fe-Cr-Al alloys were started from 1960s for use in nuclear applications for a wide range of compositions experimentally and theoretically. Essential progress was in studying material properties in such systems was achieved by using different methods of multiscale modeling scheme. Among theoretically obtained results one can issue *ab initio* calculations of energetic parameters for atoms relocations (Kresse and Hafner, 1993;

Kresse and Hafner, 1994; Kresse and Furthmüller, 1996), kinetic Monte Carlo simulations of the long-term microstructural stability of Fe-Cr-Al alloys (Ejenstam et al., 2015), molecular dynamics studying the dependence of elastic, bulk and shear moduli on alloy composition (Dai et al., 2022), classical phase field modeling precipitation kinetics [see for example, Refs. (Chen et al., 2019; Lee et al., 2020)]. A correlative theoretical and experimental research strategy has been developed in Ref. (Chang et al., 2019) to investigate the Fe-Cr-Al system, which includes an integration of *ab initio* calculations, CALPHAD, and experiments. The CALPHAD approach has been successfully applied to obtain phase diagrams at thermodynamic equilibrium by exploiting the Gibbs energy functions (Dinsdale, 1991). It serves as a powerful tool for component selection, composition design and optimization of materials for specific applications.

Recently successful progress in understanding microstructure transformation in Fe-Cr-Al systems separation kinetics of the nano-size α'-phase in Fe-Cr-Al alloys was achieved. At the same time some open questions related to study microstructure evolution of long aging time and predicting the mechanical properties of these alloys remain actual. Indeed, an influence of alloy composition and aging temperature onto volume fraction and the mean precipitate size affecting the hardness and embrittlement in Fe-Cr-Al alloys is still under discussion.

In this paper we describe properties of nano-size α'-phase precipitation in such ternary systems by considering a phase decomposition with local rearrangement of point defects. We exploit CALPHAD approach and take into account interaction of atomic subsystem with subsystem of defects. The derived model includes elastic anisotropy and can be used to study alloys with different content of doping. Main efforts are concentrated onto studying an influence of alloying elements onto kinetics of phase decomposition at different temperatures and statistical properties of growing α' precipitates. In our approach we study dynamics of precipitate size, their number density and volume fraction of precipitates at thermal treatment of solid solution for alloys with different compositions. Our study provides an insight into the physics of phase decomposition which can be generalized next in studying radiation induced precipitation and precipitates dissolution with defects clustering.

The work is organized in the following manner. In **Section 2** we describe formalism used in phase field modeling. **Section 3** is devoted to stability analysis and discussion of numerical modeling results. Here the main dynamical laws for precipitate size and their number density are shown and analysis of phase decomposition kinetics at different content of alloying elements and annealing temperatures is provided. We conclude in **Section 4**.

2 Phase field model

We describe ternary systems Fe-Cr-Al with molar concentration of Fe, Cr and Al (coinciding with atomic ones) denoted as $x_\mu = N_\mu/N$ with $\mu = \{Fe, Cr, Al\}$, where N_μ is the number of atoms of the sort μ, N is the total number of atoms, the mass conservation law is satisfied $\Sigma_\mu x_\mu = 1$. Concentrations of point defects c_d with $d = \{i, v\}$ denotes interstitial (i) and vacancies (v) is defined in the same manner. We consider introduced quantities as continuous fields evolving in space $\mathbf{r}$ and time t: $x_\mu = x_\mu(\mathbf{r}, t)$, $c_d = c_d(\mathbf{r}, t)$. We introduce point defects as additional substances allowing us to distinguish atomic and point defects subsystems. These equilibrium defects do not contribute to mass conservation due to their small concentrations.

2.1 Gibbs energy for ternary system with defects and elastic anisotropy

The total Gibbs functional for the class of considered systems has the form:

$$\mathcal{G} = \frac{1}{V_m}\int_V \left[G_{ch}\left(\{x_\mu\},\{c_d\}\right) + G_\nabla\left(\{\nabla x_\mu\},\{\nabla c_d\}\right) + G_{el}\right]\mathrm{d}\mathbf{r}, \qquad (1)$$

where the term G_{ch} relates to the chemical Gibbs energy depending on the concentrations of the alloy components and point defects; G_∇ is a gradient energy part and the last term G_{el} corresponds to an elastic contribution; V_m is the molar volume; integration is taken over the whole volume V.

The free energy density G_{ch} can be decomposed into two terms, describing atomic and defect subsystems as follows: $G_{ch} = G_{Fe-Cr-Al} + G_d$. The molar Gibbs energy of the atomic subsystem $G_{Fe-Cr-Al}$ is defined as: $G_{Fe-Cr-Al} = G^{ref}_{Fe-Cr-Al} + G^{id}_{Fe-Cr-Al} + G^{ex}_{Fe-Cr-Al}$, where $G^{ref}_{Fe-Cr-Al}$ is the reference Gibbs energy, $G^{id}_{Fe-Cr-Al}$ denotes the ideal Gibbs energy contribution due to random mixing of atoms, G^{ex} is the excess term defining a deviation from ideality. The reference Gibbs energy is written in the standard form $G^{ref}_{Fe-Cr-Al} = \sum_\mu G^0_\mu x_\mu$. The corresponding expressions for the reference energies G^0_μ can be obtained with the help of phase diagrams by using CALPHAD method (Dinsdale, 1991). The ideal part G^{id} relates to entropic contribution $G^{id} = RT\Sigma_\mu x_\mu \ln x_\mu$, where R is the universal gas constant, T is the temperature. The excess term G^{ex} is defined by temperature dependent interaction coefficients $L_{\mu\nu} = L_{\mu\nu}(T)$ in the following form: $G^{ex} = \Sigma_{\mu\neq\nu} x_\mu x_\nu L_{\mu,\nu}$. The Gibbs energy G_d for a point defect subsystem $d = \{i, v\}$ can be written as follows: $G_d = \sum_d G^f_d + G^{id}_d + G^{int}_d$. Here G^f_d is the defect formation energy. It is defined through the formation energies $G^{f,\mu}_d$ of defects in pure materials *Fe*, *Cr* and *Al* and mean concentrations of atoms in the alloy as $G^f_d = \sum_\mu G^{f,\mu}_d \bar{x}_\mu$, where $\bar{x}_\mu$ relates to nominal concentration of μ. The corresponding entropic contribution is $G^{id}_d = RTc_d ln\, c_d$. Interactions between defects with host atoms and alloying elements (G^{int}_i and G^{int}_v) can be described by the component $G^{int}_d = c_d \sum_\mu x_\mu G^{int}_{d-\mu}$, where for the defect-atom interaction energies we use definitions (Was, 2016): $G^{int}_{d-\mu} = (G^\mu_{coh} + G^{f,\mu}_d)/Z$. Here G^μ_{coh} denotes the corresponding cohesive energy, Z relates to the coordination number. Point defects formation energies for pure materials ($G^{f,\mu}_d$) and the corresponding cohesive energies (G^μ_{coh}) can be taken from the literature or can be calculated by *ab initio* calculations or molecular dynamics simulations.

By combining all above expressions, the total Gibbs energy for the ternary alloy $Fe - Cr - Al$ with point defects takes the form:

$$\begin{aligned} G_{ch}&(x_{Fe}, x_{Cr}, x_{Al}, c_v, c_i) \\ &= G^0_{Fe}x_{Fe} + G^0_{Cr}x_{Cr} + G^0_{Al}x_{Al} + G^f_v c_v + + G^f_i c_i \\ &\quad + RT\left[x_{Fe} ln\, x_{Fe} + x_{Cr} ln\, x_{Cr}\right. \\ &\quad \left. + x_{Al} ln\, x_{Al} + c_v ln\, c_v + c_i ln\, c_i\right] \\ &\quad + x_{Fe}x_{Cr}L_{Fe,Cr} + x_{Fe}x_{Al}L_{Fe,Al} + x_{Cr}x_{Al}L_{Cr,Al} \\ &\quad + c_v\left[x_{Fe}G^{int}_{v-Fe} + x_{Cr}G^{int}_{v-Cr} + x_{Al}G^{int}_{v-Al}\right] \\ &\quad + c_i\left[x_{Fe}G^{int}_{i-Fe} + x_{Cr}G^{int}_{i-Cr} + x_{Al}G^{int}_{i-Al}\right]. \end{aligned} \qquad (2)$$

The gradient term G_∇ has the form: $G_\nabla = \sum_\mu(\kappa_\mu/2)(\nabla x_\mu)^2 + \sum_d(\kappa_d/2)(\nabla c_d)^2$. The energy constants $\{\kappa_\mu\}$ are defined according to the Hilliard approach Ref. (Hilliard, 1970). Next we assume $\kappa_\mu = \kappa$, where $\kappa = L_{Fe,Cr}a^2/6$, $a = \Sigma_\mu a_\mu x_\mu$, a_μ is the lattice constant for pure materials. In order to avoid negative gradient energy and ensure the disorder of the system, for the energy constants κ_i and κ_v we use the formalism discussed in Refs. (Liang et al., 2018; Yan et al., 2020) and define them as $\kappa_d = \kappa_v = \kappa_i$.

The $\alpha - \alpha'$-interface can be considered as a semi-coherent due to small difference in lattice parameters of two main elements Fe and Cr, as usual (Ribis and Lozano-Perez, 2012). To make our description more general we consider the elastic contribution G_{el} in the Gibbs energy has the standard form $G_{el} = V_m 2C_{ijkl}(e_{ij} - e^0_{ij})(e_{kl} - e^0_{kl})/2$, here C_{ijkl} denotes the elastic constants tensor, $e_{ij} = \left(\partial_{x_i}u_j + \partial_{x_j}u_i\right)/2$ is the elastic strain tensor, where $\mathbf{u} = (u_x, u_y, u_z)$ is the displacement vector. By using the Vegard law one defines the lattice parameters misfit $e^0_\mu = (1/a)(da/dx_\mu)$ caused by introducing alloying element μ. Hence, the eigenstrain tensor e^0_{ij} acquires the general form $e^0_{ij}(\mathbf{r},t) = \delta_{ij}\sum_\mu e^0_\mu \delta x_\mu(\mathbf{r},t)$, here δ_{ij} is the Kronecker delta-symbol, $\delta x_\mu(\mathbf{r},t) = (x_\mu(\mathbf{r},t) - \bar{x}_\mu)$. By taking into account that α'-phase is hard phase, one can consider only Chromium contribution to elastic effects. In such a case eigenstrain and corresponding stress tensors acquire the form $e^0_{ij}(\mathbf{r},t) = \delta_{ij}e^0_{Cr}\delta x_{Cr}(\mathbf{r},t)$, $\sigma^0_{ij} = C_{ijkl}e^0_{kl}$ with $e^0_{Cr} = 0.00614$. The elastic energy can be decomposed into four parts: $G^0_{el} = (V_m/2)\sigma^0_{ij}e^0_{ij}$ related to eigenstrain components (proportional to squared concentration of alloying elements); $G^*_{el}(\{e_s\}^6_{s=1})$ related to elastic components defined through elementary strains e_s; G^c_{el} is responsible for coupling between deformation elastic deformations e_1 and alloying element concentration; G^a_{el} corresponds to cubic symmetry.

As was shown previously (Cahn, 1962; Onuki, 2002; Khachaturyan, 2013) in BCC metals/alloys the minimum free energy is along the soft direction ⟨100⟩. The contribution to elastic energy coming from the lattice mismatch takes the form (Cahn, 1961): $G^0_{el} = Y_{[100]}V_m(e^0_{Cr}\delta x_{Cr})^2$, $Y_{[100]} = C_{11} + C_{12} - 2(C_{12})^2/C_{11}$, where $Y_{[100]}$ is the averaged stiffness parameter for cubic crystals related to the free energy minimum along ⟨100⟩ direction.

By using standard relations between stiffness components and elastic moduli one can write a contribution coming from elastic continuum as follows (Onuki, 2002):

$$G^*_{el} = \frac{1}{2}Ke_1^2 + \mu_2\Phi(e_2,e_3) + \mu_3\Psi(e_4,e_5,e_6), \tag{3}$$

where the stretching (Φ) and shear (Ψ) contributions are defined by

$$\begin{aligned}\Phi &= \frac{1}{4\pi^2}\left[3 - cos(2\pi e_{2-}) - cos(2\pi e_{2+}) - cos\left(\frac{4\pi}{\sqrt{6}}e_3\right)\right],\\ \Psi &= \frac{1}{4\pi^2}\left[3 - cos(2\pi e_4) - cos(2\pi e_5) - cos(2\pi e_6)\right].\end{aligned} \tag{4}$$

Here elementary strain components are: $e_1 = e_{xx} + e_{yy} + e_{zz}$, $e_2 = e_{xx} - e_{yy}, e_3 = (2e_{zz} - e_{xx} - e_{yy})/\sqrt{3}$ $e_4 = e_{xy}$, $e_5 = e_{yz}$, $e_6 = e_{zx}$, $e_{2\pm} = e_2/\sqrt{2} \pm e_3/\sqrt{6}$. For small strains we get $\Phi \approx \mu_2(e_2^2 + e_3^2)/2$, and $\Psi \approx \mu_3(e_4^2 + e_5^2 + e_6^2)/2$, as usual.

The component describing coupling between deformation and concentration has the form (Onuki, 2002): $G^c_{el} = \alpha V_m \delta x_{Cr}\nabla\cdot\mathbf{u}$, where $\alpha = -e^0_{Cr}3K$. Elastic misfit results in anisotropy with a parameter $\xi_a = (C_{11} - C_{12} - 2C_{44})/C_{44}$ defining anisotropy contribution Onuki (2002).

$$G^a_{el} = \frac{V_m}{2}\tau^a\sum_{i\neq j}|\nabla_i^2\nabla_j^2 w|, \quad \tau^a = \frac{\left(e^0_{Cr}3K\right)^2\xi^a C_{44}}{C_{11}^2}, \tag{5}$$

where $\nabla_i\nabla_j w = n_i n_j \delta x_{Cr}(\mathbf{r},t)$, n_i denotes component of the interface normal $\mathbf{n}$.

In our calculations we will follow approach developed by Onuki [see Ref. (Onuki, 2002) and citations therein] and results of molecular dynamics (Dai et al., 2022) and assume that all elastic constants depend on concentration of alloying elements: $C_{ij} = \sum_\mu C^\mu_{ij}x_\mu$. A condition of mechanical equilibrium implies $\partial_{x_j}\left[C_{ijkl}\left(e_{kl} - \delta_{kl}e^0_{Cr}\delta x_{Cr}\right)\right] = 0$.

By combining all above expressions, the elastic contribution G_{el} to the total Gibbs energy for the ternary alloy $Fe - Cr - Al$ becomes the form:

$$\begin{aligned}G_{el} = &\frac{Y_{[100]}V_m}{2}\left[e^0_{Cr}\delta x_{Cr}\right]^2 + \frac{V_m\tau_a}{2}\sum_{i\neq j}|\nabla_i\nabla_j w|\\ &- V_m\left[3Ke^0_{Cr}\delta x_{Cr}\nabla\cdot\mathbf{u} + \Phi(e_2,e_3;x_{Cr})\right.\\ &\left.+\Psi(e_4,e_5,e_6;x_{Cr})\right].\end{aligned} \tag{6}$$

In our approach we use concentration dependent stiffness constants $K = K_0 + K_1x_{Cr}$, $\mu_2 = \mu_{20} + \mu_{21}x_{Cr}, \mu_3 = \mu_{30} + \mu_{31}x_{Cr}$, $\xi^a = \xi^a_0 + \xi^a_{01}x_{Cr}$, where bulk, shear moduli and anisotropy components are collected in **Table 1**. For stiffness parameter $Y_{[100]}$, next, we use elastic constants defined through the nominal compositions, i.e., $Y_{[100]} = Y_{[100]}\bar{x}_{Cr}$. By using the Hook law for elastic stress tensor $\sigma_{ij} = C_{ijkl}e_{kl} = C_{ijkl}(e_{kl} - e^0_{kl})$ one finds for diagonal components σ_{ii}: $\sigma_{xx} = \sigma_{yy} = \sigma_{zz} = (K_0 + K_1x)e_1$, for off–diagonal ones we get $\sigma_{xy} = (\mu_{30} + \mu_{31}x_{Cr})\sin(2\pi e_4)/2\pi$, $\sigma_{yz} = (\mu_{30} + \mu_{31}x_{Cr})\sin(2\pi e_5)/2\pi$, $\sigma_{xy} = (\mu_{30} + \mu_{31}x_{Cr})\sin(2\pi e_6)/2\pi$.

2.2 Evolution equations

By taking into account the mass conservation law and defining the concentration of the Iron as the host element as: $x_{Fe} = 1 - x_{Cr} - x_{Al}$ dynamics of the complete system will be governed by the following equations of the Cahn-Hilliard type (Cahn, 1962; Hilliard, 1970):

$$\begin{aligned}\partial_t x_{Cr} &= \nabla\cdot\left[M_{CrCr}\nabla\frac{\delta\mathcal{G}}{\delta x_{Cr}} + M_{CrAl}\nabla\frac{\delta\mathcal{G}}{\delta x_{Al}}\right],\\ \partial_t x_{Al} &= \nabla\cdot\left[M_{AlAl}\nabla\frac{\delta\mathcal{G}}{\delta x_{Al}} + M_{CrAl}\nabla\frac{\delta\mathcal{G}}{\delta x_{Cr}}\right],\\ \partial_t c_v &= \nabla\cdot L_v\nabla\frac{\delta\mathcal{G}}{\delta c_v},\\ \partial_t c_i &= \nabla\cdot L_i\nabla\frac{\delta\mathcal{G}}{\delta c_i}\end{aligned} \tag{7}$$

Mobility coefficients $M_{Cr,Cr}$, $M_{Al,Al}$ and $M_{Cr,Al}$ are as follows (Huang et al., 1995; Wu et al., 2001; Wu et al., 2004; Lee et al., 2020):

$$\begin{aligned}M_{Cr,Cr} &= x_{Cr}\left[(1-x_{Cr})^2M_{Cr} + x_{Cr}x_{Al}M_{Al}\right.\\ &\quad\left.+x_{Cr}x_{Fe}M_{Fe}\right],\\ M_{Al,Al} &= x_{Al}\left[(1-x_{Al})^2M_{Al} + x_{Al}x_{Fe}M_{Fe}\right.\\ &\quad\left.+x_{Al}x_{Cr}M_{Cr}\right],\\ M_{Cr,Al} &= x_{Cr}x_{Al}\left[x_{Fe}M_{Fe} - (1-x_{Cr})M_{Cr}\right.\\ &\quad\left.-(1-x_{Al})M_{Al}\right],\end{aligned} \tag{8}$$

TABLE 1 Material parameters used in simulations.

Parameter	Dimension	Value	Ref.
(a_{Fe}, a_{Cr}, a_{Al})	nm	(0.286, 0.291, 0.405)	
G^0_{Fe}	J/mol	$1225.7 + 124.134T - 23.5143T\ln(T) - 0.439752\times10^{-2}T^2 - 0.589269\times10^{-7}T^3 + \frac{77358.5}{T}$	Dinsdale, (1991)
G^0_{Cr}	J/mol	$-8856.94 + 157.48T - 26.908T\ln(T) + 0.189435\times10^{-2}T^2 - 0.147721\times10^{-5}T^3 + \frac{139250}{T}$	Dinsdale, (1991)
G^0_{Al}	J/mol	$-1193.24 + 218.235446T - 38.5844296T\ln(T) + 0.018531982T^2 - 0.576227\times10^{-5}T^3 + \frac{74092}{T}$	Dinsdale, (1991)
$L_{Fe,Cr}$	J/mol	$20,500 - 9.68T$	Dinsdale, (1991)
$L_{Cr,Al}$	J/mol	$-54,900 + 10T$	Dinsdale, (1991)
$L_{Fe,Al}$	J/mol	$-122,452.9 + 31.6455T$	Dinsdale, (1991)
κ_d	J/m	6.91×10^{-9}	Yan et al. (2020)
$E^f_{i,Fe}$	eV	3.52	Terentyev et al. (2008)
$E^f_{v,Fe}$	eV	1.4	Kim and Buyers. (1978)
G^{coh}_{Fe}	J/mol	413,000	Kittel and McEuen. (2018)
$(C^{Fe}_{11}, C^{Fe}_{12}, C^{Fe}_{44})$	Pa	$(2.3310\cdot10^{11}, 1.3544\cdot10^{11}, 1.7830\cdot10^{11})$	Dieter and Bacon. (1976)
$E^f_{i,Cr}$	eV	3.356	Terentyev et al. (2010)
$E^f_{v,Cr}$	eV	1.36	Ogorodnikov et al. (1988)
G^{coh}_{Cr}	J/mol	395,000	Kittel and McEuen. (2018)
$(C^{Cr}_{11}, C^{Cr}_{12}, C^{Cr}_{44})$	Pa	$(3.500\cdot10^{11}, 0.678\cdot10^{11}, 1.008\cdot10^{11})$	Dieter and Bacon. (1976)
K_0, K_1	(Pa)	$\frac{1}{3}\left(C^{Fe}_{11}+2C^{Fe}_{12}\right),\quad \frac{1}{3}\left(C^{Cr}_{11}-C^{Fe}_{11}+2(C^{Cr}_{12}-C^{Fe}_{12})\right)$	
μ_{20}, μ_{21}	(Pa)	$\frac{1}{2}\left(C^{Fe}_{11}-C^{Fe}_{12}\right),\quad \frac{1}{2}\left(C^{Cr}_{11}-C^{Fe}_{11}-C^{Cr}_{12}+C^{Fe}_{12}\right)$	
μ_{30}, μ_{31}	(Pa)	$C^{Fe}_{44},\quad C^{Cr}_{44}-C^{Fe}_{44}$	
ξ^a_0, ξ^a_{01}		$\frac{C^{Fe}_{11}-C^{Fe}_{12}-2C^{Fe}_{44}}{C^{Fe}_{44}},\quad \frac{C^{Cr}_{11}-C^{Cr}_{12}-2C^{Cr}_{44}-[C^{Fe}_{11}-C^{Fe}_{12}-2C^{Fe}_{44}]}{C^{Fe}_{44}}$	
D_{Fe}	m^2/s	$2.8\times10^{-4}\exp(-251000/RT)$	Nagasaki. (2004)
D_{Cr}	m^2/s	$3.7\times10^{-3}\exp(-267000/RT)$	Nagasaki. (2004)
D_{Al}	m^2/s	$5.2\times10^{-4}\exp(-246000/RT)$	Nagasaki. (2004)
D_v	m^2/s	$3.84\times10^{-4}\exp(-300000/RT)$	Yan et al. (2020)
D_i	m^2/s	$2.05\times10^{-4}\exp(-280000/RT)$	Yan et al. (2020)

where M_{Fe}, M_{Al} and M_{Cr} are the corresponding mobilities for pure elements, which are defined in the standard manner: $M_\mu = D_\mu/RT$, D_μ is the corresponding atomic diffusivity. The mobility for the ensembles of vacancies and interstitials we choose in the standard manner: $L_d = D_d c_d/RT$, defined through the corresponding point defect diffusivity D_d. Here we use a simplified model for point defects mobilities.

In the Cahn-Hilliard-Cook equation Eq. 7 with a variable mobility Eq. 8, it is not convenient to accurately discretize the gradient operator and divergence operator by using the finite-difference method. However, the Fourier spectral method developed in Refs. (Chen and Shen, 1998; Zhu et al., 1999; Kim, 2007; Canuto et al., 2012; Biner, 2017) allows us to solve numerically Eq. 7 without much more difficulty than the case with a constant mobility. In the framework of the Fourier spectral method the system of coupled non-linear differential equations takes the form:

$$
\begin{aligned}
\partial_t x_{Cr}(\mathbf{k},t) &= i\mathbf{k}\cdot\left\{M_{Cr,Cr}\big|_{\mathbf{r}}\left[i\mathbf{k}\left(\frac{\delta\mathcal{G}}{\delta x_{Cr}}\Big|_{\mathbf{k}}\right)\right]_{\mathbf{r}} + M_{Cr,Al}\big|_{\mathbf{r}}\left[i\mathbf{k}\left(\frac{\delta\mathcal{G}}{\delta x_{Al}}\Big|_{\mathbf{k}}\right)\right]_{\mathbf{r}}\right\}_{\mathbf{k}},\\
\partial_t x_{Al}(\mathbf{k},t) &= i\mathbf{k}\cdot\left\{M_{Al,Al}\big|_{\mathbf{r}}\left[i\mathbf{k}\left(\frac{\delta\mathcal{G}}{\delta x_{Al}}\Big|_{\mathbf{k}}\right)\right]_{\mathbf{r}} + M_{Cr,Al}\big|_{\mathbf{r}}\left[i\mathbf{k}\left(\frac{\delta\mathcal{G}}{\delta x_{Cr}}\Big|_{\mathbf{k}}\right)\right]_{\mathbf{r}}\right\}_{\mathbf{k}},\\
\partial_t c_v(\mathbf{k},t) &= i\mathbf{k}\cdot\left\{L_v\big|_{\mathbf{r}}\left[i\mathbf{k}\left(\frac{\delta\mathcal{G}}{\delta c_v}\Big|_{\mathbf{k}}\right)\right]_{\mathbf{r}}\right\}_{\mathbf{k}},\\
\partial_t c_i(\mathbf{k},t) &= i\mathbf{k}\cdot\left\{L_i\big|_{\mathbf{r}}\left[i\mathbf{k}\left(\frac{\delta\mathcal{G}}{\delta c_i}\Big|_{\mathbf{k}}\right)\right]_{\mathbf{r}}\right\}_{\mathbf{k}}.
\end{aligned}
\tag{9}
$$

Here, $x_{Cr,Al}(\mathbf{k},t)$, $c_{v,i}(\mathbf{k},t)$, $\delta\mathcal{G}/\delta x_{Cr,Al}\big|_{\mathbf{k}}$ and $\delta\mathcal{G}/\delta c_{v,i}\big|_{\mathbf{k}}$ represent the Fourier transforms of $x_{Cr,Al}(\mathbf{r},t)$, $c_{v,i}(\mathbf{r},t)$, $\delta\mathcal{G}/\delta x_{Cr,Al}$ and $\delta\mathcal{G}/\delta c_{v,i}$

in **r**-space, respectively. **k** is the vector in the Fourier space with the magnitude $k = \sqrt{k_x^2 + k_y^2}$; $\{\}_{\mathbf{k}}$ is the Fourier transform and $[\,]_{\mathbf{r}}$ means the inverse Fourier transform to real space.

In further modeling, we use thermodynamic and elastic parameters characterizing ternary systems collected in **Table 1**.

3 Results and discussions

3.1 Stability diagram

In order to define ranges of concentrations of alloying additions Cr and Al and temperature, when phase decomposition is possible we exploit the linear stability analysis of a homogeneous state to inhomogeneous perturbations. According to obtained kinetic equations one can find phase diagram defining critical values of concentration of alloying elements at fixed temperatures shown in **Figure 1**. It follows that phase separation related to instability of the solid solution to inhomogeneous perturbations is possible at fixed range of Chromium and Aluminum concentrations. With the temperature growth the instability domain bounded by spinodal curves shrinks. Outside of the corresponding spinodal the system is stable to homogeneous perturbations. In this domains the solid solution is realized. It is clear from this diagram that in the case of high values of the annealing temperature (see, for example, the curve at $T = 850\ K$), when precipitation is impossible in the binary Fe-Cr systems, the addition of Aluminum with a concentration >2% induces such processes. At high temperatures (see curve at $T = 900\ K$) with the temperature increase phase decomposition related to formation of α'-precipitates enriched by Cr is possible only at elevated concentration of Al and with content of Cr around 50 at%.

3.2 Numerical analysis

To study process of phase decomposition at annealing numerically we choose values of nominal concentration of two alloying elements and fix the annealing temperature according to stability diagram. We take solid solution as initial microstructure of the corresponding alloy with homogeneously distributed concentration fields of all components including point defects. As initial configurations we use: $\langle x_\mu(0)\rangle = \overline{x}_\mu$, $\langle c_d(0)\rangle = c_d^{eq}$; $\langle (x_\mu(0) - \overline{x}_\mu)^2\rangle = 10^{-3}\overline{x}_\mu$, $\langle (c_d(0) - c_d^{eq})^2\rangle = 10^{-3}c_d^{eq}$, where c_d^{eq} relate to equilibrium point defect concentration. All simulations were done on square lattice $L \times L$ of the linear size $L = N\Delta x$ with N ($N = 128$) nodes in each direction and effective lattice constant for simulations $\Delta x = 1$ by exploiting Fourier spectral method (Chen and Shen, 1998; Zhu et al., 1999; Canuto et al., 2012; Biner, 2017). We take $\Delta t' = 10^{-3}$ as dimensionless time step of integration. Our simulations were done in dimensionless time $t' = t\ell^2/D_{Al}$, for spatial coordinate we use $\mathbf{r}' = \mathbf{r}/\ell$, where ℓ is of the lattice parameter a. Boundary conditions were periodic. We discuss dynamics of α'-phase formation and growth and analyze effect of alloying elements and annealing temperature onto main statistical properties of precipitates.

According to provided stability analysis in order to study α'-phase precipitation next we consider alloy $Fe - 30\%Cr - 5\%Al$ as a model system with annealing temperature $T = 710\ K$. The main indicator of phase separation is the growth of the dispersion of the concentration field, determined in the standard way: $\langle (\delta x_\mu)^2\rangle = \langle x_\mu^2\rangle - \langle x_\mu\rangle^2$. This quantity plays the role of an effective order parameter during phase decomposition. Indeed, if $\langle (\delta x_\mu)^2\rangle$ grows in time, it means that enriched and depleted domains of μ-component are formed and can be distinguished by concentration values, therefore phase decomposition occurs (García-Ojalvo and Sancho, 2012).

Typical scenario of phase decomposition is shown in **Figure 2**. Snapshots of the concentration field of Cr and Al are shown in **Figure 2A** at time instants related to markers indicated at protocols of effective order parameters in **Figure 2B**. Form **Figure 2A** it follows that after a certain incubation period ($t < t_c$) domains enriched and depleted in the concentration of impurities emerge from the initial homogeneous distribution (solid solution). Thus, after 22 h of annealing, fine Chromium precipitates can be observed. At the same time, Aluminum is homogeneously distributed in the matrix (outside the precipitates). The number of precipitates and their size increase with time. During this nucleation stage, all formed precipitates are characterized by almost the same size. With further annealing one passes to the coarsening stage, where precipitates continue to grow and interact with each other: small precipitates dissolve, while large ones take material from the matrix and continue to grow following Ostwald ripening scenario. Detailed analysis of α'-phase precipitation can be seen from protocols of the order parameters shown in **Figure 2B**. One finds that after a certain incubation period dispersion of both x_{Cr} and x_{Al} grow rapidly, meaning a passage to the nucleation stage. At the coarsening stage the growth rate of dispersions $\langle (\delta x_{Cr})^2\rangle$ and $\langle (\delta x_{Al})^2\rangle$ decreases, they continue to increase slowly and the system goes to a quasi-stationary regime. Here the total amount of precipitates decreases with time, and the dispersion in their sizes increases.

Results of statistical analysis of precipitation are shown in **Figure 3**. Protocols for the Chromium concentration in the α'-phase and the volume fraction of precipitates are shown in **Figure 3A**. Both values grow rapidly after the incubation period t_c at the nucleation stage whilst their slow growth is observed at coarsening stage. At the physical time of ~230 hours almost 70% of Chromium is concentrated in the α'-phase, whilst the volume fraction of precipitates is about 20%. Obtained data relate well to experimental observations and results of numerical modeling Yang et al. (2020), Chen et al. (2019), Lee et al.

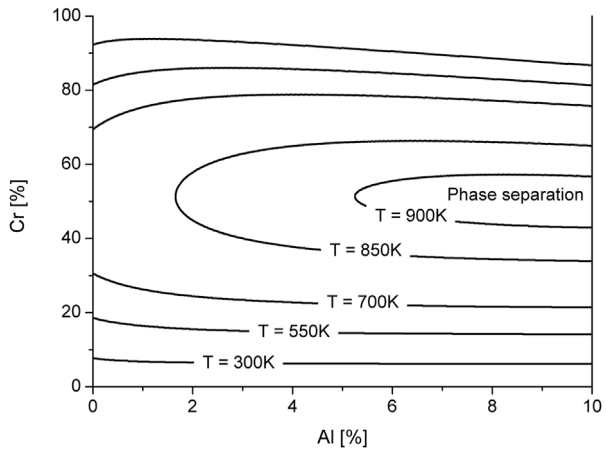

FIGURE 1
Phase diagram of the alloy $Fe - Cr - Al$ at different values of the annealing temperature.

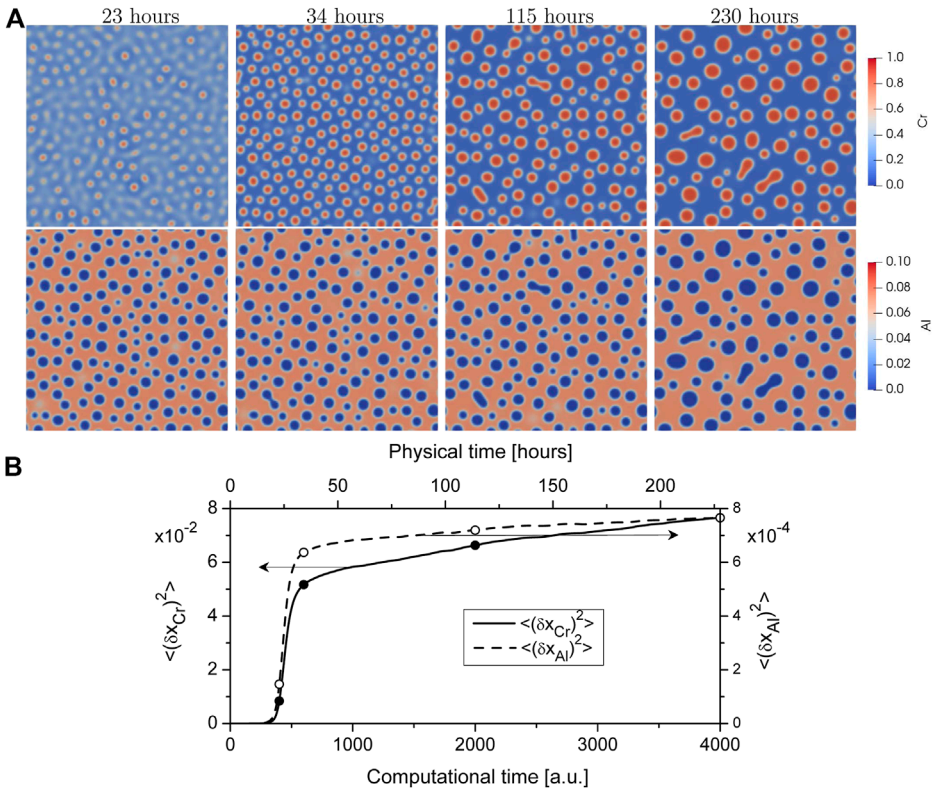

FIGURE 2
(color online) Snapshots of the microstructure evolution **(A)** and dynamics of the order parameters $\langle(\delta x_{Cr})^2\rangle$ and $\langle(\delta x_{Al})^2\rangle$ **(B)** during thermal treatment of the solid solution $Fe-30\%Cr-5\%Al$ at $T=710\ K$.

(2020). **Figure 3B** illustrates dynamics of the mean precipitate radius and their number density recalculated from obtained data. It can be seen that the number of precipitates and their mean radius rapidly increase with time at the nucleation stage. At the coarsening stage the mean precipitate size (radius) $\langle R_p\rangle$ increases according to the power-law $\langle R_p\rangle \propto t^n$ with the exponent n close to the classical Lifshits-Slyozov-Wagner (LSW) value 1/3; the total amount of precipitates at this stage decreases exponentially (see power-law and exponential decay fitting shown by dash and dash-dot lines, with fitting parameter τ). Data obtained for the mean precipitate size (around 1–1.2 nm at annealing time 300 h) and precipitate number density ($1.5\times10^{19} cm^{-3}$) for the studied alloy relate well to experimental and numerical data for class of system related to Fe-Cr-Al alloys (Messoloras et al., 1984; Chen et al., 2019; Lee et al., 2020; Yang et al., 2020). Scaling dynamics of mean precipitate size in Fe-Cr alloys was observed experimentally [see, for example, Refs. (Brenner et al., 1982; Messoloras et al., 1984; Bley, 1992; Hyde et al., 1995; Soriano-Vargas et al., 2010)], where the scaling exponent n depends on the nominal composition and annealing temperature.

Size distribution α'-phase precipitates $f(R_p/\langle R_p\rangle)$ is shown in **Figure 3C** at different time instants by markers. It can be seen that data obtained from the numerical experiment at different times relate to each other meaning an universality of the size distribution of precipitate sizes at the coarsening stage. The solid curve shows the classical universal LSW distribution (Lifshitz and Slyozov, 1961; Wagner, 1961). The obtained numerical data are in good agreement with the LSW distribution. Hence, LSW theory can be used to predicate particle size distribution in Fe-Cr-Al systems at thermal treatment.

Let us consider a behavior of defect subsystem during precipitation. From **Figure 4A** it follows that the dispersion of the vacancy concentration decreases with time, while the dispersion of the concentration of interstitials slowly increase after the decreasing. Spatial rearrangement of point defects is well seen from snapshots in **Figure 4A** (see insets). Here vacancies are quasi-homogeneously distributed in a bulk, while interstitials are mostly localized in small precipitates ($R_p < \langle R_p\rangle$) and near the phase interface in large precipitates ($R_p > \langle R_p\rangle$). Detailed information about defect distribution around precipitates can be found in profiles of alloying elements and defects shown in **Figure 4B**. Here one finds the following: the interstitial concentration is higher in precipitates compared to its value in the matrix phase; they are mostly localized at regions of precipitates with elevated curvature (see the snapshot of $c_i(\mathbf{r})$ in **Figure 4A**); vacancy concentration is locally increased around interfaces and has lower values in precipitates comparing to their values in matrix that relates to thermodynamics; α'-phase precipitates contain extremely small amount of Al atoms comparing to matrix phase.

By studying phase decomposition of alloys with different content of alloying elements and different temperatures one finds that an increase in one of the component can control time scale for precipitation kinetics. By studying α'-phase precipitation it was found that the incubation time t_c for precipitation decreases with content of Cr and Al as is shown in **Figures 5A, B**. Here we denote critical value

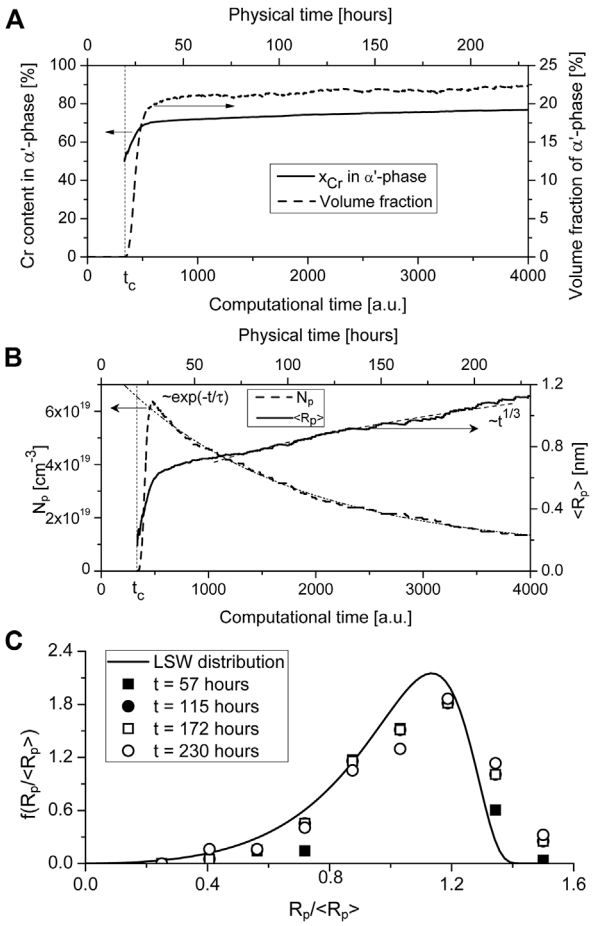

FIGURE 3
Evolution of **(A)** the Chromium concentration in the α'-phase and the volume fraction of the α'-phase precipitates and **(B)** the average size (radius) of the α'-phase precipitates and their number density; **(C)** distribution of α'-phase precipitates over size at different time instants during annealing of the solid solution *Fe – 30%Cr – 5%Al* at $T = 710$ *K*, solid line relates to LSW distribution.

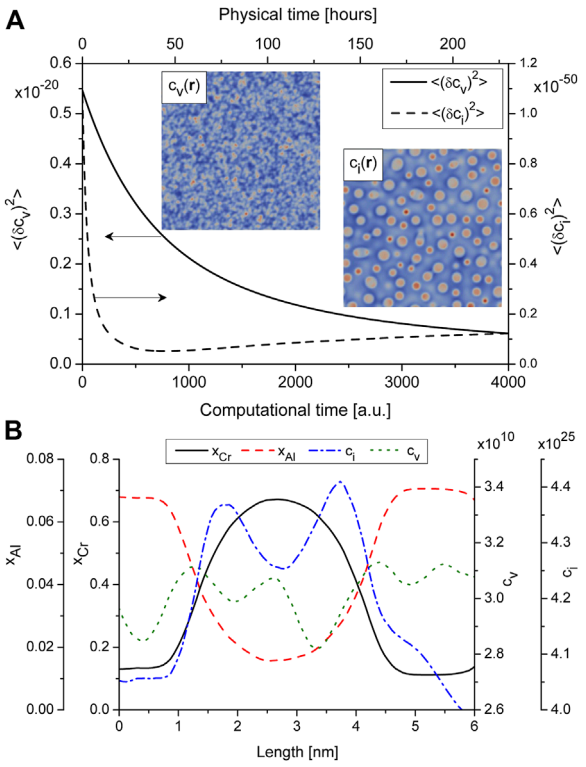

FIGURE 4
(A) (color online) Dynamics of the order parameters $\langle(\delta c_i)^2\rangle$ and $\langle(\delta c_v)^2\rangle$ at annealing of the solid solution *Fe – 30%Cr – 5%Al* at $T = 710$ *K*. In the snapshots of point defects distribution (obtained at $t = 230$ h) c_i varies from 3.6×10^{-25} (blue) to 5.9×10^{-25} (red) and c_v varies from 2.6×10^{-10} (blue) to 4.4×10^{-10} (red). **(B)** Profiles of concentration of alloying elements (solid line for Cr, dash line for Al) and point defects (dash-dot and dot lines for interstitials and vacancies, respectively) (obtained at $t = 230$ h).

for concentration of alloying elements as $x^c_{Cr,Al}$ (from phase diagram in **Figure 1**). It means that an increase in alloying element content accelerates driven forces for phase decomposition decreasing the incubation time t_c needed for emergence of precipitates. From theory of phase decomposition it is known that the quantity t_c depends on the annealing temperature (Khachaturyan, 2013). The corresponding dependence is shown in **Figure 5C** for the Fe-30%Cr-5%Al system (as an example), where one gets an infinite time needed to initiate phase decomposition in the vicinity of the critical temperature related to spinodal depicted in the phase diagram in **Figure 1**.

Effect of alloying elements and temperature influence onto dynamics of mean precipitate size, volume fraction of precipitates and precipitate size distribution is shown in **Figure 6**. In **Figures 6A, B** we plot the corresponding protocols in physical time scale according to the time related to phase decomposition starting from t_c. From obtained results it follows that an increase Al content results in slight increase in precipitate size and volume fraction (cf. curves 1 and 2), whereas Cr addition increases the corresponding values of above quantities crucially (cf. curves 1 and 3). These results are related well to previous studies [see for example, Ref. (Lee et al., 2020)]. With the temperature decrease from 710 *K* down to 690 *K* (cf. curves 1 and 4) one gets low values of the mean precipitate size and low values for volume fraction of α' precipitates that is constituent with results discussed in Ref. (Chen et al., 2019). Distributions over precipitate size in alloys with different content of Al and Cr and two different temperatures are shown in **Figure 6C**. One finds that obtained data are well predicted by classical LSW distribution. Therefore, it follows that additional introduction of Cr or Al does not change universality of precipitate size distribution at coarsening stage at different temperatures. By comparing dynamics of the precipitate size and precipitate size distributions in alloys with different content of doping one concludes that both dynamics of the system and statistical properties of growing precipitates remain universal. The difference in measured quantities (mean precipitate size, precipitate number density, precipitate volume fraction) is related mostly to scaling factors determined by nominal composition of the studied alloys.

4 Discussions

We need to stress out that the used model for microstructure transformations in Fe-Cr-Al alloy is based on equilibrium CALPHAD

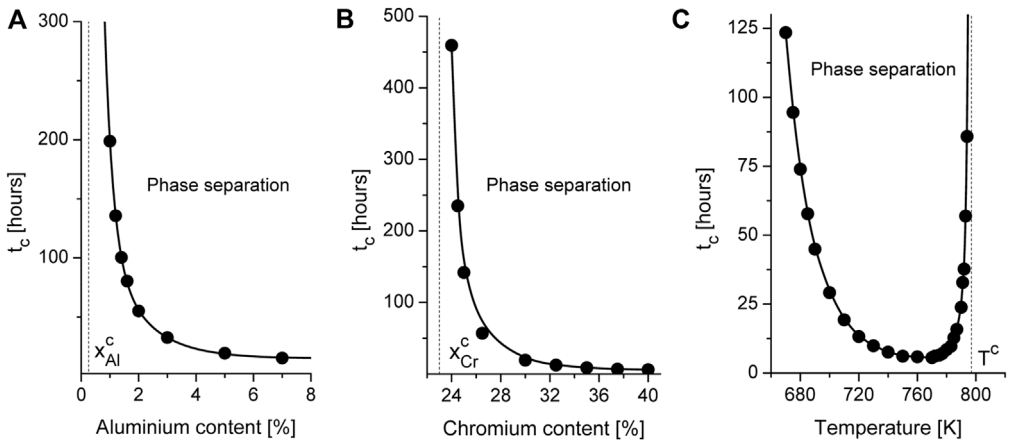

FIGURE 5
Dynamical diagram of phase decomposition at $T = 710\ K$ at fixed content of Cr ($x^0_{Cr} = 0.3$) — plot a and fixed content of Al ($x^0_{Al} = 0.05$) — plot b, dynamical diagram for Fe–30%Cr–5%Al.

free energy, however Aluminum and Chromium concentrations will be out of thermal equilibrium at cooling. Therefore, to describe more precisely free energy in metastable zone one should further incorporate corrections to the free energy related to non-equilibrium states. At the same time this generalization will not affect the final state related to equilibrium as was shown in previous studies (Chen et al., 2019; Lee et al., 2020).

In our study concentration-dependent model for stiffness constant was used for solid systems with cubic symmetry. Obtained results relate well to most of experimental observations. However, for more precise description of the system dynamics the measurement of the interface thickness obtained experimentally allows one to fix the corresponding values and thus the space scale.

For the considered class of concentrated alloys there is no formal theory for the mobilities exploited in the present study. Therefore here the model assumptions for concentration-dependent mobilities were used on the basis of previous works (Huang et al., 1995; Wu et al., 2001; Wu et al., 2004; Lee et al., 2020). This approach allows one to study transient dynamics of phase decomposition process in details, and can play a significant effect on the coarsening kinetics (Lacasta et al., 1992; Lacasta et al., 1993; Bray and Emmott, 1995; Zhu et al., 1999; Kharchenko and Dvornichenko, 2008; Kharchenko and Kharchenko, 2014; Kharchenko et al., 2022). A constant mobility model can be used in order to modeling the late time microstructure.

Nevertheless used in the present study assumptions and simplifications do not affect significantly the obtained results related well to most of experimental and theoretical predictions (Messoloras et al., 1984; Chen et al., 2019; Lee et al., 2020; Yang et al., 2020).

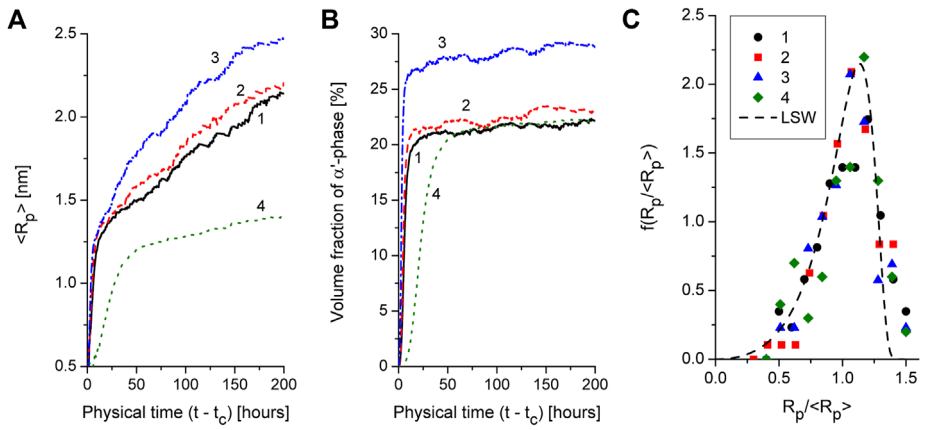

FIGURE 6
Protocols of the mean precipitate size (plot a) and volume fraction of α'-phase precipitates (plot b) at different content of Cr, Al and different temperatures: Line 1 — Fe-30%Cr-5%Al, $T = 710\ K$, line 2 — Fe–30%Cr–7%Al, $T = 710\ K$, line 3 — Fe–35%Cr–5%Al, $T = 710\ K$, line 4 — Fe–30%Cr–5%Al, $T = 690\ K$. Precipitate size distributions for different alloys and different temperatures (markers 1–4 relate to lines 1–4 in plots a and b) at coarsening stage ($t - t_c = 200\ h$), dash line relates to LSW distribution.

5 Conclusion

We have developed a phase field model to study dynamics of microstructure transformations and the evolution of defect structure during heat treatment of Fe-Cr-Al systems. Statistical and kinetic properties of evolving microstructure and defect structure in alloys with different content of alloying elements and different temperatures were studied.

In the framework of the stability analysis we obtain a phase diagram illustrating the range of concentrations of Chromium/Aluminum and annealing temperature when phase separation in Fe-Cr-Al systems accompanied by α'-phase precipitation can be realized. We exploited numerical simulations to discuss dynamics of precipitates formation, their growth, evolution of their number densities, precipitate mean size, and point defects rearrangement at precipitation. It is shown that mean precipitate size grows according to the power-law, whereas precipitate number density manifests exponential decay at coarsening stage. Precipitate size distribution function is of universal character.

It is shown that addition of Aluminum up to 8% initiates phase decomposition decreasing the incubation time for development of concentration waves. It slightly increases the mean precipitate size and volume fraction of precipitates. An increase in the nominal concentration of Chromium from 24% up to 40% increases content of Cr inside precipitates and essentially increases precipitate size with their volume fraction and accelerates phase decomposition processes. Dynamics of growing precipitates and the corresponding distribution functions over precipitate size manifest universality with scaling factors depending on the nominal compositions of alloys.

It was found that the annealing at elevated temperatures results in a decrease in the precipitates number density and in an increase their size. It was found that at high and low temperatures, precipitation processes are slowed down compared to the case of moderate temperatures.

By studying kinetics of equilibrium point defects it was shown that during annealing of solid solution vacancies are mostly homogeneously distributed in a bulk, while interstitial atoms are mostly localized in small α' precipitates and inside large precipitates near the interfaces with large curvature.

We expect that obtained results can be used to predict materials properties change at different content of alloying elements and will be useful as basic data for microstructure optimization of Fe-Cr-Al fuel cladding. Results can be used to describe radiation induced effects by incorporating ballistic mixing and dynamics of non-equilibrium defects produced by irradiation.

Data availability statement

The original contributions presented in the study are included in the article/supplementary material, further inquiries can be directed to the corresponding author.

Author contributions

LW: Conceptualization, validation. JQ: Funding acquisition, project administration, investigation. VK: Methodology, software development, simulation, writing—original draft. DK: Investigation, statistical analysis, writing—review and editing. OL: Resources, visualization, validation.

Funding

This work was supported by "National Key R&D Program of China," project number 2018YFE0207400.

Conflict of interest

The authors declare that the research was conducted in the absence of any commercial or financial relationships that could be construed as a potential conflict of interest.

Publisher's note

All claims expressed in this article are solely those of the authors and do not necessarily represent those of their affiliated organizations, or those of the publisher, the editors and the reviewers. Any product that may be evaluated in this article, or claim that may be made by its manufacturer, is not guaranteed or endorsed by the publisher.

References

Biner, S. B. (2017). *Programming phase-field modeling*. Switzerland: Springer International Publishing.

Bley, F. (1992). Neutron small-angle scattering study of unmixing in fe-cr alloys. *Acta metallurgica materialia* 40, 1505–1517. doi:10.1016/0956-7151(92)90094-u

Bray, A., and Emmott, C. (1995). Lifshitz-slyozov scaling for late-stage coarsening with an order-parameter-dependent mobility. *Phys. Rev. B* 52, R685–R688. doi:10.1103/physrevb.52.r685

Brenner, S., Miller, M., and Soffa, W. (1982). Spinodal decomposition of iron-32 at.% chromium at 470 c. *Scr. Metall.* 16, 831–836. doi:10.1016/0036-9748(82)90239-3

Cahn, J. W. (1961). On spinodal decomposition. *Acta metall.* 9, 795–801. doi:10.1016/0001-6160(61)90182-1

Cahn, J. W. (1962). On spinodal decomposition in cubic crystals. *Acta metall.* 10, 179–183. doi:10.1016/0001-6160(62)90114-1

Canuto, C., Hussaini, M. Y., Quarteroni, A., and Thomas, A.Jr (2012). *Spectral methods in fluid dynamics*. Berlin, Heidelberg: Springer Science & Business Media.

Chang, K., Meng, F., Ge, F., Zhao, G., Du, S., and Huang, F. (2019). Theory-guided bottom-up design of the fecral alloys as accident tolerant fuel cladding materials. *J. Nucl. Mater.* 516, 63–72. doi:10.1016/j.jnucmat.2019.01.002

Chen, L. Q., and Shen, J. (1998). Applications of semi-implicit Fourier-spectral method to phase field equations. *Comput. Phys. Commun.* 108, 147–158. doi:10.1016/s0010-4655(97)00115-x

Chen, S., Li, Y., Shi, S., and Jin, S. (2019). Quantitative phase-field simulation of composition partition and separation kinetics of nanoscale phase in fe-cr-al alloy. *J. Nanomater.* 2019, 1–11. doi:10.1155/2019/6862390

Dai, H., Yu, M., Dong, Y., Setyawan, W., Gao, N., and Wang, X. (2022). Effect of cr and al on elastic constants of fecral alloys investigated by molecular dynamics method. *Metals* 12, 558. doi:10.3390/met12040558

Dieter, G. E., and Bacon, D. (1976). *Mechanical metallurgy*. New York: McGraw-Hill.

Dinsdale, A. T. (1991). Sgte data for pure elements. *Calphad* 15, 317–425. doi:10.1016/0364-5916(91)90030-n

Ejenstam, J., Thuvander, M., Olsson, P., Rave, F., and Szakalos, P. (2015). Microstructural stability of fe–cr–al alloys at 450–550 c. *J. Nucl. Mater.* 457, 291–297. doi:10.1016/j.jnucmat.2014.11.101

García-Ojalvo, J., and Sancho, J. (2012). *Noise in spatially extended systems*. New York, NY: Springer Science & Business Media.

Gulbransen, E. A., and Andrew, K. F. (1959). Oxidation studies on the iron-chromium-aluminum heater alloys. *J. Electrochem. Soc.* 106, 294. doi:10.1149/1.2427333

Hilliard, J. E. (1970). *Spinodal Decomposition, in Phase Transformations*. American Society of Metals, Metals Park, 497.

Huang, C., de La Cruz, M. O., and Swift, B. (1995). Phase separation of ternary mixtures: Symmetric polymer blends. *Macromolecules* 28, 7996–8005. doi:10.1021/ma00128a005

Hyde, J., Miller, M., Hetherington, M., Cerezo, A., Smith, G., and Elliott, C. (1995). Spinodal decomposition in fe-cr alloys: Experimental study at the atomic level and comparison with computer models-ii. development of domain size and composition amplitude. *Acta metallurgica materialia* 43, 3403–3413. doi:10.1016/0956-7151(95)00041-s

Khachaturyan, A. G. (2013). *Theory of structural transformations in solids*. New York, NY: Dover Publications, Inc.,.

Kharchenko, D., and Dvornichenko, A. (2008). Phase separation in binary systems with internal multiplicative noise. *Phys. A Stat. Mech. its Appl.* 387, 5342–5354. doi:10.1016/j.physa.2008.05.041

Kharchenko, V. O., and Kharchenko, D. O. (2014). Abnormal grain growth in nonequilibrium systems: Effects of point defect patterning. *Phys. Rev. E* 89, 042133. doi:10.1103/physreve.89.042133

Kharchenko, V., Xin, T., Wu, L., Kharchenko, D., Kupriienko, V., and Shuda, I. (2022). Phase stability and precipitation modeling in neutron irradiated zr–2% nb alloy. *Model. Simul. Mater. Sci. Eng.* 30, 075006. doi:10.1088/1361-651x/ac8fad

Kim, J. (2007). A numerical method for the Cahn–Hilliard equation with a variable mobility. *Commun. Nonlinear Sci. Numer. Simul.* 12, 1560–1571. doi:10.1016/j.cnsns.2006.02.010

Kim, S., and Buyers, W. (1978). Vacancy formation energy in iron by positron annihilation. *J. Phys. F Metal Phys.* 8, L103–L108. doi:10.1088/0305-4608/8/5/001

Kittel, C., and McEuen, P. (2018). *Introduction to solid state physics* Global ed., 9th ed. New Jersey: Wiley, 692.

Kobayashi, S., and Takasugi, T. (2010). Mapping of 475 c embrittlement in ferritic fe–cr–al alloys. *Scr. Mater.* 63, 1104–1107. doi:10.1016/j.scriptamat.2010.08.015

Kresse, G., and Furthmüller, J. (1996). Efficient iterative schemes for *ab initio* total-energy calculations using a plane-wave basis set. *Phys. Rev. B* 54, 11169–11186. doi:10.1103/physrevb.54.11169

Kresse, G., and Hafner, J. (1993). *Ab initio* molecular dynamics for liquid metals. *Phys. Rev. B* 47, 558–561. doi:10.1103/physrevb.47.558

Kresse, G., and Hafner, J. (1994). Norm-conserving and ultrasoft pseudopotentials for first-row and transition elements. *J. Phys. Condens. Matter* 6, 8245–8257. doi:10.1088/0953-8984/6/40/015

Lacasta, A., Hernández-Machado, A., Sancho, J. M., and Toral, R. (1992). Domain growth in binary mixtures at low temperatures. *Phys. Rev. B* 45, 5276–5281. doi:10.1103/physrevb.45.5276

Lacasta, A., Sancho, J. M., Herna, A., and Toral, R. (1993). Effects of domain morphology in phase-separation dynamics at low temperature. *Phys. Rev. B* 48, 6854–6857. doi:10.1103/physrevb.48.6854

Lee, J., Park, K., and Chang, K. (2020). Effect of al concentration on the microstructural evolution of fe-cr-al systems: A phase-field approach. *Metals* 11, 4. doi:10.3390/met11010004

Li, W., Lu, S., Hu, Q. M., Mao, H., Johansson, B., and Vitos, L. (2013). The effect of al on the 475 c embrittlement of fe–cr alloys. *Comput. Mater. Sci.* 74, 101–106. doi:10.1016/j.commatsci.2013.03.021

Liang, L., Mei, Z. G., Kim, Y. S., Anitescu, M., and Yacout, A. M. (2018). Three-dimensional phase-field simulations of intragranular gas bubble evolution in irradiated u-mo fuel. *Comput. Mater. Sci.* 145, 86–95. doi:10.1016/j.commatsci.2017.12.061

Lifshitz, I. M., and Slyozov, V. V. (1961). The kinetics of precipitation from supersaturated solid solutions. *J. Phys. Chem. solids* 19, 35–50. doi:10.1016/0022-3697(61)90054-3

Mathon, M., De Carlan, Y., Geoffroy, G., Averty, X., Alamo, A., and De Novion, C. (2003). A sans investigation of the irradiation-enhanced α–α' phases separation in 7–12 cr martensitic steels. *J. Nucl. Mater.* 312, 236–248. doi:10.1016/s0022-3115(02)01630-6

Messoloras, S., Pike, B., Stewart, R., and Windsor, C. (1984). Precipitation in iron–chromium–aluminium alloys. *Metal Sci.* 18, 311–321. doi:10.1179/030634584790419999

Nagasaki, S. (2004). *Metals data book*. Tokyo: Japan Institute of Metals.

Ogorodnikov, V., Rakitskii, A., and Rogovoi, Y. I. (1988). Calculation of the vacancy formation energy of metals. *Sov. Powder Metall. Mater. Ceram.(Engl. Transl.)* 27, 55–60. doi:10.1007/bf00799739

Onuki, A. (2002). *Phase transition dynamics*. Cambridge: Cambridge University Press.

Qu, H., Lang, Y., Yao, C., Chen, H., and Yang, C. (2013). The effect of heat treatment on recrystallized microstructure, precipitation and ductility of hot-rolled fe–cr–al–rem ferritic stainless steel sheets. *Mater. Sci. Eng. A* 562, 9–16. doi:10.1016/j.msea.2012.11.008

Ribis, J., and Lozano-Perez, S. (2012). Orientation relationships and interface structure of α'-cr nanoclusters embedded in α-fe matrix after $\alpha - -\alpha'$ demixing in neutron irradiated oxide dispersion strengthened material. *Mater. Lett.* 74, 143–146. doi:10.1016/j.matlet.2012.01.115

Soriano-Vargas, O., Avila-Davila, E. O., Lopez-Hirata, V. M., Cayetano-Castro, N., and Gonzalez-Velazquez, J. L. (2010). Effect of spinodal decomposition on the mechanical behavior of fe–cr alloys. *Mater. Sci. Eng. A* 527, 2910–2914. doi:10.1016/j.msea.2010.01.020

Stott, F., Wood, G., and Stringer, J. (1995). The influence of alloying elements on the development and maintenance of protective scales. *Oxid. metals* 44, 113–145. doi:10.1007/bf01046725

Terentyev, D., Hafez Haghighat, S., and Schäublin, R. (2010). Strengthening due to cr-rich precipitates in fe–cr alloys: Effect of temperature and precipitate composition. *J. Appl. Phys.* 107, 061806. doi:10.1063/1.3340522

Terentyev, D., Olsson, P., Klaver, T., and Malerba, L. (2008). On the migration and trapping of single self-interstitial atoms in dilute and concentrated fe–cr alloys: Atomistic study and comparison with resistivity recovery experiments. *Comput. Mater. Sci.* 43, 1183–1192. doi:10.1016/j.commatsci.2008.03.013

Wagner, C. (1961). Theorie der Alterung von Niederschlägen durch Umlösen (Ostwald-Reifung). *Z. Elektrochem* 65, 581–591. doi:10.1002/bbpc.19610650704

Was, G. S. (2016). *Fundamentals of radiation materials science: Metals and alloys*. Berlin, Heidelberg, New York: Springer.

Wu, K., Morral, J., and Wang, Y. (2001). A phase field study of microstructural changes due to the kirkendall effect in two-phase diffusion couples. *Acta mater.* 49, 3401–3408. doi:10.1016/s1359-6454(01)00257-9

Wu, K., Morral, J., and Wang, Y. (2004). Movement of kirkendall markers, second phase particles and the type 0 boundary in two-phase diffusion couple simulations. *Acta mater.* 52, 1917–1925. doi:10.1016/j.actamat.2003.12.031

Wukusick, C. S., and Collins, J. F. (1964). An iron-chromium-aluminum alloy containing yttrium. *Mat. Res. std.* 4 (1964), 637.

Yamamoto, Y., Pint, B., Terrani, K., Field, K., Yang, Y., and Snead, L. (2015). Development and property evaluation of nuclear grade wrought fecral fuel cladding for light water reactors. *J. Nucl. Mater.* 467, 703–716. doi:10.1016/j.jnucmat.2015.10.019

Yan, Z., Shi, S., Li, Y., Chen, J., and Maqbool, S. (2020). Vacancy and interstitial atom evolution with the separation of the nanoscale phase in fe–cr alloys: Phase-field simulations. *Phys. Chem. Chem. Phys.* 22, 3611–3619. doi:10.1039/c9cp06247e

Yang, Z., Wang, Z., Xia, C., Ouyang, M., Peng, J., Zhang, H., et al. (2020). Aluminum suppression of α precipitate in model fe–cr–al alloys during long-term aging at 475 c. *Mater. Sci. Eng. A* 772, 138714. doi:10.1016/j.msea.2019.138714

Zhu, J., Chen, L. Q., Shen, J., and Tikare, V. (1999). Coarsening kinetics from a variable-mobility Cahn-Hilliard equation: Application of a semi-implicit Fourier spectral method. *Phys. Rev. E* 60, 3564–3572. doi:10.1103/physreve.60.3564

frontiers | Frontiers in Energy Research

TYPE Methods
PUBLISHED 09 February 2023
DOI 10.3389/fenrg.2023.1123714

OPEN ACCESS

EDITED BY
Jingang Liang,
Tsinghua University, China

REVIEWED BY
Kun Zhuang,
Nanjing University of Aeronautics and Astronautics, China
Xiang Wang,
Harbin Engineering University, China
Wenbin Wu,
Sun Yat-sen University, China

*CORRESPONDENCE
Bin Zhang,
jsszwtzb@163.com

SPECIALTY SECTION
This article was submitted to Nuclear Energy,
a section of the journal
Frontiers in Energy Research

RECEIVED 14 December 2022
ACCEPTED 30 January 2023
PUBLISHED 09 February 2023

CITATION
Wang L, Zhang B, Lu D, Zhao C and Liu J (2023), FSAR: Full neutron spectrum code for advanced reactor simulation.
Front. Energy Res. 11:1123714.
doi: 10.3389/fenrg.2023.1123714

FSAR: Full neutron spectrum code for advanced reactor simulation

Lianjie Wang, Bin Zhang*, Di Lu, Chen Zhao and Jiayi Liu

Science and Technology on Reactor System Design Technology Laboratory, Nuclear Power Institute of China, Chengdu, China

The full neutron spectrum code for advanced reactor simulation named FSAR has recently been developed at Nuclear Power Institute of China in order to meet the requirements of advanced reactor with large neutron energy range. Based on the two-step calculation scheme, FSAR consists of two-dimensional lattice calculation code and core calculation code. In two-dimensional lattice calculation, the subgroup method with ultrafine energy groups was implemented in the two-dimensional resonance self-shielding by incorporating the MOC to get the accurate self-shielded cross-section. For better consideration of the strong space coupling in different geometric sizes due to different mean free path of neutrons, the super-homogenization method and the leakage model were applied. In the core calculation, the discrete-ordinate method and micro burnup calculation method were used to simulate the core neutron transport and depletion. Preliminary calculation results showed that for the problems with wide spectrum, the self-shielded cross-sections have a good agreement with the Monte Carlo solution. The results shown in this paper indicate that FSAR has good performances of the cross-section generation in full neutron spectrum problem simulation.

KEYWORDS

full neutron spectrum, advanced reactor, two-dimensional lattice calculation, self-shielded cross-section, core simulation

1 Introduction

The research and development of advanced reactors has been pushed globally in recent decade (Wu, 2016) and promotes the development of reactor physics codes (Lee and Yang, 2017; Zhang and Yang, 2020). The neutron spectrum is complicate for some new reactors, especially for the special-use ones. In order to meet the requirements of the advanced reactors, it is necessary to develop the reactor analysis code with full neutron spectrum adapt ability.

At present, there are two main kinds of calculation methods for the reactor core simulation. First is the one-step calculation method (Rachamin and Kliem, 2017), which is used to simulate the core directly with as few approximations as possible. The other one is the two-step calculation method which is based on the homogenization techniques (Zhang et al., 2016). For the whole core physics simulation, the computational cost of one-step calculation with fully detailed description is too expensive using either stochastic (Wang et al., 2015) or deterministic method (Downar et al., 2016) even with the currently most advanced computing powers. So even though one-step calculation method has a lot of advantages, the dominant method for fast core simulation is the two-step scheme.

In the two-step scheme, deterministic procedures are currently the most widely used simulation methods. Compared to the traditional PWR codes, the fast reactor codes are easier to be extended for more complicated reactor design benefiting from their features of

ultrafine group cross-sections, full core transport calculation, etc. However, there are several limits of the current fast reactor codes when they are applied in the full neutron spectrum cases. The first one is the accurate heterogeneity effect estimation in complex geometries coming with wider spectral range. The long mean free path of neutrons makes the local heterogeneity effect of typical fast reactors less important, thus the equivalent homogeneous models and one-dimensional models are accurate enough for the conventional fast reactor subassemblies (Allen et al., 2011). What's more, the highly heterogeneous design has been considered as a breakthrough in the special-use advanced reactors, such as the axially heterogeneous fuel assembly design of the sodium fast reactor prototype ASTRID CFV concept (Faure et al., 2018). The homogeneous models of the conventional two-step approach are no longer applicable.

The resonance self-shielding effect is another important element. In reactor lattice analysis, the aim of resonance self-shielding calculation is to estimate the group-averaged cross-sections for solution of the core multi-group transport equation. The accuracy of the group parameters determines the precision of the core calculation. In the fast reactor analysis code, the method proposed by T. Tone (Tone, 1975) is a popular method to evaluate the self-shielded cross-sections with a set of group collision probability matrixes based on the isotope-dependent background cross-sections. Due to the calculation burden of CP matrixes, Tone's method implemented in the one-dimensional geometry shows nearly equivalent precision for the effective multiplication factor and reaction rate calculation compared to the subgroup method (Mao and Zmijarevic, 2017). However, in order to meet the needs of resonance self-shielding treatment of assemblies with more complex geometries and more larger energy range, the resonance self-shielding treatment model incorporated with the two-dimensional transport calculation method should be researched for better geometric adaptability and higher efficiency.

In this paper, an overview of the Full neutron Spectrum code for Advanced Reactor simulation named FSAR is provided which is developed by Nuclear Power Institute of China (NPIC), China National Nuclear Corporation (CNNC). The important modules and their models contained in FSAR are introduced in Section 2. Section 3 gives the preliminary calculation results of the problems with different spectrum. Section 4 summarizes this paper.

2 Models in FSAR code

The deterministic two-step calculation strategy based on the homogenization theory is utilized in FSAR to perform the reactor core neutronics analysis. Firstly, the two-dimensional lattice calculation is performed. The two-dimensional method of characteristics (Song et al., 2020a) solver in hexagonal geometry for neutron transport calculation and the subgroup method with ultrafine groups for self-shielding calculation are utilized. For the typical assemblies, ultrafine-group cross-sections and neutron flux will be determined and the few-group homogenized micro cross-sections will be collapsed based on the flux-volume weight method and the principle of conservation of reaction rate.

The second step is the core simulation, which is to simulate core neutron behaviors based on the neutron transport solvers and micro burnup calculation. The discrete-ordinate method is utilized to carry out the neutron transport calculation, and the Chebyshev rational approximation method is used to compute the exponential of the burnup matrix.

2.1 Lattice calculation

In two-dimensional lattice calculation, the subgroup method with ultrafine groups was implemented in the two-dimensional resonance self-shielding by incorporating MOC to get the accurate self-shielded cross-sections. In FSAR, the number of the ultrafine energy group is 2164 and that of subgroups is determined according to the change amplitude of the cross section (maximum is three groups). For the heterogeneous system, the neutron source term is assumed to be isotropic and the steady Boltzmann transport equation shows as follows:

$$\vec{\Omega} \cdot \nabla \phi(\vec{r}, E) + \Sigma_t(\vec{r}, E)\phi(\vec{r}, E) = Q(\vec{r}, E) \tag{1}$$

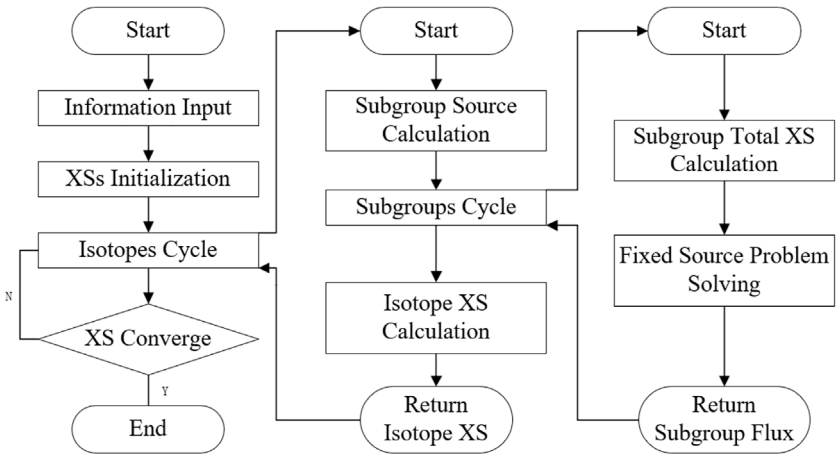

FIGURE 1
Resonance calculation flow chart.

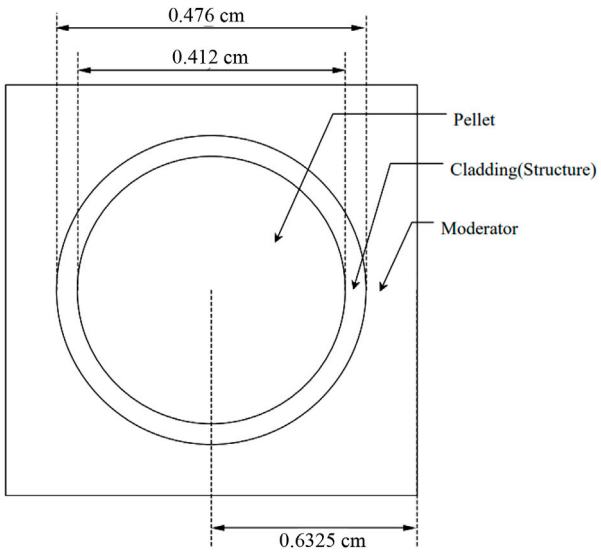

FIGURE 2
Geometry of thermal spectrum problem.

where Q is the neutron source. Based on the treatments of the neutron source, the subgroup method can be divided into the statistical model and the fixed source model (Takeda et al., 1991).

In the statistical model, the probability that the neutron source in group g lies in the subgroup sg is equal to the subgroup probability of sg. The corresponding subgroup transport equation is simplified as follow:

$$\vec{\Omega}\cdot\nabla\phi_{sg,g}(\vec{r})+\Sigma_{t,sg,g}(\vec{r})\phi_{sg,g}(\vec{r})=Q_{sg,g}(\vec{r})=p_{sg,g}Q_g(\vec{r}) \quad (2)$$

where $p_{sg,g}$ is the subgroup probability of sg. The neutron source term Q includes scattering source and fission source and the detail flux spectrum is required for the calculation of the scattering source and the fission source. In this way, the resonance calculation and the transport calculation are coupled together in the statistical model and completed in one time.

In the fixed source model, the narrow resonance approximation is implemented, the corresponding subgroup transport is simplified as below:

$$\vec{\Omega}\cdot\nabla\phi_{sg,g}(\vec{r})+\Sigma_{t,sg,g}(\vec{r})\phi_{sg,g}(\vec{r})=\frac{\Sigma_p(\vec{r})}{4\pi} \quad (3)$$

where Σ_p is the macroscopic potential cross section.

Compared to the statistical model, the fixed source model has better parallel performance. The subgroup flux of different subgroups in the entire energy range is coupled with each other, and can be calculated together. The self-shielding cross section is collapsed as:

$$\sigma_{x,g}(\vec{r})=\frac{\sum_{sg\in g}p_{sg,g}\sigma_{x,sg,g}\phi_{sg,g}(\vec{r})}{\sum_{sg\in g}p_{sg,g}\phi_{sg,g}(\vec{r})} \quad (4)$$

Comparing the above two models, it can be noticed that the statistical model needs iterations, while the fixed source model does not. It means that the latter requires fewer fixed source iterations. In the lattice calculation, the bondarenko iteration (Stamm'ler and Abbate, 1983) is used to deal with the resonance interference effect. When one isotope is treated as a resonance isotope, the other isotopes are treated as non-resonant isotopes, and the subgroup total cross section is written as follows:

$$\Sigma_{t,sg,g}(\vec{r})=N_r(\vec{r})\sigma_{t,sg,g}+\sum_{k\neq r}N_k(\vec{r})\sigma_{t,g,k}(\vec{r}) \quad (5)$$

The subgroup flux is then calculated by Eq. 3. The new self-shielding cross section of isotope r is updated by Eq. 4. The flow chart of the resonance calculation is shown in Figure 1.

The single assembly problems with reflective boundary condition are used to determine the homogenized cross-sections of fuel material. For better consideration of the strong space coupling in different geometric sizes due to different mean free path of neutrons, the super homogenization method (Zhang et al., 2016) is optional to be used as the homogenization technique. For the structural materials and other non-fuel materials, the super cell or assembly models are used to determine the SPH factors and the cross-sections. The cross-sections are modified as follows:

$$\tilde{\Sigma}_{i,g}^{hom}=\mu_{i,g}\Sigma_{i,g}^{hom} \quad (6)$$

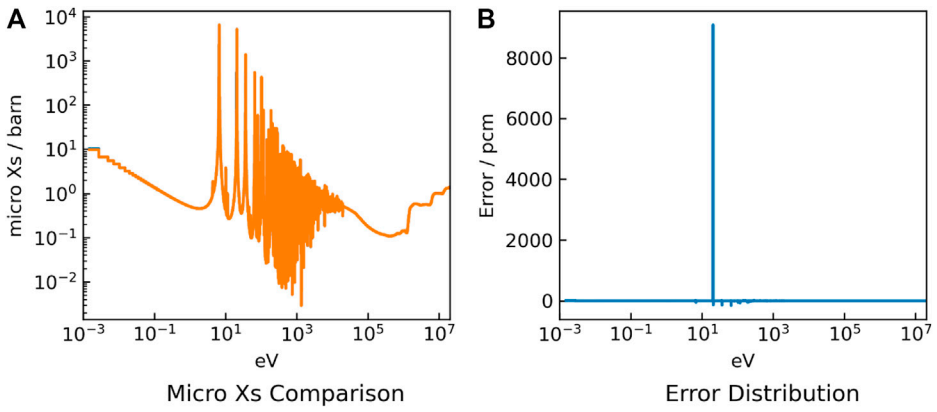

FIGURE 3
^{238}U absorption cross section results **(A)** and errors **(B)** for the UO_2 problem with thermal spectrum.

TABLE 1 JAEA pin cell eigenvalue.

Pin cell type	Open MC	FSAR	Error/pcm
UO_2	1.53270 ± 9pcm	1.52928	−342
MOX	1.28279 ± 8pcm	1.28234	−45

2.2 Core simulation

Based on the multi-group cross-sections generated by the lattice calculation, the three-dimensional whole core calculation is carried out by the core simulator. The S_N method with triangular grid is applied as the solver of the transport equations. The three-dimensional multi-group neutron transport equation within the triangular prism grid can be written as follows, which assumes that the fission source is isotropic and scattering sources is anisotropic in the derivation.

$$\mu^m \frac{\partial \Psi_g^m(x,y,z)}{\partial x} + \eta^m \frac{\partial \Psi_g^m(x,y,z)}{\partial y} + \frac{\xi^m}{h_z} \frac{\partial \Psi_g^m(x,y,z)}{\partial z} + \Sigma_t^g \Psi_g^m(x,y,z) = \hat{Q}_g(x,y,z) \tag{7}$$

where m represents a certain angular direction, μ^m, η^m, ξ^m is the component of the angular direction m on the coordinate axis (x, y, z), $\Psi_g^m(x,y,z)$ is the angular flux of the g-th group.

For the reactor system without outer neutron source, the source $\hat{Q}_g$ includes fission source and scattering source. The fission source is usually assumed to be isotropic, while the scattering source is anisotropic in reactor system. The assumption that the scattering source is isotropic limits the application of the triangular discrete ordinate nodal method in practical problems. The isotropic scattering source written as follows is considered in FSAR:

$$Q_s(\boldsymbol{r}, E, \boldsymbol{\Omega}) = \int_0^\infty \int_{4\pi} \Sigma_s(\boldsymbol{r}, E') f(\boldsymbol{r}, E' \to E, \boldsymbol{\Omega}' \to \boldsymbol{\Omega}) \psi(\boldsymbol{r}, E', \boldsymbol{\Omega}') d\boldsymbol{\Omega}' dE' \tag{8}$$

where f represents the scattering function.

The micro-depletion scheme is applied to simulate the core burn up and the Chebyshev Rational Approximation Method is used to solve the depletion equation. In FSAR, the depletion chains containing 21 heavy isotopes and 49 fission products is provided for the advanced reactor core system.

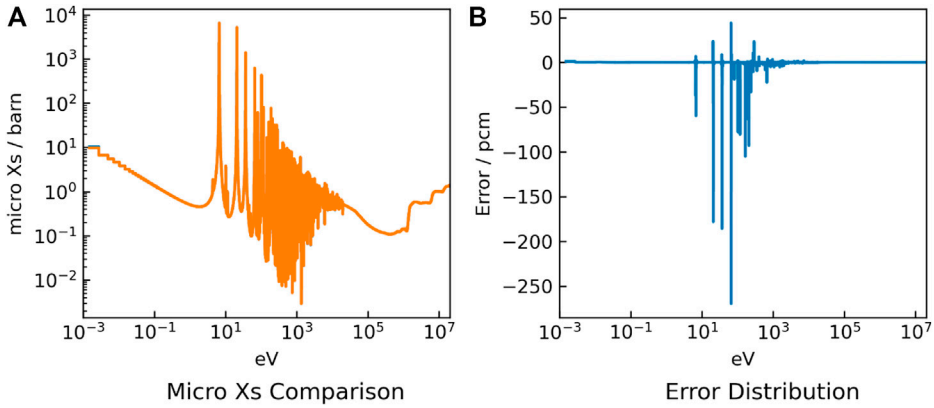

FIGURE 4
^{238}U absorption cross section results **(A)** and errors **(B)** for the MOX problem with thermal spectrum.

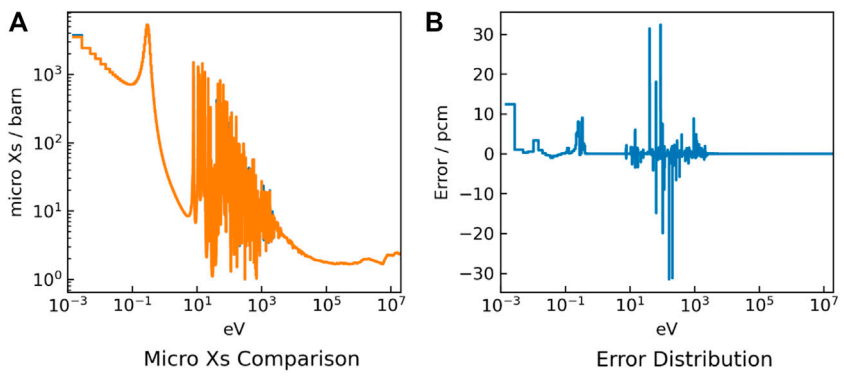

FIGURE 5
^{239}Pu absorption cross section results **(A)** and errors **(B)** for the MOX problem with thermal spectrum.

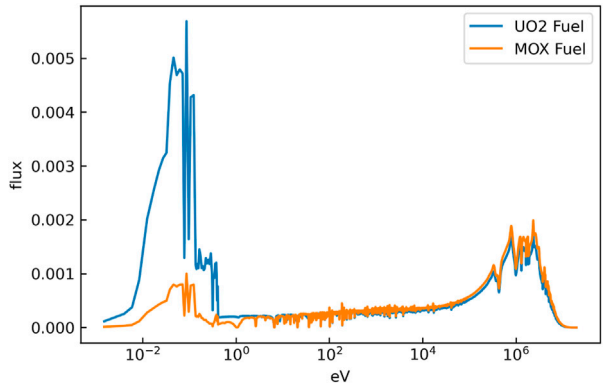

FIGURE 6
Flux comparison in fuel region.

TABLE 2 UO_2 **pin cell eigenvalue error.**

	OpenMC	Multi-group OpenMC	FSAR
Eigenvalue	1.53270 ± 9pcm	1.52975 ± 6pcm	1.52928
Error		−295	−342

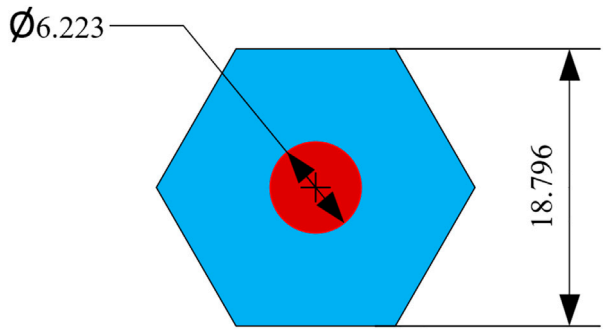

FIGURE 7
Geometry of intermediate spectrum problem (unit: mm).

3 Numerical results

To verify the effectiveness of the method used in this paper, we test different spectrum and different scale problems. The ultrafine group library used in this section is made by the NJOY program (Macfarlane et al., 2016) based on ENDF/B-VII.0 library. The reference solutions are provided by the Monte Carlo code OpenMC (Romano et al., 2015).

In this section, the serval pin cell problems with different spectrum characteristics are selected as the verification problems. The results for the eigenvalue k_{eff} and for the absorption cross-sections of ^{238}U and ^{239}Pu are compared to the reference results.

3.1 Thermal spectrum problem

UO_2 and MOX pin cell problems from JAEA benchmark (Yamamoto et al., 2002) are utilized for the thermal spectrum and the geometry is shown in Figure 2. The two problems have the same mesh division. In the radial direction, the fuel, clad and moderator are divided into three and one and two equal-volume rings respectively. Each ring is divided into 8 equal-volume sectors. The MOC parameters are set to be three polar angles and 16 angles per octant, and 0.01 cm ray spacing. The multigroup transport equation with P_0 scattering was solved with the pure MOC calculation without any accelerations. In the calculations, the inter-molecular thermal scattering effect is not considered.

For the thermal spectrum problems, the results of eigenvalue are presented in Table 1, and the self-shielding cross section errors are shown in Figures 3, 4, 5. In the table, the errors of eigenvalue are calculated as follows:

$$Err_k = \left(k_{MOC} - k_{ref}\right) * 10^5 \tag{9}$$

In the figures, the errors of cross section are calculated as follows:

$$Err_{xs} = \frac{\left(\sigma_{g,MOC} - \sigma_{g,ref}\right) * \phi_{g,ref}}{\sum_{g \in G} \sigma_{g,ref} \phi_{g,ref}} * 10^5 \tag{7b}$$

It can be found that the cross-sections have high accuracy for most groups. However, in the UO_2 problem, the absorption cross section of

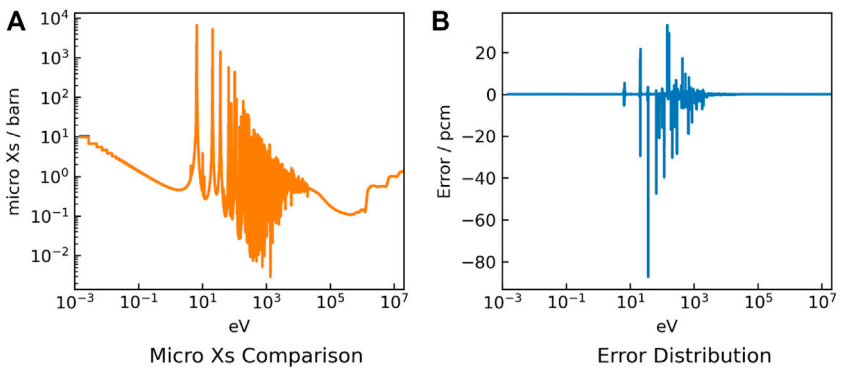

FIGURE 8
^{238}U absorption cross section results **(A)** and errors **(B)** for the intermediate spectrum problem.

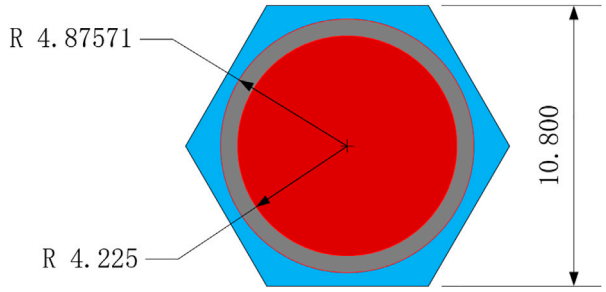

FIGURE 9
Geometry of fast spectrum problem (unit: mm).

TABLE 3 Fast spectrum problem eigenvalue.

Pin cell type	OpenMC	FSAR	Error/pcm
MOX-SS316-Na	1.53697 ± 7pcm	1.53679	−18
UO2-SS316-K	1.39732 ± 7pcm	1.39648	−84

^{238}U has a large deviation at 20 eV energy. While the absorption cross section error of ^{238}U at 20 eV energy of the MOX problem is smaller. This is because the MOX fuel including serval Pu isotopes hardens the neutron flux spectrum, as shown in Figure 6. Furthermore, affected by the harder flux spectrum, there is no significant increase in the errors of eigenvalue for the MOX fuel problem, even the obvious differences of the cross-sections appear in the energy range between 10 and 100 eV.

In order to determine the error source of the eigenvalue, the cross-sections tallied from OpenMC are used to get the macroscopic cross-sections. The multi-group model in OpenMC is used to perform the transport calculation. The results are shown in Table 2. It can be found that the result of FSAR and multi-group OpenMC is close and the anisotropic scattering effect would be the main error source.

3.2 Intermediate spectrum problem

The hexagonal UO_2 cell with high enrichment (Lee, 2014) is utilized as the intermediate spectrum problem. The graphite is used as the moderator. The geometry is shown in Figure 7. Both fuel and moderator are divided into one ring. Each ring is divided into 6 equal-volume sectors.

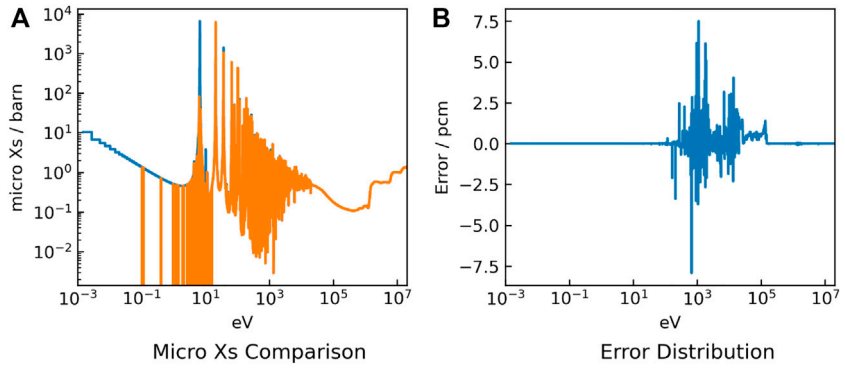

FIGURE 10
^{238}U absorption cross section results **(A)** and errors **(B)** for the MOX problem with fast spectrum.

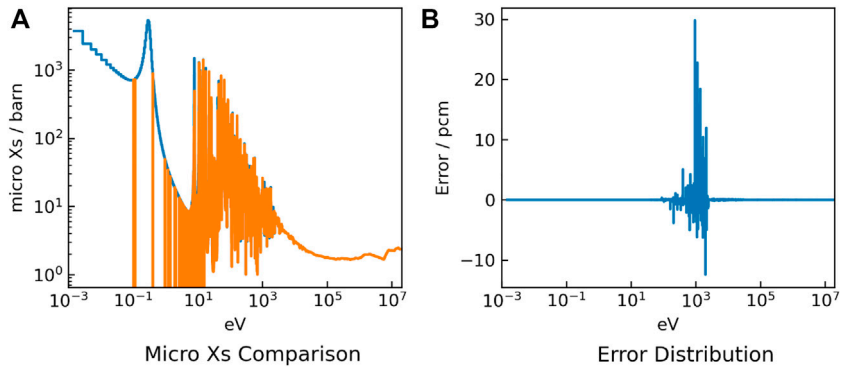

FIGURE 11
^{239}Pu absorption cross section results **(A)** and errors **(B)** for the MOX problem with fast spectrum.

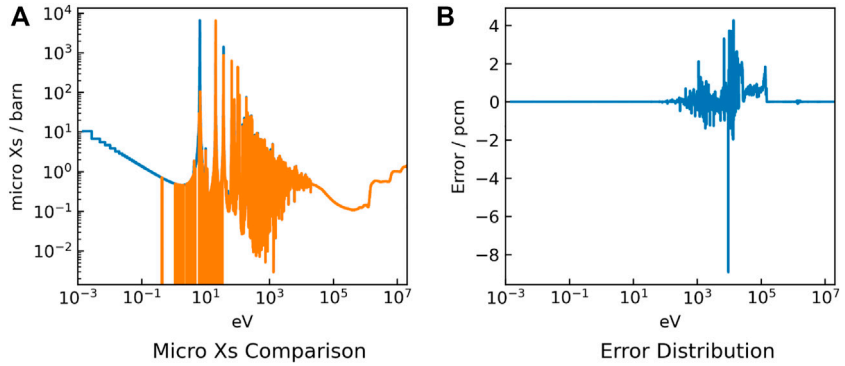

FIGURE 12
^{238}U absorption cross section results **(A)** and errors **(B)** for the UO_2 problem with fast spectrum.

For the intermediate spectrum problem, the reference eigenvalue obtained by OpenMC is 1.28829 ± 8 pcm and the value of FSAR is 1.28465. The results of cross-sections are shown in Figure 8. The error results are similar to that of the UO_2 problem. There is also a significant deviation at 20 eV energy and small deviations at other positions. It can be explained by the invalidation of narrow approximation around 20 eV.

3.3 Fast spectrum problem

In order to test the performance of FSAR in the fast reactor, the calculations of UO_2 cell with high enrichment and MOX cell are carried out. The same hexagonal geometry of the two problems is shown in Figure 9. The clad material is SS 316 alloy, and two conventional coolants in fast reactors, sodium and potassium, are selected in this section. The compositions of the materials are obtained from the reference (Li et al., 2017). Finally, two fast spectrum problems are formed, expressed as MOX-SS316-Na and UO_2-SS316-K respectively.

The eigenvalue results are shown in Table 3. The errors of cross-sections are shown in Figures 10, 11, 12. The numerical results indicate that the calculation in fast spectrum problems has higher accuracy than that of other problems. This is because the resonance peak is narrower in the high energy range and the resonance effect treatment is more applicable.

4 Conclusion

The full neutron spectrum code for advanced reactor simulation named FSAR developed by NPIC, CNNC is introduced in this paper. The deterministic two-step calculation strategy based on the homogenization theory is utilized in FSAR. In the lattice calculation, the MOC method is used to determine the neutron flux, and the subgroup method with ultrafine energy groups was implemented to get the accurate self-shielded cross-section. In the core calculation, the discrete-ordinate method and micro burnup calculation method were used to simulate the core neutron transport and depletion. The preliminary verifications have been carried out, and the results indicated that FSAR has good performances in dealing with the resonance self-shielding effect of the full-range spectrum problems. In the near future, the verification of each module and the whole code system will be carried out. What's more, other calculation functions such as thermal feedback module are being developed.

Data availability statement

The original contributions presented in the study are included in the article/supplementary material, further inquiries can be directed to the corresponding author.

Author contributions

LW: Methodology, Software, Investigation, Numerical Analysis, Writing—Original Draft; BZ: Methodology, Numerical Analysis; DL: Numerical Analysis; CZ: Methodology; JL: Writing—Original Draft.

Funding

This research is supported by the National Natural Science Foundation of China (Approved number Nos.12075228 and Nos.12205283). All the authors would like to thank Zhejiang University for the help with resonance self-shielding treatment model.

Conflict of interest

The authors declare that the research was conducted in the absence of any commercial or financial relationships that could be construed as a potential conflict of interest.

Publisher's note

References

Allen, K., Knight, T., and Bays, S. (2011). Benchmark of advanced burner test reactor model using MCNPX 2.6.0 and ERANOS 2.1. *Prog. Nucl. Energy* 53 (6), 633–644. doi:10.1016/j.pnucene.2011.01.007

Downar, T., Kochunas, B., and Collins, B. (2016). *Validation and verification of the MPACT code[C]*. United states: American Nuclear Society, 2961–2978.

Faure, B., Archier, P., Vidal, J.-F., Palau, J. M., and Buiron, L. (2018). Neutronic calculation of an axially heterogeneous ASTRID fuel assembly with APOLLO3: Analysis of biases and foreseen improvements. *Ann. Nucl. Energy*. 115, 88–104. doi:10.1016/j.anucene.2017.12.035

Lee, C. (2014). *Development of a generalized cross section library applicable to various reactor types[C]*. Japan: PHYSOR2014.

Lee, C. H., and Yang, W. S. (2017). MC2 -3: Multigroup cross section generation code for fast reactor analysis. *Nucl. Sci. Eng.* 187, 268–290. doi:10.1080/00295639.2017.1320893

Li, M., Zmijarevic, I., and Sanchez, R. (2017). Resonance self-shielding methods for fast reactor calculations—comparison of a new Tone's method with the subgroup method in APOLLO3®. *Nucl. Sci. Eng.* 188 (1), 15–32. doi:10.1080/00295639.2017.1332890

Macfarlane, R., Muir, D. W., Boicourt, R. M., Kahler, A. C., and Conlin, J. L. (2016). *The NJOY nuclear data processing system, version 2016*. USA: Los Alamos National Laboratory, 17–22.

Mao, L., and Zmijarevic, I. (2017). "A new Tone's method in APOLLO3 and its application to ZPPR benchmarks," in *Proc. M&C 2017* (Jeju, Korea: APOLLO).

Rachamin, R., and Kliem, S. (2017). Validation of the dyn3d-serpent code system for SFR cores using selected BFS experiments. Part I: Serpent calculations. *Ann. Nucl. Energy* 102, 158–167. doi:10.1016/j.anucene.2016.12.023

Romano, P. K., Horelik, N. E., Herman, B. R., Nelson, A. G., Forget, B., and Smith, K. (2015). OpenMC: A state-of-the-art Monte Carlo code for research and development. *Ann. Nucl. Energy* 82, 90–97. doi:10.1016/j.anucene.2014.07.048

Song, P., Zhang, Z., Zhang, Q., Liang, L., and Zhao, Q. (2020a). Implementation of the CPU/GPU hybrid parallel method of characteristics neutron transport calculation using the heterogeneous cluster with dynamic workload assignment. *Ann. Nucl. Energy* 135, 106957. doi:10.1016/j.anucene.2019.106957

Stamm'ler, R. J., and Abbate, M. J. (1983). *Methods of steady-state reactor physics in nuclear design [M]*. London: Academic Press, 286–355.

Takeda, T., Fujimoto, H., and Sengoku, K. (1991). Application of multi-band method to KUCA tight–pinch lattice code. *J. Nucl. Sci. Technol.* 28, 836–869.

Tone, T. (1975). A numerical study of heterogeneity effects in fast reactor critical assemblies. *J. Nucl. Sci. Technol.* 12 (8), 467–481. doi:10.1080/18811248.1975.9733139

Wang, K., Li, Z. G., She, D., Liang, J., Xu, Q., Qiu, Y., et al. (2015). Rmc – a Monte Carlo code for reactor core analysis. *Ann. Nucl. Eng.* 82, 121–129. doi:10.1016/j.anucene.2014.08.048

Wu, Y. C. (2016). Design and R&D progress of China lead-based reactor for ads research facility. *Engineering* 2 (1), 124–131. doi:10.1016/j.eng.2016.01.023

Yamamoto, A., Ikehara, T., Ito, T., and Saji, E. (2002). Benchmark problem suite for reactor physics study of LWR next generation fuels. *J. Nucl. Sci. Technol.* 39 (8), 900–912. doi:10.1080/18811248.2002.9715275

Zhang, B., Li, Y. Z., Wu, H. C., Cao, L., and Shen, W. (2016). Evaluation of pin-cell homogenization techniques for PWR pin-by-pin calculation. *Nucl. Sci. Eng.* 186 (2), 134–146. doi:10.1080/00295639.2016.1273018

Zhang, G., and Yang, W. S. (2020). Quadratic axial expansion function with sub-plane acceleration scheme for the high-fidelity transport code PROTEUS-MOC. *Ann. Nucl. Energy*. 148, 107713. doi:10.1016/j.anucene.2020.107713

frontiers | Frontiers in Energy Research

TYPE Original Research
PUBLISHED 27 February 2023
DOI 10.3389/fenrg.2023.1145046

OPEN ACCESS

EDITED BY
Shichang Liu,
North China Electric Power University, China

REVIEWED BY
Di Yun,
Xi'an Jiaotong University, China
Rong Liu,
South China University of Technology, China
Liuxuan Cao,
Xiamen University, China
Yanan He,
Xi'an Jiaotong University, China

*CORRESPONDENCE
Zhenhai Liu,
1989lzhh@sina.com
Wei Zeng,
zengwei02@sina.com

SPECIALTY SECTION
This article was submitted to Nuclear Energy, a section of the journal Frontiers in Energy Research

RECEIVED 15 January 2023
ACCEPTED 15 February 2023
PUBLISHED 27 February 2023

CITATION
Liu Z, Zeng W, Qi F, Zhou Y, Li Q, Chen P, Yin C, Liu Y, Zhao W, Wang H and Huang Y (2023), Development of multiphysics coupling system for nuclear fuel rod with COMSOL and RMC.
Front. Energy Res. 11:1145046.
doi: 10.3389/fenrg.2023.1145046

Development of multiphysics coupling system for nuclear fuel rod with COMSOL and RMC

Zhenhai Liu*, Wei Zeng*, Feipeng Qi, Yi Zhou, Quan Li, Ping Chen, Chunyu Yin, Yong Liu, Wenbo Zhao, Haoyu Wang and Yongzhong Huang

Science and Technology on Reactor System Design Technology Laboratory, Nuclear Power Institute of China, Chengdu, China

Coupling fuel performance and neutronics can help improve the prediction accuracy of fuel rod behavior, which is important for fuel design and performance evaluation. A fuel rod multiphysics coupled system was developed with multiphysics software COMSOL and 3D Monte Carlo neutron transport code RMC. The fuel performance analysis module was built on top of COMSOL with the ability to simulate the fuel behavior in two-dimensional axisymmetric (2D-RZ) or three-dimensional (3D) mode. RMC was innovatively wrapped as a component of COMSOL to communicate with the fuel performance analysis module. The data transferring and the coupling process was maintained using COMSOL's functionality. Two-way coupling was achieved by mapping power distribution and fast neutron flux fields from RMC to COMSOL and the temperature and coolant density fields from COMSOL to RMC. A fuel rod pin lattice was modeled to demonstrate the coupling. Results show that the calculated power and temperature distributions are reasonable. Considering the flexibility of the coupled system, it can be applied to the performance evaluation of new fuel design.

KEYWORDS

multiphysics coupling, fuel performance, fuel rod, COMSOL, RMC

1 Introduction

The traditional fuel performance analysis code is decoupled with neutronics. The neutronics code calculates the axial distribution of linear power, which is used to reconstruct the local power of the pellet based on the radial power density distribution. The radial profiles deviate significantly from uniformity as irradiation proceeds due to epithermal neutrons' capture and self-shielding in rim region known as the neutronic rim effect. The fission rate density at the outer edge of the pellet is higher than the inner region due to the ^{235}Pu enrichment and self-shielding (Van Uffelen et al., 2019) (Palmer et al., 1982). The neutronic rim effect is significant at higher burnup, which have a significant effect on the radial temperature distribution. The radial profiles must be provided beforehand or calculated using external neutronics calculation formed surrogate model (Jacoud and Vesco., 2000) or simplified neutron diffusion-based model, such as RADAR model (Palmer et al., 1982), TUBRNP model (Lassmann et al., 1994), RAPID model (Lee et al., 2000). However, there are several limitations concerning these treatments, including difficulties when applied to other types of fuel, inability to account for feedbacks of real temperature and coolant density distributions, etc.

With the rapid development of computer hardware, it is possible to couple sub-pin level neutron code with fuel performance code to perform high-fidelity simulations to address these limitations. Research work in this area is currently underway. The radiation transport program Denovo was coupled to multiphysics nuclear fuel Performance program AMPFuel by transferring the power distribution from Denovo to AMPFuel (i.e., one-way coupling) (Clarno et al., 2012). The deterministic core analysis code DeCART was coupled with BISION using one-way and iterative two-way strategies (Gleicher et al., 2013). In CASL project (CASL, 2020), the MOOSE based applications Rattlesnake (neutronic transport simulation), BISON (fuel performance analysis) and RELAP-7 (nuclear reactor system safety analysis) have been coupled tightly under MAMMOTH package. A single fuel pin was modeled under irradiation and station blackout conditions using the coupled approach (Gleicher et al., 2016). The OpenFOAM Fuel Behavior Analysis Tool OFFBEAT was coupled with Monte Carlo code Serpent for determining an accurate fuel radial power profile (Scolaro et al., 2019). The Monte Carlo neutron transport code SERPENT 2 was coupled with the fuel performance code TRANSURANUS in two-way strategy to enhance fuel performance analyses (Suikkanen et al., 2020) and the Monte Carlo code RMC was coupled with multiphysics software COMSOL for FCM fuel segment (Weng et al., 2021). Recently, coupling between the fuel performance code TRANSURANUS and neutronics solver Serpent was further improved by transferring and utilizing nuclide compositions within the coupled calculations (Rintala et al., 2022). There are many challenges for coupling codes, such as communication of data across different mesh grids, convergence of the nonlinear coupling to some tolerance value. Different researchers overcome these issues in different ways.

A fuel rod performance analysis module based on the COMSOL Multiphysics software with the ability to simulate the fuel behavior in 2D-RZ or 3D was built and coupled with Monte Carlo reactor physics code RMC (Wang et al., 2015). The motivation for coupling the two codes is to establish a fuel rod multiphysics coupling system. Compared with the traditional 1.5D fuel rod performance analysis code, we build the fuel rod multiphysics coupling system with fewer assumptions, higher accuracy, and the ability to catch local behavior. The accuracy of the fuel performance calculation results is improved by coupling with the neutron transport code. Fine parameters (sub-pin level) such as power density, burnup and neutron flux distribution are introduced to replace the traditional limited method. Section 2 describes the coupled system. Section 3 presents the demonstration calculation using the coupled system. Section 4 shows the results of the demonstration calculation. The conclusion is shown in Section 5.

2 Description of the coupled system

2.1 COMSOL fuel performance module

The main function of the fuel performance analysis module is to predict the evolution of thermo-mechanical and irradiation behavior of the fuel rod under the given power history and coolant boundary conditions. The built-in modules of heat transfer, solid mechanics, and custom partial/ordinary differential equations in COMSOL Multiphysics software are used to construct the fuel performance analysis module. At present, the module is developed for the steady state coupling at the beginning of life (BOL). The main models involved are as follows.

2.1.1 Heat transfer models

The temperature distribution of fuel pellet and cladding is given in terms of solid heat conduction equation omitted time derivation term for quasi-steady study:

$$\nabla \cdot (\mathbf{K}\nabla \mathbf{T}) + \mathbf{S} = \mathbf{0} \tag{1}$$

where $\boldsymbol{T}$, $\mathbf{K}$ are the temperature and thermal conductivity, respectively, and $\mathbf{S}$ is the volumetric energy source used to specify the energy produced in fuel pellet *via* fission. The above equation is solved by the solid heat transfer module of COMSOL.

The thermal conductivity of UO_2 is defined using the modified NFI model (Lusher et al., 2015):

$$K_{95} = \frac{1}{0.0452 + 2.46 \times 10^{-4} T + f(Bu) + (1 - 0.9\exp(-0.04Bu))g(Bu)h(T) + \frac{3.5 \times 10^{9}}{T^{2}} \exp\left(-\frac{-16361}{T}\right)} \tag{2}$$

where K_{95} is UO_2 thermal conductivity of 95% fuel density (W/(m*K)), $\boldsymbol{T}$ is temperature(K), $\boldsymbol{Bu}$ is burnup (MWd/tU), $\boldsymbol{f}(\boldsymbol{Bu})$ is the effect of solution fission products in crystal matrix, $\boldsymbol{g}(\boldsymbol{Bu})$ is the effect of irradiation defects, and $\boldsymbol{h}(\boldsymbol{T})$ is the temperature dependence of annealing on irradiation defects. The above model is then adjusted for as-fabricated fuel density using the Lucuta recommendation for spherical-shaped pores.

The thermal conductivity of zircaloy cladding is as follows (Lusher et al., 2015):

$$K = 7.51 + 2.09 \times 10^{-2} T - 1.45 \times 10^{-5} T^{2} + 7.67 \times 10^{-9} T^{3} \tag{3}$$

where $\boldsymbol{K}$ is the thermal conductivity (W/(m*K)) and $\boldsymbol{T}$ is temperature (K).

The fuel-cladding gap controls the heat transfer from the fuel pellet to the cladding, as well as the mechanical interaction between fuel pellet and cladding. The heat transfer in the pellet-cladding gap is realized by the thermal contact pair in the COMSOL, the control equations are as follows:

$$n_{dst} \cdot q_{dst} = h_{gap}(T_{src} - T_{dst}) \tag{4}$$

$$n_{src} \cdot q_{dst} = h_{gap}(T_{dst} - T_{src}) \tag{5}$$

$$h_{gap} = h_r + h_g + h_s \tag{6}$$

where the subscripts dst and src represent the destination surface and the source surface, respectively. The outer surface of the pellet is used as the source surface and the inner surface of the cladding is used as the destination surface. n is the surface normal vector, q is the surface heat flux, and h_{gap} is the gap equivalent heat transfer coefficient, the sum of radiation heat transfer coefficient h_r, gap gas heat transfer coefficient h_g and contact heat transfer coefficient h_s. The radiation heat transfer coefficient is calculated using the classical radiation heat transfer relationship. The gap gas heat transfer coefficient is calculated by the model proposed by Ross and Stoute (Ross and Stoute, 1962), and the contact heat transfer coefficient after the contact between pellet and cladding is calculated by the model proposed by Olander (Olander, 1976).

The coolant flow heat transfer outside the fuel rod is modeled by single channel model (Geelhood et al., 2015). The equation of coolant enthalpy rise is as follows:

$$GA\frac{dH}{dz} = \pi d q_{co} \tag{7}$$

where G is the mass flow velocity, A is the cross section of equivalent channel, H is the specific enthalpy, d is the equivalent diameter and q_{co} is the cladding outside surface heat flux.

The coolant may change from single-phase to two-phase flow during the flow. The fuel rod outer surface temperature T_w and effective heat transfer coefficient h_{eff} are calculated as follows:

$$T_w = \min\left(T_f + \frac{q_{co}}{h}, T_{sat} + \Delta T_{sat}\right) \tag{8}$$

$$h_{eff} = \frac{q_{co}}{T_w - T_f} \tag{9}$$

where T_f is the coolant mainstream temperature, h is the single phase forced convection heat transfer coefficient, which is predicted with the Dittus-Boelter equation. During two phase forced convection, the difference ΔT_{sat} between the fuel rod outer surface temperature T_w and the saturation temperature T_{sat} is predicted with the Jens Lottes equation. The coolant mainstream temperature and mean density is calculated based on system pressure and specific enthalpy using the IAPWS-IF97 water and steam properties. The coefficient form PDE interfaces of COMSOL are used to solve the coolant enthalpy rise equation. The third kind boundary condition is applied on the outside of cladding to couple the coolant enthalpy rise equation and cladding heat conduction equation.

2.1.2 Solid mechanical models

In the mechanical analysis of fuel rod, it is assumed that the pellet and cladding are in mechanical equilibrium in each time step, and the equilibrium equation is as follows:

$$\nabla \cdot \sigma + f = 0 \tag{10}$$

where σ is the cauchy stress, f is the body force per unit volume.

The stress-strain relationship is described by the constitutive equation:

$$\sigma = 2G\varepsilon_{el} + \lambda Tr(\varepsilon_{el})I \tag{11}$$

$$\varepsilon = \varepsilon_{el} + \varepsilon_{iel} \tag{12}$$

where G is the shear modulus, λ is Lamé parameter, ε is the strain tensor, which is the sum of elastic strain tensor ε_{el} and inelastic strain tensor ε_{iel}. The inelastic strain term can be decomposed into the sum of different inelastic strain terms such as thermal expansion strain, irradiation induced swelling strain, densification strain, relocation strain, irradiation growth strain and creep strain. Since the fuel performance analysis module is developed for the steady state coupling at the BOL at present, only the thermal expansion of pellet and cladding, the pellet relocation strain caused by crack are considered.

The UO_2 thermal expansion strain ε_{th,UO_2} is a function of temperature (Lusher et al., 2015):

$$\varepsilon_{th,UO_2} = 9.8 \times 10^{-6} T - 2.61 \times 10^{-3} + 3.16 \times 10^{-1} \exp\left(-\frac{E_D}{kT}\right) \tag{13}$$

where T is temperature (K) and E_D is the energy of formation of a defect (J), which is $1.32 \times 10^{-19} J$.

The correlations used to calculate the thermal expansion in the cladding are as follows (Lusher et al., 2015):

$$\varepsilon_{th,axial} = -2.506 \times 10^{-5} + 4.441 \times 10^{-6} T \tag{14}$$

$$\varepsilon_{th,diametral} = -2.373 \times 10^{-4} + 6.721 \times 10^{-6} T \tag{15}$$

where $\varepsilon_{th,axial}$, $\varepsilon_{th,diametral}$ are the axial and diametral components of thermal expansion in the cladding, T is the temperature (K).

When the stress gradients exceed the fuel fracture stress as the power rising up, the pellet will crack. The crack result in a overall increase of pellet diameter. The ESCORE relocation model (Kramman and Freeburn, 1987) is used to calculate this strain, which is given as

$$\varepsilon_{reloc} = 0.8Q\frac{G_t}{D_o(0.005Bu^{0.3} - 0.2D_o + 0.3)} \tag{16}$$

$$Q = \begin{cases} 0, q_l \le 6\text{kW/ft} \\ (q_l - 6)^{\frac{1}{3}}, 6\text{kW/ft} < q_l \le 14\text{kW/ft} \\ \dfrac{q_l - 10}{2}, q_l > 14\text{kW/ft} \end{cases} \tag{17}$$

where ε_{reloc} is the diametral strain due to relocation, G_t is the as-fabricated cold diametral gap (in), D_o is the as-fabricated cold diameter of the pellet (in), Bu is the pellet average fuel burnup (MWd/tU) and q_l is the pellet average linear heating rate (kW/ft).

2.2 RMC code

RMC (Reactor Monte Carlo Code) is a Monte Carlo (MC) transport code developed by Department of Engineering Physics, Tsinghua University, Beijing (Wang et al., 2015). RMC is designed for reactor neutron transport analysis applicable to arbitrary geometry using continuous energy point-wise cross sections of different materials and temperatures.

RMC employs ACE format cross-section data in simulation. To accelerate energy searching processes, a method named 1-step searching method is adopted when incident energy is specified. The Monte Carlo method is used to simulate neutron histories by tracking each neutron through different regions in the geometry. Both ray-tracking and delta-tracking methods are supported in RMC, and users can choose either method independently according to the problem they encountered. RMC uses the constructive solid geometry (CSG) representation to build complex geometry. In the study, a 3D fuel pin geometry was created through logical combination of half-spaces defined by cylindrical and plane surfaces using CSG functionality in RMC.

The main steps of point-burnup calculation in RMC include: 1) transport calculation: performing MC transport calculation based on the current material information, then counting neutron flux as well as single group sections of nuclei reactions, 2) energy distributing: calculating power of each burnup zone according to the total energy, 3) cross-section replacement: replacing the corresponding cross-sections in data library with the single group sections obtained in MC calculation in step 1, 4) point-burnup calculation: updating nuclei densities in each burnup zone based on

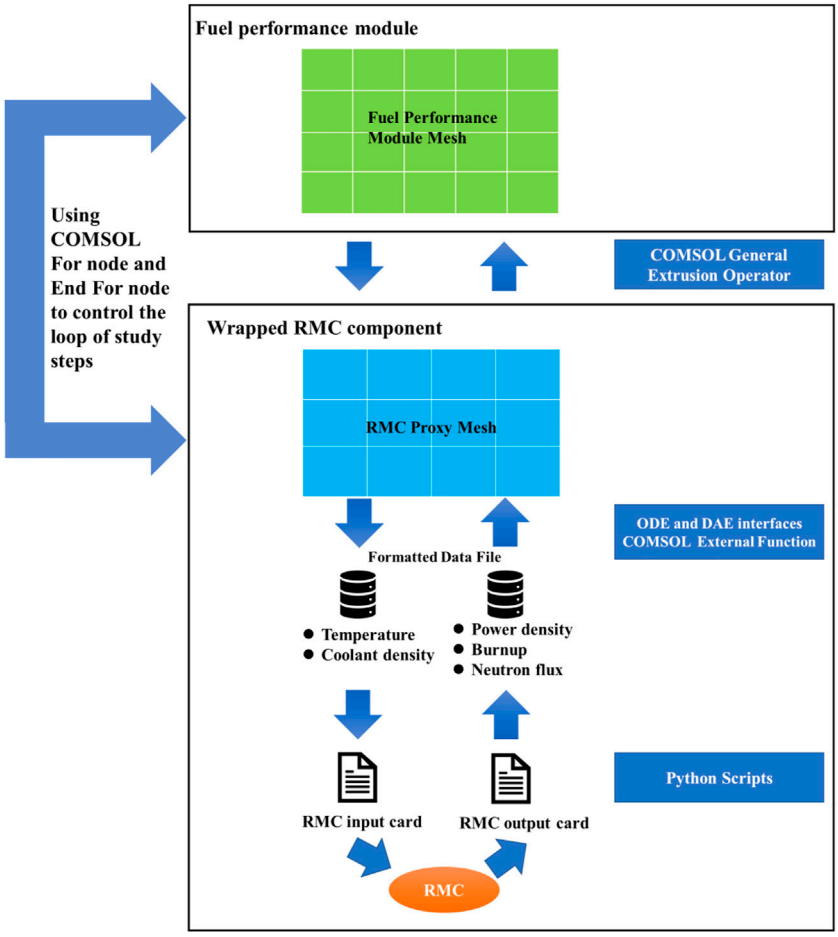

FIGURE 1
Schematic diagram of COMSOL coupling with external code RMC.

the initial densities. Then repeat the above steps until the calculation is completed. RMC has good parallel computing ability. It can be scaled up to thousands of cores and maintain high parallel efficiency.

From the perspective of coupling, RMC can accept the fuel temperature, coolant temperature and density as inputs, meanwhile, outputs the power density, burnup and neutron flux in each cell. These characteristics make it possible to couple with external fuel performance code.

2.3 Coupling methodology

The main coupling methods can be divided into external coupling and internal coupling. External coupling refers to data transfer between different modules through external files. The advantage of this method is that there is no need to modify the source code of the modules participating in the coupling. The subsequent upgrade and maintenance of each module can be carried out independently. The disadvantage is that it is limited by the speed of the IO interface. If large amounts of data need to be transferred, the efficiency is affected. For problems with time advancement, the modules participating in the coupling need to have restart function. Internal coupling refers to data transfer between different modules through memory. The advantage of this method is that the data transfer efficiency is high. A flexible coupling can be achieved by designing the data structure form. The disadvantage of this method is that source code of the modules participating in the coupling need to be modified. If the module needs subsequent upgrades, the coupling interface also needs to be maintained.

The coupling in this work is based on external coupling, since the COMSOL Multiphysics is commercial software. In addition, the data to be transmitted in this study is small, so the IO cost comparing to the computation of RMC can be omitted. Multiphysics coupling is relatively straightforward inside COMSOL. But according to our limited knowledge, COMSOL does not directly provide coupling interfaces for external coupling. Careful designed combinations of “External function” (C function interface), “ODE and DAE interfaces” of COMSOL for coupling external code are carried out in this work. The main idea is creating RMC proxy mesh in COMSOL and wrapping RMC as a component of COMSOL using the above utilities. Data transfer between components is performed using the COMSOL built-in “General Extrusion” coupling operator, and the iterative study steps are controlled using “For” and “End For” nodes in COMSOL. The schematic diagram is shown in Figure 1.

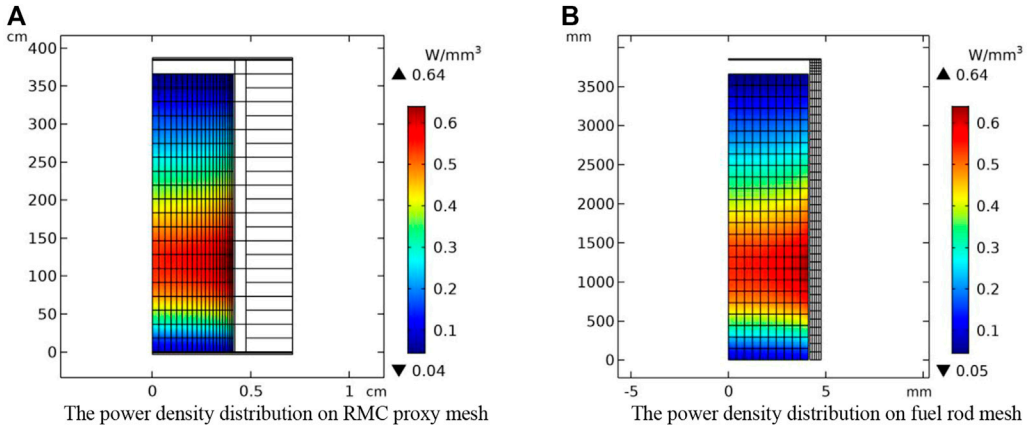

FIGURE 2
Power density distribution on RMC proxy mesh **(A)** and fuel rod mesh **(B)**.

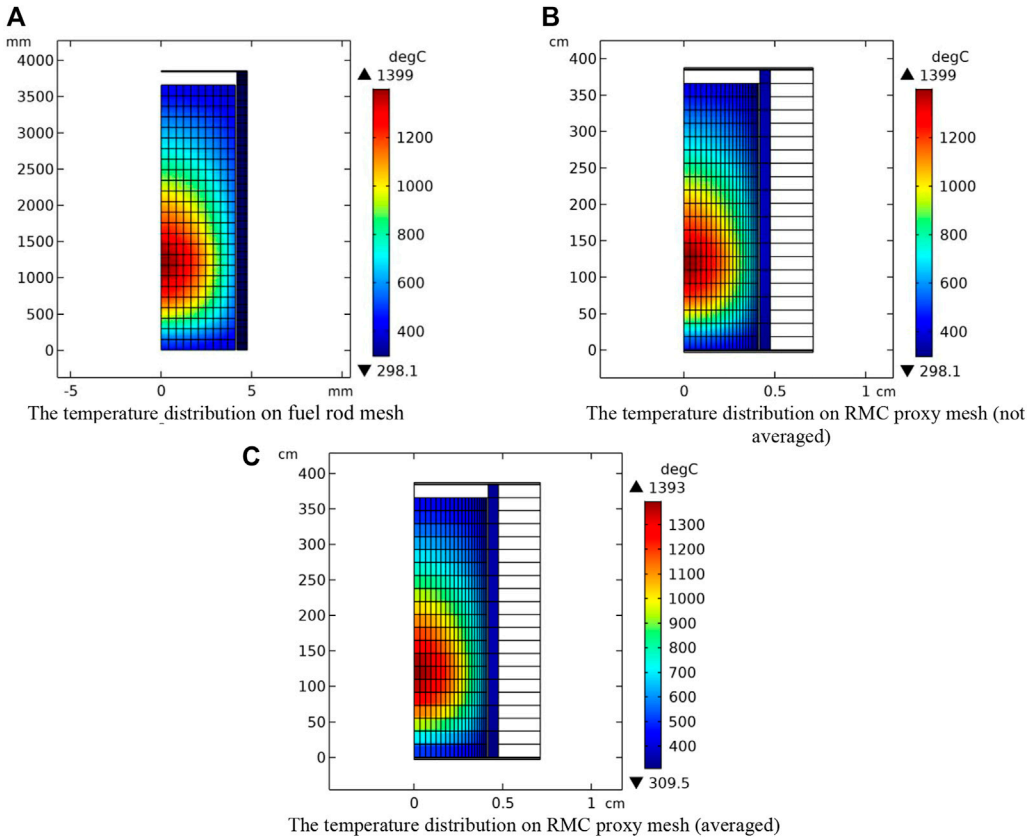

FIGURE 3
Temperature distribution on fuel rod mesh **(A)**, RMC proxy mesh (not averaged) **(B)** and RMC proxy mesh (averaged) **(C)**.

2.3.1 Wrapped RMC component

In RMC modeling, the fuel rod is described in CSG format cells by radial rings and axial segments. These cells can be represented by rectangular elements in the RZ coordinate system. Based on this idea, the RMC proxy mesh can be created in COMSOL using its geometry and mesh tools. An RMC input card generation code was developed, which can read the RMC proxy mesh data file (.nas format, generated from the mesh created in COMSOL) and generate cells in the RMC

TABLE 1 Statistical values of variables on different meshes.

	RMC proxy mesh	Fuel rod mesh	Relative error (%)
Power density integration value (W)	66907	66911	0.006
Power density maximum value (W/mm3)	0.63940	0.63938	0.003
Power density minimum value (W/mm3)	0.044908	0.044945	0.082
Temperature integration value (K*mm3)	226761935 226874565 (averaged)	226758181	0.002
Temperature maximum value (degC)	1398.9 1393.0 (averaged)	1398.9	0.000
Temperature minimum value (degC)	298.11 309.48 (averaged)	298.11	0.000

input card in CSG format according to the mesh node coordinates and mesh element connection information.

Through the COMSOL "External function" and "ODE and DAE interfaces", with the mesh element number as the function parameter, the fuel rod temperature and coolant density on the RMC proxy mesh are output to external data files which can be used to update the RMC input card. The RMC output results can be transferred back to the proxy mesh using the same method. The example of equations defined in ordinary differential equation module of COMSOL are as follows:

$$\text{T\_status} - \text{Export\_temperature}(\text{meshelement}, \text{T}) = 0 \quad (18)$$

$$\text{Qv} - \text{Import\_power\_density}(\text{meshelement}) = 0 \quad (19)$$

The Eq. 18 plays the role of exporting the data on the COMSOL mesh to the memory. T_status is the variable defined in the domain of RMC proxy mesh used to indicate whether the export is successful or not. The meshelement is a COMSOL's built-in variable, which is the number of mesh element. Export_temperature is a C function, which can receive the mesh element number and corresponding temperature and store into the memory, these data are then used as data source for RMC input card temperature modification. The Eq. 19 plays the role of importing the outside data to the COMSOL mesh. Qv is the power density variable defined in the domain of RMC proxy mesh. Import_power_density is a C function, which can receive the mesh element number and return the corresponding power density value. The type of Qv variable defined in the domain of RMC proxy mesh is Lagrange linear, which will provide a smooth field over the domain. The results calculated by RMC, such as power density, burnup and neutron flux can be imported to the proxy mesh through the above methods.

TABLE 2 Main modeling parameters.

Parameters	Value
^{235}U enrichment, %	4.45
Pellet diameter, mm	8.2
Active length of fuel, mm	3660
Gap distance, mm	0.08
Cladding thickness, mm	0.58
Cladding outside diameter, mm	9.5
Plenum length, mm	180
Fuel pin pitch, mm	12.6
Top and bottom water reflectors height, mm	20
Inlet coolant temperature, degC	292.8
Cold plenum pressure, MPa	2.1
Fuel rod power, kW	65.68
Specific power, W/gHM	37.7

The global equation module of COMSOL is used to trigger the operation of RMC *via* the C function Run_RMC, the equation is as follows:

$$\text{rmc\_status} - \text{Run\_RMC}(\text{t}) = 0 \quad (20)$$

where rmc_status is a global variable used to indicate whether the running of rmc is successful or not. Different Python functions are developed to 1) update the RMC input card based on temperature and density data file; 2) read the power density from the RMC output file and generate the power density data file. These data files are column-based text file about cell number and corresponding values, which can be easily processed. These Python functions are called inside the C function Run_RMC.

These thin wrappers can allow the RMC to plug in and communicate with other components of COMSOL.

2.3.2 Transferring data

Data transfer between different computing modules is an important part of multiphysics coupling. When different physics fields are solved on the same mesh, data transfer between fields is straightforward. However, in practical situations, it is often necessary to divide the meshes separately considering the different characteristics of different physical fields. For neutronics, the cladding thickness is very thin and has minor effect on neutron behavior, one mesh layer may just be fine. For fuel performance, to obtain fine cladding temperature, stress and strain, it is necessary to divide multi-layer meshes along the thickness. Data transfer with different meshing is a problem worthy of study in multiphysics coupling. There are some open-source frameworks to deal with this problem, such as MOOSE framework (Gaston et al., 2009), Medcoupling (MED, 2022). In this work, the "General Extrusion" coupling operator of COMSOL with closest point setting is used to map physical fields on different mesh. For an evaluation point in the destination, the "General Extrusion" coupling

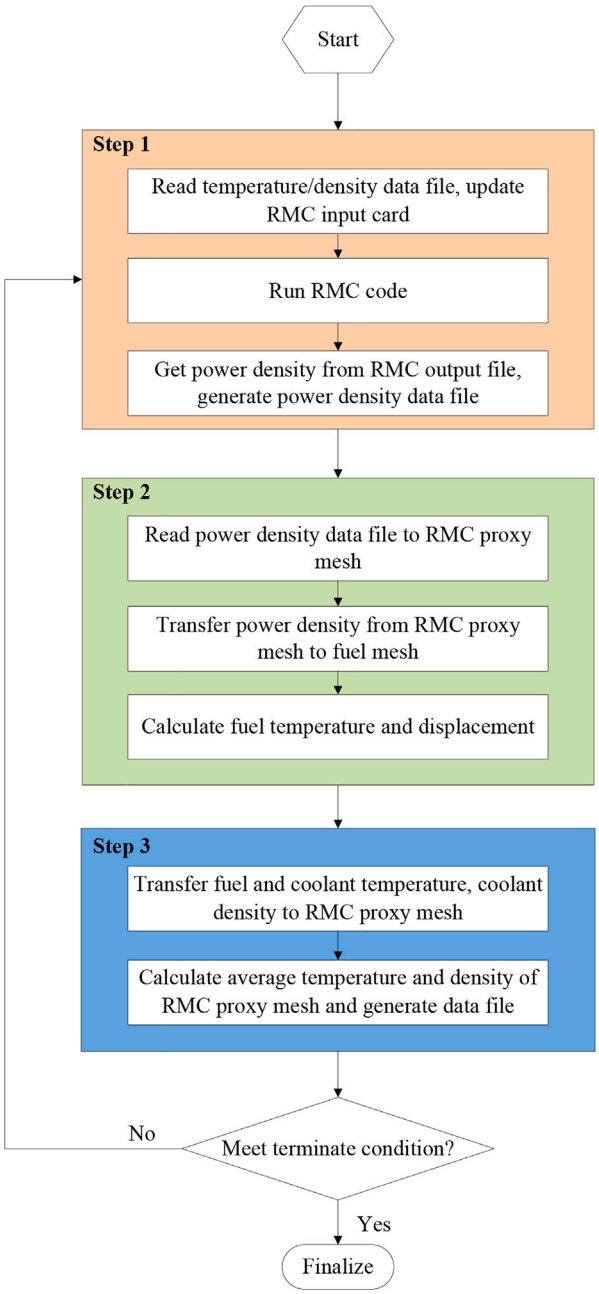

FIGURE 4
Control flow chart of coupling.

operator can find the corresponding point on the source based on coordinates and use the shape function interpolation to obtain the physical field value on the point as the value of evaluation point in the destination. If an evaluation point in the destination is mapped outside the source, the closest point in the source selection is used. The mesh of fuel performance module deforms during the simulation, but the RMC proxy mesh does not. So, the coordinates in the material frame coordinate (corresponding to initial geometry) are used in the "General Extrusion" coupling operator to reduce the errors in data transfer between different meshes. The data mappings include:

TABLE 3 Fuel rod mesh parameters used by fuel performance analysis module.

Domain	Direction	Number of intervals
Pellets	Axial	40
	Radial	20
Cladding	Axial (active length of fuel)	80
	Radial	5

1) Mapping the power density, burnup and neutron flux on the RMC proxy mesh to the fuel rod mesh.
2) Mapping the fuel rod temperature, coolant temperature and density on the fuel rod mesh to the RMC proxy mesh.

Take the mapping of power density as an example to illustrate the process of data transfer. The fuel temperature calculation adopts the finite element method, which requires the power density at the integration point of mesh element. These values are obtained through the coupling operator (search on the RMC proxy mesh, find the point corresponding to the integration point, and use the shape function of the RMC proxy mesh to interpolate the power density field to obtain the value). Since each RMC cell needs one temperature and density value, the temperature and density variables on RMC proxy mesh are volume averaged on each mesh element using integral algorithm. So, the error of data transfer is affected by the mesh size and integration order (the number of integration points in the mesh element). In this study, relatively fine mesh division are used both in RMC and fuel performance module. The default integration order of COMSOL is used. The comparisons below show that these settings are appropriate. Figure 2 shows the power density distribution mapping from RMC proxy mesh to fuel pellet mesh; Figure 3 shows the temperature distribution mapping from fuel rod mesh to RMC proxy mesh. The RMC proxy mesh and fuel rod mesh have different mesh setting. To better illustrate the performance of the data transfer method, the fuel rod mesh is modified more differently (coarser in radial direction, misaligned in axial direction) from RMC proxy mesh. The statistical values of variables on different meshes are listed in Table 1. The statistical values show that the variable mapping between different meshes can be accomplished with high accuracy.

2.3.3 Coupling control flow

Three different study steps of COMSOL are created to control the running sequences. All three study steps are under the control of the "For" node and "End For" node which are solution utility nodes of COMSOL. The study steps are executed circularly to realize the neutronics and fuel performance calculations iteration. The coupling control flow chart and the specific computation tasks of each step are listed in Figure 4. There are different termination methods for the "For" node, such as fixed number of iterations or convergence of global variable or minimization of global variable. The convergence of effective multiplication factor of RMC is used to determine the termination of iterations for simplification, the convergence formulation is given as:

$$\mathbf{err} = \left| \frac{K_{eff\_1} - K_{eff\_0}}{\max\left(K_{eff\_1}, K_{eff\_r}\right)} \right| \leq \mathrm{tol} \tag{21}$$

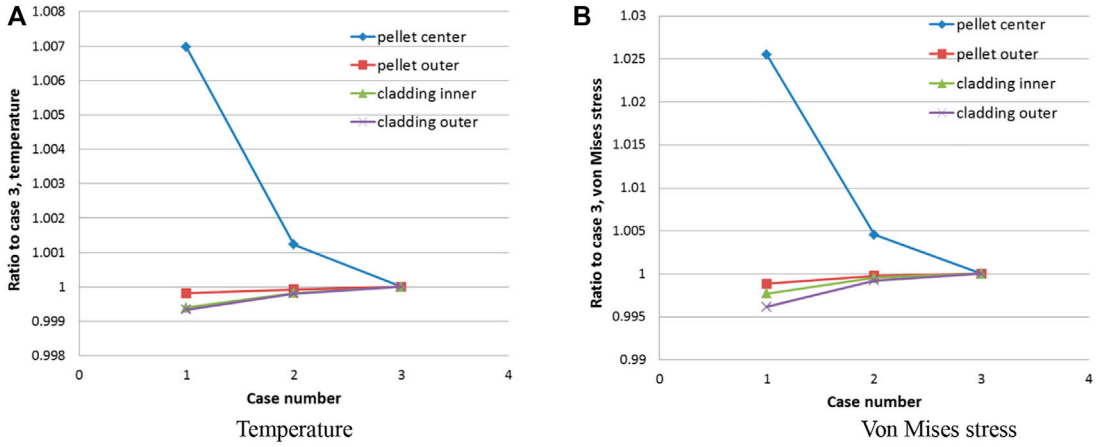

FIGURE 5
Effects of different mesh divisions on fuel rod temperature **(A)** and von Mises stress **(B)**.

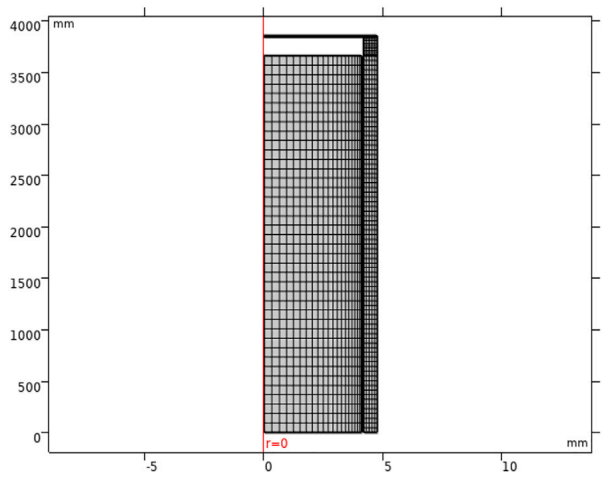

FIGURE 6
Fuel rod mesh used by fuel performance analysis module.

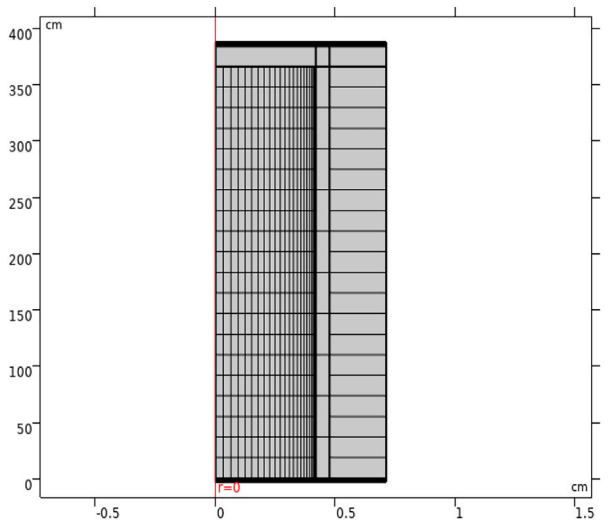

FIGURE 7
Proxy mesh of RMC in COMSOL.

TABLE 4 Fuel rod lattice mesh parameters used by RMC.

Domain	Direction	Number of intervals
Pellets	Axial	20
	Radial	20
Cladding	Axial (active length of fuel)	10
	Radial	1
Gap	Axial (active length of fuel)	10
	Radial	1
Water	Axial (active length of fuel)	20
	Radial	1

where **err** is the relative error, K_{eff_1} is the value of the effective multiplication factor from the current iteration, K_{eff_0} is the value from the previous iteration, K_{eff_r} is the relative tolerance threshold, 1.0 is used, and tol is the relative tolerance, 1e-4 is used.

3 Demonstration calculations

A typical PWR coupled calculation is used to demonstrate the coupled system. The fuel rod lattice includes UO_2 pellet, zircaloy cladding and outside coolant. The steady state coupled problem at the BOL is calculated. Subsequently, with the improvement of the coupled system, it will be further extended to burnup depletion in the whole life cycle. The main modeling parameters are listed in Table 2.

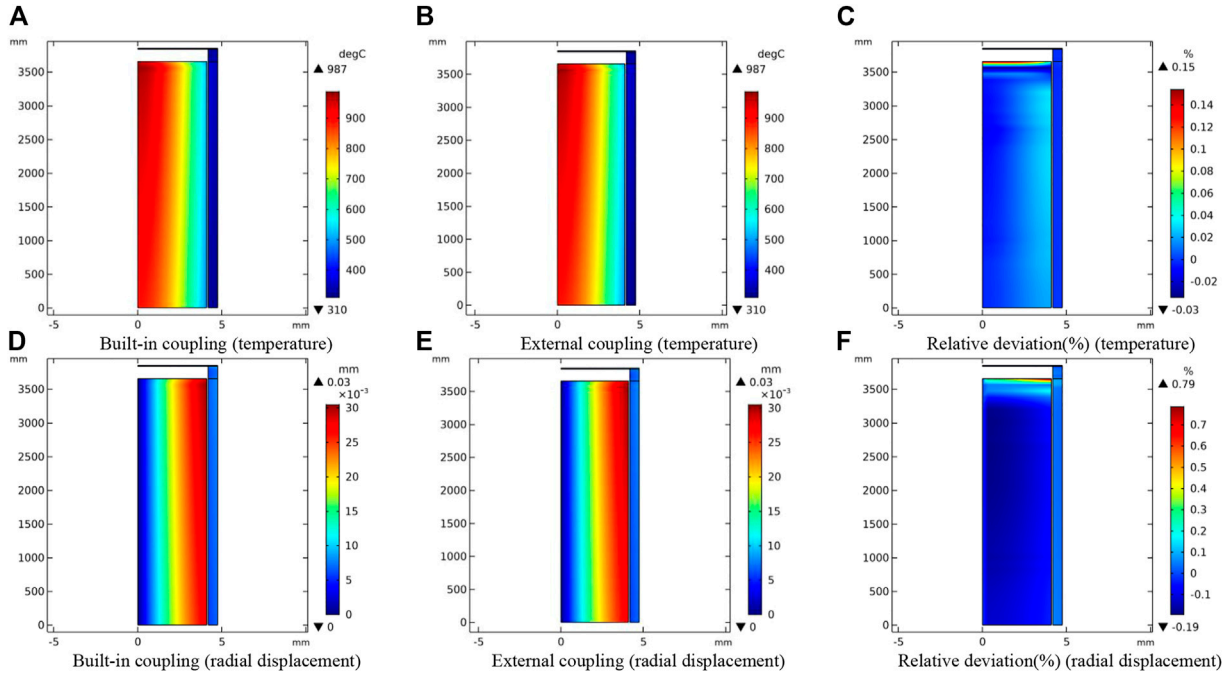

FIGURE 8
Comparison of the temperature **(A–C)** and radial displacement **(D–F)** by the two coupling methods.

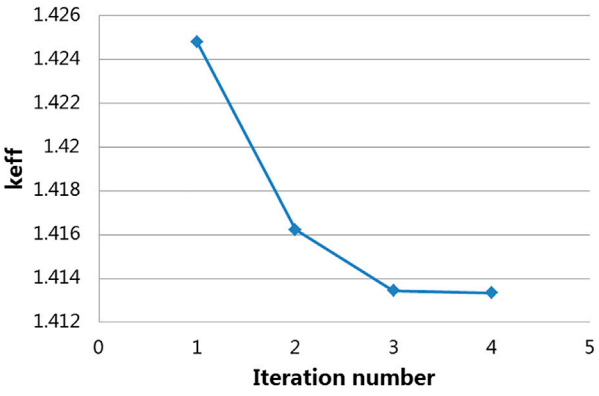

FIGURE 9
Variation of effective multiplication factor with Iteration number.

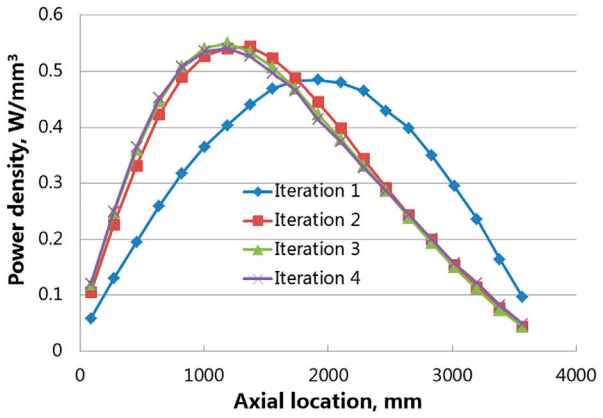

FIGURE 10
Power density along the center axis of the fuel rod during iterations.

3.1 Fuel performance calculation model

The 2D RZ axisymmetric analysis mode is used for the fuel performance calculation, and pellet, cladding and upper end plug are modeled. The detailed pellet geometry is not considered in the modeling to reducing the amount of mesh elements. The flow heat transfer of the coolant is solved axially on the outer surface of the cladding. The pressure boundary conditions are set on the outer surface of the pellet and the inner surface of the cladding, and the load is the internal pressure, which will be update based on the deformed geometry. The constant system pressure is loaded on the outer surface of the cladding. The axial displacement of pellet bottom surface is fixed, and the same for cladding bottom surface.

The outer surface of the pellet and the inner surface of the cladding are set as a contact pair to support the heat transfer and possible mechanical interaction between the pellet and cladding. The inner surface of the cladding is set as destination surface, so the mesh is refined to obtain stable calculation results. The mesh element type for thermal analysis is Lagrange linear, and the mesh element type

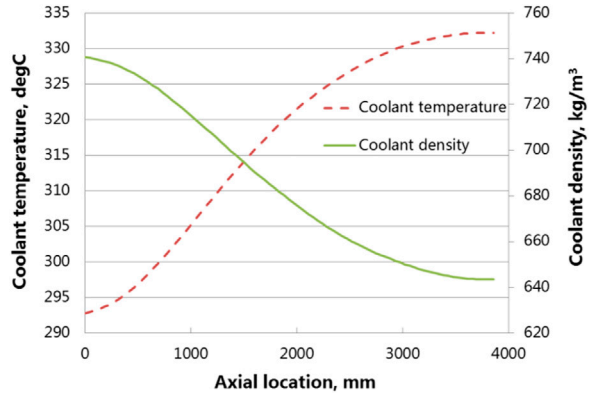

FIGURE 11
Coolant temperature and density distribution after convergence.

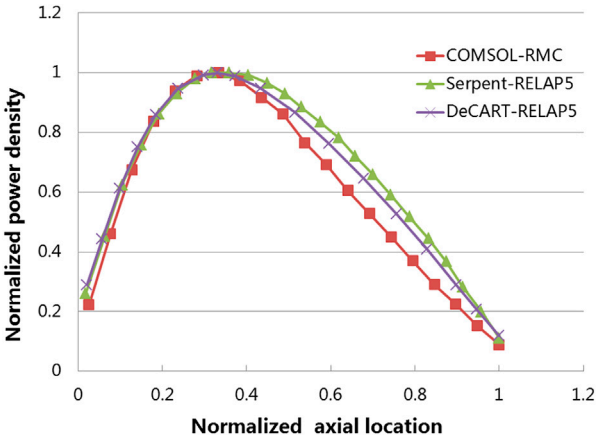

FIGURE 12
Normalized axial power density distributions comparison.

for mechanical analysis is Lagrange quadratic. This will ensure that the thermal strain is of the same order as the total strain, both first orders. Considering the steep radial power distribution at the edge of the pellet, a non-uniform mesh is used, and the mesh density near the edge is higher. Three different pellet and cladding radial mesh divisions (case 1 (10, 3), case 2 (20, 5), case 3 (30, 7)) were established to study the influence of mesh division on temperature and stress calculation. The results are shown in Figure 5. The temperature and stress vary little from case to case. Considering the balance between efficiency and accuracy, case 2 was selected. The fuel rod mesh parameters are listed in Table 3, and the mesh is shown in Figure 6.

3.2 RMC calculation model

Firstly, the proxy mesh of RMC was established in COMSOL, and then the corresponding input card was generated using the RMC input card generation code. The fuel rod lattice mesh parameters are listed in Table 4. A non-uniform division is used to catch the steep radial power distribution at the edge of the pellet. The proxy mesh of RMC in 2D RZ axisymmetric configuration is shown in Figure 7. It is worth noting that the geometry described by RMC is 3D. The pellets, the pellet-cladding gap, the cladding, the upper and lower end plugs, the coolant outside the cladding, and the upper and lower water layers are considered in the RMC modeling. The coolant cylindrical outer surface adopts the total reflection boundary condition, and the boundaries of the bottom and top water reflectors adopt the vacuum boundary condition. This setting approximates a repeating cell arrangement in an infinite space. The representative power distribution will be obtained. If a more accurate distribution is desired, the model needs to scale up to one fuel assembly, or even multiple fuel assemblies, to consider more realistic structural material distributions.

The generations of particles and the number of particles used in the RMC calculation have a significant impact on the calculation results. In this work, the calculation accuracy and efficiency are comprehensively considered, and 1000 are used. The first 200 generations are inactive generations, and the number of particles in each generation is 100000. More initial fission sources in the axial direction can improve the convergence of local power, so 30 initial fission sources are evenly arranged along the axial direction.

4 Results and discussion

4.1 Verification

A simplified case of fuel performance analysis coupled with an external program was constructed to verify the correctness of the coupling methodology proposed in this study. A simple python program was written to represent the calculation of RMC. The program can read the temperature of the mesh element and write the corresponding power density to the hard disk. Assuming that the power density is a function of temperature, the following equation is used to calculate the power density:

$$\mathbf{qv} = \frac{\mathbf{T_{ave}}}{\mathbf{3000}} \tag{22}$$

Following the coupling methodology described in Section 2.3: 1) the average temperature values on the RMC proxy mesh were exported to data file, 2) the python program read the temperature and written the corresponding power density to date file, 3) the power density values were imported into RMC proxy mesh and transferred to the mesh of fuel performance module, 4) after fuel performance analysis was completed, the temperature values were transferred to the RMC proxy mesh and volume averaged. Then repeat the above steps until the calculation is completed. The external coupling was carried out in this way of Picard iteration. The convergence of fuel rod maximum temperature is used to determine the termination of iterations, relative tolerance 1e-3 is used. After 10 iterations, the convergence requirement was met.

The same case was also solved using COMSOL built-in coupling functionality as reference. Figure 8 shows the comparison of temperature and radial displacement distribution of two coupling methods. The maximum relative deviations for temperature and

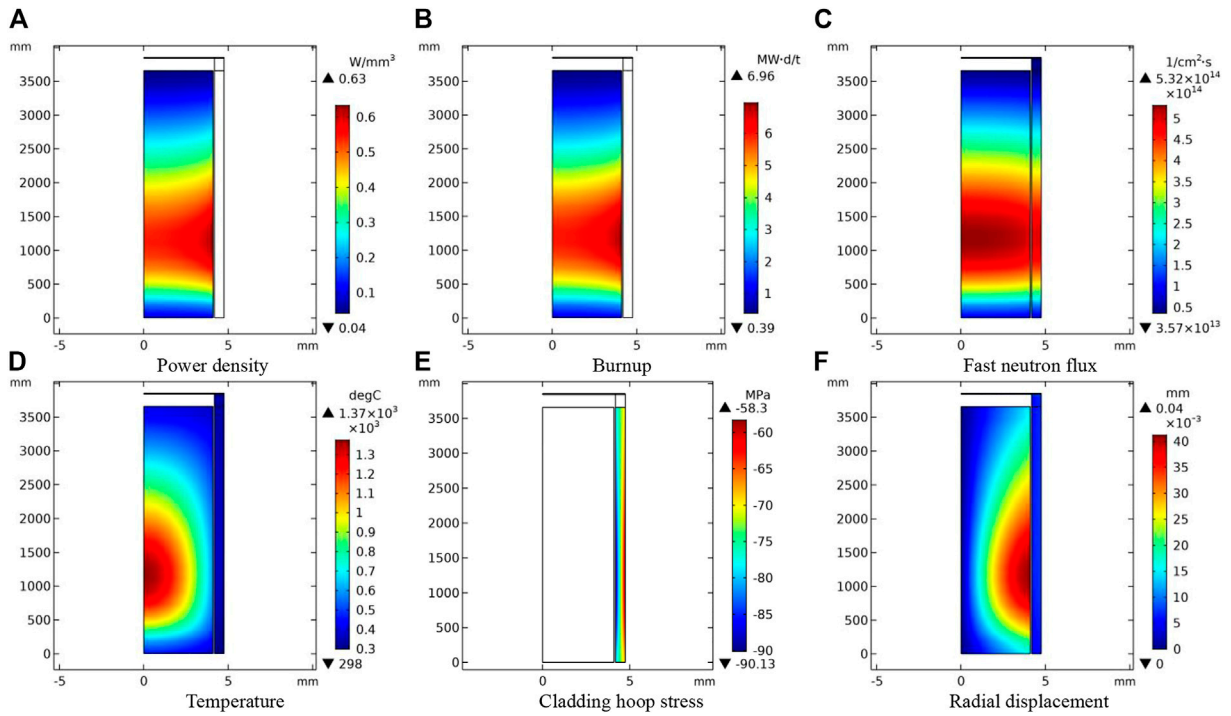

FIGURE 13
Fuel rod performance results: power density **(A)**, burnup **(B)**, fast neutron flux **(C)**, temperature **(D)**, cladding hoop stress **(E)** and radial displacement **(F)** after convergence.

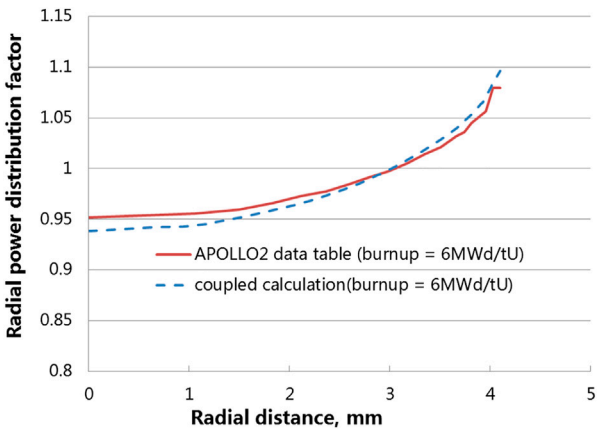

FIGURE 14
Distributions of radial power after convergence.

radial displacement are about 0.15% and 0.79%, indicating that the coupling method proposed in this study is feasible.

4.2 Demonstration case

The fuel rod performance analysis and neutronics demonstration case was solved. Figure 9 shows the variation of effective multiplication factor keff with the number of coupling iterations. It is clear that keff reached steady after 3 iterations in the calculation, and the last two results (the 3rd and 4th iteration) are basically identical according to Figure 9, which means the multiphysics coupling problem is converged after only few iterations.

Power density along the center axis of the fuel rod during iterations was plotted in Figure 10. The power density obtained from RMC under the initial constant temperature filled of 20°C is distributed symmetrically along the axial direction, as illustrated by the blue curve of the first iteration in Figure 10, and the maximum power occurs near the half height of the fuel rod. After that, the peak of power density shifts toward the lower side of the fuel rod in subsequent iterations during calculation. Power density curves other than the initial iteration match well with each other according to Figure 10, especially for results from the last two iterations. Figure 11 shows the coolant temperature and density distribution after convergence, due to the low temperature and high density of the coolant at the lower end, its moderating ability is greater than that of the coolant at the outlet side, so the proportion of thermal neutrons is large, and the fission reaction rate is large. So, the peak of power density is at the lower side of the fuel rod. The coupled Serpent/RELAP5 and DeCart/RELAP5 results for UO_2 single assembly BOL were provided in the literature (Wu and Kozlowski, 2015), the results are comparable with this work. The comparison of normalized axial power density distributions is shown in Figure 12. The locations of power peak are almost consistent. There are some differences in the upper part. The discrepancy could be due to several factors, such as differences in models, input parameters or analysis scale (fuel rod lattice vs. single assembly).

Figure 13 shows distributions of power density (Figure 13A), burnup (Figure 13B), fast neutron flux (Figure 13C), temperature (Figure 13D), cladding hoop stress (Figure 13E) and radial displacement (Figure 13F) in the fuel rod after convergence. The peak of these parameters is located at almost a same height in lower middle area of the fuel rod. The power density and burnup have a similar distribution as expected. The values are higher at the edge of the pellet due to the neutronic rim effect. In contrast, the fast neutron flux is higher in the center of the pellet. The maximum temperature is about 1370°C and occurs in the pellet center of the same height as the peak of power density shown in Figure 13A. Since the external pressure on the cladding is greater than the internal pressure, the cladding is in compressed state, and the hoop compressive stress on the inner side is greater than that on the outer side. Apparently, thermal expansion of the fuel pellets under high temperature is the main driving force for radial displacement during this start-up phase of the reactor. Consequently, the maximum radial displacement or the minimum gap width locates at the height corresponding to the hottest region of the fuel rod, i.e., near 1100 mm in axial direction.

The comparison between the radial power distribution obtained by the coupled system and the APOLLO2 data table from COPERNIC fuel performance code (Jacoud and Vesco, 2000) is shown in Figure 14. The APOLLO2 data table values are linearly interpolated between 0MWd/tU and 2000MWd/tU. The power density at the outer edge of the pellet is higher than the inner region as expected. Since the ^{239}Pu is not enriched significantly at the BOL, such radial distribution is mainly caused by self-shielding. The power distribution obtained by the coupled system and the APOLLO2 data table are similar. The value of the coupling result near the edge of the pellet is a bit higher, and the value at the center of the pellet is a bit lower. APOLLO2 data table is related to burnup and radial position. It reflects the average radial power profile of different radial temperature distribution under the same burnup. The radial power profile from coupling system presented in Figure 14 is corresponding to a specific radial temperature distribution. This may be the reason for the discrepancy.

5 Conclusion

To establish a fuel multiphysics coupling system, a fuel performance analysis module based on the COMSOL Multiphysics software is developed and coupled to Monte Carlo reactor physics code RMC using a novel and robust method. RMC was wrapped as a component of COMSOL to communicate with the fuel performance analysis module. The data transferring and the coupling process was maintained using COMSOL's functionality. The feasibility of the coupling method is verified using typical case. A fuel rod lattice steady state coupling at the BOL is used to demonstrate the coupled system. Through the coupling of neutronics and fuel performance, axial and radial results are obtained considering temperature feedback, coolant density feedback and self-shielding. Although this is a relatively simple case, the calculation results show the potential of the coupled system. Due to the flexible architecture of the coupled system, it is not limited to a specific fuel type. The performance of new designed fuel rod can be analyzed with reasonable setting using the coupled system. Alternatively, the coupled system could be used to derive the fitting parameters for calibrating the neutronics model for a specific and unusual fuel type to speed up the analysis. As for further improvement of the coupled system, burnup depletion will be included to the coupling and fuel assembly scale coupling will be carried out to test the ability of the system.

Data availability statement

The original contributions presented in the study are included in the article/Supplementary Material, further inquiries can be directed to the corresponding authors.

Author contributions

ZL: methodology, fuel performance module development and data analysis. WiZ: conceptualization and supervision. FQ: coupling interface development. YZ: methodology. QL: validation. PC: supervision. CY: project administration. YL: neutronics modelling. WbZ: neutronics modelling. HW: data analysis and check. YH: data analysis and check.

Funding

This study was supported by the National Key Research and Development Program of China (No. 2022YFB1902300).

Conflict of interest

The authors declare that the research was conducted in the absence of any commercial or financial relationships that could be construed as a potential conflict of interest.

Publisher's note

References

CASL (2020). Consortium for advanced simulation of light water reactors (CASL). Available http://www.casl.gov/ (Accessed February 10, 2023).

Clarno, K. T., Hamilton, S. P., Philip, B., Berrill, M. A., Sampath, R. S., Allu, S., et al. (2012). "Integrated radiation transport and nuclear fuel performance for assembly-level simulations,". ORNL/TM-2012/33.

Gaston, D., Newman, C., Hansen, G., and Lebrun-Grandié, D. (2009). Moose: A parallel computational framework for coupled systems of nonlinear equations. *Nucl. Eng. Des.* 239, 1768–1778. doi:10.1016/j.nucengdes.2009.05.021

Geelhood, K. J., Lusher, W. G., Raynaud, P. A., and Porter, I. E. (2015). "FRAPCON-4.0: A computer code for the calculation of steady-state, thermal-mechanical behavior of oxide fuel rods for high burnup,". PNNL-19418, Vol. 1 Rev. 2.

Gleicher, F. N., Spencer, B., Novascone, S., Williamson, R., Martineau, R. C., Rose, M., et al. (2013). *Coupling the core analysis program DeCART to the fuel performance application BISON, international conference on mathematics and computational methods applied to nuclear science and engineering*. Austria: IAEA.

Gleicher, F., Ortensi, J., DeHart, M., Wang, Y., Schunert, S., Novascone, S., et al. (2016). *The application of MAMMOTH for a detailed strongly coupled fuel pin simulation with a station blackout, top fuel 2016, september 2016*. USA: Idaho National Laboratory.

Jacoud, J. L., and Vesco, P. (2000). "Description and qualification of the COPERNIC/TRANSURANUS (update of may 2000) fuel rod design code, framatome nuclear fuel,". TFJCDC1556.

Kramman, E. M., and Freeburn, H. R. (1987). "Escore–the epri steady-state core reload evaluator code: General description,". Technical Report EPRI NP-5100.

Lassmann, K., O'Carroll, C., van de Laar, J., and Walker, C. T. (1994). The radial distribution of plutonium in high burnup UO2 fuels. *J. Nucl. Mater.* 208, 223–231. doi:10.1016/0022-3115(94)90331-x

Lee, C. B., Kim, D. H., Song, J. S., Bang, J. G., and Jung, Y. H. (2000). RAPID model to predict radial burnup distribution in LWR UO2 fuel. *J. Nucl. Mater.* 282, 196–204. doi:10.1016/s0022-3115(00)00408-6

Lusher, W. G., Geelhood, K. J., and Porter, I. E. (2015). "Material property correlations: Comparisons between FRAPCON-4.0, FRAPTRAN-2.0, and MATPRO,". PNNL-19417 Rev. 2.

MED (2022). MEDCoupling developer's guide, SALOME-platform. Available https://docs.salome-platform.org/latest/dev/MEDCoupling/developer/reference.html (Accessed February 10, 2023).

Olander, D. R. (1976). Fundamental aspects of nuclear reactor fuel elements. *Tech. Inf. Cent. Office Public Aff.*, 137–138.

Palmer, I. D., Hesketh, K. W., and Jackson, P. A. (1982). *A model for predicting the radial power profile in a fuel pin, Specialists' meeting on fuel element performance computer modelling*. United Kingdom: British Nuclear Fuels Ltd.

Rintala, V., Suikkanen, H., Schubert, A., and Van Uffelen, P. (2022). Supplementing fuel behaviour analyses via coupled Monte Carlo neutronics and fission product solution. *Nucl. Eng. Des.* 389 (111668), 111668. doi:10.1016/j.nucengdes.2022.111668

Ross, A. M., and Stoute, R. L. (1962). *Heat transfer coeffient between UO2 and Zircaloy-2*. Canada: Atomic Energy of Canada Technical Report.

Scolaro, Y., Robert, I., Clifford, C., and Fiorina, A. P. (2019). *Coupling methodology for the multidimensional fuel performance code offbeat and the Monte Carlo neutron transport code SERPENT, Top Fuel 2019*. Seattle, WA.

Suikkanen, H., Rintala, V., Schubert, A., and Van Uffelen, P. (2020). Development of coupled neutronics and fuel performance analysis capabilities between Serpent and TRANSURANUS. *Nucl. Eng. Des.* 359 (110450), 110450. doi:10.1016/j.nucengdes.2019.110450

Van Uffelen, P., Hales, J., Li, W., Rossiter, G., and Williamson, R. (2019). A review of fuel performance modelling. *J. Nucl. Mater.* 516, 373–412. doi:10.1016/j.jnucmat.2018.12.037

Wang, K., Li, Z., She, D., Liang, J., Xu, Q., Qiu, Y., et al. (2015). Rmc – a Monte Carlo code for reactor core analysis. *Ann. Nucl. Energy* 516, 121–129. doi:10.1016/j.anucene.2014.08.048

Weng, M., Liu, S., Liu, Z., Qi, F., Zhou, Y., and Chen, Y. (2021). Development and application of Monte Carlo and COMSOL coupling code for neutronics/thermohydraulics coupled analysis. *Ann. Nucl. Energy* 161 (108459), 108459. doi:10.1016/j.anucene.2021.108459

Wu, X., and Kozlowski, T. (2015). Coupling of system thermal–hydraulics and Monte-Carlo code: Convergence criteria and quantification of correlation between statistical uncertainty and coupled error. *Ann. Nucl. Energy* 75, 377–387. doi:10.1016/j.anucene.2014.08.016

frontiers | Frontiers in Energy Research

TYPE Original Research
PUBLISHED 17 March 2023
DOI 10.3389/fenrg.2023.1092433

OPEN ACCESS

EDITED BY
Shichang Liu,
North China Electric Power University, China

REVIEWED BY
Rong Liu,
South China University of Technology, China
Yuexia Wang,
Fudan University, China

*CORRESPONDENCE
Lu Wu,
wulu1002@qq.com
Jing Zhang,
Jingzhang@nwpu.edu.cn

SPECIALTY SECTION
This article was submitted to Nuclear Energy, a section of the journal Frontiers in Energy Research

RECEIVED 08 November 2022
ACCEPTED 07 March 2023
PUBLISHED 17 March 2023

CITATION
Ma C, Liu C, Zhao M, Xin T, Wu L, Pan R, Qin J and Zhang J (2023), Phase-field study of the effect of stress field and fission rate on intragranular Xe bubble evolution in U_3Si_2 nuclear fuel. *Front. Energy Res.* 11:1092433. doi: 10.3389/fenrg.2023.1092433

Phase-field study of the effect of stress field and fission rate on intragranular Xe bubble evolution in U_3Si_2 nuclear fuel

Cong Ma[1], Caiyan Liu[2], Min Zhao[1], Tianyuan Xin[1], Lu Wu[1]*, Rongjian Pan[1], Jiantao Qin[1] and Jing Zhang[3]*

[1]The First Sub-Institute, Nuclear Power Institute of China, Chengdu, China, [2]School of Materials Science and Engineering, Xi'an University of Technology, Xi'an, China, [3]School of Material Science and Engineering, Northwestern Polytechnical University, Xi'an, China

Due to the superior thermal conductivity and high uranium density, U_3Si_2 is an excellent candidate for conventional UO_2 nuclear fuel and shows great potential application in accident-tolerant fuel (ATF) assembly of light water reactors (LWRs). Currently, the behavior of Xe bubbles with internal or applied stress is rarely investigated, restricting further understanding of swelling in U_3Si_2. The mesoscopic phase-field method has been developed in this work to study the spatial and temporal Xe bubble evolution in U_3Si_2. The results show that the bubble density and its average size increase as the fission rate increases. Applied stress accelerates the nucleation and growth of gas bubbles, reshaping the bubbles' morphology from spherical in a stress-free state into elongated along the applied direction in a stressed state. The gas bubbles in a local dislocation stress field nucleate preferentially at stress-concentrated sites and spread over the whole system in succession, and the bubble coarsening is controlled by the stress overlap of the dislocation pair. The results show a practical phase-field method for Xe bubble evolution study in U_3Si_2, which can be expanded into swelling behavior investigation in other fuels and lay a solid foundation for the development of ATF assembly.

KEYWORDS

U_3Si_2 fuel, phase-field simulation, Xe bubble evolution, fission rate, applied stress, dislocation stress field

1 Introduction

U_3Si_2 has been considered a promising accident-tolerant fuel (ATF) to take the place of the UO_2 pellets clad in Zircaloy used in light water reactors (LWRs) since the Fukushima-Daiichi accident (Bischoff, 2014). The reasons ascribed to the U_3Si_2 show higher thermal conductivity and uranium density than UO_2 (White et al., 2015) though it has a lower melting temperature than UO_2 (Miao et al., 2018). Owing to the extremely low solubility in the nuclear fuel, the fission gas atoms produced during the nuclear reaction process tend to accumulate in voids or grain boundaries. The voids or grain boundaries filled with gases form gas bubbles, leading to fuel pellets' volume swelling and cracking, affecting fuel performance and the reactors' safety. Hence, predicting and understanding gas bubble evolution is crucial for the scientific design of U_3Si_2 nuclear fuel, optimizing fuel operation, and reducing uncertainty in operational and safety margins. We know that the swelling of dispersion U_3Si_2 fuel is a significant issue in research reactors (Finlay et al., 2004); however, the swelling

mechanism remains unclear when U_3Si_2 fuel is used in the typical temperature and fission rate of commercial LWRs.

Up to now, we lack available experimental data in light water reactors due to the oxidation of the U_3Si_2 samples at a specific temperature and fission rate. Therefore, researchers are considering using computer simulation to study the performance of U_3Si_2 fuel. On the other hand, gas bubble evolution in U_3Si_2 nuclear fuel is a highly complex process that involves tremendous time and length scales from the scale of femtoseconds and nanometers to the scale of years and meters; thus, it is popular to study U_3Si_2 using a multiscale simulation method. The phase-field simulation is a mesoscopic method based on the Ginzburg–Landau phase transition theory. It can deal with large length and time-scale issues such as the evolution of voids and bubbles under irradiation. Other approaches with comparable length and time-scales to the phase-field are kinetic Monte Carlo methods (KMC) (Soneda et al., 2003; Caturla et al., 2006; Torre et al., 2006), object kinetic Monte Carlo (OKMC) (Domain et al., 2004; Surh et al., 2004), cluster dynamics (Xu et al., 2012a; Xu et al., 2012b), and rate theory (Veshchunov, 2000; Surh et al., 2005; Bonilla et al., 2006; Veshchunov et al., 2006; Ortiz et al., 2007; Veshchunov et al., 2007). These studies have been used to study nuclear materials and provide us with helpful knowledge. The phase-field method is advantageous in taking into account the local microstructure inhomogeneity and long-range elastic interactions, making it capable of modeling the evolution of the microstructure and properties in U_3Si_2 and bridging atomistic and macroscopic simulations.

The evolution of gas bubbles is affected by two main factors: fuel fabrication conditions, such as stress and grain size, and operation conditions of reactors, such as temperature and fission rate. Due to the initial stage of different types of bubbles being considered to be similar that start as isolated fission gas atoms inside grains, understanding the mechanism of the nucleation and growth of intragranular bubbles plays a critical role. Some typical phase-field models have been proposed to study the evolution of bubbles in irradiated materials (Stan et al., 2007; Hu et al., 2009; Hu et al., 2010; Millett et al., 2011; Millett and Tonks, 2011; Millett et al., 2012a; Millett et al., 2012b; Li et al., 2013; Hu et al., 2015; Hu et al., 2016; Xiao et al., 2020). Few phase-field models can reproduce the stable intragranular gas bubble morphological changes upon irradiation. These models consider factors such as initial bubble density and the contact angle. However, they do not sufficiently consider the fuel fabrication conditions, such as stress and operating conditions of reactors in service, especially related to the extremely important ATF fuel U_3Si_2. Aagesen et al. (2020) developed a model for U_3Si_2 intergranular fission gas bubble behavior in LWRs. This phase-field model studied the growth, interconnection, and venting of intergranular fission gas bubbles, as well as determined fractional grain boundary coverage at gas saturation. Larry revealed the behaviors of intergranular fission gas bubbles but did not refer to intragranular gas bubbles in U_3Si_2 under different operating conditions. Wang et al. (2022) employed a phase-field model to describe the evolution of intragranular gas bubbles in tungsten under external loading. They found that intragranular fission gas bubbles vary with the direction and magnitude of external loading, and bubbles growth is accelerated along the loading direction. All the aforementioned studies provide us with a knowledgeable understanding of bubbles. It is well known that microstructures inhomogeneous are pretty common in materials in service.

The microstructures' inhomogeneity will cause local elastic energy or interface energy, which will not only affect the spatial distribution of the vacancy and gas atom but also their combination in the crystal, further affecting the formation of bubbles. The influence of internal microstructures on bubble formation is scarcely mentioned. The stress, irradiation, and microstructures' inhomogeneous effect on gas bubble formation wait to be revealed. Our current work provides a more comprehensive phase-field model of gas bubble evolution, a better understanding of intragranular Xe bubble evolution, and a solid foundation for the future study of the nucleation and growth of intergranular Xe bubble in U_3Si_2 fuel.

In this work, we mainly control three variables, the fission rate, applied stress, and dislocation stress field, to study their influence on intragranular Xe bubble evolution. The work is organized as follows. Section 2 presents the functional free energy and equation of motion to illustrate the model construction procedure. Section 3 demonstrates the Xe bubble evolution diagram for various fission rates (Section 3.1), bubbles upon applied stress (Section 3.2), and bubbles in a dislocation dipole stress field (Section 3.3). Section 4 draws the main conclusions.

2 Phase-field model formulation and parametrization

In this section, we develop a two-dimensional phase-field model with the assumption that the dominant defect species are U vacancies and fission gas atoms on U lattice sites. The insoluble fission gas atoms are described as Xe on U sites due to Xe production occurring at a rate nearly ten times that of Kr (Olander, 1976). Moreover, the phase-field model describes the evolution of intragranular Xe bubbles in U_3Si_2 fuels under irradiation conditions. The irradiated interstitials diffuse several orders of magnitude faster than vacancies; they either recombine quickly with vacancies or become trapped by dislocations and grain boundaries, leaving abundant vacancies and fission gas atoms interior. Hence, only gas atoms and vacancies are considered in formulating the functional free energy. In general, the total free energy F of the system is written as a function of phase-field variables c_{gas} (for gaseous atoms) and c_{vac} (for vacancies).

$$F = \int_V \left[f\left(c_{gas}, c_{vac}\right) + \frac{\kappa_{gas}}{2}\left|\nabla c_{gas}\right|^2 + \frac{\kappa_{vac}}{2}\left|\nabla c_{vac}\right|^2 + F^{elastic} \right] dV. \quad (1)$$

The total free energy F is a volume integral of free energy density, which consists of chemical energy, gradient energy, and elastic interaction energy. $F(c_{gas}, c_{vac})$ is the chemical energy. κ_{gas} and κ_{vac} are gradient coefficients associated with the gradient energy of gas bubbles, $F^{elastic}$ is the elastic energy associated with the stress field, and $c_{gas}(r,t)$ and $c_{vac}(r,t)$ represent the gas atom concentration and vacancy concentration at site r and time t.

2.1 Chemical energy

The evolution of Xe bubbles in the phase-field model is driven by the minimization of the total free energy of the system. Chemical

energy is a crucial part of the total free energy of the system, and it is usually difficult to calculate the chemical free energy of U_3Si_2 fuel when defects and irradiation-induced phases are considered. Based on the simulation observations of gas bubbles (Hu et al., 2009), we give the form of chemical energy as

$$f\left(c_{gas}, c_{vac}\right) = f_{vac}\left(c_{vac}^4 + b_3 c_{vac}^3 + b_2 c_{vac}^2 + b_1 c_{vac} + b_0\right) + f_{gas}\left(c_{gas} - c_{gas}^0\right)^2 + f_{bind}\left(c_{gas} - c_{gas}^0\right)\left(c_{vac} - c_{vac}^0\right), \tag{2}$$

where f_{vac}, f_{gas}, f_{bind}, b_0, b_1, b_2, and b_3 are constants, and constant f_{bind} is associated with the binding energy between vacancy and gas atom. Here, f_{gas}, f_{vac}, b_0, b_1, b_2, and b_3 are affected by the equilibrium properties, and c_{gas}^0 and c_{vac}^0 are the solubility of the gas atom and vacancy in the matrix phase, respectively.

2.2 Elastic energy

The fuels suffer mechanical or thermal stress upon processing or heat treatment, and they may also be subjected to complicated applied stress in service. In addition to that, various inner inhomogeneous microstructures, such as dislocations or defect clusters, will also inevitably introduce local distortion. These applied or internal stresses cause gas atoms or vacancies to diffuse directionally, reshaping the bubbles' morphology (Braski et al., 1979; Suzuki et al., 1990; Wang et al., 2022). It is necessary to consider the elastic effects in the bubbles model for U_3Si_2. In this study, both the applied stress and dislocation stress field were considered in the elastic term, and the elastic energy $F^{elastic}$ is given by

$$F^{elastic} = \frac{1}{2}\lambda_{ijkl}\varepsilon_{ij}^{ei}\varepsilon_{kl}^{ei}, \tag{3}$$

where $\varepsilon_{ij}^{ei}, \varepsilon_{kl}^{ei}$ are the elastic strain and λ_{ijkl} is the elastic stiffness tensor. Here, the elastic stiffness is assumed to be inhomogeneous and is described as a statistical average of the stiffness of the matrix and gas (Hu et al., 2009).

$$\lambda_{ijkl} = \lambda_{ijkl}^0\left(1 - c_{vac}\right) + \lambda_{ijkl}^{'} c_{gas}. \tag{4}$$

The formula ensures elastic constants are zero in voids where $c_{vac} = 1$ and $c_{gas} = 0$. In gas bubbles where c_{vac} equals 1, the elastic constants depend on the gas concentration c_{gas}. The effect of dislocation on the Xe bubble is introduced through a pair of stable dislocation configurations into the elastic term of the free energy density. Then, the intrinsic strain is composed of three parts, which can be written as

$$\varepsilon_{ij}^{*} = \varepsilon_{ij}^{vac} + \varepsilon_{ij}^{gas} + \varepsilon_{ij}^{dis}, \tag{5}$$

where ε_{ij}^{vac} is the eigenstrain related to vacancy, ε_{ij}^{gas} is the eigenstrain related to gas atom, and ε_{ij}^{dis} is the eigenstrain associated with a spatial distribution of dislocations. The dislocation stress field causes the change of elastic energy in the form of eigenstrain, and the formula is as follows:

$$\varepsilon_{ij}^{dis} = \frac{1}{2d}\left(b_i n_j + b_j n_i\right). \tag{6}$$

TABLE 1 Parameters used for phase-field simulations.

Parameter	Value
F^{*}	−0.2
t^{*}	0.0005
f_{gas}^{*}	0.1
f_{vac}^{*}	1.102
κ_{gas}^{*}	0.076
κ_{vac}^{*}	0.076
c_{gas}^{0}	0.012
c_{vac}^{0}	0.032
b_0	−0.012
b_1	0.357
b_2	0.313
b_3	−1.663
C_{11}	155 GPa
C_{12}	47 GPa
C_{44}	65 GPa
M_{gas}^{*}	36.4
M_{vac}^{*}	36.4
T	1200K
$\dot{f}^{*}$	0,0.0126,0.0326,0.0526,0.0726
Y_{Xe}	0.2156

Here, $b_{i,j}$, $n_{i,j}$, and d are the Burgers vector, the normal of the slip plane, and the interplanar distance of the slip plane, respectively.

In this work, a pair of dislocation dipoles (consisting of two edge dislocations) is introduced on the (110) slip plane. We choose the crystal direction $[\bar{1}10]$, [110], and $[00\bar{2}]$ as the x-, y-, and z-axis, respectively, and inserted the edge dislocation with Burgers vector $b = \frac{a_0}{2}[\bar{1}10]$ in the (110) plane, where a_0 is the lattice constant.

2.3 Evolution equations and parametrization

The movement of vacancy and gas atoms is described by the Cahn–Hilliard equations (Cahn, 1961).

$$\frac{\partial c_{gas}}{\partial t} = \nabla \cdot M_{gas}\nabla\frac{\delta F}{\delta c_{gas}} + \dot{g}_{gas}, \tag{7}$$

$$\frac{\partial c_{vac}}{\partial t} = \nabla \cdot M_{vac}\nabla\frac{\delta F}{\delta c_{vac}} + \dot{g}_{vac}, \tag{8}$$

where M_{gas} and M_{vac} are the mobility of gas atoms and vacancies, respectively. Here, F is the total free energy given by Eq. 1, and $\dot{g}_{gas}$ and $\dot{g}_{vac}$ are the generation rates of gas atoms and vacancies, respectively.

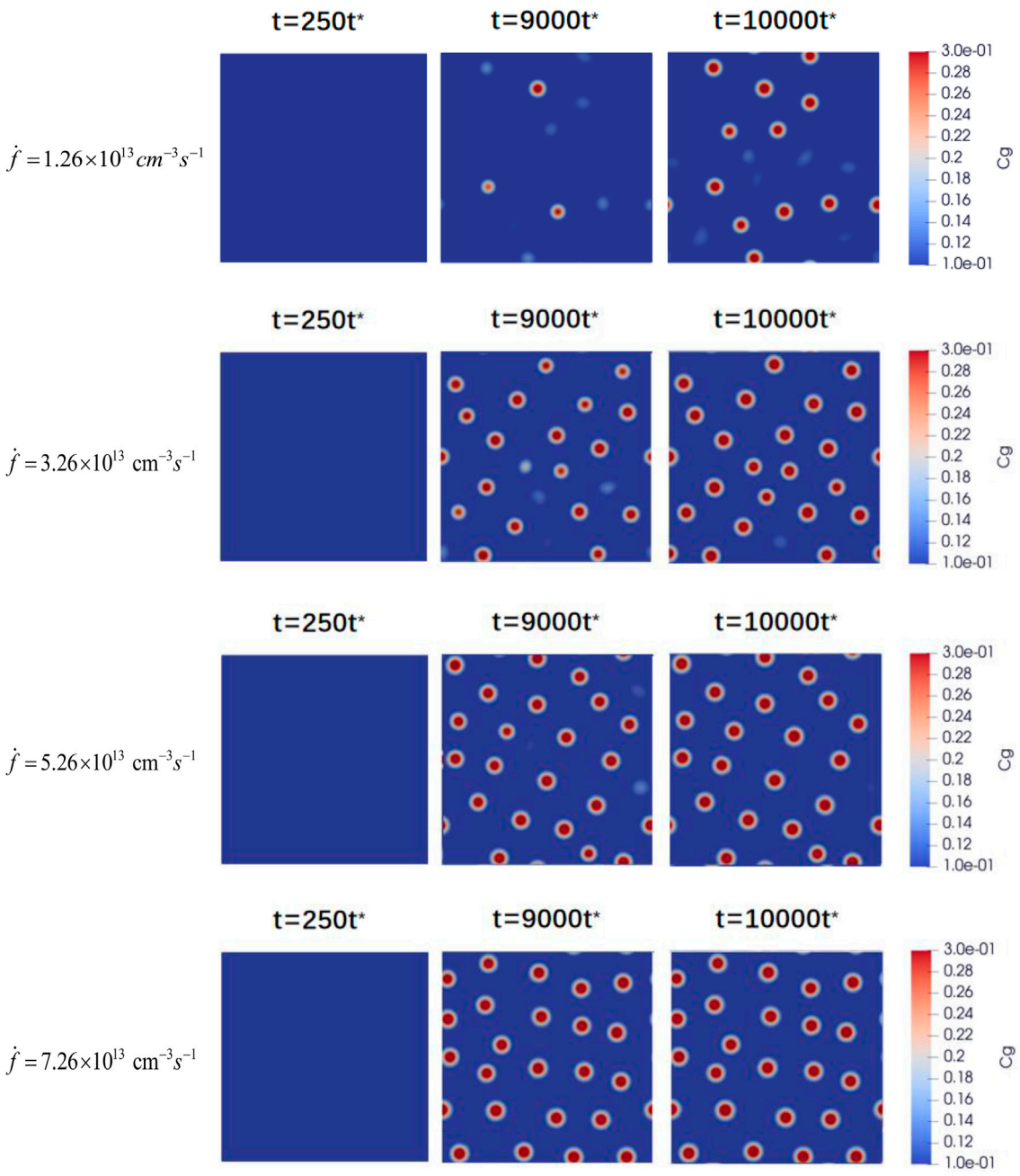

FIGURE 1
Two-dimension evolution diagram of the Xe bubbles at time t = 250t*, 9000t*, and 10000t* under fission rates of 1.26×10^{13} cm^{-3}s^{-1}, 3.26×10^{13} cm^{-3}s^{-1}, 5.26×10^{13} cm^{-3}s^{-1}, and 7.26×10^{13} cm^{-3}s^{-1}.

The generation rates of gas atoms and vacancies terms are given by

$$\dot{g}_{gas} = g^0_{gas} h_m, \tag{9}$$

$$\dot{g}_{\mathrm{vac}} = g^0_{vac} h_m, \tag{10}$$

where g^0_{gas} is a constant rate of Xe production and h_{m} is a switching function that has the value of 1 in the fuel matrix and 0 inside the bubble.

The Xe production rate is written as

$$g^0_{gas} = \dot{f} Y_{Xe}, \tag{11}$$

where $\dot{f}$ is the fission rate and Y_{Xe} is the fission yield of Xe; Y_{Xe} equals 0.2156 based on the thermal neutron Xe yield for U-235 (Agency, 2017). Based on the typical operating conditions for commercial LWRs (Olander, 1976), $\dot{f}$ can be estimated to be 1.26×10^{13} cm^{-3}s^{-1}, 3.26×10^{13} cm^{-3}s^{-1}, 5.26×10^{13} cm^{-3}s^{-1}, and 7.26×10^{13} cm^{-3}s^{-1}; in addition, a zero fission rate condition is also included in our simulation. The generation rates of vacancies have not been determined to our knowledge, and we assume a value of $g^0_{\mathrm{vac}} = g^0_{gas}$.

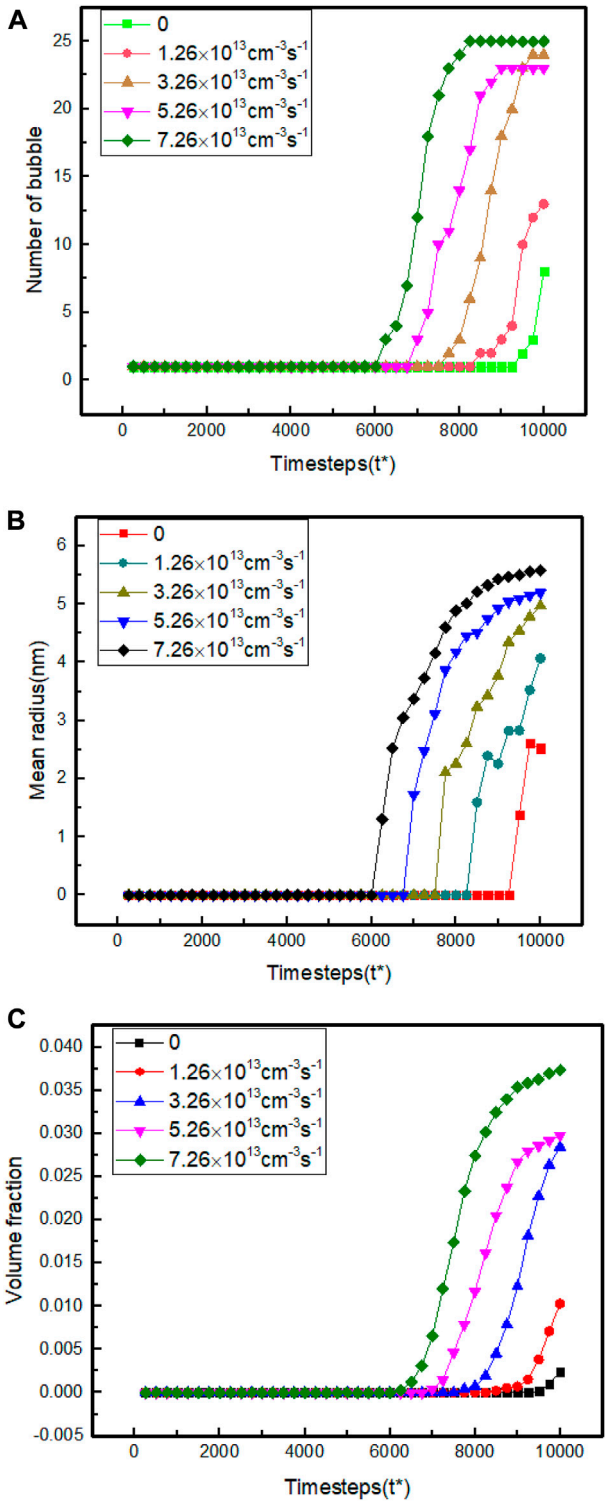

FIGURE 2
Comparison of the **(A)** number, **(B)** mean radius, and **(C)** volume fraction of Xe bubbles at different fission rates.

To improve solution efficiency and ensure all quantities are of order unity, the governing equations Eqs 8, 9 were non-dimensionalized, using the characteristic length $r_0 = 0.1\,\mu m$, and the shear modulus of the matrix can be seen in Chattaraj and Majumder (2018).

$$r_i^* = r_i/r_0, t^* = M_{gas}^0 t/r_0^2 C_{44}, F^* = F/C_{44}, f_{gas}^* = f_{gas}/C_{44},$$
$$f_{vac}^* = f_{vac}/C_{44}, \kappa_{gas}^* = \kappa_{gas}/r_0^2 C_{44}, \kappa_{vac}^* = \kappa_{vac}/r_0^2 C_{44}, \quad (12)$$
$$M_{gas}^* = M_{gas}/M_{gas}^0, M_{vac}^* = M_{vac}/M_{vac}^0, \dot{f}^* = \dot{f}/r_0,$$

where C_{44} is the shear modulus of the matrix and $M_{gas/vac}^0$ is the characteristic mobility. Table1 shows the value of the model parameters used in our simulations.

3 Results and discussion

3.1 Xe bubble evolution under different fission rates

First, a comparative study of the intragranular Xe bubbles at typical fission rate conditions in LWRs is checked, and the fission rates' effect on bubble morphology is explored. The stress effects are not considered to clarify the fission rate's contribution. The simulations were implemented at a typical temperature of 1200K in LWRs, with a mesh grid of 128 and $\Delta l = 0.2$ nm, using the implicit Fourier transformation method. To improve evolution efficiency and enhance the simulation effect, we introduce $\xi_g = 0.0025$ and $\xi_v = 0.0025$ as the thermal fluctuations of gas atoms and vacancies, respectively. The simulation evolution results of the intragranular Xe bubbles under different fission rates and statistical analysis are shown in Figure 1 and Figure 2, respectively.

$$\dot{f} = 1.26 \times 10^{13} cm^{-3} s^{-1},$$
$$\dot{f} = 3.26 \times 10^{13} \mathrm{cm}^{-3} s^{-1},$$
$$\dot{f} = 5.26 \times 10^{13} \mathrm{cm}^{-3} s^{-1},$$
$$\dot{f} = 7.26 \times 10^{13} \mathrm{cm}^{-3} s^{-1}.$$

The predicted effect of the fission rate on the intragranular Xe bubble evolution in fuel U_3Si_2 is displayed in Figure 1 and Figure 2. Five typical fission rate conditions of 0, 1.26×10^{13} $cm^{-3}s^{-1}$, 3.26×10^{13} $cm^{-3}s^{-1}$, 5.26×10^{13} $cm^{-3}s^{-1}$, and 7.26×10^{13} $cm^{-3}s^{-1}$ are investigated in the simulations. The concentrated vacancies generated upon irradiation segregate and form vacancies clusters at the beginning. The limited solubility of fission gases in the U_3Si_2 matrix drives the gases to fill into these clusters through short-range diffusion steps. The void nucleation and gas filling co-occur, and gases swelling and void shrinkage effect attains equilibrium at the gas concentration approaches roughly 0.3 in a void. The voids persistently grow and coarsen by absorbing both vacancies and gases in such an equilibrium state for an extended period. With the increased fission rate, the incubation period of Xe bubbles is generally advanced, and the final bubble number, the average radius, and the volume fraction are enhanced. The volume fraction of Xe bubbles is highest for the enormous fission rate. As presented in Eqs 7, 9, the defect production rate is proportional to the fission rate; the point defects then rises with an increased fission rate. Although the defects annihilate simultaneously, numerous defects accumulation are generally found with enhanced

10.3389/fenrg.2023.1092433

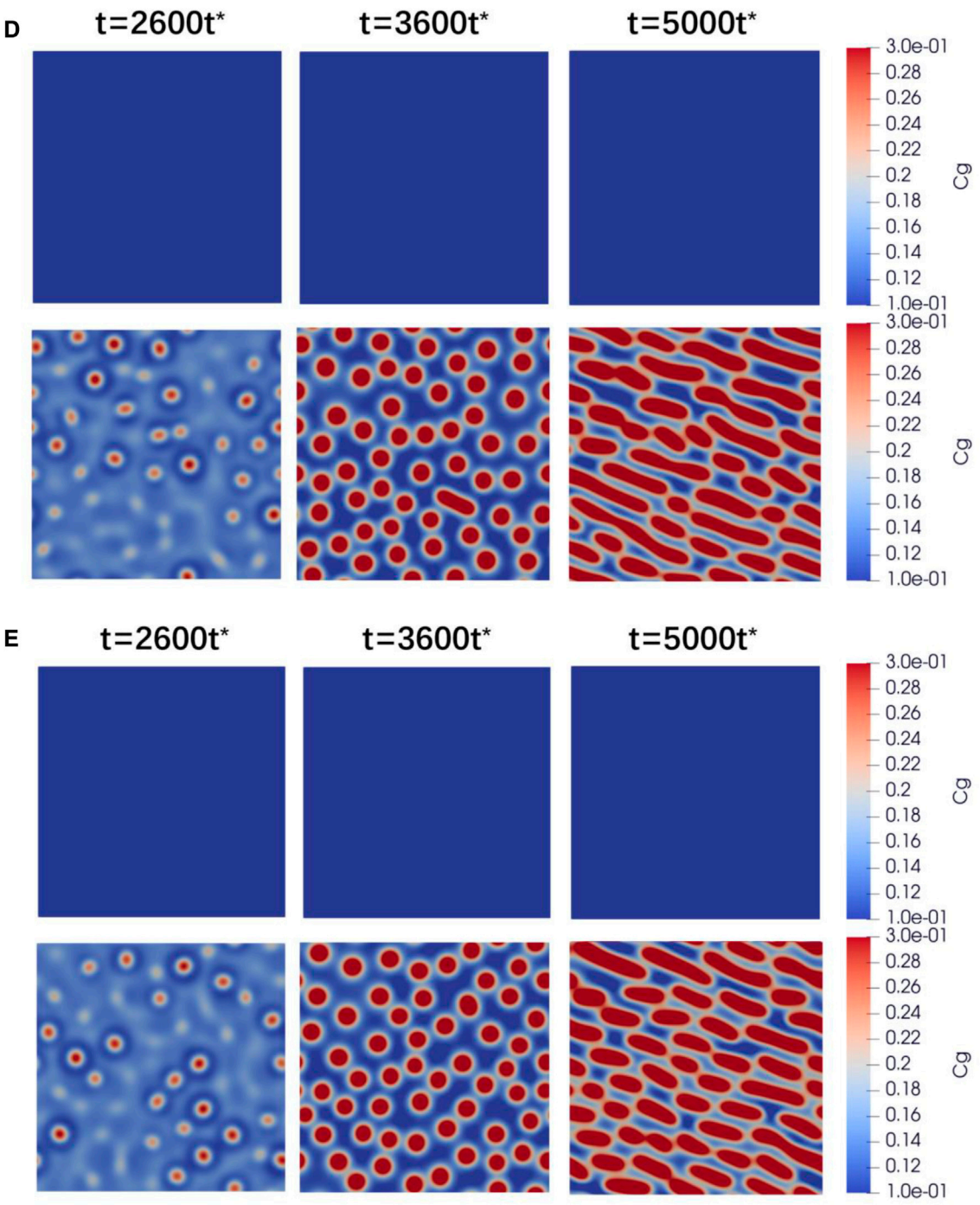

FIGURE 3
Xe bubble evolution with applied stress under different fission rates **(D)** 1.26×10^{13} $cm^{-3}s^{-1}$ and **(E)** 7.26×10^{13} $cm^{-3}s^{-1}$.

fission rate, and the defects are condensed in high fission rate conditions. The condensed vacancies and gases in higher fission rate conditions accelerate the incubation process, and Xe bubbles appear significantly advanced. Compared to the drastically reduced incubation period and enlarged volume fraction of bubbles upon enhanced fission rate, the average size is not severely coarsened.

3.2 Xe bubble evolution under applied stress

The fuels are suffering stress originating from the processing process, in-service environments, or inhomogeneous microstructures, which makes the bubbles in a stress state different from those in the stress-free state, as previously described. To clarify the Xe bubble evolution in U_3Si_2 in a stress

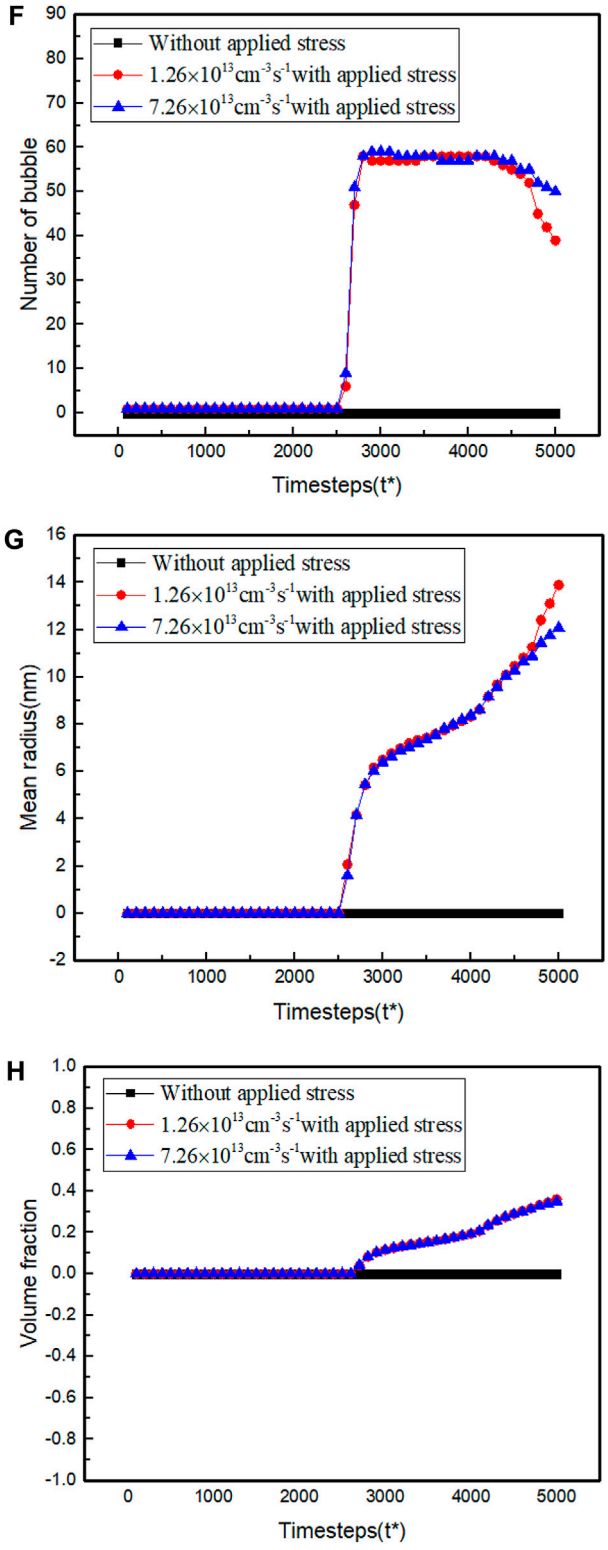

FIGURE 4
Comparison of the **(F)** number, **(G)** mean radius, and **(H)** volume fraction of Xe bubbles at 1.26×10^{13} $cm^{-3}s^{-1}$ and 7.26×10^{13} $cm^{-3}s^{-1}$.

state, we consider the external stress and elastic inhomogeneity in the mathematic model in Eq. 3, based on the linear elasticity assumption caused by those stress. The conditions under the fission rates of 1.26×10^{13} $cm^{-3}s^{-1}$ and 7.26×10^{13} $cm^{-3}s^{-1}$ with applied stress were performed, and we obtained the evolution results and statistical analysis as exhibited in Figure 3 and Figure 4, respectively.

As shown in Figure 3, the predicted bubble pattern under applied stress is quite different from that in a stress-free state. The applied stress induces bubbles' nucleation and accelerates the growth and coarsening. After 5000 steps of time evolution, the stress-free bubbles are still incubating; however, coalescence and Ostwald ripening occur in the stress-assisted bubbles. The stress state of a system is metastable, and void or bubble formation occurs as a consequence of stress relaxation. Voids or bubbles formation is accomplished through the interior gases and vacancies diffusion guided by the stress. With continuous production of point defects and gas atoms, the bubbles grow faster in the direction parallel to the applied stress, and the cross-sectional shape of bubbles with applied stress becomes stripped eventually. According to our analysis, the applied stress can significantly promote the growth rate of the bubble along with the applied stress and can help gases and vacancies overcome the energy barrier of bubble nucleation. To quantitatively evaluate the applied stress effect on the evolution feature of the Xe bubble, the number, mean radius, and volume fraction of bubbles are statistically displayed in Figure 4. By comparing the curves of bubbles evolution in Figure 4, the applied stress boosts the increment of the number, mean radius, and volume fraction of bubbles, manifesting severe irradiation damage.

3.3 Xe bubble evolution under dislocation stress field

Intrinsic line defects, such as edge/screw dislocations or dislocation loops, widely existed in irradiation samples. U_3Si_2 fuel that suffers severe irradiation will produce massive defects, causing dislocation boosts. The high dislocation densities inevitably reshape the Xe bubble arrangement or morphology. A typical experimentally observed dislocation configuration consisting of a pair of dislocations with opposite signs is considered to investigate the dislocation-induced bubble formation. Based on the linear elasticity assumption and inclusion theory, the strain caused by the dislocation pairs is taken as inclusion; the strain is thus given by Eqs 5 and 6. The Xe bubble nucleation effect can be studied by adding an elastic energy term caused by the dislocation pair through the generalized Hooke law. At the fission rates of 1.26×10^{13} $cm^{-3}s^{-1}$ and 7.26×10^{13} $cm^{-3}s^{-1}$, we obtain the evolution results and statistical analysis that are displayed in Figure 5 and Figure 6, respectively.

In this case, the dislocation dipole set in the investigated system causes local elastic inhomogeneous. According to the analysis of Section 3.2, this inhomogeneous local stress will induce bubbles formation. As shown in Figures 5J and K, two bubbles form first near the dislocation dipole. The local stress concentrates nearby the line core, attracting vacancies and gases to relax the severe dislocation stress nearby. The segregation of vacancies and gases leads to microstructure instability, forming two bubbles at the most stress-concentrated sites. The local inhomogeneous stress breaks

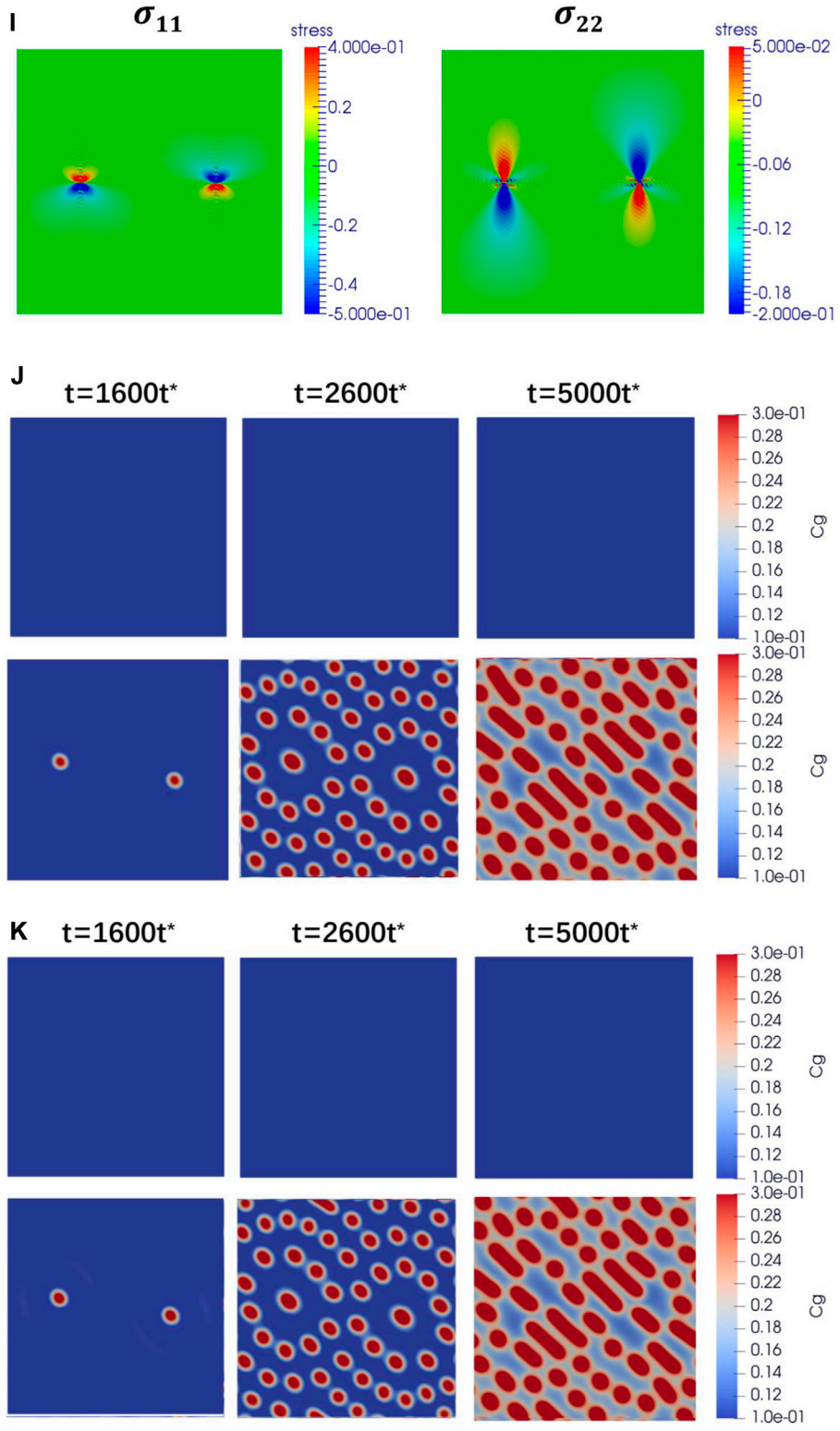

FIGURE 5
Dislocation dipole distribution model **(I)** and Xe bubble evolution with dislocation stress field under **(J)** 1.26×10^{13} cm^{-3}s^{-1} and **(K)** 7.26×10^{13} cm^{-3}s^{-1}.

the homogenous nucleation of bubbles for the primary Xe bubbles to deplete the surrounding vacancies and gases, and then the rest nucleate in succession a little far away from the primary ones. These secondary Xe bubbles form at the periphery of the primary ones, arranged in dot-like layers roughly in two. With prolonged time, these bubbles coarsen in the dislocation stress at a different pace;

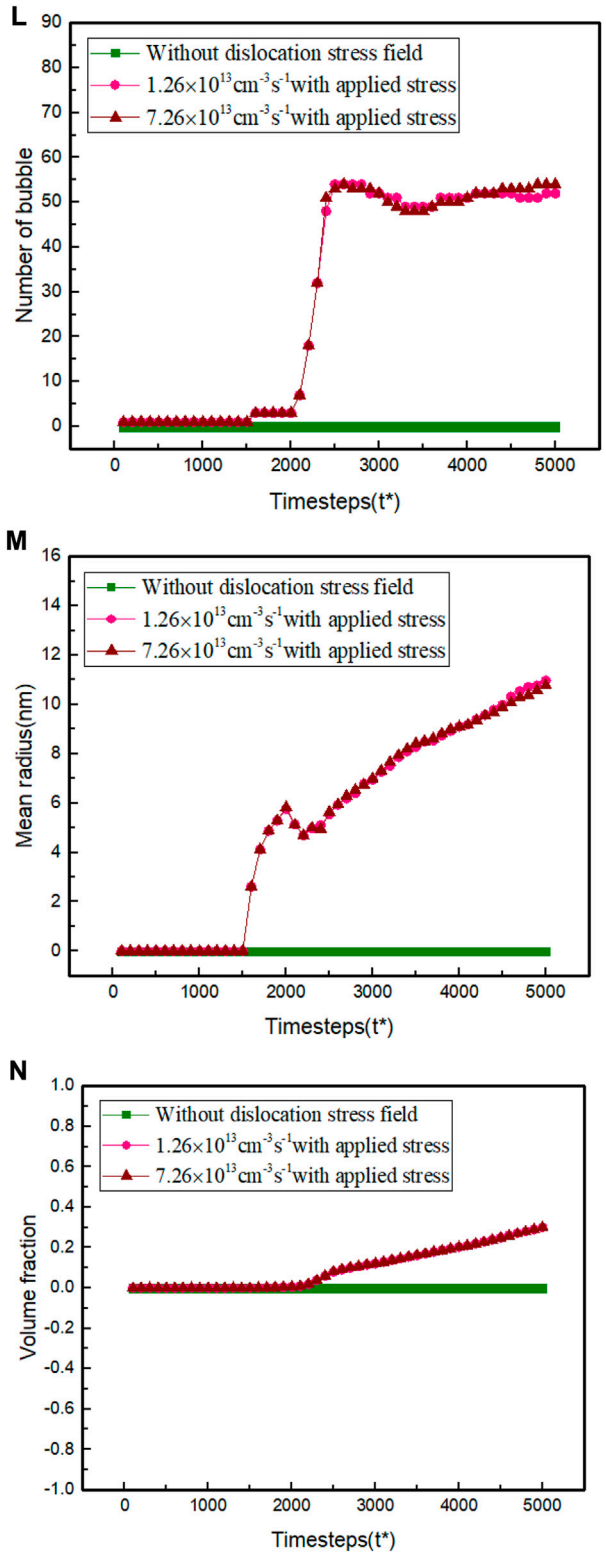

FIGURE 6
Comparison of the **(L)** number, **(M)** mean radius, and **(N)** volume fraction of Xe bubbles at 1.26×10^{13} $cm^{-3}s^{-1}$ and 7.26×10^{13} $cm^{-3}s^{-1}$.

some are elongated, and some are still spherical. These multiple morphologies of the bubbles are believed to be related to the stress overlap of the two dislocation pair, and it leads to the stress being reinforced in some regions while stress is offset in others. Bubbles nearby the stress-reinforced region coarsen faster than those in the stress-offsetted region. Eventually, these bubbles evolve into different cross-sectional shapes.

For a better prediction of the dislocation stress field on the evolution of Xe bubbles, the number, mean radius, and volume fraction of bubbles are statistically shown in Figure 6. Based on the analysis of Figure 6, the dislocation stress field encourages the nucleation and growth rate of bubbles around this pair of dislocations. In view of this phenomenon, it is believed that the elastic energy introduced by the dislocation pair drives gas atoms and vacancies to overcome the energy barrier of nucleation, providing heterogeneous nucleation sites. The inhomogeneous interior microstructures and local stress concentration caused by these microstructures are essential factors that contribute to bubble swelling.

4 Conclusion

In this work, typical irradiation and fabricated conditions for U_3Si_2 fuel are used in the simulations; i.e., the fission rates are 1.26×10^{13} $cm^{-3}s^{-1}$, 3.26×10^{13} $cm^{-3}s^{-1}$, 5.26×10^{13} $cm^{-3}s^{-1}$, and 7.26×10^{13} $cm^{-3}s^{-1}$, and the temperature is 1200K. Within our framework of the phase-field model, we systematically investigate the nucleation and growth of irradiation-induced intragranular Xe bubbles in U_3Si_2 fuel under different fission rates, applied stress, and dislocation stress field. From the simulated results, the following conclusions are summarized:

1) The intragranular Xe bubbles are sensitive to the fission rates. With increased fission rate, the bubble incubation periods are advanced, and the bubbles' final number and average radius rise but are not severely coarsened.
2) The Xe bubbles, from their evolution process and their morphologies, are significantly affected by the applied stress. The stress induces the nucleation process, generating more bubble nucleus in a shorter time than those in the stress-free system. The stress-guided vacancies and gas diffusion reshapes the bubbles' morphology, cause directional growth and coarsening along the load direction, and form elongated and strip bubble arrangement.
3) The Xe bubbles will preferentially nucleate nearby the stress-concentrated sites of the dislocation pair. The primary Xe bubbles deplete the surrounding vacancies and gases, leading to the non-random nucleation of roughly two-layers of secondary bubbles aligned at the periphery of the primary ones. The subsequent coarsening is influenced by the overlapped stress of the dislocation pair, forming elongated shapes in stress-reinforced regions and spherical ones in stress offset regions.

Our simulations demonstrate that the phase-field method is a promising and predictable computational tool for quantitatively studying and predicting microstructure evolution in U_3Si_2 fuel. Moreover, our study shows that the fuel fabrication and irradiation conditions may be used to control the bubble-induced swelling in U_3Si_2 fuel. Undoubtedly, the evolution of intergranular

Xe bubbles can also be affected by different fission rates, applied stress, and dislocation stress field. Hence, future studies should be extended to consider the nucleation and evolution of intergranular Xe bubbles under fuel fabrication and irradiation conditions.

Data availability statement

The original contributions presented in the study are included in the article/supplementary materials; further inquiries can be directed to the corresponding authors.

Author contributions

CM: model development, data analysis, and writing original draft. CL: investigation, validation, and writing original draft. MZ: data analysis and checking. TX: conceptualization and methodology. LW: conceptualization, supervision, and funding acquisition. RP: methodology and data analysis. JQ: software, methodology, and data analysis. JZ: methodology, software, and supervision.

Funding

This work was supported by the National Key R&D Program of China (Grant No. 2018YFE0207400) and National Natural Science Foundation of China (Grant No. U2167217).

Conflict of interest

The authors declare that the research was conducted in the absence of any commercial or financial relationships that could be construed as a potential conflict of interest.

Publisher's note

All claims expressed in this article are solely those of the authors and do not necessarily represent those of their affiliated organizations, or those of the publisher, the editors, and the reviewers. Any product that may be evaluated in this article, or claim that may be made by its manufacturer, is not guaranteed or endorsed by the publisher.

References

Aagesen, L. K., Andersson, D., Beeler, B. W., Cooper, M. W., Gamble, K. A., Miao, Y., et al. (2020). Phase-field simulations of intergranular fission gas bubble behavior in U_3Si_2 nuclear fuel. *J. Nucl. Mater.* 541, 152415. doi:10.1016/j.jnucmat.2020.152415

Agency, I. A. E. (2017). Chain fission yields. Available at: https://www-nds.iaea.org/sgnucdat/c1.htm (accessed Apr 13, 2017).

Bischoff, J. (2014). Development of fuels with enhanced accident tolerance, accident tolerant fuel concepts for light water reactors. *IAEA Tecdoc* 1797, 22–29.

Bonilla, L. L., Carpio, A., Neu, J., and Wolfer, W. (2006). Kinetics of helium bubble formation in nuclear materials. *Phys. D.* 222, 131–140. doi:10.1016/j.physd.2006.07.029

Braski, D. N., Schroeder, H., and Ullmaier, H. (1979). The effect of tensile stress on the growth of helium bubbles in an austenitic stainless steel. *J. Nucl. Mater.* 83, 265–277. doi:10.1016/0022-3115(79)90611-1

Cahn, J. W. (1961). On spinodal decomposition. *Acta Metall. Mater.* 9, 795–801. doi:10.1016/0001-6160(61)90182-1

Caturla, M. J., Soneda, N., Diaz de la Rubia, T., and Fluss, M. (2006). Kinetic Monte Carlo simulations applied to irradiated materials: The effect of cascade damage in defect nucleation and growth. *J. Nucl. Mater.* 351, 78–87. doi:10.1016/j.jnucmat.2006.02.019

Chattaraj, D., and Majumder, C. (2018). Structural, electronic, elastic, vibrational and thermodynamic properties of U_3Si_2: A comprehensive study using dft [J]. *J.All.And Comp.* 732, 160–166. doi:10.1016/j.jallcom.2017.10.174

Domain, C., Becquart, C., and Malerba, L. (2004). Simulation of radiation damage in Fe alloys: An object kinetic Monte Carlo approach. *J. Nucl. Mater.* 335, 121–145. doi:10.1016/j.jnucmat.2004.07.037

Finlay, M. R., Hofman, G., and Snelgrove, J. (2004). Irradiation behaviour of uranium silicide compounds. *J. Nucl. Mater.* 325, 118–128. doi:10.1016/j.jnucmat.2003.11.009

Hu, S., Burkes, D. E., Lavender, C. A., Senor, D. J., Setyawan, W., and Xu, Z. (2016). Formation mechanism of gas bubble superlattice in UMo metal fuels: Phase-field modeling investigation. *J. Nucl.Mater.* 479, 202–215. doi:10.1016/j.jnucmat.2016.07.012

Hu, S., Casella, A. M., Lavender, C. A., Senor, D. J., and Burkes, D. E. (2015). Assessment of effective thermal conductivity in U-Mo metallic fuels with distributed gas bubbles. *J. Nucl. Mater.* 462, 64–76. doi:10.1016/j.jnucmat.2015.03.039

Hu, S., Henager, C. H., Heinisch, H. L., Stan, M., Baskes, M. I., and Valone, S. M. (2009). Phase-field modeling of gas bubbles and thermal conductivity evolution in nuclear fuels. *J. Nucl. Mater.* 392, 292–300. doi:10.1016/j.jnucmat.2009.03.017

Hu, S., Li, Y., Sun, X., Gao, F., Devanathan, R., Henager, C. H., et al. (2010). Application of the phase-field method in predicting gas bubble microstructure evolution in nuclear fuels. *J.Mater. Res.* 101, 515–522. doi:10.3139/146.110304

Li, Y., Hu, S., Montgomery, R., Gao, F., and Sun, X. (2013). Phase-field simulations of intragranular fission gas bubble evolution in UO_2 under post-irradiation thermal annealing. *Nucl. Instrum. Methods Phys. Res. B* 303, 62–67. doi:10.1016/j.nimb.2012.11.028

Miao, Y. B., Gamble, K. A., Andersson, D., Mei, Z. G., and Yacout, A. M. (2018). Rate theory scenarios study on fission gas behavior of U_3Si_2 under LOCA conditions in LWRs. *Nucl. Eng. Des.* 326, 371–382. doi:10.1016/j.nucengdes.2017.11.034

Millett, P. C., El-Azab, A., and Wolf, D. (2011). Phase-field simulation of irradiated metals Part II: Gas bubble kinetics. *Comput. Mater. Sci.* 50, 960–970. doi:10.1016/j.commatsci.2010.10.032

Millett, P. C., Tonks, M., and Biner, S. B. (2012). Mesoscale modeling of intergranular bubble percolation in nuclear fuels. *J. Appl. Phys.* 111, 083511. doi:10.1063/1.3702872

Millett, P. C., and Tonks, M. (2011). Phase-field simulations of gas density within bubbles in metals under irradiation. *Comput. Mater. Sci.* 50, 2044–2050. doi:10.1016/j.commatsci.2011.02.006

Millett, P. C., Tonks, M. R., Biner, S., Zhang, L., Chockalingam, K., and Zhang, Y. (2012). Phase-field simulation of intergranular bubble growth and percolation in bicrystals. *J. Nucl.Mater.* 425, 130–135. doi:10.1016/j.jnucmat.2011.07.034

Olander, D. R. (1976). *Fundamental aspects of nuclear reactor fuel elements* (California Univ., Berkeley, CA: Technical Information Center, Energy Research and Development Administration.

Ortiz, C. J., Caturla, M. J., Fu, C. C., and Willaime, F. (2007). He diffusion in irradiatedα–Fe: An*ab-initio*-based rate theory model. *Phys. Rev. B* 75, 100102. doi:10.1103/physrevb.75.100102

Soneda, N., Ishino, S., Takahashi, A., and Dohi, K. (2003). Modeling the microstructural evolution in bcc-Fe during irradiation using kinetic Monte Carlo computer simulation. *J. Nucl. Mater.* 323, 169–180. doi:10.1016/j.jnucmat.2003.08.021

Stan, M., Ramirez, J., Cristea, P., Hu, S., Deo, C., Uberuaga, B., et al. (2007). Models and simulations of nuclear fuel materials properties. *J.Alloy. Compd.* 444, 415–423. doi:10.1016/j.jallcom.2007.01.102

Surh, M. P., Sturgeon, J., and Wolfer, W. (2004). Master equation and Fokker-Planck methods for void nucleation and growth in irradiation swelling. *J. Nucl. Mater.* 325, 44–52. doi:10.1016/j.jnucmat.2003.10.013

Surh, M. P., Sturgeon, J., and Wolfer, W. (2005). Radiation swelling behavior and its dependence on temperature, dose rate and dislocation structure evolution. *J. Nucl. Mater.* 341, 235–236. Erratum to: 'Master equation and Fokker–Planck methods for void nucleation and growth in irradiation swelling' [J. Nucl. Mater. 325 (2004) 44], 'Vacancy cluster evolution and swelling in irradiated 316 stainless steel' [J. Nucl. Mater. 328 (2004) 107] and. doi:10.1016/j.jnucmat.2005.03.002

Suzuki, T., Yano, T., Iseki, T., and Mori, T. (1990). Effects of external stress on defect annihilation and bubble swelling during annealing of neutron-irradiated silicon carbide. *J. Am. Ceram. Soc.* 73, 2435–2440. doi:10.1111/j.1151-2916.1990.tb07609.x

Torre, J. D., Fu, C. C., Willaime, F., Barbu, A., and Bocquet, J. L. (2006). Resistivity recovery simulations of electron-irradiated iron: Kinetic Monte Carlo versus cluster dynamics. *J. Nucl. Mater.* 352, 42–49. doi:10.1016/j.jnucmat.2006.02.040

Veshchunov, M. S., Dubourg, R., Ozrin, V., Shestak, V., and Tarasov, V. (2007). Mechanistic modelling of urania fuel evolution and fission product migration during irradiation and heating. *J. Nucl.Mater.* 362, 327–335. doi:10.1016/j.jnucmat.2007.01.081

Veshchunov, M. S. (2000). On the theory of fission gas bubble evolution in irradiated UO_2 fuel. *J. Nucl. Mater.* 277, 67–81. doi:10.1016/s0022-3115(99)00136-1

Veshchunov, M. S., Ozrin, V., Shestak, V., Tarasov, V., Dubourg, R., and Nicaise, G. (2006). Development of the mechanistic code MFPR for modelling fission-product release from irradiated UO_2 fuel. *Nucl. Eng. Des.* 236, 179–200. doi:10.1016/j.nucengdes.2005.08.006

Wang, Y., Zhao, J., Ding, J., and Zhao, J. (2022). Modeling irradiation-induced intragranular gas bubble in tungsten under external tensile loading. *Int. J.Refract.Met.Hard Mater.* 105, 105824. doi:10.1016/j.ijrmhm.2022.105824

White, J. T., Nelson, A., Dunwoody, J., Byler, D., Safarik, D., and McClellan, K. (2015). Thermophysical properties of U_3Si_2 to 1773 K. *J. Nucl. Mater.* 464, 275–280. doi:10.1016/j.jnucmat.2015.04.031

Xiao, Z., Wang, Y., Hu, S., Li, Y., and Shi, S. Q. (2020). A quantitative phase-field model of gas bubble evolution in UO_2. *Comput. Mater. Sci.* 184, 109867. doi:10.1016/j.commatsci.2020.109867

Xu, D. H., Wirth, B. D., Li, M., and Kirk, M. A. (2012). Combining *in situ* transmission electron microscopy irradiation experiments with cluster dynamics modeling to study nanoscale defect agglomeration in structural metals. *Acta Mater* 60, 4286–4302. doi:10.1016/j.actamat.2012.03.055

Xu, D. H., Wirth, B. D., Li, M., and Kirk, M. A. (2012). Defect microstructural evolution in ion irradiated metallic nanofoils: Kinetic Monte Carlo simulation versus cluster dynamics modeling and *in situ* transmission electron microscopy experiments. *Appl. Phys. Lett.* 101, 101905. doi:10.1063/1.4748980

frontiers | Frontiers in Energy Research

TYPE Original Research
PUBLISHED 09 November 2023
DOI 10.3389/fenrg.2023.1028079

OPEN ACCESS

EDITED BY
Qingming He,
Xi'an Jiaotong University, China

REVIEWED BY
Mingjun Wang,
Xi'an Jiaotong University, China
Kui Zhang,
Xi'an Jiaotong University, China
Sudipta Saha,
Corning Inc., United States

*CORRESPONDENCE
Lixin Chen,
chenlixin@nint.ac.cn

RECEIVED 25 August 2022
ACCEPTED 25 October 2023
PUBLISHED 09 November 2023

CITATION
Hu P, Ma Z, Ma T, Wang B, Tang X, Su C, Yang N and Chen L (2023), Analysis of fluid structure interaction between fuel elements and the coolant in Xi'an Pulsed Reactor core under seismic conditions. *Front. Energy Res.* 11:1028079. doi: 10.3389/fenrg.2023.1028079

Analysis of fluid structure interaction between fuel elements and the coolant in Xi'an Pulsed Reactor core under seismic conditions

Pan Hu, Zhenhui Ma, Tengyue Ma, Baosheng Wang, Xiuhuan Tang, Chunlei Su, Ning Yang and Lixin Chen*

Northwest Institute of Nuclear Technology, Xi'an, China

The phenomenon of fluid structure interaction exists widely in nuclear facilities, and it is of great significance to the safety of nuclear facilities. Xi'an Pulsed Reactor (XAPR) is a pool research reactor with good inherent safety. It has been operating safely since the loading criticality. However, researches on fluid structure interaction have not yet been carried out on Xi'an Pulsed Reactor which was built in the 1990s because of the limitation by the technical conditions and safety evaluation range at that time. In order to fill the technical blank mentioned above, the fluid structure interaction between fuel elements and the coolant in Xi'an Pulsed Reactor core is simulated by finite element method for the first time. In this method, the interaction between solid component deformation and flow field is considered alternatively, and some results are obtained. The maximum value of the deformation of fuel elements cladding tube do not exceed 0.1 mm, and the equivalent von-Mises stress is about 4.4683×10^7 Pa under given conditions, which is less than the tensile strength and yield strength of the material. The results show that the fluid structure interaction effect between fuel elements and the coolant in Xi'an Pulsed Reactor core is very weak under the given seismic conditions, and thus will not affect the safety of the reactor core and can be ignored.

KEYWORDS

XAPR, fluid structure interaction, finite element analysis, seismic, deformation

1 Introduction

The phenomenon of fluid structure interaction is widespread in nuclear facilities, and the structural dynamics problems caused by this phenomenon have an important influence on the structural integrity and safety of nuclear facilities. For example, the direct reason for the structural damage of the anti-break support assembly at the lower part of the reactor basket at Qinshan No. 1 Nuclear Power Plant is flow-induced vibration (Qian et al., 2011); In the second phase of Qinshan Nuclear Power Plant, the main coolant circuit thermometer casing also occurred the structural failure due to the flow-induced vibration during operation (Yu et al., 2016). Christon et al. believe that more than 70% of the fuel rod leaks are directly related to the wear between the locating grid and the fuel rod, while the fuel rod casing wear is mainly caused by the flow-induced vibration (Qian et al., 2011); Flow-induced vibration will also lead to the nuclear power plant heat exchanger pipe micro-dynamic wear and fatigue instability problems

(Ding et al., 2021); The steam generator of the No. 3 unit of the San Onofre nuclear power plant in California suffered severe flow bomb instability, which caused extensive wear of the heat transfer tube and caused coolant leakage in the primary loop (TANG et al., 2019).

At present, there are more and more researches on fluid structure interaction in nuclear facilities at home and abroad, including numerical simulation and experimental research. Hao Qian et al. analyzed the modal and flow-induced vibration of the secondary support assembly of AP1000 reactor components without considering the action of flow distribution skirt with Finite Element Method, and obtained the natural frequencies, the modal shapes of AP1000 components and loads on the second support assembly due to flow-induced vibration (Qian et al., 2011). Fenggang Zang et al. calculated the natural frequency and vortex shedding frequency of the thermometer casing in the reactor coolant circuit, and made the fatigue analysis of the flow-induced vibration of the tube with a simplified engineering method (Zang and Liu, 2005). Guitao Cao et al. analyzed the three-dimensional nonlinear shock-resistant dynamic response of the reactor structure, and established the hydrodynamic mass matrix to simulate the fluid structure interaction between the related components, and made a validation with ANSYS (Cao et al., 2021). Guangdong Bao et al. studied the liquid sloshing problem in the shrinkage ratio model of fast reactor with ANSYS, and studied the inherent vibration characteristics and liquid sloshing characteristics of the structure by modal analysis, and obtained the wave height, the liquid pressure, the structural stress strength, the combined forces and torque et al. by dynamic time history analysis and spectrum analysis (Bao, 2019). Jing Xu et al. completed the flow-induced vibration test under different working conditions on the hydraulic simulation loop based on the 1:6 model of CAP 1400 reactor, and obtained complete test data, and analyzed and evaluated the test data in detail (Xu et al., 2016). Qizhen Ye et al. measured the flow-induced vibration of the components in the reactor of Qinshan No. 2 Nuclear Power Plant during the thermal function test, and the measured data was in good agreement with the predicted value in theory (Ye et al., 2003). Jie Yang et al. carried out a flow-induced vibration test of 1: 5 model of HPR1000 components, and made a finite element analysis (Yang et al., 2016). Mingjun Wang, et al. performed the structure stress analysis to investigate the stress distribution features utilizing thermal-mechanical coupling method in the complex mixing phenomenon simulation in a 45° T junction during the injecting process (Wang et al., 2018). Haoyu Liao et al. conducted a three-dimensional fluid-solid coupling simulation with the full consideration of irradiation effects for plate-type nuclear fuel assemblies by FLUENT-MpCCI-ABAQUS, and they investigated the influence of radiation swelling and bending deformation on fluid thermal-hydraulic characteristics (Liao et al., 2020). Mingjun Wang, et al. performed AP1000 RPV stress analysis using Finite Element Analysis (FEA) method, and they found the stress was mainly induced by high temperature gradient and the maximum stress occurred when the wall temperature has the largest reduce rate (Wang et al., 2017). Yangbin Deng, et al. developed a non-rigid Pellet-Clad Mechanical Interaction (PCMI) calculation model with the consideration of plenum spring. They modified the FROBA-ROD code and performed the behavior simulation for accident tolerant fuels (ATFs) (Deng et al., 2017). Chenxi Li, et al. analyzed the behavior of dispersed plate-type fuel based on fluid-solid coupling method, "FLUENT-ABAQUS-MpCCI" (Li et al., 2020). Mingjun Wang, et al. established the mathematical models of complicate two-phase boiling phenomena and thermal hydraulic features under the motion conditions, and developed the nuclear reactor multi-scale and multi-physics coupling platforms on the basis of CFD codes (Wang et al., 2021). Yingjie Wang, et al. proposed and employed a fluid-structure coupling model and thermal fatigue assessment methodology to study the thermal fatigue of structures subjected to liquid mental jets at the core outlet of the SFR (Wang et al., 2022).

So far, we haven't seen the research results of fluid structure interaction in XAPR, so the Finite Element Method is used to simulate the fluid structure interaction between fuel elements and coolant in XAPR core for the first time. The fluid structure interaction of XAPR core under given seismic conditions is studied, and its effect on the safety of XAPR is analyzed. Under seismic conditions, the phenomena of fluid structure interaction related to XAPR include the interaction between the core components and the coolant, the impact of the free liquid level sloshing of the pool water on the reactor vessel, the flutter of the fluid pipe under the action of fluid, the interaction between the pump and the coolant, et al. In this paper, only the fluid structure interaction between fuel elements and coolant is considered under seismic conditions. More specifically, this paper analyzes the deformation, strain and stress distribution of the fuel element cladding tube due to the fluid structure interaction between the tube and coolant under set seismic conditions, and then evaluates the safety of the XAPR by judging whether the fuel element cladding tube will be damaged, broken or occur an unrecoverable deformation.

When an earthquake occurs, the reactor vibrates under the drive of the surface layer, and the core fuel element in the water in the reactor pool vibrates under the action of earthquake, which causes the coolant flow field parameters to change accordingly. The change of coolant flow field parameters in turn changes the load acting on the surface of fuel element, which leads to the change of the deformation of fuel element and internal stress distribution. If the deformation of the fuel element exceeds the acceptable range, or if it breaks because the stress is over a certain limit, it will cause radioactive leakage, which will affect the safety of the reactor, personnel and environment. Therefore, it is of positive significance to study the fluid structure interaction between the fuel element and the coolant in XAPR core caused by the earthquake for the reactor, personnel and environmental safety.

One of the purposes of this paper is to establish a method to study the fluid structure interaction between fuel elements and coolant. The basic approach of this method is to consider the influence of the solid parts on the flow field first, then consider the effect of the flow field on the solid part, then iterate until the convergence solution is obtained. Therefore, this method can be used not only in XAPR, but also in other research reactors.

2 Materials and methods

2.1 Principles of calculation

Fluid flow should follow the law of physical conservation, which includes the law of mass conservation, the law of momentum conservation and the law of energy conservation. If the fluid

includes other different components of the mixture, the system also follows the law of conservation of components.

Mass conservation equation, also known as continuity equation (Zhou et al., 2011):

$$\frac{\partial \rho}{\partial t} + \nabla \cdot (\rho \vec{v}) = 0 \tag{1}$$

and in (1), ρ is the fluid density, t is the time, $\vec{v}$ is fluid velocity. Formula 1 is a universal equation. In XAPR under the seismic conditions set in this paper, the coolant flow in the reactor core can be regarded as an incompressible flow, thus Formula 1 can be transformed into Formula 2:

$$\nabla \cdot \vec{v} = 0 \tag{2}$$

For an incompressible flow, momentum conservation equation:

$$\rho \frac{\mathrm{D}\vec{v}}{\mathrm{D}t} = \rho \vec{F}_{\mathrm{b}} - \nabla p + \mu \nabla^2 \vec{v} \tag{3}$$

(3) is also known as the Navier-Stokes equation. $\vec{F}_{\mathrm{b}}$ is the mass force on the unit mass fluid, p is the fluid pressure, μ is the fluid viscosity coefficient, $\frac{\mathrm{D}}{\mathrm{D}t}$ is the adjoint derivative, and its formula is as follows:

$$\frac{\mathrm{D}}{\mathrm{D}t} = \frac{\partial}{\partial t} + (\vec{v} \cdot \nabla) \tag{4}$$

Energy conservation equation:

$$\rho \frac{\mathrm{D}}{\mathrm{D}t} e_{\mathrm{s}} = \rho \vec{F}_{\mathrm{b1}} \cdot \vec{v} + \nabla \cdot (\boldsymbol{P} \cdot \vec{v}) + \nabla \cdot (k \nabla T) + \rho q \tag{5}$$

where, e_{s} is the stored energy per unit mass fluid, and its formula is as follows:

$$e_{\mathrm{s}} = e + \frac{1}{2} v^2 + \mathrm{g}z \tag{6}$$

and in (5), $e, \frac{1}{2}v^2, \mathrm{g}z$ represent the internal energy, kinetic energy and gravitational potential energy of a unit mass fluid, respectively. g is the acceleration of gravity. $\vec{F}_{\mathrm{b1}}$ is the mass force (excluding gravity) on a unit mass fluid, $\boldsymbol{P}$ is the stress tensor, k is the fluid thermal conductivity, q is the heat of a unit mass fluid transmitted by radiation in a unit time.

The solid part follows the structural dynamic equilibrium equation (Chen et al., 2010).

$$[M]\{\ddot{x}\} + [C]\{\dot{x}\} + [K]\{x\} = \{F(t)\} \tag{7}$$

in (6), $[M]$ is the mass matrix, $[C]$ is the damping matrix, $[K]$ is the stiffness matrix, $\{x\}$, $\{\dot{x}\}$, $\{\ddot{x}\}$ and $\{F(t)\}$ represent the displacement vector, the velocity vector, the acceleration vector and the force vector respectively.

2.2 Model establishment

The configuration of XAPR standard fuel element is shown in Figure 1.The standard fuel element has a coarse rod shape, the outer diameter is 37.2 mm, and the total length is 760.5 mm. It is consisted of stainless steel cladding tube, fuel block, Zr-4 mandrel, graphite block and upper and lower end plugs. The thickness of the fuel element cladding tube is 0.5 mm. The gap

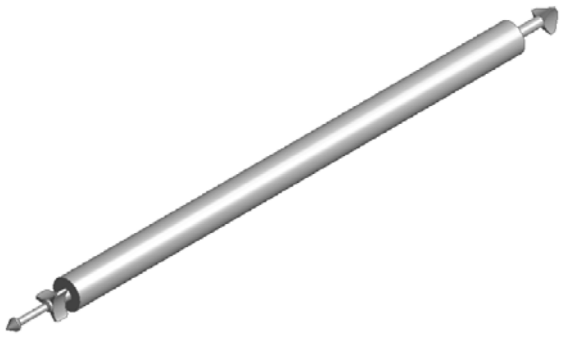

FIGURE 1
Standard fuel element.

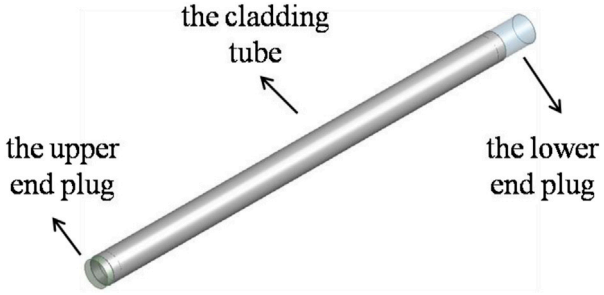

FIGURE 2
Simplified model of fuel element.

between the fuel block and the cladding tube is filled with helium gas. The upper and lower end plugs are equipped with a uniform three-lobe structure to make the fuel element located in the grid plate, and the water-passing area of the grid plate is larger than 70% of the core channel area. This structure will result in more grids and more computation, so the upper and lower end plugs will be simplified into a cylinder in the preliminary analysis, as shown in Figure 2.This simplification is reasonable because this paper is more concerned with the question of whether the deformation of the fuel element cladding tube under the action of hydraulic pressure is within acceptable range and whether there will be damage.

XAPR core contains fuel elements, control rods, neutron source elements, graphite elements, stainless steel ash body elements, and so on. The total number is about 198. The upper and lower grid plates of the core barrel are distributed with element holes to provide positioning and support for the elements. It can be seen that the core structure of XAPR is complex and there are many kinds of components. If a complete core geometry model is established, the model is too complex, the meshing is difficult and it is not realistic to calculate and solve. In order to simplify the problem, In this paper, according to the characteristics of fuel elements symmetrical layout in XAPR core, a geometric model is established by selecting local region. The geometric model of single/multi-fuel element and coolant has been established in order to analyze the fluid structure interaction between

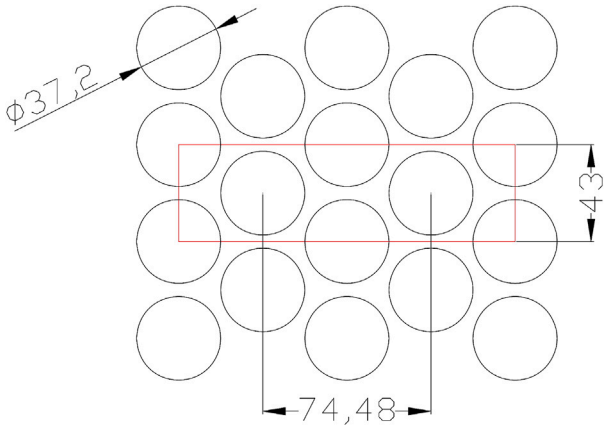

FIGURE 3
Schematic of local region of the core of XAPR.

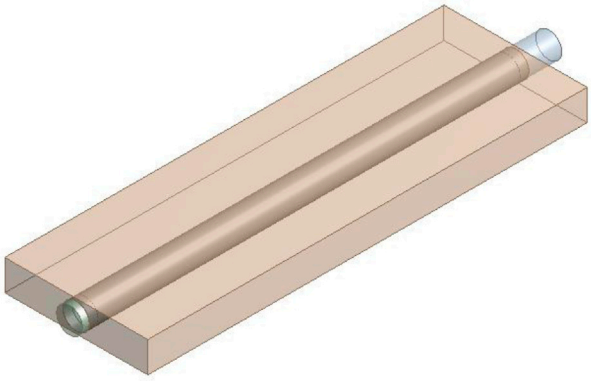

FIGURE 4
Single element model.

single/multi-fuel element and coolant. Firstly, make preliminary unidirectional fluid structure interaction analysis with 3 different geometric models, which contain 1, 2, and 4 fuel elements respectively; Secondly, analyze the influence of the number of fuel elements contained in the model on the calculation results; Thirdly, select the most suitable one from the 3 different geometric models, and then refine the model; Fourthly, make further unidirectional and bidirectional fluid structure interaction analysis with the selected model.

The fuel element in the core of XAPR is arranged in an equilateral triangle, as in Figure 3, the distance between the center line of the adjacent two fuel elements is 43 mm, the diameter of the fuel element is 37.2 mm, and the channel width between the adjacent two fuel elements is only 5.8 mm at the narrowest point. According to the symmetry, geometric model can be established by selecting local regions rather than intact cores. In Figure 3, the region within the rectangle frame (43 mm in width) is an option based on symmetry. The region consists of 2 intact fuel elements, 2 1/2 fuel elements and 4 1/4 fuel elements. On this basis, the number of fuel elements can be reduced further, and three geometric models are established: single element model, two elements model and four elements model, as shown in Figure 4 ~ Figure 6. In Figure 4, there is only one fuel element along the flow direction located in the center of the water region, and the model does not take into account the influence of the fuel element around it on the calculation results; In Figure 5, there are two fuel elements along the flow direction, and the distance between the axis of them is 43 mm. The model only considers the influence of the adjacent fuel element along the flow direction. In Figure 6, there are four fuel elements, two of which are intact, and the distance between the axis of them is 74.48 mm, and the other two are selected only 1/2 according to symmetry, and the distance between the axis of them is 43 mm. The model considers the influence of adjacent fuel elements along the flow direction and in the lateral direction on the calculation results. In all three models, the upper and

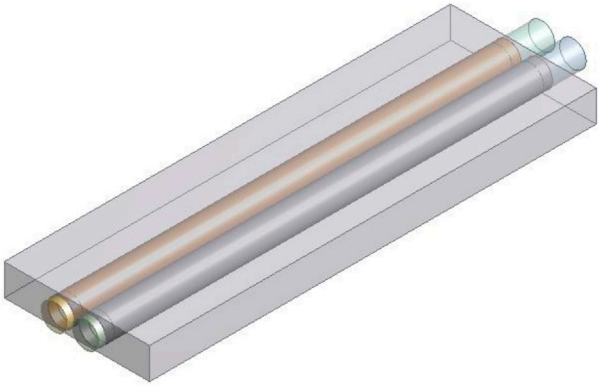

FIGURE 5
Two elements model.

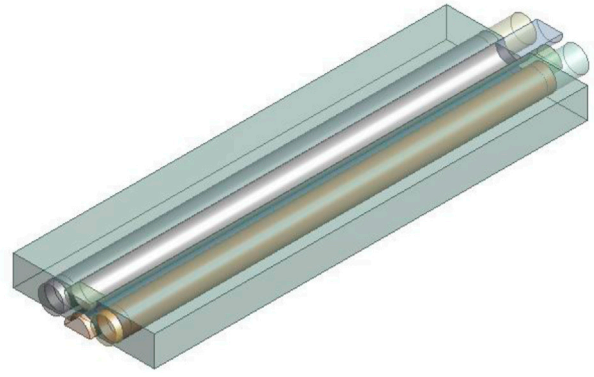

FIGURE 6
Four elements model.

TABLE 1 Comparison between the results of the three models.

Calculation results	Single element model	Two elements model	Four elements model
Deformation (min)	0 m	0 m	0 m
Deformation (max)	2.8128×10^{-5} m	2.8969×10^{-5} m	2.9333×10^{-5} m
Equivalent elastic strain (min)	7.9992×10^{-8} m/m	4.0533×10^{-8} m/m	2.9205×10^{-8} m/m
Equivalent elastic strain (max)	4.3821×10^{-5} m/m	4.5224×10^{-5} m/m	4.4188×10^{-5} m/m
Equivalent stress (min)	10538 Pa	4850.8 Pa	1086.5 Pa
Equivalent stress (max)	8.7416×10^{6} Pa	9.0241×10^{6} Pa	8.8173×10^{6} Pa

lower end plugs of the fuel element are simplified into cylinders. The water region sizes of the three models are 200 mm × 43 mm × 614 mm. The fuel element components that exposed to the outside and interact with the water flow include the upper and lower end plugs and the cladding tube which is the most fragile, so this paper focuses on the deformation of the cladding tube under the action of water flow, so the water region is 614 mm in depth, the same length as the cladding tube.

According to the "Investigation Report on Seismic Intensity and Activity Fault of Xi 'an Pulsed Reactor Site," the basic seismic intensity of XAPR site is VIII degree. The maximum impact intensity of historical earthquakes is set to IX degree. According to the relevant design documents, the designed seismic intensity of XAPR site is set to IX degree. Corresponding to this designed intensity level, the design acceleration value of the hard bearing layer is:

$$a_b = 0.15g \tag{7}$$

For Class III subsoil, the magnification coefficient of the formation covering the hard bearing layer $\gamma = 1.5$. Therefore, the design value of the ground acceleration a_g is determined by the Formula 8:

$$a_g = \gamma a_b = 0.225g \tag{8}$$

in (8), g is gravitational acceleration, the value is 9.8 m/s^2, so a_g = 2.205 m/s^2.

When the seismic intensity is IX degree, the peak velocity of ground motion in the horizontal direction is about 0.50 m/s (Zhao, 2012). It can be deduced that the peak relative velocity between coolant and fuel elements is about 0.5 m/s, so the inlet velocity is set to 0.5 m/s in the model. The boundary condition type of the outlet in the model is set to "open," and the relative pressure is set to 0 Pa; Two sides are defined as symmetrical boundaries. The pressure distribution in the fluid domain is calculated first, and the fluid dynamics analysis results are used as the load transferred to the structural analysis modules, and fixed constraints are added to the two ends of the fuel element to calculate the stress and strain in the fuel element. The results are shown in Table 1.

As shown in Table 1, the maximum deformation, equivalent elastic strain and equivalent stress of fuel elements calculated by the three models are very close to each other, and the maximum deviation is about 4%. Therefore, it can be concluded that the results obtained by the three models are in agreement with each other. Considering that the more components in the model, the larger the amount of computation, especially in the bidirectional fluid structure interaction analysis, the calculation process is time-consuming, so for the sake of simplicity, the single element model is chosen, and the geometric model is refined, to do further fluid structure interaction analysis.

Using a more accurate fuel element model and adding a water region around it, the model shown in Figure 7 is established as follows. The water region size is 74.48 mm × 43 mm × 614 mm.

2.3 Sensitivity analysis of the size of water region

To analyze the impact of water region size on the calculation results, water region size is designed as x × 43 mm × 614 mm, and the parameter x takes values of 50, 100, 200, 300 mm, respectively. The inlet velocity is set to 0.5 m/s in the model. The boundary condition type of the outlet in the model is set to "open," and the relative pressure is set to 0 Pa; Two sides are defined as symmetrical boundaries. The calculation results of the pressure of the water flow on the cladding tube per unit length are shown in Table 2. The parameter F represents the pressure of the water flow on the cladding tube per unit length. It can be seen that the parameter F is basically unchanged when the water region size parameter x varies from 50 mm to 300 mm.

2.4 Sensitivity analysis of the grid size

The deformation of the fuel element cladding tube is directly related to the action of water flow on it. The force put on the fuel element cladding tube by water flow is calculated under different grid size conditions. In order to simplify the question, a two-dimensional model was chosen for grid sensitivity analysis. According to the symmetry, half of the region is selected as the computation domain. The geometric model is shown in Figure 8.

The geometric model is meshed with different grid sizes, and the calculation results obtained by using these meshes are shown in Table 3. It can be seen that the grid independent solution is basically reached when the grid size is 5×10^{-4} m. Therefore, the grid size of 5×10^{-4} m is selected in the subsequent analyses and calculations.

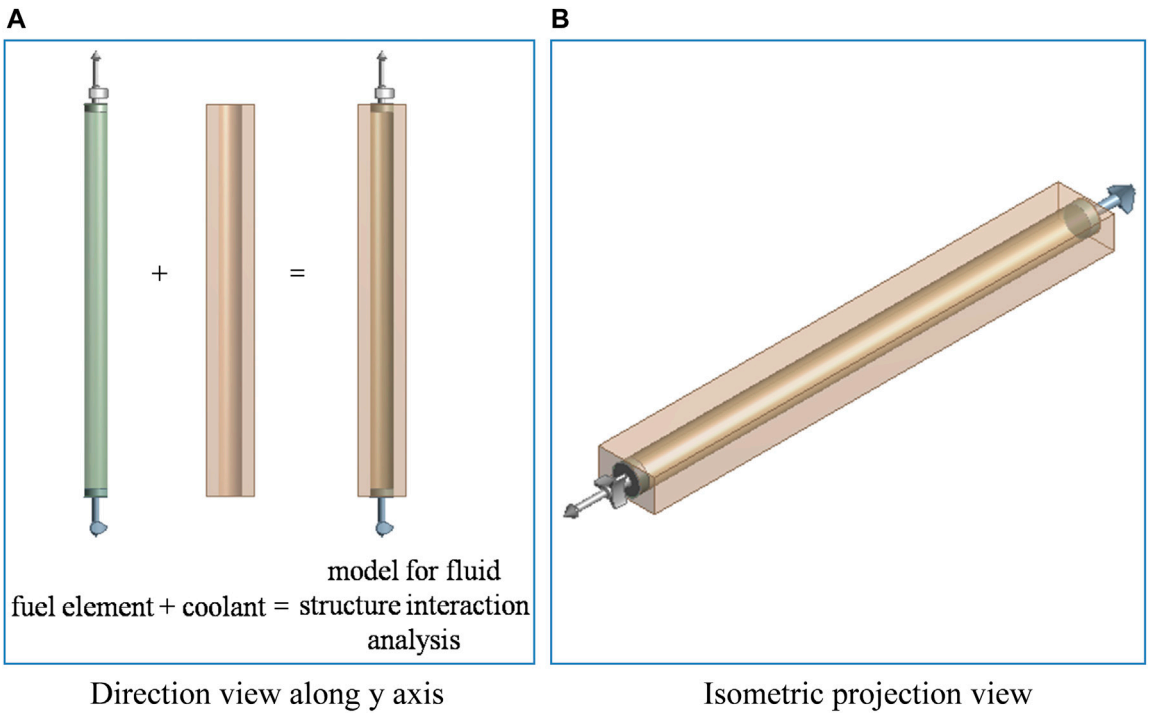

FIGURE 7
Fluid structure interaction analysis model. **(A)** Direction view along y axis. **(B)** Isometric projection view.

TABLE 2 The calculation results of the pressure of the water flow on the cladding tube.

x/mm	50	100	200	300
F/(N/m)	178.8	186.8	185.2	185.6

3 Results

3.1 Unidirectional fluid structure interaction analysis

The inlet velocity is set to 0.5 m/s and the exit is set to open boundary. The rest of the wall is defined as a symmetric boundary. The results are shown in Figure 9–Figure 11.

The fuel element cladding tube is pressed because of the maximum fluid pressure in the incoming flow direction. On both sides, the fluid pressure reaches a minimum, and the fuel element cladding is stretched to both sides. As can be seen in Figure 9, the maximum deformation of the fuel element is located approximately in the middle part. The maximum deformation is 8.3921×10^{-5} m, less than 0.1 mm. The fuel element has a diameter of 37.2 mm and a length of 760.5 mm. In contrast, the deformation of less than 0.1 mm is completely negligible. As shown in Figure 10, the maximum equivalent elastic strain of the fuel element cladding tube is 8.5799e-5 m/m, which is very small. The higher the temperature, the less tensile strength and yield strength of stainless steel. The maximum temperature of XAPR fuel element cladding under steady state operation conditions is 153.6°C (Northwest Institute of Nuclear Technology, 2000). At this temperature, the tensile strength of stainless steel is about 4.55×10^8 Pa and the yield strength is about 1.59×10^8 Pa (Assembly Preparation Team, 1975). As can be seen in Figure 11, the maximum equivalent stress in the fuel element cladding tube is about 1.57×10^7 Pa, which is much less than the tensile strength and yield strength of the material, so it can be concluded that the fuel element

FIGURE 8
Geometric model for sensitivity analysis of the grid size.

TABLE 3 The calculation results of the pressure of the sensitivity analysis of the grid size.

No.	Grid sizes/m	Number of nodes	Number of elements	Total number of grids	Number of steps	Results(1/2 model)	Results(intact model)
1	1×10^{-3}	1379	1267	2646	450	88.8	177.6
2	8×10^{-4}	2071	1936	4007	450	89.2	178.4
3	6×10^{-4}	3448	3269	6717	450	91.1	182.1
4	5×10^{-4}	4852	4638	9490	550	92.8	185.7
5	4×10^{-4}	7499	7232	14731	950	92.2	184.4
6	3×10^{-4}	13339	12988	26327	2200	91.3	182.5
7	2×10^{-4}	30903	30396	61299	6050	94.2	188.4

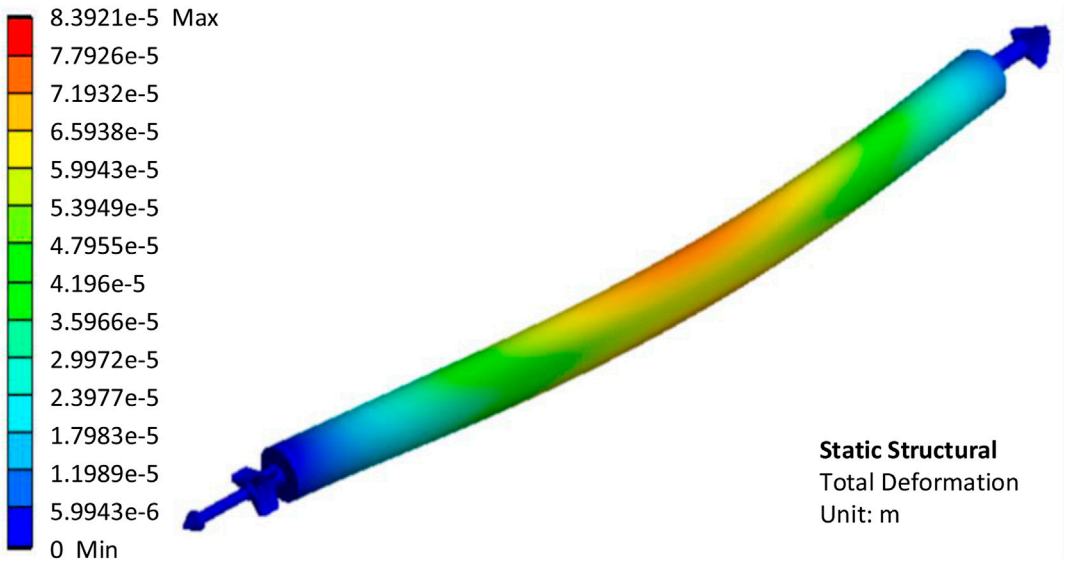

FIGURE 9
Calculation results of deformation of the fuel element in unidirectional fluid structure interaction analysis.

cladding tube will not be damaged, and there will not be an unrecoverable deformation.

3.2 Bidirectional fluid structure interaction analysis

Because of the lack of seismic data, the relation between displacement of the fuel element, s, and time, t, is assumed to be sinusoidal as Formula 9 for the sake of simplification:

$$s = A \sin \omega t \tag{9}$$

The velocity, v, and acceleration, a, of the fuel element in the vibration during a seismic are respectively:

$$v = A\omega \cos \omega t \tag{10}$$

$$a = -A\omega^2 \sin \omega t \tag{11}$$

Taking into account that the acceleration of the ground a_g = 2.205 m/s^2, the period is 0.4 s (Li, 2002), it can be deduced that:

$$\begin{cases} \frac{2\pi}{\omega} = 0.4 \\ A\omega^2 = 2.205 \end{cases} \tag{12}$$

It can be calculated that $\omega \approx 15.7$ rad/s, $A \approx 0.00894$ m, so there is a Eq. 13:

$$s = 0.00894 \sin (15.7t) \tag{13}$$

The geometric model established for bidirectional fluid structure interaction analysis is the same as that used in unidirectional fluid structure interaction analysis, but the specific setting in the software is very different. The constraint condition about the displacement of the fuel element as shown in Eq. 13 is used in the calculation, the fluid structure interface is set reasonably by selecting the correct interface between the fuel element and the coolant, and the simulation time is set to a period of 0.4 s.

Calculation results show that deformation in x, y, and z direction are the largest when t = 0.08 s, the values are 3×10^{-5} m, 5.8036×10^{-7} m, and 4.8929×10^{-6} m, respectively. So the deformation in the x

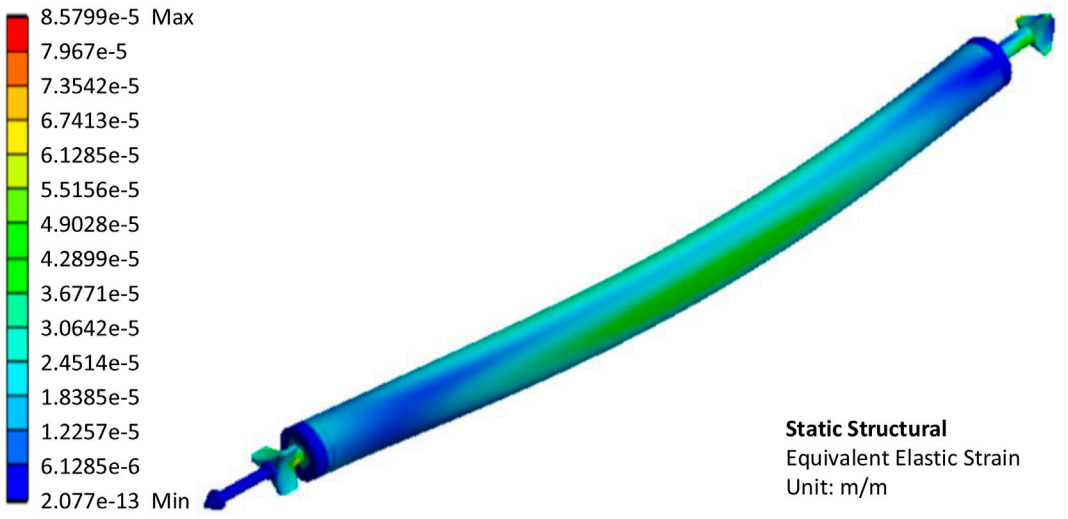

FIGURE 10
Calculation results of equivalent elastic strain of the fuel element in unidirectional fluid structure interaction analysis.

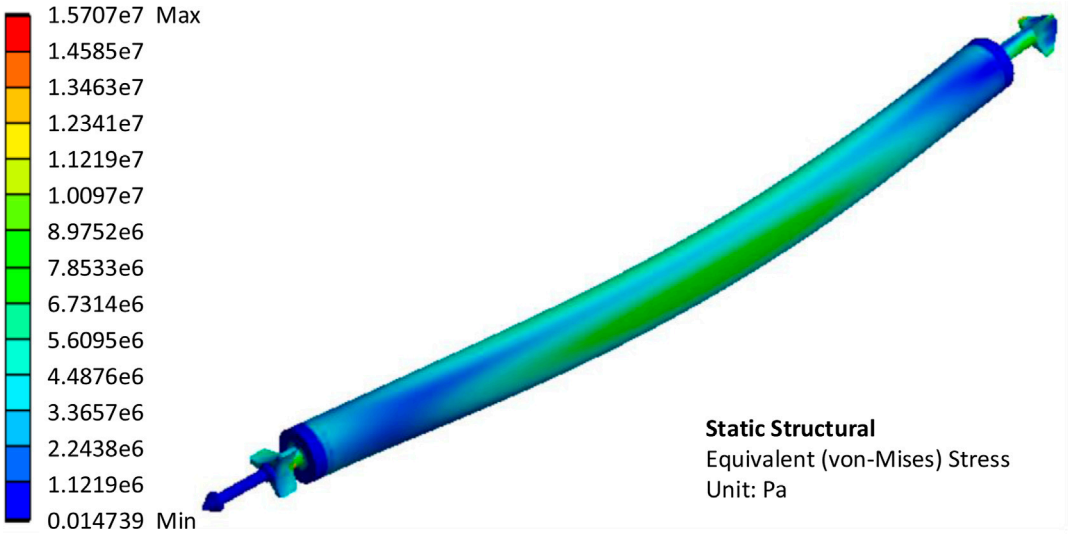

FIGURE 11
Calculation results of equivalent stress of the fuel element in unidirectional fluid structure interaction analysis.

direction (along the flow direction) is most important, which is consistent with the fact. The maximum deformation is only 0.03 mm, which can be ignored. The equivalent elastic strain and equivalent stress are also obtained when t = 0.08 s, which are 2.3152×10^{-4} m/m, 4.4683×10^{7} Pa, respectively. The equivalent stress is less than the tensile strength and yield strength of the material, so it can be concluded that the fuel element cladding tube will not be damaged, and there will not be an unrecoverable deformation.

The results show that the fluid structure interaction between the coolant and the fuel element in XAPR is very weak and negligible under the seismic conditions set in this paper.

4 Discussion

In this paper, first, assume that there is no deformation in the solid component (fuel element). According to the geometric symmetry, the local region in the core is selected to establish the model and carry out the fluid flow analysis. The inlet boundary condition is velocity inlet, the outlet boundary condition is pressure outlet, and the rest is symmetric boundary. By solving the hydrodynamic equation, the coolant pressure distribution on the cladding surface of fuel element is obtained. Then the structural analysis is made for the fuel element cladding, the pressure distribution on the cladding surface is taken as the boundary condition,

the elastic modulus, Poisson's ratio and other parameters of the material are set, and the constraint conditions are put on the contact surfaces between the fuel element cladding and the upper and lower grid plates, and the deformation and internal stress distribution of the cladding are obtained. According to the deformation of the fuel element cladding, the fluid domain in the geometric model is modified, and the fluid flow analysis is carried out again, and the coolant pressure distribution on the fuel element cladding surface is obtained, and then the structural analysis is carried out again. So iterate until the final convergence solution is obtained. In the process of solution, it is necessary to ensure that the pressure load can be transferred correctly at the interface of fluid and solid domain, and that the nodes in fluid and solid domain should be consistent at the interface.

It can be concluded that the fluid structure interaction between the fuel element cladding tube and the coolant in XAPR results in the deformation of the fuel element cladding tube under the action of the horizontal acceleration. The size of the deformation is related to the additional pressure applied by the coolant to the cladding tube and the tensile strength and yield strength of the cladding tube material. The pressure is related to the magnitude of the horizontal acceleration, coolant density, fuel element layout and other factors. The tensile strength and yield strength of cladding tube materials are related to the material type and temperature. An acceptable deformation should be within the elastic deformation range, in which case the cladding tube can be restored to its original state when the additional pressure applied by the coolant to the cladding tube is removed. When the seismic intensity is higher, resulting in greater horizontal acceleration, or when the reactor is in an accident state, such as large-break LOCA, the cladding tube has a higher temperature and its strength decreases, which can lead to significant deformation.

The geometric model of single/multi-fuel element and coolant is established based on that the upper and lower end plugs of fuel element in the core of XAPR are simplified into cylinders. The fluid structure interaction between single/multi-fuel element and coolant is studied with the finite element method. The effect of the number of fuel elements on calculation results is analyzed by comparing the results obtained from the three different geometric models. It can be seen that the results are basically in agreement with each other. For the sake of simplicity, the single fuel element model is selected and the fuel element model is refined properly. Under the given seismic conditions, unidirectional and bidirectional fluid structure interaction analysis between the fuel element and coolant are carried out, and the internal stress and strain distribution in the fuel element cladding tube are obtained, and some conclusions can be made as follow.

(1) The effect of the number of fuel elements in the model on the calculation result is slight in the fluid structure interaction analysis for XAPR under the given seismic conditions;
(2) The maximum equivalent stress in the fuel element cladding tube is much less than the tensile strength of the material, so the fuel element cladding tube will not be damaged or fractured;
(3) The maximum equivalent stress in the fuel element cladding tube is much less than the yield strength of the material, so there will not be an unrecoverable deformation;
(4) The deformation of the fuel element cladding tube is very small, less than 0.1 mm.

It can be concluded that the fluid structure interaction between the fuel element and the coolant in XAPR core is very weak under the seismic conditions set in this paper, and it will not pose a threat to the safety of XAPR, so it can be neglected.

Data availability statement

The original contributions presented in the study are included in the article/Supplementary material, further inquiries can be directed to the corresponding author.

Author contributions

All authors listed have made a substantial, direct, and intellectual contribution to the work and approved it for publication.

Conflict of interest

The authors declare that the research was conducted in the absence of any commercial or financial relationships that could be construed as a potential conflict of interest.

Publisher's note

All claims expressed in this article are solely those of the authors and do not necessarily represent those of their affiliated organizations, or those of the publisher, the editors and the reviewers. Any product that may be evaluated in this article, or claim that may be made by its manufacturer, is not guaranteed or endorsed by the publisher.

References

Assembly Preparation Team (1975). *Nuclear reactor material performance data assembly*. Beijing: Atomic Energy Publishing House, 199.

Bao, G. (2019). *The numerical study on sloshing liquid in fast reactor vessel considering fluid-structure interaction*. Beijing: School of Nuclear Science and Engineering of North China Electric Power University, 7.

Cao, G., Zhu, He, and Ye, X. (2021). Analysis of three-dimensional nonlinear impact on reactor structure. *Nucl. Power Eng.* 42 (1), 70–74. doi:10.13832/j.jnpe.2021.01.0070

Chen, X., Yuan, D., and Yang, M. (2010). Blade stress of the reactor coolant pump of 300 MWe nuclear power plant in China based on fluid-solid coupling method. *J. Mech. Eng.* 46 (4), 112. doi:10.3901/JME.2010.04.111

Christon, M. A., Lu, R., Bakosi, J., Nadiga, B. T., Karoutas, Z., and Berndt, M. (2016). Large-eddy simulation, fuel rod vibration and grid-to-rod fretting in pressurized water reactors. *J. Comput. Phys.* 322, 142–161. doi:10.1016/j.jcp.2016.06.042

Deng, Y., Wu, Y., Qiu, B., Zhang, D., Wang, M., Tian, W., et al. (2017). Development of a new pellet-clad mechanical interaction (PCMI) model and its application in ATFs. *Ann. Nucl. Energy* 104, 146–156. doi:10.1016/j.anucene.2017.02.022

Ding, L., He, H., and Yang, Z. (2021). Thermal-fluid-solid coupling characteristics of a circular tube in two degrees of freedom flow-induced vibration. *Nucl. Power Eng.* 42 (2), 131. doi:10.13832/j.jnpe.2021.02.0131

Li, C., Wu, Y., Wang, Y., Wang, K., Wang, M., Tian, W., et al. (2020). Analysis on the behavior of dispersed plate-type fuel based on fluid-solid coupling method. *Prog. Nucl. Energy* 126, 103398. doi:10.1016/j.pnucene.2020.103398

Li, S. (2002). Calculation of anti-seismic design for xi'an pulsed reactor. *Nucl. Power Eng.* 23 (6), 12–15.

Liao, H., Wang, Y., Li, Y., Wang, K., Deng, Y., Su, M., et al. (2020). 3D fluid-solid coupling simulation for plate-type nuclear fuel assemblies under the irradiation condition. *Prog. Nucl. Energy* 126, 103428. doi:10.1016/j.pnucene.2020.103428

Northwest Institute of Nuclear Technology (2000). *Xi 'an pulsed reactor training textbook*. Appendix-2 (Internal Information).

Qian, H., Xie, Y., and Zhang, K. (2011). Preliminary analysis of flow induced vibration for AP1000 secondary core support assembly. *Nucl. Power Eng.* 32 (1), 145–148.

Tang, D., Bao, S., Lv, B., Cui, H., Luo, L., and Xu, M. (2019). Investigation of shedding patterns and its influences on lift performances of a cylinder bundle in cross flow. *J. Mech. Sci. Technol.* 33 (6), 2651–2663. doi:10.1007/s12206-019-0513-9

Wang, M., Bai, L., Wang, L., Qiu, S., Tian, W., and Su, G. (2017). Thermal hydraulic and stress coupling analysis for AP1000 Pressurized Thermal Shock (PTS) study under SBLOCA scenario. *Appl. Therm. Eng.* 122, 158–170. doi:10.1016/j.applthermaleng.2017.04.106

Wang, M., Fang, Di, Xiang, Y., Fei, Y., Wang, Y., Ren, W., et al. (2018). Study on the coolant mixing phenomenon in a 45° T junction based on the thermal-mechanical coupling method. *Appl. Therm. Eng.* 144, 600–613. doi:10.1016/j.applthermaleng.2018.08.073

Wang, M., Wang, Y., Tian, W., Qiu, S., and Su, G. (2021). Recent progress of CFD applications in PWR thermal hydraulics study and future directions. *Ann. Nucl. Energy* 150, 107836. doi:10.1016/j.anucene.2020.107836

Wang, Y., Wang, M., Jia, K., Tian, W., Qiu, S., and Su, G. (2022). Thermal fatigue analysis of structures subjected to liquid metal jets at different temperatures in the Gen-IV nuclear energy system. *Energy* 256, 124681. doi:10.1016/j.energy.2022.124681

Xu, J., Liu, L., and Yu, D. (2016). Research of flow induced vibration test for CAP1400 reactor internals. *Nucl. Power Eng.* 37 (2), 40–43.

Yang, J., Xi, Z., and Yu, D. (2016). Study on flow induced vibration in reactor internals of HPR1000. *Nucl. Power Eng.* 37 (S2), 37–39.

Ye, Q., Yu, D., and Fang, X. (2003). Flow induced vibration test for reactor internals for qinshan phase II NPP project. *Nucl. Power Eng.* 24 (1), 87–90.

Yu, D., Ma, J., and Xi, Z. (2016). Review of experimental research of flow-induced vibration of reactor internals. *Nucl. Power Eng.* 37 (2), 47.

Zang, F., and Liu, W. (2005). Flow induced vibration analysis of thermo-well at main pipe of reactor coolant loop. *Nucl. Power Eng.* 26 (4), 360–362.

Zhao, C. (2012). *An introduction to seismology*. Beijing: Peking University Press, 127.

Zhou, G., Yan, Z., and Xu, S. (2011). *Fluid mechanics*. second edition. Beijing: Higher Education Press, 114.

Frontiers in
Energy Research

Advances and innovation in sustainable, reliable and affordable energy

Explores sustainable and environmental developments in energy. It focuses on technological advances supporting Sustainable Development Goal 7: access to affordable, reliable, sustainable and modern energy for all.

Discover the latest Research Topics

See more →

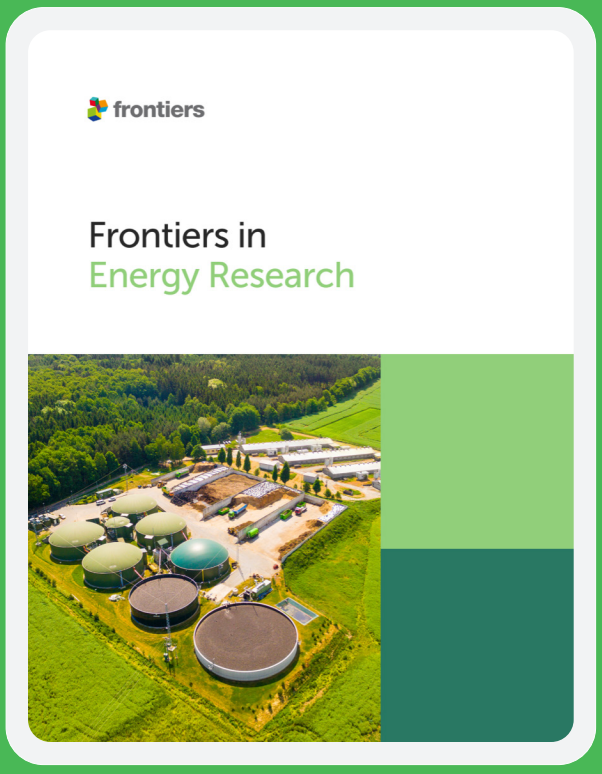

Frontiers

Avenue du Tribunal-Fédéral 34
1005 Lausanne, Switzerland
frontiersin.org

Contact us

+41 (0)21 510 17 00
frontiersin.org/about/contact